Vacuum Harmonic Generation in Slowly Varying Electromagnetic Backgrounds

Patrick Albert Böhl

München 2016

Vacuum Harmonic Generation in Slowly Varying Electromagnetic Backgrounds

Patrick Albert Böhl

Dissertation
an der Fakultät für Physik
der Ludwig–Maximilians–Universität
München

vorgelegt von
Patrick Albert Böhl
aus Bad Aibling

München, den 18.07.2016

Erstgutachter: Prof. Dr. Hartmut Ruhl
Zweitgutachter: Dr. Ben King
Tag der mündlichen Prüfung: 19.09.2016

Meinen Eltern gewidmet

Zusammenfassung

Relativistische Quantentheorie sagt die Existenz von virtuellen Elektron-Positron-Paaren vorher, die innerhalb einer typischen Zeitskala, der Compton-Zeit des Elektrons, erzeugt und wieder vernichtet werden. Diese virtuellen Dipole machen das Vakuum zu einem polarisierbaren Medium, was zu einer Abänderung der klassischen Maxwell-Gleichungen führt. Falls die Photonen eine Energie haben, welche deutlich kleiner ist als die Ruheenergie des Elektrons, werden diese Effekte durch die "Heisenberg-Euler"-Lagrange-Dichte im Rahmen der Quantenelektrodynamik beschrieben. Für Feldstärken, die klein sind im Vergleich zu dem "kritischen" Feld $E_{\mathrm{cr}} = 1.3 \cdot 10^{16}$ Vcm^{-1}, können diese Korrekturen zur Ausbreitung von elektromagnetischen Wellen explizit ausgewertet werden.

In dieser Arbeit werden die Maxwell-Gleichungen mitsamt dieser Korrekturen für schwache Felder numerisch in einer Anregungs-Abfrage-Konfiguration von zwei zusammenstoßenden, ebenen Wellen gelöst. Die entsprechende Wellengleichung wird dann analytisch gelöst. Die Anfangsbedingungen bestehen dabei aus einem (optischen) gaußschen "Abfrage"-Puls, der sich entgegengesetzt der "Anregung" in Form eines nur schwach variierenden, starken Hintergrunds, ausbreitet. Dabei werden Vakuumpolarisations-Effekte wie Doppelbrechung und die Erzeugung von Harmonischen (ähnlich zu Prozessen in einem nichtlinearen Kerr-Medium) untersucht.

Der erste Teil dieser Arbeit befasst sich mit der Analyse der zeitaufgelösten Dynamik der Kollision des Abfrage-Pulses mit einem gaußförmigen, starken Hintergrund. Dabei wird ein "Überlappungs"-Feld identifiziert, welches nur im Wechselwirkungsbereich vorhanden ist und verschwindet, wenn die Pulse weit voneinander entfernt sind.

Der zweite Teil untersucht die Erzeugung von höheren Harmonischen im Vakuum, wobei der Hintergrund nun als ebene Welle mit verschwindender Frequenz gewählt wird. Falls die Weglänge des Abfrage-Pulses im externen Feld groß genug ist, können höhere Harmonische durch hintereinander stattfindende Streuprozesse erzeugt werden. Für parallele Polarisationen der beiden Pulse wird ein Multi-Skalen-Parameter identifiziert, welcher angibt, wann diese Selbstwechselwirkung relevant wird. Wenn dieser Parameter gegen eins strebt, entwickelt der Abfrage-Puls eine Unstetigkeit in der Trägerfrequenz, welche auch "Schock" genannt wird.

Abstract

Relativistic quantum theory predicts the existence of virtual electron-positron pairs that are generated and annihilated over a typical time scale given by the electron Compton time. These virtual dipoles render the vacuum a polarisable medium thereby modifying the classical Maxwell vacuum equations. For photons with energy much smaller than the electron rest energy, these effects are well-described by the "Heisenberg-Euler" Lagrangian within the framework of Quantum Electrodynamics. In the case of field strengths that are small compared to the "critical" field $E_{\mathrm{cr}} = 1.3 \cdot 10^{16}\ \mathrm{Vcm}^{-1}$, the resulting nonlinear corrections to the electromagnetic wave propagation can be evaluated explicitly.

In this thesis, Maxwell equations that include these weak-field corrections are solved numerically for a "pump-probe" setup of two colliding plane waves. The corresponding wave equation is then solved analytically. The inital configuration is a weak (optical) Gaussian probe pulse that counterpropagates with a slowly-varying strong "background". Vacuum polarisation effects such as birefringence and the generation of harmonics (similar to processes in a nonlinear Kerr-medium) are analysed.

The first part of the thesis is dedicated to the study of the time-resolved dynamics when the probe collides with a Gaussian strong pulse and an "overlap" signal is identified, which is only present in the interaction region and disappears when the pulses are well separated.

The second part of the thesis considers vacuum high harmonic generation in a plane wave background of vanishing frequency. If the propagation length of the probe in the external field is long enough, higher harmonics of the probe frequency can be generated due to multiple scattering events. For parallel polarisations of probe and strong pulse, a multi-scale parameter is identified which indicates when this self-interaction becomes important. If this parameter approaches unity, the probe pulse develops a discontinuity or "shock" in the carrier wave.

Contents

1 Introduction **1**

1.1 Classical Electrodynamics 1

1.2 Electrodynamics in Media: Polarisation and Magnetisation 2

1.3 Development of QED and the Notion of Vacuum Polarisation 2

1.4 QED as a Lorentz Invariant Gauge Theory 5

2 Effective Field Theory and Modified Wave Propagation **9**

2.1 Path Integrals in QFT and Generating Functionals 9

2.2 Schwinger's Proper Time Formalism 11

2.3 Effective Action for QED 13

2.3.1 Propagator for Quadratic Hamiltonians 16

2.3.2 The Heisenberg-Euler Lagrangian 21

2.3.3 Weak-field Expansion 24

2.4 Modified Electromagnetic Wave Propagation 26

2.5 Scattering of Two Plane Wave Pulses 27

2.5.1 Diagrammatic Approach and Wave Mixing 28

2.5.2 Pump-Probe Setup with Quasi-constant Backgrounds 32

2.5.3 Dressed Diagrams for Four- and Six-photon Scattering 33

3 Solution of the Nonlinear Equations of Motion **35**

3.1 Analytical Solution of the Wave Equation 35

3.1.1 Forward and Backward Scattering 36

3.1.2 Overlap and Asymptotic Field 38

3.1.3 Lowest Order Iterations 40

3.1.4 Higher Iterations 43

3.2 Numerical Solution of Maxwell's Equations 47
3.2.1 Linear Case 47
3.2.2 Nonlinear Case 48

4 Harmonic-Generation and Shockwaves 51

4.1 Overlap Dynamics 51
4.1.1 Simulational Setup 51
4.1.2 Fundamental Harmonic 52
4.1.3 Second Harmonic 56
4.1.4 DC Component 61
4.1.5 Higher Harmonics 66
4.1.6 Discussion 67
4.2 Higher-order Processes and VHHG 70
4.2.1 Simulational Setup 71
4.2.2 All-order Phase Shift from Four-photon Scattering 72
4.2.3 All-order Solution for Six-photon Scattering 74
4.2.4 Other Processes in Vacuum Harmonic Generation 75
4.2.5 VHHG and Electromagnetic Shockwave 78
4.2.6 Polarisation Dependency 87
4.2.7 Strongly-dispersive Vacuum $\upsilon_1 \gg \nu_2$ 93
4.3 Discussion for VHHG 95
4.3.1 Ultra-short Probe Pulses 95
4.3.2 VHHG in Inhomogeneous Backgrounds 96
4.3.3 Comparison with Harmonic Generation in Laser-irradiated Plasmas 98
4.3.4 Validity of Approach 100
4.3.5 Measurability 101

5 Conclusions and Outlook 103

5.1 Conclusions 103
5.2 Outlook 104

Publications 105

Appendices **107**

A Conventions and Notation **109**

A.1 Conventions 109

A.2 List of Symbols 110

B Details for the HE Lagrangian **115**

B.1 Uniqueness of Flows on a Manifold 115

B.2 Relations Between the Matrix Blocks of S^t 116

B.3 Proof of $R(S^t) = 1\ \forall t$ 117

B.4 Symplectic Flow for Constant Electromagnetic Fields 118

B.5 $\det\exp\big(-g^{-1}Ft\big)$ and $\det\big(\frac{e}{2}F/\sinh\big(\frac{e}{2}g^{-1}Ft\big)\big)$ 120

B.6 $\operatorname{tr}\exp\big(\mathrm{i}\frac{e}{4}t\sigma^{\mu\nu}F_{\mu\nu}\big)$ 123

C Maxwell and Wave Equations in Polarisable Vacuum **125**

C.1 Nonlinear Maxwell Equations from an Interaction Lagrangian $\mathcal{L}_{\text{int}}(\mathcal{F},\mathcal{G})$. 125

C.2 Wave Equation with Source Terms 126

C.3 Covariant Maxwell Equations with Coefficients C_i 127

D Green's Function for the Wave Equation in $(1+1)$ Dimensions **135**

E Numerical Method **139**

E.1 Biased Finite Differences 139

E.2 Matrices $\mathbf{X}$ and $\mathbf{Y}$ 140

Chapter 1

Introduction

1.1 Classical Electrodynamics

Classical Maxwell theory describes an enormous variety of phenomena, ranging from long radio waves (wavelength $\lambda \approx 10^8$ cm) to microwaves $\lambda \approx 1$ cm down to x-rays with $\lambda \approx 10^{-8}$ cm and even hard γ-radiation on the femtometre scale or smaller. Electromagnetism is not only about the propagation of light in vacuum, but also the interaction with charged, massive particles. The set of partial differential equations describing the interaction of light with matter are the four Maxwell equations (in Gaussian cgs units with $c = 1$),

$$\begin{aligned} \nabla \wedge \mathbf{B} - \partial_t \mathbf{E} &= 4\pi \mathbf{J}_{\text{matter}} \ , \\ \nabla \cdot \mathbf{E} &= 4\pi \rho_{\text{matter}} \ , \\ \nabla \wedge \mathbf{E} + \partial_t \mathbf{B} &= 0 \ , \\ \nabla \cdot \mathbf{B} &= 0 \ , \end{aligned} \tag{1.1}$$

together with the Lorentz force equation

$$\frac{\mathrm{d}\mathbf{p}}{\mathrm{d}t} = q(\mathbf{E} + \mathbf{v} \wedge \mathbf{B}) \ ,$$

where $\mathbf{E}$ and $\mathbf{B}$ are the electric and magnetic field, $\mathbf{J}_{\text{matter}}$ and ρ_{matter} are the current and charge density, $\mathbf{p} = m\mathbf{v}$ the momentum, q the charge and m the mass of the particle. One of the major characteristics of Maxwell equations is that they are a set of linear differential equations and the superposition principle holds: The sum of two solutions to (1.1) is again a solution. This is due to the fact that, classically, light does not interact with light.
An alternative and equivalent formulation of the system of coupled first order differential equations (1.1) are the inhomogeneous wave equations for the electric and magnetic fields (which are derived in Appendix C.2)

$$\begin{aligned} \Box \mathbf{E}(t, \mathbf{x}) &= -4\pi \nabla \rho_{\text{matter}} - 4\pi \partial_t \mathbf{J}_{\text{matter}} \ , \\ \Box \mathbf{B}(t, \mathbf{x}) &= 4\pi \nabla \wedge \mathbf{J}_{\text{matter}} \ , \end{aligned}$$

where $\Box := \partial_t^2 - \Delta$ is the d'Alembert operator. The Maxwell equations can also be modified to describe wave propagation in media as we see in the next section.

1.2 Electrodynamics in Media: Polarisation and Magnetisation

For electromagnetic waves in media, the equations (1.1) now include two additional fields

$$\begin{aligned} \nabla \cdot \mathbf{D} &= 4\pi\rho_{\text{matter}} \ , \\ \nabla \wedge \mathbf{H} - \partial_t \mathbf{D} &= 4\pi \mathbf{J}_{\text{matter}} \ , \\ \nabla \cdot \mathbf{B} &= 0 \ , \\ \nabla \wedge \mathbf{E} + \partial_t \mathbf{B} &= 0 \end{aligned} \tag{1.2}$$

with the electric displacement field $\mathbf{D}$ and the magnetising field $\mathbf{H}$. The electric displacement thereby consists of two parts

$$\mathbf{D} = \mathbf{E} + 4\pi\mathbf{P} \ . \tag{1.3}$$

$\mathbf{P}$ is called *polarisation* and can be interpreted as the response of the medium when an external field electric field $\mathbf{E}$ is applied. Due to the external field $\mathbf{E}$, the electric charges in the medium are separated and generate an additional polarisation field $\mathbf{P}$, the resulting field is then given by $\mathbf{D}$.
Similarly, the magnetising field $\mathbf{H}$ consists of the sum of the applied magnetic field $\mathbf{B}$ and the response in form of the *magnetisation* $\mathbf{M}$:

$$\mathbf{H} = \mathbf{B} - 4\pi\mathbf{M} \ . \tag{1.4}$$

We note that in vacuum the relations

$$\mathbf{E} = \mathbf{D} \ , \qquad\qquad \mathbf{B} = \mathbf{H}$$

hold as $\mathbf{M} = \mathbf{P} = \mathbf{0}$.
Since the fields $\mathbf{P}$ and $\mathbf{M}$ can be interpreted as the response to the external applied fields, one can make an ansatz of a power series in the external fields [FW63] for both fields:

$$\begin{aligned} P_i &= \sum_j (\chi_{\text{e}}^{(1)})_{ij} E^j + \sum_{jk} (\chi_{\text{e}}^{(2)})_{ijk} E^j E^k + \sum_{jkl} (\chi_{\text{e}}^{(3)})_{ijkl} E^j E^k E^l \ , \\ M_i &= \sum_j (\chi_{\text{m}}^{(1)})_{ij} B^j + \sum_{jk} (\chi_{\text{m}}^{(2)})_{ijk} B^j B^k + \sum_{jkl} (\chi_{\text{m}}^{(3)})_{ijkl} B^j B^k B^l \ , \end{aligned} \tag{1.5}$$

where $\chi_{\text{e,m}}^{(n)}$ are the n-th electric/magnetic susceptibility tensors. For example, $\chi_{\text{e}}^{(1)} \neq 0$ corresponds to a linear dispersive medium and $\chi_{\text{e}}^{(3)} \neq 0$ is typical for a nonlinear Kerr-medium.

1.3 Development of QED and the Notion of Vacuum Polarisation

While Maxwell already formulated his theory of electromagnetism in 1863 [Max63], several decades later, at the beginning of the 20th century, a new era of modern physics began as (non-relativistic) quantum theory was invented by Planck, Einstein, Pauli, Bohr and many others. It took more than 20 years to put it in its modern form of matrix mechanics developed by Heisenberg, Jordan and Born and, equivalently, wave

mechanics based on the Schrödinger equation.
The first relativistic theory of the electron was devised by Dirac in 1927 [Dir27]. The positive energy solutions to the Dirac equation, which is introduced later, were interpreted as "holes" in the sense of a lack of electrons in the "Dirac sea", an infinite accumulation of particles with negative energy. Only four years later, Dirac postulated that these holes should be interpreted as positrons [Dir31], the anti-particle of the electron with identical quantum numbers but opposite charge.
That was the birth of what is today known as "Quantum Electrodynamics" (QED).
In the same period, Sauter [Sau31] solved the Dirac equation in a homogeneous electric field and was able to confirm Bohr's conjecture that finite field gradients comparable to or higher than the rest energy of the electron mc^2 over a Compton wavelength $\lambda_C = h/mc$, yield a finite probability to create real electron-positron pairs.
This led to the notion of the "critical" or "Sauter" field (later also called "Schwinger" field)

$$E_{\mathrm{cr}} = \frac{m^2c^2}{e\hbar} \approx 1.3 \cdot 10^{16} \ \frac{\mathrm{V}}{\mathrm{cm}} \ . \tag{1.6}$$

E_{cr} is the field needed to create the difference of potential energy of the size of the electron rest energy over a Compton-wavelength λ_C.
The associated "critical" magnetic field is $B_{\mathrm{cr}} = 4.4 \cdot 10^{13}$ G. If not written explicitly, we use natural units such that $\hbar = c = 1$ throughout such that the electric and magnetic fields have the same units, $E_{\mathrm{cr}} = B_{\mathrm{cr}}$.
Soon afterwards, Halpern [Hal33] and Debye (see footnote in [EK35]) hypothesised the interaction of light with light via virtual electron-positron pairs, which obviously violates the classical superposition principle. Following this hypothesis, Euler and Kockel [EK35] calculated the effective Lagrangian for light-by-light scattering in the limit of weak fields compared to the critical field E_{cr} and low frequencies $\hbar\omega \ll mc^2$ and were the first to give the order of magnitude of the light-by-light scattering cross-section, which is [BLP82]

$$\sigma_{\gamma\gamma} = \frac{973}{10125\pi}\alpha^4 \left(\frac{\omega}{m}\right)^6 \lambda\!\!\!^{-2}_{\mathrm{C}} \tag{1.7}$$

in this limit and $\lambda\!\!\!^{-}_{\mathrm{C}} = \lambda_C/2\pi$ is the reduced Compton wavelength. For an optical photon with $\hbar\omega = 2$ eV (corresponding to a wavelength $\lambda = 0.62$ μm) the cross-section is $\sigma_{\gamma\gamma} = 4.4 \cdot 10^{-64}$ cm and as such, extremely small.
While Euler and Kockel calculated corrections nonlinear in the fields, Uehling [Ueh35] and Serber [Ser35] calculated the corrections nonlinear in the coordinates, including a logarithmic correction to the Coulomb potential at small distances induced from virtual e^+e^- pairs.
In 1936, Heisenberg and Euler were able generalise the results from Euler and Kockel to an analytical all-order expression for the nonlinear corrections in the electromagnetic fields valid for arbitrary strong field amplitudes in the limit of constant fields [HE36].
Soon after the derivation of what is nowadays called the "Heisenberg-Euler" Lagrangian (HE Lagrangian), Weisskopf [Wei36] was able to re-derive the Lagrangian in a simpler way and stated clearly, that empty space or the "vacuum" can be seen as a polarisable medium with field-dependent electric and magnetic polarisability. For a more extensive review of the historical developments, the reader is refered to [Dun12].
The quantum vacuum can therefore be imagined as virtual electron-positron pairs that are generated and annihilated within a reduced Compton wavelength and "live" for a (reduced) Compton time $t_C = \lambda_C/c$ as it is allowed by the time-energy uncertainty [SN11]

$$\Delta E \Delta t \approx \hbar \ . \tag{1.8}$$

This idea is illustrated in the left panel of Fig. 1.1 with a random orientation of the dipole moments of the e^+e^- pairs. The reduced Compton-wavelength $\lambda\!\!\!^{-}_{\mathrm{C}}$ and reduced Compton-time give therefore naturally the typical length- and timescales of QED with [MNT15]:

$$\lambda\!\!\!^{-}_{\mathrm{C}} \approx 3.86 \cdot 10^{-11}\ \mathrm{cm} = 3.11 \cdot 10^{-7}\ \tfrac{1}{\mathrm{eV}}\ ,$$
$$t_{\mathrm{C}} \approx 1.29 \cdot 10^{-21}\ \mathrm{s} = 3.11 \cdot 10^{-7}\ \tfrac{1}{\mathrm{eV}}\ .$$

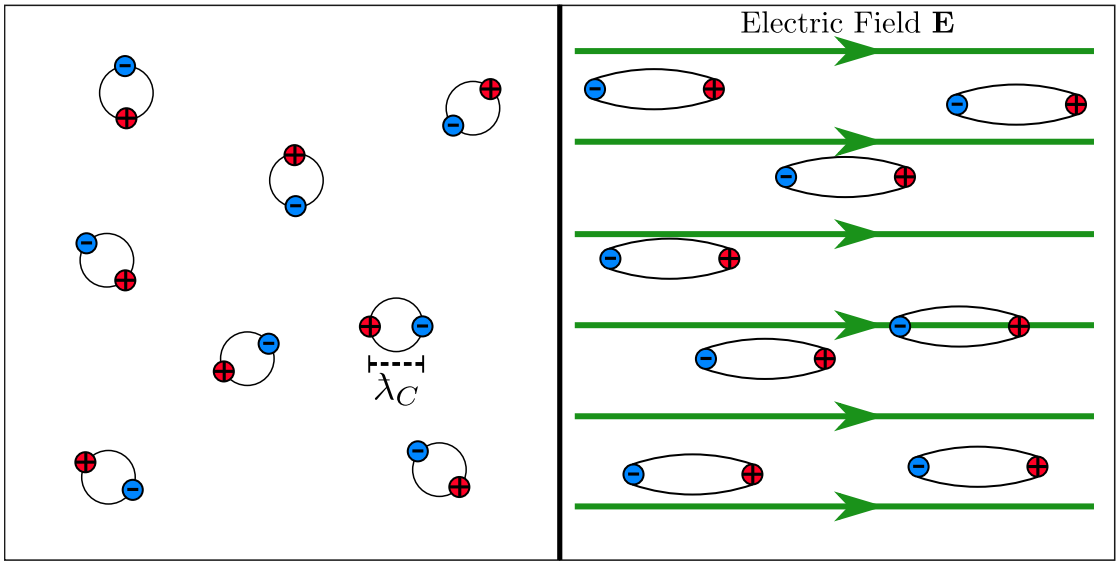

Figure 1.1: In the left panel virtual electron-positron pairs are created and annihilated in vacuum within a Compton-wavelength $\lambda\!\!\!^{-}_{\mathrm{C}}$ with a corresponding "life-time" (Compton-time) t_{C} with arbitrary relative orientation. If an electric field is applied, these pairs polarise the vacuum as it shown in the right panel.

The behaviour of the virtual pairs changes in the presence of a background field as it is shown for an electric field in the right panel of Fig. 1.1. The dipoles align according to the external field similar to a "normal" polarisable medium. With the interpretation of the vacuum as a polarisable (nonlinear) medium, one expects similar effects as in classical electrodynamics. Among the most prominent predictions are vacuum birefringence [Tol52; BB67a] with resulting polarisation rotation [Kin10], vacuum diffraction [DHK06; KPK10], the generation of higher harmonics [FN07; BB81] and photon splitting [Adl71; BB70]. The effects of birefringence and harmonic generation are studied in this thesis and explained later in more detail, for a comprehensive review of the other phenomena, the reader is refered to [MS06; Di +12; KH16].
In the next section we introduce the QED-action and make the connection between terms in the Lagrangian and the polarisation $\mathbf{P}$ and magnetisation $\mathbf{M}$.

1.4 QED as a Lorentz Invariant Gauge Theory

As Maxwell's theory is invariant under Lorentz transformations, it can also be put in a manifestly covariant form. The equations (1.1) can then be compactly written as

$$\partial_\mu F^{\mu\nu} = 4\pi J^\mu_{\text{matter}} \ , \tag{1.9}$$
$$\partial_\mu \star F^{\mu\nu} = 0 \ , \tag{1.10}$$

where $F_{\mu\nu}$ is the Faraday tensor, $F_{\mu\nu} = \partial_\mu A_\nu - \partial_\nu A_\mu$ with A_μ being the gauge potential, $\star F_{\mu\nu}$ its dual and $j^\mu_{\text{matter}} = (\rho_{\text{matter}}, \mathbf{J}_{\text{matter}})$. The components of F and $\star F$ are given in Appendix A.1.
There are two fundamental principles for modern quantum field theories. The first one is the postulation of gauge symmetry under a certain gauge group, which is simply $U(1)$ in the case of QED. Furthermore, the equations of motion should be derived from an action principle, which is in the Lagrangian description

$$\delta S_{\text{QED}} = \delta \int \mathrm{d}^4x \ \mathcal{L}_{\text{QED}} = 0 \ , \tag{1.11}$$

where the QED action S_{QED} is given by the integral $S_{\text{QED}} = \int \mathrm{d}^4x \ \mathcal{L}_{\text{QED}}$ over the Lagrangian density $\mathcal{L}_{\text{QED}}$.
The massive particles (electrons and positrons) in QED are represented as spinor fields Ψ that are minimally coupled to the gauge (photon) field A_μ. The equation of motion for the spinor fields is the Dirac equation

$$(i\not{D} - m)\Psi = (i\not{\partial} - e\not{A} - m)\Psi = 0 \ , \tag{1.12}$$

where $\not{D} = \gamma^\mu D_\mu$ with γ^μ being the Dirac matrices satisfying the Clifford algebra $\gamma^\mu\gamma^\nu + \gamma^\nu\gamma^\mu = 2g^{\mu\nu}$ and $D_\mu := \partial_\mu + ieA_\mu$ is the covariant derivative.
A suitable Lagrangian that reproduces (1.9) and (1.12) is given by

$$\begin{aligned} \mathcal{L}_{\text{QED}} &= \mathcal{L}_{\text{MW}} + \bar{\Psi}(i\not{D} - m)\Psi \\ &= -\frac{1}{16\pi} F_{\mu\nu}F^{\mu\nu} + \bar{\Psi}(i\not{\partial} - m)\Psi - A_\mu J^\mu_{\text{matter}} \ , \end{aligned} \tag{1.13}$$

where we defined the free Maxwell Lagrangian as $\mathcal{L}_{\text{MW}} = -\frac{1}{16\pi}F_{\mu\nu}F^{\mu\nu}$, the current $J^\mu_{\text{matter}} := e\bar{\Psi}\gamma^\mu\Psi$ and $\bar{\Psi} := \Psi^\dagger\gamma^0$ is the Dirac conjugate of Ψ. $\delta S_{\text{QED}} = 0$ is then equivalent to the Euler-Lagrange equations

$$\begin{aligned} \partial_\mu \frac{\partial \mathcal{L}_{\text{QED}}}{\partial(\partial_\mu A_\nu)} - \frac{\partial \mathcal{L}_{\text{QED}}}{\partial A_\nu} &= 0 \ , \\ \partial_\mu \frac{\partial \mathcal{L}_{\text{QED}}}{\partial(\partial_\mu \bar{\Psi})} - \frac{\partial \mathcal{L}_{\text{QED}}}{\partial \bar{\Psi}} &= 0 \ , \\ \partial_\mu \frac{\partial \mathcal{L}_{\text{QED}}}{\partial(\partial_\mu \Psi)} - \frac{\partial \mathcal{L}_{\text{QED}}}{\partial \Psi} &= 0 \ , \end{aligned}$$

where the first equation yields (1.9) and the second and third equation yield the Dirac equation (1.12) and its conjugate. We note that (1.10) is the Bianchi-identity [Sza11] which is automatically fulfilled due to the gauge symmetry.
The QED Lagrangian (1.13) is quadratic in the electromagnetic fields $F_{\mu\nu}$ which corresponds to free photon propagation with one incoming and one outgoing photon. That photons do not interact classically with each other (and the equations of motion are therefore linear, as explained above) is a direct consequence of the fact that photons are

uncharged under the Abelian gauge group $U(1)$.
Now the only gauge and Lorentz invariants that can be constructed for the electromagnetic field are (up to constants)

$$\begin{aligned} \mathcal{F} &= -\frac{1}{4} F_{\mu\nu} F^{\mu\nu} = \frac{1}{2}(E^2 - B^2) \ , \\ \mathcal{G} &= -\frac{1}{4} F_{\mu\nu} \star F^{\mu\nu} = \mathbf{E} \cdot \mathbf{B} \ . \end{aligned} \tag{1.14}$$

Since every interaction term for pure light-light interaction must be Lorentz and gauge invariant, it can only be constructed as functions (most of the time polynomials) of $\mathcal{F}$ and $\mathcal{G}$, where each factor in the polynomials corresponds to two external photons. A term $\sim (g_1 \mathcal{F}^2 + g_2 \mathcal{G}^2)$ with some coupling constants g_1, g_2 then describes four-photon interaction and in general $\sim g \mathcal{F}^i \mathcal{G}^{2j}$ corresponds to $2(i + 2j)$-photon scattering, where i, j are integers. We note that only even powers of $\mathcal{G}$ can appear as $\mathcal{G}$ is a pseudo-scalar and the Lagrangian needs to be a proper Lorentz scalar.
So under the assumption that the Lagrangian includes an additional interaction $\mathcal{L}_{\text{int}}(\mathcal{F}, \mathcal{G})$ for purely photons (which corresponds to taking vacuum polarisation into account) that depends only on the field invariants, it is shown in Appendix C.1 that these terms give precisely contributions to the Maxwell equations (1.2) that can be interpreted as polarisation $\mathbf{P}$ and magnetisation $\mathbf{M}$ (as they are used in e.g. [BB81] or [DHK06]) where

$$\mathbf{P} = \frac{\partial \mathcal{L}_{\text{int}}}{\partial \mathbf{E}} \qquad\qquad \mathbf{M} = \frac{\partial \mathcal{L}_{\text{int}}}{\partial \mathbf{B}} \ . \tag{1.15}$$

Being a relativistic effect however, the magnetic and the electric field appear in on an equal footing in both $\mathbf{P}$ and $\mathbf{M}$ in contrast to the ansatz (1.5) in normal polarisable media.

As we now have introduced the notion of vacuum polarisation and certain relations of this effect to quantities in the Lagrangian, we give the outline of the thesis:

- In the next chapter we re-derive the HE Lagrangian for constant electromagnetic fields. As a first step we briefly introduce generating functionals for correlation functions in the path integral formalism. Then the effective action Γ for QED is introduced using Schwinger's "proper time" method. The calculation of Γ is thereby reduced to finding the Klein-Gordon-propagator in position space in a constant external field. Then a general formula for the propagator of an arbitrary quadratic Hamiltonian with constant metric is derived. The case of the Klein-Gordon-propagator is then an application of the result for a quadratic Hamiltonian and the HE Lagrangian is derived in its final form, where the details are given in Appendix B. Employing a weak-field expansion, corrections (corresponding to four-, six- and eight-photon scattering) to Maxwell's equations and the wave equation are derived and the pump-probe setup of two colliding plane waves is introduced. As the effect of the strong pulse (pump) on the probe is treated classically in the fourth chapter, dressed diagrams for the probe propagation are also introduced.

- In the third chapter, the two different approaches to nonlinear wave propagation used in this thesis are presented. First, the analytical solution of the wave equation using an iterative ansatz based on the appropriate Green's function in $(1 + 1)$

dimensions is introduced that naturally leads to the notion of forward (along the direction of the probe propagation) and backward scattered (along with the strong pulse) signals. From the first iteration, the "overlap" signal is identified as a boundary term in the integration of the wave equation, which is only present in the interaction region of both pulses and disappears when both are well-separated. Then higher iterations neglecting the change of the strong field are carried out and interpreted using the dressed diagrams from chapter two. The second part of the chapter is dedicated to the numerical solution of the Maxwell equations including the weak-field nonlinearities. For the plane-wave setup, these equations can be written in matrix form and brought to an explicit form of first-order partial differential equations via matrix inversion. The equations are then discretised in space using the "Pseudo-characteristic Method of Lines" yielding a coupled system of ordinary differential equations (ODEs) and then integrated using the ODE-solver CVODE.

- The fourth chapter is then the application of the numerical and analytical methods and consists of two parts. The first one treats the time-resolved dynamics of the interaction including four- and six-photon scattering of a Gaussian optical probe and (strong) slowly-varying Gaussian pulse including an analysis of the "overlap" signal introduced in chapter 2. Thereby changes in the first harmonic of the probe can be interpreted as polarisation dependent vacuum birefringence due to the strong pulse, but also higher harmonics of the probe pulse are generated. The back-reaction of the probe on the strong pulse also leads to components with frequencies much smaller than the probe frequency. Finally, a comparison between the generation of the second harmonic from the asymptotic signal from six-photon scattering and the overlap field from four-photon scattering is given.
  In the second part of this chapter, the Gaussian background is replaced by a "square pulse" with vanishing frequency. In the analytical model, an all-order-solution for the forward-scattered probe field in the case of parallel polarisations of the probe and strong pulse is derived. This solution can be written in terms of the original probe with a probe-dependent refractive index and a multi-scale parameter is identified. This parameter depends on the propagation length in the strong background and it is found that if this parameter approaches unity, the probe develops a discontinuity or shock due to high harmonics in the spectrum. For non-parallel polarisations it is found numerically, that generation of these higher frequency components is strongly suppressed and also very sensitive to dispersive effects. Finally, we conclude with a comparison to plasma physics and a discussion of the applicability and the possible generalisation of the results obtained in this thesis.

- Appendix A summarises the conventions used in this thesis, in Appendix C the formulas for the Maxwell and wave equations for additional photon-photon interactions are derived. The general form of Maxwell's equations for a Lagrangian that depends on the secular invariants is calculated and the coefficients appearing in this expression can be used to express the coefficient matrices for the numerical method. In Appendix D the Green's function for the wave equation in $(1 + 1)$ dimensions is derived. Finally, the formulas for the biased finite differences and the nonlinear matrices used in the numerical simulation are given.

Chapter 2

Effective Field Theory and Modified Wave Propagation

We introduce path integrals and the one-loop effective action for QED using Schwinger's proper time method. The Heisenberg-Euler Lagrangian, the effective Lagrangian for QED in constant electromagnetic backgrounds, is then re-derived from the general expression of the Green's function for a quadratic Hamiltonian on phase space. A weak-field expansion of the Lagrangian is given and the resulting nonlinear Maxwell and wave equations are derived. The setup of two counter-propagating plane-wave pulses considered in the thesis is introduced and we comment on the allowed possible processes for two colliding plane waves.

2.1 Path Integrals in QFT and Generating Functionals

In this section we briefly review the concept of generating functionals for correlation functions. We use the case of a free Klein-Gordon field to show how to obtain only the connected correlation functions from the generating functional. The same argument is then be used in section 2.3 to obtain the connected correlation function in the interacting case, the fully dressed propagator. For an extensive introduction, the reader is referred to standard text books like [PS95; Sch13; Ryd96].
Among the main (measurable) quantities one is interested in in Quantum field Theory (QFT) are cross-sections and decay rates. Those quantities can be calculated using the so-called *S-Matrix*. If one considers a process of incoming particles whose initial configuration is α and end up in a final configuration β, then the probability amplitude for this process to happen is denoted as $S_{\beta\alpha}$. The main idea is to consider the states α asymptotically as free states, when all interaction is turned off. The transition amplitude is then defined as

$$S_{\beta\alpha} = \langle \beta, t \to \infty | \alpha, t \to -\infty \rangle \ .$$

Via the LSZ-reduction formula, the calculation of the S-matrix can be related to the calculation of n-point correlation functions $G_n(x_1, x_2, \ldots, x_n)$ which are defined as time-ordered vacuum expectation values of certain (possibly different) fields. Let us first consider a free uncharged scalar field ϕ which satisfies the Klein-Gordon equation

$$(\Box + m^2)\phi(x) = 0 \ , \tag{2.1}$$

where $\Box := \partial_t^2 - \Delta$ is the d'Alembert operator and we set $\hbar = c = 1$. Then the n-point correlation functions $G_n(x_1, x_2, \ldots, x_n)$ are defined as vacuum expectation values of time-ordered products of the field ϕ:

$$G_n(x_1, x_2 \ldots, x_n) = \langle 0| \, T \left\{ \phi(x_1)\phi(x_2) \ldots \phi(x_n) \right\} |0\rangle \ .$$

Now one way to calculate the vacuum expectation value of time ordered products of field operators is via the path integral formulation:

$$\langle 0| \, T \left\{ \phi(x_1)\phi(x_2) \ldots \phi(x_n) \right\} |0\rangle = \frac{\int \mathcal{D}\phi \ \phi(x_1)\phi(x_2) \ldots \phi(x_n) \ \mathrm{e}^{iS_{\mathrm{cl}}[\phi]}}{\int \mathcal{D}\phi \ \mathrm{e}^{iS_{\mathrm{cl}}[\phi]}} \ ,$$

where $\mathcal{D}\phi$ means the integration over all classical field-configurations $\phi(x)$ which are weighted by the factor $\mathrm{e}^{iS_{\mathrm{cl}}[\phi]}$ where $S_{\mathrm{cl}}[\phi] = \int \mathrm{d}^4x \ \mathcal{L}(\phi)$ is the classical action.
To calculate the quantities $\int \mathcal{D}\phi \ \phi(x_1)\phi(x_2) \ldots \phi(x_n) \ \mathrm{e}^{iS_{\mathrm{cl}}[\phi]}$, it is convenient to introduce an external source j (which is not to be confused with J_{matter}) which couples to the field ϕ. Then one can define a generating functional $Z[j]$ for the n-point correlation function as the path integral

$$Z[j] = \int \mathcal{D}\phi \exp\left(-i \int \mathrm{d}^4x (\frac{1}{2}\phi(\Box + m^2 - i\epsilon)\phi - j\phi) \right) \ , \tag{2.2}$$

where the $i\epsilon$ is introduced to assure the proper boundary conditions. Then all correlation functions can be expressed as functional derivatives of $Z[j]$ with respect to the source j:

$$\langle 0| \, T \left\{ \phi(x_1)\phi(x_2) \ldots \phi(x_n) \right\} |0\rangle = \frac{1}{i^n} \frac{1}{Z[0]} \frac{\delta^n Z}{\delta j(x_1) \ldots \delta j(x_n)} \Big|_{j=0} \ ,$$

where one sets the currents j to zero after evaluating the derivatives. Using the identity

$$\int \mathcal{D}\phi \exp\left(-[\frac{1}{2}(\phi A \phi) + b\phi] \right) = \exp\left(\frac{1}{2}(bA^{-1}b) \right) \det(A)^{-\frac{1}{2}} \ ,$$

$Z[j]$ can be written as

$$Z[j] = \mathcal{N} \exp\left(\frac{1}{2} \int \mathrm{d}^4x \ \mathrm{d}^4y \ j(x) S_{\mathrm{F}}(x-y) j(y) \right) \ , \tag{2.3}$$

where

$$\mathcal{N} = \int \mathcal{D}\phi \exp\left[-\frac{i}{2} \int \mathrm{d}^4x \ \phi(\Box + m^2 - i\epsilon)\phi \right]$$

is an (infinite) constant and $S_{\mathrm{F}}(x-y)$ is the Feynman propagator satisfying

$$(\Box + m^2 - i\epsilon) S_{\mathrm{F}}(x - x') = -i\delta^4(x - x') \ . \tag{2.4}$$

Using the expression (2.3), one can expand the exponential pictorially (ignoring $\mathcal{N}$) which is shown in Fig. 2.1.

Apart from the first two terms, all higher graphs are disconnected. One can further define a generating functional which only gives the connected Feynman diagrams,

$$W[j] = -i \ln Z[j] \tag{2.5}$$

such that the only connected n-point correlation function generated by $W[j]$ is the Feynman propagator. So we note that taking the logarithm of the generating functional

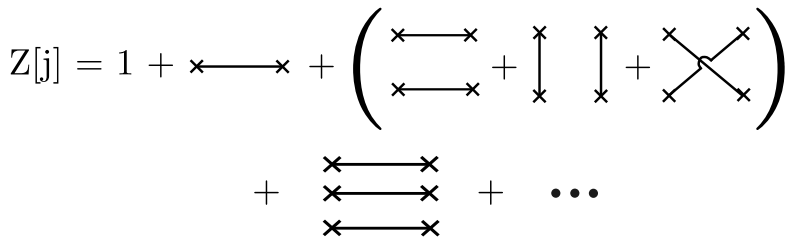

Figure 2.1: Pictorial expansion of the generating functional $Z[j]$ (ignoring the constant $\mathcal{N}$) into a trivial part denoted by 1, the Feynman propagator as a straight line and all higher order graphs that are disconnected consisting only of free propagators. The crosses indicate the coupling to the current j.

of the free theory gives only the second term in Fig. 2.1, the free propagator when the js are set to zero.
In the next section we introduce Schwinger's proper time formalism which is used to relate the Feynman propagator (the connected correlation function for the Klein-Gordon equation) to the amplitude $\langle x|\, \mathrm{e}^{-is\hat{H}}\, |x'\rangle$ with a certain Hamiltonian $\hat{H}$ and the additional proper time parameter s, which is not to be confused with the proper time on the world line of the particle, most of the time called τ. This connection is then used to motivate the notion of the *one-loop effective action*.

2.2 Schwinger's Proper Time Formalism

This section is based on [Sch13].
In non-relativistic quantum mechanics, the fundamental objects of interest are observables that are represented as self-adjoint operators like position $\hat{\vec{x}}$ or mentum $\hat{\vec{p}}$ whereas time is mostly only considered as a parameter. Now for relativistic theories both time and space must be on equal footings. So there are two possible ways out [Sre07]:
Introduce the notion of a time-operator or degrade also position to be a parameter or label.
Pauli already pointed out in 1933 ([Pau33; Pau+58], see [Bus08] for an extensive review) that the existence of a self-adjoint time-operator would lead to an energy spectrum $E \in [-\infty, \infty]$ in the range of the entire real line. He concluded that for most physical relevant systems, which have discrete, bounded or semi-bounded energy spectra, the concept of a self-adjoint time-operator "must fundamentally be abandoned" [Bus08]. Although Pauli's statement is not entirely correct, introducing a time-operator in quantum mechanics is difficult in practice [Sre07]. The second choice, taking also the coordinates $\vec{x}$ as parameter, is the base of modern quantum field theory in which the main objects are fields that are operators depending on the local coordinates $(t, \vec{x})$ as "parameters".
Now Schwinger's idea is to view the considered system as a four-dimensional non-relativistic quantum mechanics with an additional (proper) time parameter s. To illustrate further the interpretation of what is called "proper time method", we consider again the Feynman propagator of the Klein-Gordon-Equation

$$(\Box + m^2 - i\epsilon) S_{\mathrm{F}}(x, x') = -i\delta^4(x - x') \ ,$$

where $\epsilon > 0$ is there to ensure the appropriate boundary conditions [Ryd96]. The key observation for the whole formalism is the identity

$$\frac{i}{A + i\epsilon} = \int_0^\infty \mathrm{d}s \ \mathrm{e}^{is(A+i\epsilon)} \ , \tag{2.6}$$

where again $\epsilon > 0$. Now we express $S_{\mathrm{F}}(x)$ by the inverse of its Fourier transform $\tilde{G}(p, m)$:

$$S_{\mathrm{F}}(x, x') = \int \frac{\mathrm{d}^4 p}{(2\pi)^4}\, \mathrm{e}^{ip(x-x')}\, \tilde{G}(p, m)\ .$$

Here we assumed translational invariance such that the Fourier transform depends only on the difference $(x - x')$. Applying the Klein-Gordon-operator $\Box + m^2 - i\epsilon$ then yields

$$(\Box + m^2 - i\epsilon) S_{\mathrm{F}}(x, x') = \int \frac{\mathrm{d}^4 p}{(2\pi)^4}\, \mathrm{e}^{ip(x-x')} \tilde{G}(p, m)(-p^2 + m^2 - i\epsilon)\ . \tag{2.7}$$

Using the identity

$$\delta^4(x - x') = \int \frac{\mathrm{d}^4 p}{(2\pi)^4}\, \mathrm{e}^{ip(x-x')}$$

on the right-hand side of (2.4) then gives the expression for the propagator in momentum space

$$\tilde{G}(p, m) = \frac{i}{p^2 - m^2 + i\epsilon}\ .$$

With (2.6), we can write

$$S_{\mathrm{F}}(x, x') = \int \frac{\mathrm{d}^4 p}{(2\pi)^4} \mathrm{e}^{ip(x-x')} \int_0^\infty \mathrm{d}s\, \mathrm{e}^{\, is(p^2 - m^2 + i\epsilon)}\ . \tag{2.8}$$

Now we proceed by introducing the one-particle Hilbert space with state vectors $|x\rangle\,, |p\rangle$ and introduce operators $\hat{p}^\mu, \hat{x}^\mu$ satisfying the eigenvalue equations $\hat{p}^\mu |p\rangle = p^\mu |p\rangle$ and $\hat{x}^\mu |x\rangle = x^\mu |x\rangle$. Further, we assume that these states form a complete basis:

$$\mathbb{1} = \int \frac{\mathrm{d}^4 x}{(2\pi)^4} |x\rangle\langle x| = \int \frac{\mathrm{d}^4 p}{(2\pi)^4} |p\rangle\langle p|\ .$$

The momentum eigenfunctions in position space are given by

$$\langle x|p\rangle = \mathrm{e}^{ipx}\ .$$

Using these eigenfunctions, we can write

$$\begin{aligned} S_{\mathrm{F}}(x, x') &= \int \frac{\mathrm{d}^4 p}{(2\pi)^4} \int_0^\infty \mathrm{d}s\, \mathrm{e}^{ip(x-x')} \mathrm{e}^{is(p^2 - m^2 + i\epsilon)} \\ &= \int \frac{\mathrm{d}^4 p}{(2\pi)^4} \int_0^\infty \mathrm{d}s\ \langle x|p\rangle \left\langle p\middle|x'\right\rangle\ \mathrm{e}^{is(p^2 - m^2 + i\epsilon)} \\ &= \int \frac{\mathrm{d}^4 p}{(2\pi)^4} \langle x|p\rangle \langle p| \int_0^\infty \mathrm{d}s\, \mathrm{e}^{\, is(\hat{p}^2 - m^2 + i\epsilon)} \left|x'\right\rangle \\ &= \int_0^\infty \mathrm{d}s\, \mathrm{e}^{-ism^2} \mathrm{e}^{-s\epsilon} \langle x|\, \mathrm{e}^{is\hat{p}^2} \left|x'\right\rangle\ . \end{aligned}$$

Defining (proper) time-dependent states $|x; s\rangle := \mathrm{e}^{-is\mathcal{H}} |x\rangle$ with $\mathcal{H} = -\hat{p}^2$, this can be rewritten as

$$\begin{aligned} S_{\mathrm{F}}(x; x') &= \int_0^\infty \mathrm{d}s\, \mathrm{e}^{-ism^2} \mathrm{e}^{-s\epsilon} \langle x|\, \mathrm{e}^{-i\mathcal{H}} \left|x'\right\rangle \\ &= \int_0^\infty \mathrm{d}s\, \mathrm{e}^{-ism^2} \mathrm{e}^{-s\epsilon} \left\langle x; 0\middle|x'; s\right\rangle\ . \end{aligned}$$

So apart from the factor $\mathrm{e}^{-s\epsilon}$, which ensures convergence, and the mass-dependent quantity e^{-ism^2}, the propagator $S_{\mathrm{F}}(x; x')$ can be interpreted as the probability for a particle located at time $s = 0$ at position x to propagate to position x' within the proper time s and integrated over all possible values of the proper time.

2.3 Effective Action for QED

An effective action is an action that approximates the "proper" action of the theory in a certain parameter regime such that both actions yield the same correlation functions under these assumptions. For the case of QED, the effective Heisenberg-Euler action should be valid for photon energies much smaller than the rest mass of the electrons, $\hbar\omega \ll mc^2$, as derivative expansions [GS96; GS99; DH99] and world line calculations [GR11] suggest.
We already know from (1.13), that the full QED-Lagrangian is given by

$$\mathcal{L}_{\text{QED}} = -\frac{1}{16\pi} F_{\mu\nu}F^{\mu\nu} + \bar{\Psi}(i\not{D} - m)\Psi \ .$$

Using the language of path integrals, one can use of the assumption of $\omega \ll m$ to integrate out heavy degrees of freedom [Din16], namely the massive fermions. The effective action $\Gamma[A]$ is then defined via the path integral where the integration is only on the gauge degrees of freedom:

$$\int \mathcal{D}A \mathrm{e}^{i\Gamma[A]} = \int \mathcal{D}A\mathcal{D}\Psi\mathcal{D}\bar{\Psi} \ \exp\left\{ i \int \mathrm{d}^4x \left[-\frac{1}{16\pi} F_{\mu\nu}F^{\mu\nu} + \bar{\Psi}(i\not{D} - m + i\epsilon)\Psi \right] \right\}$$

with

$$\mathrm{e}^{i\Gamma[A]} = \int \mathcal{D}\Psi\mathcal{D}\bar{\Psi} \ \exp\left\{ i \int \mathrm{d}^4x \left[-\frac{1}{16\pi} F_{\mu\nu}F^{\mu\nu} + \bar{\Psi}(i\not{D} - m + i\epsilon)\Psi \right] \right\} \ . \tag{2.9}$$

Now the path integral is an infinite version of a Gaussian integral over Grassman-valued fields, which evaluates to the determinant:

$$\int \mathcal{D}\bar{\Psi}\mathcal{D}\Psi \ \exp\left\{ i \int \mathrm{d}x^4 \left[\bar{\Psi}(i\not{D} - (m - i\epsilon))\Psi \right] \right\} = \mathcal{N} \det\left(i\not{D} - m + i\epsilon\right)$$

with some infinite normalisation constant $\mathcal{N}$. Therefore,

$$\int \mathcal{D}A \mathrm{e}^{i\Gamma[A]} = \int \mathcal{D}A \exp\left\{ i \int \mathrm{d}x^4 (-\frac{1}{16\pi} F_{\mu\nu}F^{\mu\nu}) \right\} \mathcal{N} \det\left(i\not{D} - m + i\epsilon\right) \ .$$

Comparing the integrands and taking the logarithm on both sides, we obtain the explicit expression for the effective action

$$i\Gamma[A] = i \int \mathrm{d}x^4 (-\frac{1}{16\pi} F_{\mu\nu}F^{\mu\nu}) + \ln\det\left(i\not{D} - m + i\epsilon\right) + \ln\mathcal{N} \ . \tag{2.10}$$

Using the identity

$$\operatorname{Tr}\ln\mathbf{M} = \ln\det\mathbf{M}$$

for a diagonalisable matrix $\mathbf{M}$, we can rewrite (2.10) as

$$i\Gamma[A] = i \int \mathrm{d}^4x (-\frac{1}{16\pi} F_{\mu\nu}F^{\mu\nu}) + \operatorname{Tr}\ln\left(i\not{D} - m + i\epsilon\right) + \ln\mathcal{N} \ .$$

Since the trace is independent of the basis and we want to combine the logarithm into an effective action, we chose the position basis $|x\rangle$ to evaluate the trace:

$$i\Gamma[A] = i \int \mathrm{d}x^4 \left(-\frac{1}{16\pi} F_{\mu\nu}F^{\mu\nu} - i \operatorname{tr} \langle x| \ln\left(i\not{D} - m + i\epsilon\right) |x\rangle \right) + \ln\mathcal{N}$$

and tr is the leftover trace over spinor indices. So the effective Lagrangian is given by

$$\mathcal{L}_{\text{eff}} = -\frac{1}{16\pi} F_{\mu\nu}F^{\mu\nu} - i\,\mathrm{tr}\big(\langle x|\ln\big(i\not{D} - m + i\epsilon\big)\,|x\rangle\big) + const.\,. \tag{2.11}$$

Following the analogy of the real Klein-Gordon-field in section 2.1, one can define a generating functional $Z_A[j]$ for the n-point correlation functions where the vacuum $|0\rangle$ is now replaced by an interacting vacuum $|\Omega\rangle_A$ with the gauge field A_μ present. The generating functional for the connected correlation functions is given by $W[j] = -i\ln Z[j]$ and we saw that taking this logarithm removed all unconnected correlation functions and only the free propagator survived. In the same sense here now the fully dressed propagator satisfying

$$\big(i\not{D} - (m - i\epsilon)\big)\,S_A(x - x') = -i\delta^4(x - x')$$

is obtained as the connected two-point-function. From the Schwinger-Dyson equation it is known that S_A can be expanded perturbatively and this expansion has the following pictorial representation, where the double-dashed line is the fully-dressed propagator:

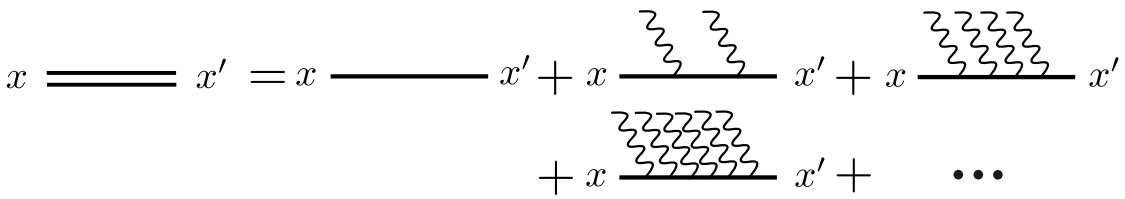

Figure 2.2: Iterative solution of the Schwinger-Dyson equation for the fully-dressed fermion propagator with a classical electromagnetic field. Only even numbers of photons are present due to Furry's theorem.

Here we already anticipated Furry's theorem that only an even number of external photons are allowed due to CPT-invariance [PS95].

Now taking the trace sets $x = x'$, which means pictorially that one joins the ends of the fermion lines in Fig. 2.2 such that one obtains the fully-dressed, closed loop shown in Fig. 2.3 together with its perturbative interpretation. We note that this is similar to the explanation of the proper time interpretation at the end of the last section for the free case.

To further simplify the expression for the effective action, we go back to (2.11) and take the derivative with respect to m^2 [Sch13]

$$\begin{aligned}
\frac{\partial\mathcal{L}_{\text{eff}}}{\partial m^2} &= -i\frac{\partial}{\partial m^2}\,\mathrm{tr}\Big(\langle x|\ln\Big(i\not{D} - \sqrt{m^2} + i\epsilon\Big)\,|x\rangle\Big) \\
&= \frac{i}{2m}\,\mathrm{tr}\Big(\langle x|\,\frac{1}{i\not{D} - m + i\epsilon}\,|x\rangle\Big) \\
&= \frac{i}{2m}\,\mathrm{tr}\Big(\langle x|\,\frac{i\not{D} + m}{-\not{D}^2 - m^2 + i\epsilon}\,|x\rangle\Big)\,.
\end{aligned}$$

If one now makes a Taylor-Expansion of the $1/(-\not{D}^2 - m^2 + i\epsilon)$ term, one gets a power series in even powers of γ-matrices. Since this series multiplies the enumerator and the

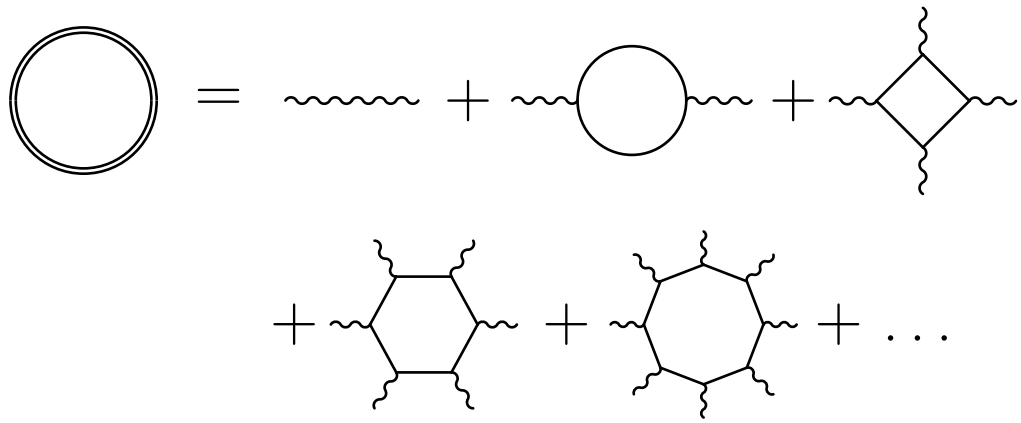

Figure 2.3: Expansion of the effective action into a perturbative series of Feynman diagrams. Only an even number of external photons are present due to Furry's theorem.

trace over odd powers of Dirac-matrices vanishes, we are left with

$$\begin{aligned}\frac{\partial \mathcal{L}_{\text{eff}}}{\partial m^2} &= \frac{i}{2}\,\mathrm{tr}\Big(\langle x|\,\frac{1}{-\not{D}^2 - m^2 + i\epsilon}\,|x\rangle\Big) \\ &= \frac{1}{2}\int_0^\infty \mathrm{d}s\; \mathrm{e}^{-\epsilon s}\mathrm{e}^{-ism^2}\,\mathrm{tr}\Big(\langle x|\,\mathrm{e}^{-i\not{D}^2 s}\,|x\rangle\Big)\;.\end{aligned}$$

Integrating again with respect to m^2 one obtains

$$\mathcal{L}_{\text{eff}} = -\frac{1}{16\pi}F_{\mu\nu}F^{\mu\nu} + \frac{i}{2}\int_0^\infty \mathrm{d}s\; \mathrm{e}^{-\epsilon s}\frac{\mathrm{e}^{-ism^2}}{s}\,\mathrm{tr}\Big(\langle x|\,\mathrm{e}^{-i\not{D}^2 s}\,|x\rangle\Big)\;,$$

where we installed again the linear Maxwell Lagrangian and dropped the constant as it does not effect the equations of motion. Now we can use

$$\not{D}^2 = \frac{1}{2}\left(\{\gamma^\mu,\gamma^\nu\} + [\gamma^\mu,\gamma^\nu]\right)D_\mu D_\nu = D^2 + \frac{e}{2}\sigma^{\mu\nu}F_{\mu\nu}$$

with

$$\begin{aligned}\{\gamma^\mu,\gamma^\nu\} &= 2g^{\mu\nu}\;,\\ [D_\mu, D_\nu] &= ieF_{\mu\nu}\;,\end{aligned}$$

where $\{A,B\} := AB + BA$, $[A,B] := AB - BA$ and

$$\sigma^{\mu\nu} := \frac{i}{2}[\gamma^\mu,\gamma^\nu]\;. \tag{2.12}$$

By making the replacement

$$i(\partial_\mu + ieA_\mu) \to \Pi_\mu = p_\mu - eA_\mu \tag{2.13}$$

we obtain

$$\not{D}^2 = D^2 + \frac{e}{2}\sigma^{\mu\nu}F_{\mu\nu} \to \not{D}^2 = -\Pi^2 + \frac{e}{2}\sigma^{\mu\nu}F_{\mu\nu}$$

and therefore

$$\mathcal{L}_{\text{eff}} = -\frac{1}{16\pi}F_{\mu\nu}F^{\mu\nu} + \frac{i}{2}\int_0^\infty \frac{\mathrm{d}s}{s}\;\mathrm{e}^{-ism^2}\;\mathrm{e}^{-\epsilon s}\,\mathrm{tr}\big(\langle x|\,\mathrm{e}^{-is\mathcal{H}_{\text{pt}}}\,|x\rangle\big)\;, \tag{2.14}$$

where we defined a proper time Hamiltonian

$$\mathcal{H}_{\text{pt}} = -\Pi^2 + \frac{e}{2}\sigma^{\mu\nu}F_{\mu\nu} \ . \tag{2.15}$$

We can interpret again the effective action as the propagation of a particle from position x, time-evolved with the dressed Hamiltonian $\mathcal{H}_{\text{pt}}$ and propagated back to position x, integrated over all proper times s. It runs around a loop in proper time s where the complete interaction with the external field A_μ is taken into account. Therefore, one can interpret $\Gamma[A] = \int \mathrm{d}^4x \ \mathcal{L}_{\text{eff}}$ as the one-loop effective action for QED in agreement with Fig. 2.3.
Now we reduced the problem of integrating out the fermion dynamics to finding an expression for the propagator in position space

$$\langle x|\, \mathrm{e}^{-is\mathcal{H}_{\text{pt}}}\, |y\rangle \ . \tag{2.16}$$

As we saw from (2.15), $\mathcal{H}_{\text{pt}}$ consists of two parts:

$$\mathcal{H}_{\text{pt}} = \mathcal{H}_1 + \mathcal{H}_2 \ ,$$

where $\mathcal{H}_1 = -\Pi^2$ and $\mathcal{H}_2 = \frac{e}{2}\sigma^{\mu\nu}F_{\mu\nu}$. As we assume $F_{\mu\nu}$ in $\mathcal{H}_2$ to be a function of the position operator,

$$F_{\mu\nu} = F_{\mu\nu}(\hat{x}) \ ,$$

we can write

$$\langle x|\, \mathrm{e}^{-is(\mathcal{H}_1 + \frac{e}{2}\sigma^{\mu\nu}F^{\mu\nu}(\hat{x}))}\, |y\rangle = \langle x|\, \mathrm{e}^{-is\mathcal{H}_1}\, |y\rangle \ \mathrm{e}^{-is\frac{e}{2}\sigma^{\mu\nu}F_{\mu\nu}(y)} \ . \tag{2.17}$$

The main task is now to derive the explicit expression for

$$\langle x|\, \mathrm{e}^{-is\mathcal{H}_1}\, |y\rangle \ . \tag{2.18}$$

In the next section we are going to derive an expression of the propagator for a general quadratic Hamiltonian $\mathcal{H}$ with constant metric on a $2n$-dimensional phase space using techniques from symplectic geometry. This machinery then allows us to derive the Heisenberg-Euler Lagrangian in an alternative way as a special case with $n = 4$.

2.3.1 Propagator for Quadratic Hamiltonians

It's a pleasure to thank Michael M. Kay for showing and carefully explaining to me the derivation presented in this section [Kay16].

In this section we derive an explicit formula for the propagator for an arbitrary quadratic Hamiltonian on a $2n$-dimensional phase space with constant metric:

$$\langle x|\, \mathrm{e}^{-it\mathcal{H}}\, |y\rangle \tag{2.19}$$

with a Hamiltonian

$$\mathcal{H} = \frac{1}{2}(\hat{x}^T G_1 \hat{x} + \hat{x}^T G_2 \hat{p} + \hat{p}^T G_3 \hat{x} + \hat{p}^T G_4 \hat{p}) \ , \tag{2.20}$$

where $\hat{x}$ and $\hat{p}$ are operators on the $2n$-dimensional phase space and the G_i are constant $n \times n$-dimensional matrices with $i = 1, 2, 3, 4$. We note that in the one-dimensional case

with $G_1 = G_4 = 1$ and $G_2 = G_3 = 0$, $\mathcal{H}$ is simply the Hamiltonian of a one-dimensional harmonic oscillator

$$\mathcal{H} = \frac{1}{2}(\hat{p}^2 + \hat{x}^2) \ .$$

The connection between (2.19) and the propagator appearing in the effective Lagrangian (2.14) is made explicit later.
In this chapter we change notation from Greek indices $\mu, \nu, \ldots$ to lowercase letters $i, k, l, \ldots$ which run from $1, 2, \ldots, n$ where n is the dimension of the space. If we now introduce the $2n$-dimensional coordinate operator $\hat{X} = (\hat{x}, \hat{p})$, then we can write the Hamiltonian as

$$\mathcal{H} = \frac{1}{2}\langle \hat{X}, G\hat{X}\rangle := \frac{1}{2}\sum_{I,J=0}^{2n} \hat{X}^I G_{IJ} \hat{X}^J \ , \tag{2.21}$$

where $\langle , \rangle$ denotes the standard Euclidean scalar product. The capital indices $I, J, \ldots$ run from $1, \ldots, 2n$ over the whole phase space and the metric G is given by a the block matrix

$$G = \begin{pmatrix} G_1 & G_2 \\ G_3 & G_4 \end{pmatrix} \ .$$

The idea is now to view the propagator $\langle x| \, \mathrm{e}^{-i\mathcal{H}t} \, |y\rangle$ as the wave function $\langle x|\psi(y,t)\rangle$ of the state $|\psi(y,t)\rangle$ where

$$|\psi(y,t)\rangle := \mathrm{e}^{-i\mathcal{H}t} \, |y\rangle \tag{2.22}$$

and use that $|\psi(y,t)\rangle$ is a solution to the Schrödinger equation

$$i\frac{\mathrm{d}}{\mathrm{d}t} \, |\psi(y,t)\rangle = \mathcal{H} \, |\psi(y,t)\rangle \tag{2.23}$$

with initial condition $|\psi(y,0)\rangle = |y\rangle$. This equation is hard to solve directly, but one can replace it with a first order partial differential equation which is the statement that $|\psi(y,t)\rangle$ is an eigenstate of a certain "time-evolved" operator. This condition then fixes the state up to a phase which is in the end determined by explicitly requiring that the constructed state solves the Schrödinger equation (2.23).
Specifically, we have

$$\mathrm{e}^{-i\mathcal{H}t}\hat{x}^k \mathrm{e}^{i\mathcal{H}t} \mathrm{e}^{-i\mathcal{H}t} \, |y\rangle = y^k \mathrm{e}^{-i\mathcal{H}t} \, |y\rangle \tag{2.24}$$

which follows from multiplying $\hat{x}^k \, |y\rangle = y^k \, |y\rangle$ with $\mathrm{e}^{-i\mathcal{H}t}$ from the left. So $|\psi(y,t)\rangle$ is an eigenstate of the "time-evolved" position operator

$$\hat{x}^k(t) := \mathrm{e}^{-i\mathcal{H}t}\hat{x}^k \mathrm{e}^{i\mathcal{H}t} \ . \tag{2.25}$$

In general, we define the time-evolved operators $\hat{X}^K(t)$ as

$$\hat{X}^K(t) := \mathrm{e}^{-i\mathcal{H}t}\hat{X}^K \mathrm{e}^{i\mathcal{H}t} \ .$$

The corresponding equation of motion for $X^K(t)$ is then

$$\begin{aligned} \frac{\mathrm{d}}{\mathrm{d}t}\hat{X}^K(t) &= -i[\mathcal{H}, \hat{X}^K(t)] \\ &= -i\mathrm{e}^{-i\mathcal{H}t}[\mathcal{H}, \hat{X}^K]\mathrm{e}^{i\mathcal{H}t} \ . \end{aligned} \tag{2.26}$$

To further simplify this expression, we introduce the standard symplectic matrix Ω given by

$$\Omega = \begin{pmatrix} 0 & -\mathbb{1}_n \\ \mathbb{1}_n & 0 \end{pmatrix} , \tag{2.27}$$

where $\mathbb{1}_n$ is the identity matrix in n dimensions. The canonical commutation relation

$$[\hat{x}^i, \hat{p}_k] = i\delta^i_k$$

can then be written as

$$[\hat{X}^I, \hat{X}^J] = i\Omega^{IJ} .$$

We note that that Ω^{IJ} are the components of Ω^{-1}. For the commutator $-i[\mathcal{H}, \hat{X}^K]$ we therefore obtain

$$-i[\mathcal{H}, \hat{X}^K] = -i \sum_{I,J=0}^{2n} \hat{X}^I G_{IJ} [\hat{X}^J, \hat{X}^K] \tag{2.28}$$

$$= \sum_{I,J=0}^{2n} \hat{X}^I G_{IJ} \Omega^{JK} \tag{2.29}$$

$$= -\sum_{I=0}^{2n} (\Omega^{-1} G)^K_I \hat{X}^I \tag{2.30}$$

$$=: -\sum_{I=0}^{2n} \Lambda^K_I \hat{X}^I \tag{2.31}$$

where we used $(\Omega^{-1})^T = -\Omega^{-1}$, $G = G^T$ and defined

$$\Lambda := (\Omega^{-1} G) . \tag{2.32}$$

The equation of motion (2.26) can be rewritten as

$$\frac{\mathrm{d}}{\mathrm{d}t} \hat{X}^K(t) = -\sum_{I=0}^{2n} \Lambda^K_I \hat{X}^I(t) . \tag{2.33}$$

Now we know that the general solution to (2.26) is given by the flow

$$\varphi_1(t, \hat{X}) := \begin{pmatrix} \hat{x}(t) \\ \hat{p}(t) \end{pmatrix} = \mathrm{e}^{-it\mathcal{H}} \begin{pmatrix} \hat{x} \\ \hat{p} \end{pmatrix} \mathrm{e}^{it\mathcal{H}} , \tag{2.34}$$

where a flow on a manifold M is defined as a map

$$\varphi : \mathbb{R} \times M \to M$$

such that

$$\varphi(0, p) = p ,$$
$$\varphi(t, \phi(s, p)) = \varphi(t + s, p) .$$

Now we define another (symplectic) flow

$$\varphi_2(t, \hat{X}) = S^t \hat{X} , \tag{2.35}$$

where

$$S^t := \mathrm{e}^{-t\Lambda} \ . \tag{2.36}$$

In Appendix B.1 it is shown that two flows on a manifold M are identical if their derivatives at $t = 0$ are identical. So since

$$\frac{\mathrm{d}}{\mathrm{d}t}\varphi_2(t,\hat{X})\Big|_{t=0} = -i[\mathcal{H},\hat{X}] = \frac{\mathrm{d}}{\mathrm{d}t}\varphi_1(t,\hat{X})\Big|_{t=0} \tag{2.37}$$

it follows that $\varphi_1 = \varphi_2$. As a consequence the position operator $\hat{x}^k$ obeys

$$\mathrm{e}^{-i\mathcal{H}t}\hat{x}^k\mathrm{e}^{i\mathcal{H}t} = \sum_{I=0}^{2n}(S^t)^k_I X^I \ . \tag{2.38}$$

Now we need some information on the operator $S^t = \mathrm{e}^{-t\Lambda}$. We note that Λ is an element of the Lie-Algebra $sp(2n)$ of the symplectic group $Sp(2n)$, whose defining property is

$$\Omega M + M^T\Omega = 0$$

for $M \in sp(2n)$. If we take $M = \Omega^{-1}G$, we have

$$\Omega\Omega^{-1}G + G(\Omega^{-1})^T\Omega = 0 \ ,$$

where we used $\Omega^T = -\Omega$ and $G = G^T$. Therefore, $\Lambda \in sp(2n)$.
Since Λ is an element of $sp(2n)$, S^t is a symplectic matrix where the defining property of the symplectic group $Sp(2n)$ is leaving the standard skew-symmetric matrix Ω invariant:

$$P^T\Omega P = \Omega \tag{2.39}$$

for $P \in Sp(2n)$. We denote the $n \times n$-blocks of S^t as

$$S^t =: \begin{pmatrix} S^t_1 & S^t_2 \\ S^t_3 & S^t_4 \end{pmatrix} \ . \tag{2.40}$$

The relation (2.39) gives certain conditions on the blocks S^t_i which are collected in Appendix B.2.
Now we use this information to derive a differential equation for the propagator in position space.
As we have seen in (2.24), we have the eigenvalue equation

$$\mathrm{e}^{-it\mathcal{H}}x^k\mathrm{e}^{it\mathcal{H}}\,|\psi(y,t)\rangle = y^k\,|\psi(y,t)\rangle \ . \tag{2.41}$$

Using (2.38), this can be rewritten as

$$\sum_{I=0}^{2n}(S^t)^k_I X^I\,|\psi(y,t)\rangle = y^k\,|\psi(y,t)\rangle \ . \tag{2.42}$$

Multiplying (2.42) from the left with $\langle x|$, we obtain the differential equation

$$(S^t_1 x - iS^t_2\nabla)\,\langle x|\psi(y,t)\rangle = y\,\langle x|\psi(y,t)\rangle$$

or, equivalently,

$$(S^t_1 x - iS^t_2\nabla)\psi^t_y(x) = y\psi^t_y(x) \ , \tag{2.43}$$

where we defined

$$\psi_y^t(x) := \langle x|\psi(y,t)\rangle \ .$$

Now we want to solve (2.43) for $\nabla\psi_y^t(x)$. This requires the inverse $(S_2^t)^{-1}$, which we assume to exist for simplicity. Under this assumption we obtain

$$\nabla\psi_y^t(x) = i(S_2^t)^{-1}(y - S_1^t x)\psi_y^t(x) \ , \tag{2.44}$$

which has the solution

$$\psi_y^t(x) = f(y,S^t)\exp\Big(-\frac{i}{2}\langle x,(S_2^t)^{-1}S_1^t x\rangle + i\langle (S_2^t)^{-1}y,x\rangle\Big) \tag{2.45}$$

with an arbitrary function $f(y,S^t)$ which still has to be determined and we used that $(S_2^t)^{-1}S_1^t$ is symmetric, which follows from (B.5). As the time evolution is unitary, we know

$$\psi_y^t(x) = \langle x|\,\mathrm{e}^{-it\mathcal{H}}\,|y\rangle = \overline{\psi_x^{-t}(y)} \tag{2.46}$$

and therefore

$$\psi_y^t(x) = \overline{f(x,S^{-t})}\exp\Big(\frac{i}{2}\langle y,(S_2^{-t})^{-1}S_1^{-t}y\rangle - i\langle (S_2^{-t})^{-1}x,y\rangle\Big) \ . \tag{2.47}$$

Now we can use (B.5) to rewrite (2.47) as

$$\psi_y^t(x) = \overline{f(x,S^{-t})}\exp\Big(\frac{i}{2}\langle y,(S_2^{-t})^{-1}S_1^{-t}y\rangle + i\langle (x,S_2^{-t}y\rangle\Big) \ . \tag{2.48}$$

Comparing equations (2.45) and (2.48) yields

$$f(y,S^t) = N(S^t)\exp\Big(\frac{i}{2}\langle y,(S_2^{-t})^{-1}S_1^{-t}y\rangle\Big) \ . \tag{2.49}$$

So the full propagator $\psi_y^t(x)$ is determined up to the unknown function $N(S^t)$:

$$\psi_y^t(x) = N(S^t)\Phi_y^t(x) \ , \tag{2.50}$$

where

$$\Phi_y^t(x) := \exp\Big(\frac{i}{2}\langle y,(S_2^{-t})^{-1}(S_1^{-t})y\rangle - \frac{i}{2}\langle x,(S_2^t)^{-1}S_1^t x\rangle + i\langle (S_2^t)^{-1}y,x\rangle\Big) \ . \tag{2.51}$$

For later use we express

$$\begin{aligned}(S_2^{-t})^{-1}S_1^{-t} &= -[(S_2^t)^T]^{-1}(S_4^t)^T \\ &= -S_4^t(S_2^t)^{-1}\end{aligned}$$

(which follows from (B.5)) and therefore

$$\Phi_y^t(x) = \exp\Big(-\frac{i}{2}\langle y,S_4^t(S_2^t)^{-1}y\rangle - \frac{i}{2}\langle x,(S_2^t)^{-1}S_1^t x\rangle + i\langle (S_2^t)^{-1}y,x\rangle\Big) \ .$$

Finally, we need to find the function

$$N(S)$$

for S in the Lie Algebra of $Sp(2n)$. The condition (2.46) implies

$$N(S^{-1}) = \overline{N(S)} \ .$$

Now we consider the flow condition

$$\begin{aligned}\psi_y^{s+t}(x) &= \langle x|\, \mathrm{e}^{-i\mathcal{H}s}\mathrm{e}^{-i\mathcal{H}t}\, |y\rangle = \int_{\mathbb{R}^n} \mathrm{d}^n u\ \langle x|\, \mathrm{e}^{-i\mathcal{H}s}\, |u\rangle\langle u|\, \mathrm{e}^{-i\mathcal{H}t}\, |y\rangle \\ &= \int_{\mathbb{R}^n} \mathrm{d}^n u\ \psi_u^s(x)\psi_y^t(u)\ . \end{aligned} \tag{2.52}$$

Setting $x = y = 0$ in this relation gives

$$N(S^{s+t}) = N(S^s)N(S^t)\int_{\mathbb{R}^n} \mathrm{d}^n u\ \Phi_u^s(0)\Phi_0^t(u) \tag{2.53}$$

and the integral can be evaluated:

$$\begin{aligned}\int_{\mathbb{R}^n} \mathrm{d}^n u\ \Phi_u^s(0)\Phi_0^t(u) &= \int_{\mathbb{R}^n} \mathrm{d}^n u\ \exp\Big(-\frac{i}{2}\langle u, (S_4^s(S_2^s)^{-1} + (S_2^t)^{-1}(S_1^t))u\rangle\Big) \\ &= (-2\pi i)^{\frac{n}{2}}\det\big((S_4^s)(S_2^s)^{-1} + (S_2^t)^{-1}(S_1^t)\big)^{-\frac{1}{2}}\ .\end{aligned}$$

Next we manipulate further the determinant

$$\begin{aligned}\det\big((S_4^s)(S_2^s)^{-1} + (S_2^t)^{-1}(S_1^t)\big) &= \det(S_2^s)^{-1}\det\big((S_4^s) + (S_2^t)^{-1}S_1^tS_2^s\big) \\ &= \det(S_2^s)^{-1}\det\big(S_2^t\big)^{-1}\det\big(S_2^tS_4^s + S_1^tS_2^s\big) \\ &= \det(S_2^s))^{-1}(\det\big(S_2^t\big))^{-1}\det\big((S^sS^t)_2\big)\ .\end{aligned}$$

So (2.53) is then given by

$$N(S^s)N(S^t) = (-2\pi i)^{\frac{n}{2}}N(S^{s+t})(\det(S_2^s))^{-\frac{1}{2}}(\det\big(S_2^t\big))^{-\frac{1}{2}}\det\big((S^sS^t)_2\big)^{\frac{1}{2}}\ ,$$

which is satisfied if one defines

$$N(S^t) = \left(\frac{i}{2\pi}\right)^{\frac{n}{2}}(\det\big(S_2^t\big))^{-\frac{1}{2}}R(S^t)\ , \tag{2.54}$$

where $R(S^t)$ is an arbitrary function that fulfils

$$R(S^s)R(S^t) = R(S^{t+s})\ .$$

As a last step we show that actually $R(S^a) = 1\ \forall a$ by requiring that $\psi_y^t(x)$ satisfies the Schrödinger-equation, which completes the calculation. This is done in Appendix B.3. The final result is therefore given by

$$\begin{aligned}\langle x|\, \mathrm{e}^{-i\mathcal{H}t}\, |y\rangle = \left(\frac{i}{2\pi}\right)^{n/2}(\det S_2^t)^{-1/2}\exp\Big(-\frac{i}{2}\langle y, S_4^t(S_2^t)^{-1}y\rangle - \frac{i}{2}\langle x, (S_2^t)^{-1}S_1^tx\rangle\Big) \\ \cdot\exp\Big(i\langle (S_2^t)^{-1}y, x\rangle\Big)\ .\end{aligned} \tag{2.55}$$

2.3.2 The Heisenberg-Euler Lagrangian

Now as we have the expression for the propagator for an arbitrary Hamiltonian $\mathcal{H} = \frac{1}{2}\langle X, GX\rangle$ for a constant metric G, we can proceed to derive the Heisenberg-Euler Lagrangian. The expression we want to calculate is (2.14):

$$\mathcal{L}_{\text{eff}} = -\frac{1}{16\pi}F_{\mu\nu}F^{\mu\nu} + \frac{i}{2}\int_0^\infty \frac{\mathrm{d}s}{s}\ \mathrm{e}^{-ism^2}\ \mathrm{e}^{-\epsilon s}\,\mathrm{tr}\big(\langle x|\, \mathrm{e}^{-i\mathcal{H}_{pt}s}\, |x\rangle\big)\ .$$

Now to use (2.55), we make the substitution $s \to -\frac{t}{2}$, such that

$$\mathcal{L}_{\text{eff}} = -\frac{1}{16\pi} F_{\mu\nu}F^{\mu\nu} + \frac{i}{2}\int_{-\infty}^{0} \frac{\mathrm{d}t}{t}\, \mathrm{e}^{i\frac{t}{2}m^2}\, \mathrm{e}^{\epsilon\frac{t}{2}}\, \mathrm{tr}\big(\langle x|\, \mathrm{e}^{-i\mathcal{H}t}\, |x\rangle\big)$$

with Hamiltonian

$$\mathcal{H} = \frac{1}{2}\Pi^2 - \frac{e}{4}\sigma^{\mu\nu}F_{\mu\nu}$$

and we saw in (2.17) that the propagator for the full Hamiltonian reduced to

$$\langle x|\, \mathrm{e}^{-is(-\frac{1}{2}\Pi^2 + \frac{e}{4}\sigma^{\mu\nu}F_{\mu\nu}(\hat{x}))}\, |y\rangle = \langle x|\, \mathrm{e}^{-i\frac{1}{2}\Pi^2 t}\, |y\rangle\ \ \mathrm{e}^{it\frac{e}{4}\sigma^{\mu\nu}F_{\mu\nu}(y)}\ ,$$

where $\Pi_\mu = p - eA_\mu$. Now we assume constant electromagnetic fields such that $F_{\mu\nu} = \partial_\mu A_\nu - \partial_\nu A_\mu = const.$. To describe constant fields $F_{\mu\nu}$, we chose the Schwinger-Fock gauge [Foc37; Sch51]

$$A_\mu = -\frac{1}{2}F_{\mu\alpha}x^\alpha\ .$$

So Π^2 can be written as

$$\begin{aligned}\Pi^2 &= g^{\mu\nu}(p_\mu + \frac{e}{2}F_{\mu\alpha}x^\alpha)(p_\nu + \frac{e}{2}F_{\nu\beta}x^\beta)\\ &= p_\mu g^{\mu\nu}p_\nu - \frac{e}{2}x^\alpha F_{\alpha\mu}g^{\mu\nu}p_\nu + \frac{e}{2}p_\mu g^{\mu\nu}F_{\nu\beta}x^\beta - \frac{e^2}{4}x^\alpha F_{\alpha\mu}g^{\mu\nu}F_{\nu\beta}x^\beta\ .\end{aligned} \tag{2.56}$$

Now we introduce a metric G

$$G = \begin{pmatrix} \frac{e^2}{4}F^T g^{-1}F & \frac{e}{2}F^T g^{-1} \\ \frac{e}{2}g^{-1}F & g^{-1}\end{pmatrix}\ ,$$

such that (2.56) can be written as

$$\begin{aligned}\mathcal{H} &= \frac{1}{2}(\langle p, g^{-1}p\rangle + \frac{e}{2}\langle x, F^T g^{-1}p\rangle + \frac{e}{2}\langle p, g^{-1}Fx\rangle + \frac{e^2}{4}\langle x, F^T g^{-1}Fx\rangle)\\ &= \frac{1}{2}\langle X, GX\rangle\end{aligned}$$

and we used that F is anti-symmetric.
Then Λ is given by

$$\Lambda = \Omega^{-1}G = \begin{pmatrix} \frac{e}{2}g^{-1}F & g^{-1} \\ \frac{e^2}{4}Fg^{-1}F & \frac{e}{2}Fg^{-1}\end{pmatrix}\ . \tag{2.57}$$

As the next step we need to evaluate (2.55) with $n = 4$. For the exponential in (2.55) we obtain (see (B.11) in Appendix B.4)

$$\Phi_y^t(x) = \exp\Big[\frac{i}{4}\langle (y-x), eF\coth\Big(\frac{e}{2}g^{-1}Ft\Big)(y-x)\rangle - i\langle x, \frac{e}{2}Fy\rangle\Big)\Big] \tag{2.58}$$

from which we infer that $\Phi(x,x) = 1$ since F is antisymmetric.
The determinant of $(S_2^t)^{-1}$ (c.f. (B.10)) factorises into

$$\det\big(S_2^t\big)^{-1} = \det\frac{e}{2}F\det\exp\Big(\frac{e}{2}g^{-1}Ft\Big)\det\sinh\Big(\frac{e}{2}g^{-1}Ft\Big)^{-1}\ . \tag{2.59}$$

In Appendix B.5 it is shown that

$$\det \exp\Big(\frac{e}{2} g^{-1} F t\Big) = 1$$

by using the antisymmetry of $g^{-1}F$. Further, from (B.18) we know

$$\det\left(\frac{\frac{e}{2}F}{\sinh\frac{e}{2}g^{-1}Ft}\right)^{\frac{1}{2}} = i\frac{e^2 ab}{4\sinh\frac{e}{2}at\sin\frac{e}{2}bt}\ ,$$

which is shown by determining the eigenvalues of $g^{-1}F$ and the secular invariants a and b are defined as

$$a = \sqrt{\sqrt{\mathcal{F}^2+\mathcal{G}^2}+\mathcal{F}}\ , \qquad\qquad b = \sqrt{\sqrt{\mathcal{F}^2+\mathcal{G}^2}-\mathcal{F}}\ .$$

Therefore,

$$\det\big(S_2^t\big)^{\frac{1}{2}} = i\frac{e^2 ab}{4\sinh\big(\frac{e}{2}at\big)\sin\big(\frac{e}{2}bt\big)}\ .$$

What is left to calculate the Heisenberg-Euler Lagrangian (2.14) is to evaluate

$$\operatorname{tr} \mathrm{e}^{iet\frac{1}{4}\sigma F} = \sum_i \mathrm{e}^{ie\lambda_i t} = 4\cosh\Big(\frac{e}{2}at\Big)\cos\Big(\frac{e}{2}bt\Big) \tag{2.60}$$

which is done in Appendix B.6.

The effective Lagrangian is then given by

$$\mathcal{L}_{\text{eff}} = -\frac{1}{16\pi}F_{\mu\nu}F^{\mu\nu} - \frac{e^2}{8\pi^2}\int_{-\infty}^{0}\frac{\mathrm{d}t}{t}\,\mathrm{e}^{i\frac{t}{2}m^2}\,ab\coth\Big(\frac{e}{2}at\Big)\cot\Big(\frac{e}{2}bt\Big)\ .$$

We note that we dropped the ϵ-term as it is not needed here [Sch13]. Now we substitute back $t \to -2s$, rotate along the imaginary axis $s \to -is$ and apply Cauchy's Theorem to obtain

$$\mathcal{L}_{\text{eff}} = -\frac{1}{16\pi}F_{\mu\nu}F^{\mu\nu} - \frac{e^2}{8\pi^2}\int_{0}^{\infty}\frac{\mathrm{d}s}{s}\,\mathrm{e}^{-sm^2}\,ab\cot(eas)\coth(ebs)\ .$$

For later convenience, we rescale $s \to s/m^2$ such that

$$\mathcal{L}_{\text{eff}} = -\frac{1}{16\pi}F_{\mu\nu}F^{\mu\nu} - \frac{e^2}{8\pi^2}\int_{0}^{\infty}\frac{\mathrm{d}s}{s}\,\mathrm{e}^{-s}\,ab\cot\big(eas/m^2\big)\coth\big(ebs/m^2\big)$$

and introduce dimensionless variables $e/m^2 a \to a$ and $e/m^2 b \to b$. The Heisenberg-Euler Lagrangian is then

$$\mathcal{L}_{\text{HE}} = -\frac{m^4}{8\pi^2}\int_{0}^{\infty}\frac{\mathrm{d}s}{s}\,\mathrm{e}^{-s}\,ab\cot(as)\coth(bs) \tag{2.61}$$

and the effective Lagrangian reads

$$\mathcal{L}_{\text{eff}} = -\frac{1}{16\pi}F_{\mu\nu}F^{\mu\nu} + \mathcal{L}_{\text{HE}}\ .$$

Now the damping term e^{-s} in $\mathcal{L}_{\mathrm{HE}}$ ensures convergence of the integrand for large values of s, but if one expands the integrand for small values of s, one sees from

$$ab\cot(as)\coth(bs) = \frac{1}{s^2} + \frac{1}{3}(-a^2+b^2) - \frac{1}{45}(a^4+5a^2b^2+b^4)s^2 + \mathcal{O}(s^4) \tag{2.62}$$

that the integrand is divergent for small values of the proper time s. To renormalise the Lagrangian we use "minimal substraction" [Sch13] and substract the divergent parts from (2.62).
So the final result for the renormalised Heisenberg-Euler Lagrangian is

$$\boxed{\mathcal{L}_{\mathrm{HE}} = -\frac{m^4}{8\pi^2}\int_0^\infty \mathrm{d}s\,\frac{\mathrm{e}^{-s}}{s^3}\left[s^2 ab\cot as\coth bs - 1 + \frac{s^2}{3}(a^2-b^2)\right]}\,. \tag{2.63}$$

We note again that all fields appearing in (2.63) are normalised to E_{cr}.

2.3.3 Weak-field Expansion

In the case of fields with $E \ll 1$, the full Heisenberg-Euler Lagrangian (2.63) can be expanded into a power series and the integral evaluated explicitly for the first terms in the expansion.
The applicability of this weak-field expansion is connected to the probability of real e^+e^--creation. Schwinger [Sch51] was the first to give an explicit expression for the probability of this process in a volume equal to the reduced Compton wavelength $\lambda = \hbar/mc$ cubed in the Compton time λ/c:

$$P = E^2\exp(-\pi/E)/4\pi^3\ .$$

The non-perturbative character of the exponential leads to an exponential suppression of real electron-positron pair-creation. So for $E \ll 1$ a weak-field expansion should be valid and dissipative effects like pair-creation heavily suppressed.
As we have already seen, the un-renormalised one-loop-effective action had the pictorial representation Fig. 2.3. Using minimal substraction at the end of the last section, we removed one diagram to ensure the correct normalisation for free photon propagation and the graph corresponding to charge-renormalisation. The weak-field expansion of the renormalised effective action is therefore pictorially:

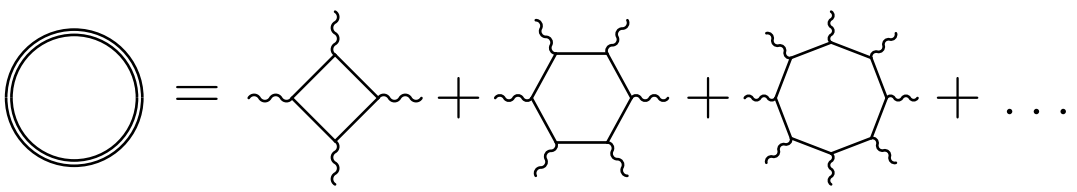

Figure 2.4: Perturbative pictorial expansion of the renormalised effective action.

Now the Heisenberg-Euler Lagrangian is the effective Lagrangian in the limit $\omega \ll m$, so the fermion loops are replaced by effective vertices as it is shown in Fig. 2.5. Due to the shape of the original diagrams, we also refer to the effective diagrams for four-, six- and eight-photon scattering as box-, hexagon- and octagon-diagrams interchangeably.

Applying a weak-field expansion of (2.63) for $E \ll 1$ yields:

$$\mathcal{L}_{\mathrm{HE}} = \frac{m^4}{\alpha} \sum_{i=1}^{\infty} \mathcal{L}_i \ , \tag{2.64}$$

$$\mathcal{L}_1 = \frac{\mu_1}{4\pi} \left[\left(E^2 - B^2\right)^2 + 7(\mathbf{E}\cdot\mathbf{B})^2 \right] \ , \tag{2.65}$$

$$\mathcal{L}_2 = \frac{\mu_2}{4\pi} \left(E^2 - B^2\right) \left[2\left(E^2 - B^2\right)^2 + 13\left(\mathbf{E}\cdot\mathbf{B}\right)^2 \right] \ , \tag{2.66}$$

$$\mathcal{L}_3 = \frac{\mu_3}{4\pi} \Big[3\left(E^2 - B^2\right)^4 + 22\left(E^2 - B^2\right)^2 \left(\mathbf{E}\cdot\mathbf{B}\right)^2 + 19\left(\mathbf{E}\cdot\mathbf{B}\right)^4 \Big] \ , \tag{2.67}$$

where

$$\mu_1 = \frac{\alpha}{90\pi} \ , \qquad \mu_2 = \frac{\alpha}{315\pi} \ , \qquad \mu_3 = \frac{4\alpha}{945\pi} \ . \tag{2.68}$$

We note that $\mathcal{L}_1$, $\mathcal{L}_2$ and $\mathcal{L}_3$ have directly the interpretation of the effective vertices shown in the right-hand side of Fig. 2.5. Indeed, it has been shown that the leading-order term of the weak-field expansion agrees with the direct calculation of the four-photon box diagram in the low-frequency limit $\hbar\omega \ll mc^2$ [KN50].
In the next section we give the corresponding Maxwell and wave equations that follow from the Heisenberg-Euler Lagrangian.

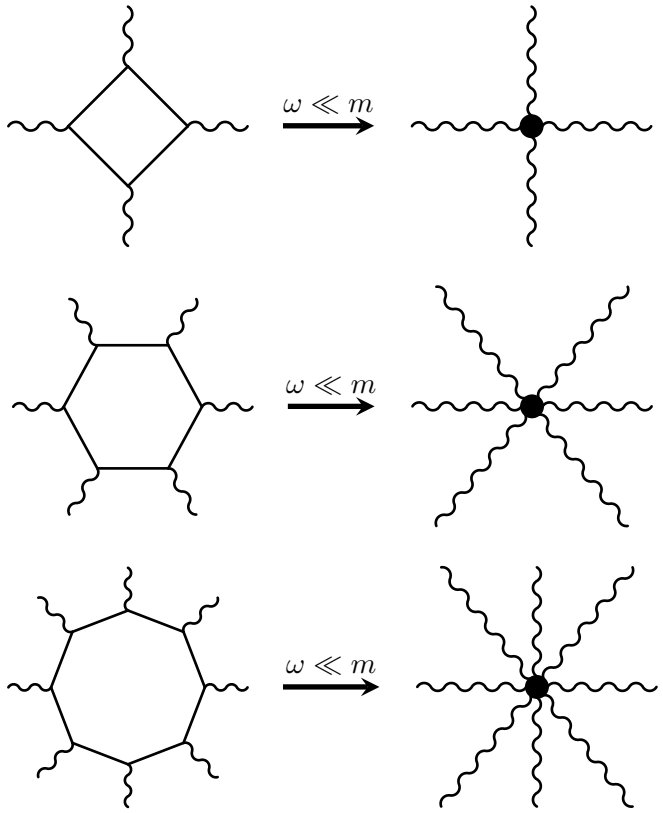

Figure 2.5: In the limit of photon energies $\omega \ll m$, the loop diagrams involving even numbers of external photons are replaced by effective vertices denoted by solid dots as they are described by the effective Lagrangian densities consisting of the corresponding polynomials in the field in variants $\mathcal{F}$ and $\mathcal{G}$.

2.4 Modified Electromagnetic Wave Propagation

As it was derived in (2.63), the Heisenberg-Euler Lagrangian is given by

$$\mathcal{L}_{\rm HE} = -\frac{m^4}{8\pi^2}\int_0^\infty \mathrm{d}s\,\frac{\mathrm{e}^{-s}}{s^3}\Big[s^2 ab\cot as\coth bs - 1 + \frac{s^2}{3}(a^2-b^2)\Big]\ ,$$

where the secular invariants a and b are given by

$$a = \Big[\sqrt{\mathcal{F}^2+\mathcal{G}^2}+\mathcal{F}\Big]^{1/2}\ , \qquad\qquad b = \Big[\sqrt{\mathcal{F}^2+\mathcal{G}^2}-\mathcal{F}\Big]^{1/2} \tag{2.69}$$

and we recall that electric and magnetic fields are in units of the critical field $E_{\rm cr}$.
The linear Maxwell Lagrangian in this normalisation is then

$$\mathcal{L}_{\rm MW} = -\frac{m^4}{16\pi\alpha}F_{\mu\nu}F^{\mu\nu}\ .$$

The equations of motion are obtained by applying the Euler-Lagrange equations to the Lagrangian $\mathcal{L} = \mathcal{L}_{\rm MW} + \mathcal{L}_{\rm HE}$. Therefore, the nonlinear Maxwell equations in covariant form read

$$\begin{aligned}\partial_\mu F^{\mu\nu} = 4\pi\Big((C_1\,\partial_\mu F^{\mu\nu} + C_2\,F^{\mu\nu}\partial_\mu(F_{\alpha\beta}F^{\alpha\beta}) + C_3\,{\star F}^{\mu\nu}\partial_\mu({\star F}_{\alpha\beta}F^{\alpha\beta})\\ + C_4\big[\,{\star F}^{\mu\nu}\partial_\mu(F_{\alpha\beta}F^{\alpha\beta}) + F^{\mu\nu}\partial_\mu({\star F}_{\alpha\beta}F^{\alpha\beta})\big]\Big)\ ,\end{aligned} \tag{2.70}$$

$$\partial_\mu\,{\star F}^{\mu\nu} = 0\ . \tag{2.71}$$

The general expressions for the coefficients C_i are derived in App. C.3.
For the first and second order weak-field expansion of (2.63), the coefficients C_i in (2.70) that follow from $\mathcal{L}_1$ and $\mathcal{L}_2$ are given by

$$\begin{aligned} C_{1,\rm box} &= \frac{\alpha}{90\pi^2}(E^2-B^2)\ , & C_{2,\rm box} &= -\frac{\alpha}{180\pi^2}\ ,\\ C_{3,\rm box} &= \frac{7}{4}C_{2,\rm Box}\ , & C_{4,\rm box} &= 0\ ,\end{aligned} \tag{2.72}$$

$$\begin{aligned} C_{1,\rm hex} &= \frac{\alpha}{630\pi^2}[6(E^2-B^2)^2+13(\mathbf{E}\cdot\mathbf{B})^2]\ , & C_{2,\rm hex} &= -\frac{\alpha}{105\pi^2}(E^2-B^2)\ ,\\ C_{3,\rm hex} &= \frac{13}{24}C_{2,\rm hex}\ , & C_{4,\rm hex} &= -\frac{13\alpha}{1260\pi^2}|(\mathbf{E}\cdot\mathbf{B})|\ .\end{aligned} \tag{2.73}$$

We note that only the dynamical equation that couples to matter is modified while the Bianchi Identity (2.71) remains untouched.
Expressing Maxwell's equations equations in electric and magnetic fields, we acquire

$$\nabla\wedge\mathbf{E} + \partial_t\mathbf{B} = 0\ , \tag{2.74}$$

$$\nabla\wedge\mathbf{B} - \partial_t\mathbf{E} = 4\pi\mathbf{J}[\mathbf{E},\mathbf{B}] \tag{2.75}$$

with

$$\begin{aligned}\mathbf{J}[\mathbf{E},\mathbf{B}] = \big[&C_1\,(\partial_t\mathbf{E}-\nabla\wedge\mathbf{B}) + (C_2\mathbf{E}+C_4\mathbf{B})\,\partial_t(F_{\mu\nu}F^{\mu\nu})\\ &+ (C_2\mathbf{B}-C_4\mathbf{E})\wedge\nabla(F_{\mu\nu}F^{\mu\nu})\\ &+ (C_4\mathbf{B}-C_3\mathbf{E})\wedge\nabla(F_{\mu\nu}\,{\star F}^{\mu\nu})\\ &+ (C_3\mathbf{B}+C_4\mathbf{E})\,\partial_t(F_{\mu\nu}\,{\star F}^{\mu\nu})\big]\ .\end{aligned} \tag{2.76}$$

We note that the current (2.76) is equivalent to

$$\mathbf{J}[\mathbf{E},\mathbf{B}] = (\nabla \wedge \mathbf{M} + \partial_t \mathbf{P}) \tag{2.77}$$

as it is used in Appendix C.2 where the dimensionless magnetisation $\mathbf{M}$ and dimensionless polarisation $\mathbf{P}$ are defined as

$$\mathbf{M} = \frac{\partial \mathcal{L}_{\mathrm{HE}}}{\partial \mathbf{B}} \ , \qquad\qquad \mathbf{P} = \frac{\partial \mathcal{L}_{\mathrm{HE}}}{\partial \mathbf{E}} \ .$$

Another way to study the modified propagation of light due to vacuum polarisation is to solve the corresponding wave equation for the electric field (which is derived in Appendix C.2)

$$\Box \mathbf{E} = \mathbf{T}[\mathbf{E},\mathbf{B}] \ , \tag{2.78}$$

where $\Box = \partial_t^2 - \nabla^2$ and the source term is given by

$$\mathbf{T} = -4\pi \left[\nabla \wedge \partial_t \mathbf{M} + \partial_t^2 \mathbf{P} - \nabla(\nabla \cdot \mathbf{P})\right] \ . \tag{2.79}$$

We note that $\mathbf{T}$ is related to the current $\mathbf{J}$ via $\mathbf{T} = -4\pi\partial_t \mathbf{J} + 4\pi\nabla(\nabla \cdot \mathbf{P})$. Since we work with the weak-field expansion (2.64), we can write the current $\mathbf{J}$ and the source $\mathbf{T}$ as

$$\mathbf{J} = \sum_{i=1}^{\infty} \mathbf{J}_i \ , \qquad \text{and} \qquad \mathbf{T} = \sum_{i=1}^{\infty} \mathbf{T}_i \tag{2.80}$$

with

$$\begin{aligned} \mathbf{J}_i &= [\nabla \wedge \mathbf{M}_i + \partial_t \mathbf{P}_i] \ , \\ \mathbf{T}_i &= -4\pi \left[\nabla \wedge \partial_t \mathbf{M}_i + \partial_t^2 \mathbf{P}_i - \nabla(\nabla \cdot \mathbf{P}_i)\right] \end{aligned}$$

and the polarisations and magnetisations are correspondingly defined as

$$\mathbf{M}_i = \frac{\partial \mathcal{L}_i}{\partial \mathbf{B}} \ , \qquad\qquad \mathbf{P}_i = \frac{\partial \mathcal{L}_i}{\partial \mathbf{E}} \ . \tag{2.81}$$

Before proceeding further with the solution of the Maxwell equation and the wave equation, we introduce the initial setups studied in this thesis.

2.5 Scattering of Two Plane Wave Pulses

We consider a pump-probe setup of two counter-propagating pulses which are approximated as plane waves. Thereby an optical probe with a finite envelope function and carrier frequency ω_p propagates along the characteristic $x^- := t - z$ and collides with a slowly-varying strong or pump pulse that counter-propagates along $x^+ := t + z$. $x^\pm$ are also called "light cone coordinates". The analytic expression for the initial probe is thereby taken to be

$$\mathbf{E}_p^{(0)}(x^-) = \boldsymbol{\varepsilon}_p E_p^{(0)}(x^-) = \boldsymbol{\varepsilon}_p \mathcal{E}_p f_p(x^-/\tau_p) \cos\big(\omega_p x^-\big) \tag{2.82}$$

with $E_p^{(0)}(x^-) := \mathcal{E}_p f_p(x^-/\tau_p)\cos(\omega_p x^-)$, a field amplitude $\mathcal{E}_p$, the envelope function f_p with pulse duration given by τ_p and a polarisation vector $\boldsymbol{\varepsilon}_p$. The quantity $\omega_p x^-$ can be written as the Lorentz invariant phase $\varphi_p := k_p x = \omega_p x^-$ with wave four-vector

$k_p = \omega_p(1, \hat{k}_p)$ and $\hat{k}_p = (0, 0, 1)$. We use the space-time dependence $\mathbf{E}_p(x^-)$ and $\mathbf{E}_p(\varphi_p)$ interchangeably. The envelope function $f_p(x^-/\tau_p)$ is, if not mentioned otherwise, always chosen such that

$$|\partial_{t,z} f_p(x^-/\tau_p)| \ll |\omega_p f_p(x^-/\tau_p)| \quad . \tag{2.83}$$

So, apart from from the analysis of the overlap-signal in section 4.1 and the numerical study of a few-cycle-pulse in section 4.3.1, we work in a slowly-varying-envelope approximation [BC91] and neglect any contribution of the derivative of f_p. In the numerical solution no such approximation is made.
The initial strong pulse is assumed to be peaked around the carrier frequency $\omega_s \approx 0$, such that

$$\mathbf{E}_s^{(0)}(x^+) = \boldsymbol{\varepsilon}_s E_s^{(0)}(x^+) = \boldsymbol{\varepsilon}_s \mathcal{E}_s f_s(x^-/\tau_s) \cos\big(\omega_s x^+\big) \tag{2.84}$$

$$\approx \boldsymbol{\varepsilon}_s \mathcal{E}_s f_s(x^+/\tau_s) \ . \tag{2.85}$$

$E_s^{(0)}(x^+) := \mathcal{E}_s f_s(x^+/\tau_s)$ with amplitude $\mathcal{E}_s$, polarisation vector $\boldsymbol{\varepsilon}_s$, $\varphi_s := k_s x^+ = \omega_s x^+$ with wave four-vector $k_s = \omega_s(1, \hat{k}_s)$ and $\hat{k}_s = (0, 0, -1)$. In contrast to the probe pulse, we always assume in the analytical calculation

$$|\partial_{t,z} f_s(x^+/\tau_s)| \gg |\omega_s f_s(x^+/\tau_s)| \tag{2.86}$$

such that only the derivative of the envelope has to be taken into account.
Since both probe and strong field are plane waves, we can express their magnetic fields via the electric fields:

$$\mathbf{B}_{p,s}^{(0)} = \hat{k}_{p,s} \wedge \mathbf{E}_{p,s}^{(0)} \ . \tag{2.87}$$

In the following section we introduce the corresponding diagrams for the processes which are allowed for our plane-wave pump-probe setup.

2.5.1 Diagrammatic Approach and Wave Mixing

The universality of the coupling allows us to simply insert the sum of field of the electic fields $\mathbf{E} = \mathbf{E}_s + \mathbf{E}_p$ and magnetic fields $\mathbf{B} = \mathbf{B}_s + \mathbf{B}_p$ into the weak-field expansion (2.64). For four-photon scattering (box diagram), the Lagrangian is given by (2.65), which translates into

$$\begin{aligned}\mathcal{L}_1 &= \frac{\mu_1}{4\pi}\left((E^2 - B^2)^2 + 7(\mathbf{E}\cdot\mathbf{B})^2\right) \\ &= \frac{\mu_1}{4\pi}\Big[4\Big((\mathbf{E}_p\cdot\mathbf{E}_s)^2 - 2(\mathbf{E}_p\cdot\mathbf{E}_s)(\mathbf{B}_p\cdot\mathbf{B}_s) + (\mathbf{B}_p\cdot\mathbf{B}_s)^2\Big) \\ &\qquad + 7\Big((\mathbf{E_p}\cdot\mathbf{B}_s) + (\mathbf{E_s}\cdot\mathbf{B}_p)\Big)^2\Big] \ .\end{aligned}$$

Here we used that the field invariants of the probe and strong field vanish separately. If we now express the magnetic fields via the electric fields as explained above, it is enough to consider the contributions from the electric fields and we can draw the vertex diagrams for $\mathcal{L}_1$ which is depicted in Fig. 2.6.
Let us for now look only at the energy-conservation from Fig. 2.6 as we are interested in the mixed frequencies and higher harmonics later on. The full energy/momentum conservation then leads to certain further constraints as it is explained shortly. From the viewpoint of energy conservation, the allowed processes are shown in Fig. 2.7, where the right external leg in each diagram is taken to be the generated signal from the process for

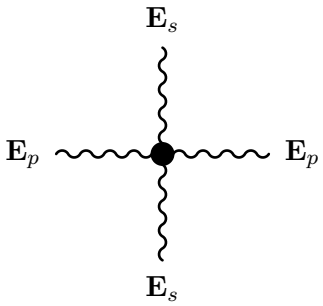

Figure 2.6: Vertex for four-photon scattering in the plane wave pump-probe setup.

convenience. The plus/minus signs at the other legs correspond to the positive/negative frequency components in the cos-terms in the initial pulse profiles (2.82) and (2.84). Since also the observed resulting signal with frequency ω_j is real, we need here to treat the positive and negative frequency contributions symmetrically.

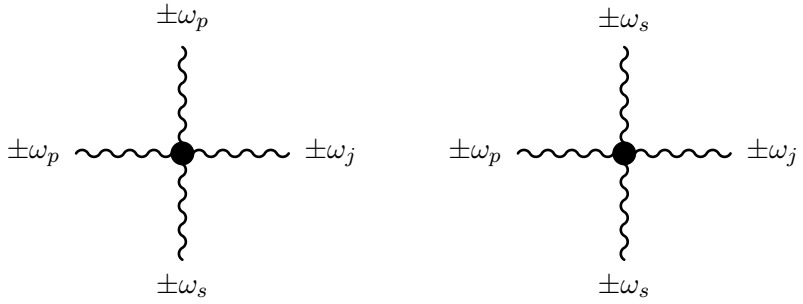

(a) $\omega_j \in \{2\omega_p \pm \omega_s, \omega_s\}$ (b) $\omega_j \in \{\omega_p, \omega_p \pm 2\omega_s\}$

Figure 2.7: Shown are the different combinations of frequencies that follow from pure energy conservation in Fig. 2.6. We will see shortly that the assumption of plane waves leads to further constraints on these processes. The right leg is chosen for convenience to be the generated signal. The plus/minus signs indicate incoming/outgoing frequencies as the initial pulses consist of positive and negative frequency components: $\cos(\omega x) = \frac{1}{2}(\mathrm{e}^{i\omega x} + \mathrm{e}^{-i\omega x})$. Since also the generated signal with frequency ω_j is real, we need to consider $\pm\omega_j$ in the diagram.

If we consider the scattering process in Fig. 2.7a with the scattering of $\omega_p+\omega_p+\omega_s \to \omega_j$ with the resulting frequency $\omega_j = 2\omega_p+\omega_s$, we have to distinguish two different processes. One where the wave vector of the outgoing signal is parallel to $\hat{k}_p$ and therefore propagating along the probe light cone, and the one which propagates in the opposite direction along with the strong pulse. Therefore, the former signal is called "forward-scattered" and the latter the „backward-scattered" signal. Let us now consider energy/momentum conservation for both cases.
For the forward-scattered signal we have

$$k_j = \omega_j \begin{pmatrix} 1 \\ \widehat{\mathbf{k}}_p \end{pmatrix} = 2\omega_p \begin{pmatrix} 1 \\ \widehat{\mathbf{k}}_p \end{pmatrix} + \omega_s \begin{pmatrix} 1 \\ -\widehat{\mathbf{k}}_p \end{pmatrix} , \tag{2.88}$$

where we used $\widehat{\mathbf{k}}_p = -\widehat{\mathbf{k}}_s$. As the asymptotic signal with k_j has to be on-shell with $(k_j)^2 = 0$ when both pulses are well-separated again, we obtain the contradiction

$$0 = 4\omega_p\omega_s \neq 0 \tag{2.89}$$

from (2.88) since $k_p^2 = k_s^2 = 0$ and we infer that this forward-scattering is not allowed. The other possibility could be that the signal is backward-scattered, so we have

$$k' = \omega' \begin{pmatrix} 1 \\ -\widehat{\mathbf{k}}_p \end{pmatrix} = 2\omega_p \begin{pmatrix} 1 \\ \widehat{\mathbf{k}}_p \end{pmatrix} + \omega_s \begin{pmatrix} 1 \\ -\widehat{\mathbf{k}}_p \end{pmatrix}$$

from which we also get a contradiction. So both processes are actually not allowed.
We see that the assumption of plane wave pulses leads to such strong constraints that it forbids "wave mixing" with $\omega_j = n\omega_p + m\omega_s$ due to energy-momentum conservation [BKR16].
So, as we see in more detail in section 4.1, for Fig. 2.7a only $\omega_j = \omega_s$ is allowed and can therefore be seen as a change in the strong pulse. Similarly, in Fig. 2.7b only $\omega_j = \omega_p$ is allowed and has to be interpreted as a change in the probe pulse.
The situation is different for the overlap signal, there also all mixed frequencies appear, depending on the order of the weak-field expansion. So to observe wave mixing in the asymptotic limit a non-vanishing angle between the $\vec{k}$-vectors of the colliding pulses is needed.

For six-photon scattering (the hexagon diagram), we have the Lagrangian density for the plane-wave setup

$$\begin{aligned}
\mathcal{L}_2 &= \frac{\mu_2}{4\pi}\left[2(E^2 - B^2)^3 + 13(E^2 - B^2)(\mathbf{E}\cdot\mathbf{B})^2\right] \\
&= \frac{\mu_2}{4\pi}\Big[16\,(\mathbf{E}_p\cdot\mathbf{E}_s)^3 - 16\,(\mathbf{B}_p\cdot\mathbf{B}_s)^3 - 48\,(\mathbf{E}_p\cdot\mathbf{E}_s)^2\,(\mathbf{B}_p\cdot\mathbf{B}_s) + 14(\mathbf{E}_p\cdot\mathbf{E}_s)\,(\mathbf{E}_p\cdot\mathbf{B}_s)^2 \\
&\quad + 14(\mathbf{E}_p\cdot\mathbf{E}_s)\,(\mathbf{B}_p\cdot\mathbf{E}_s)^2 + 48(\mathbf{E}_p\cdot\mathbf{E}_s)\,(\mathbf{B}_p\cdot\mathbf{B}_s)^2 + 28(\mathbf{E}_p\cdot\mathbf{E}_s)(\mathbf{E}_p\cdot\mathbf{B}_s)(\mathbf{B}_p\cdot\mathbf{E}_s) \\
&\quad - 14(\mathbf{B}_p\cdot\mathbf{B}_s)\,(\mathbf{E}_p\cdot\mathbf{B}_s)^2 - 14(\mathbf{B}_p\cdot\mathbf{B}_s)\,(\mathbf{B}_p\cdot\mathbf{E}_s)^2 - 28(\mathbf{B}_p\cdot\mathbf{B}_s)(\mathbf{E}_p\cdot\mathbf{B}_s)(\mathbf{B}_p\cdot\mathbf{E}_s)\Big]\,.
\end{aligned}$$

The corresponding effective vertex is shown in Fig. 2.8. The possible processes allowed from pure energy conservation are given by Fig. 2.9 and we note again that no mixed frequencies like $\omega_j = 2\omega_p \pm 3\omega_s$ in Fig. 2.9a or $\omega_j = 3\omega_p \pm 2\omega_s$ in Fig. 2.9b are allowed due to the same argument of energy/momentum conservation as for the box diagram. The detailed analysis of the allowed processes from the hexagon diagram is given in section 4.1.

In general, the weak-field expansion leads to

$$\mathcal{L}_n \sim (\mathbf{E}_p\cdot\mathbf{E}_s)^{n+1} + \text{ similar terms}\,,$$

where the similar terms involve also the magnetic fields in expressions like $(\mathbf{B}_p\cdot\mathbf{E}_s)$, so in the corresponding vertex diagram $(n+1)$ legs stem from the strong and $(n+1)$ from the probe field.
As we now have seen that the assumption of plane waves puts certain additional constraints of the allowed processes, we introduce the main setups considered in this thesis.

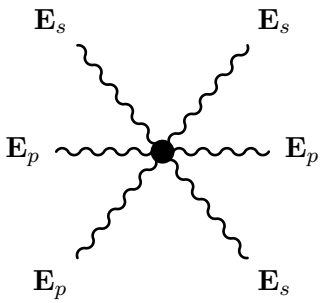

Figure 2.8: Effective vertex from the hexagon diagram for a plane wave pump-probe setup.

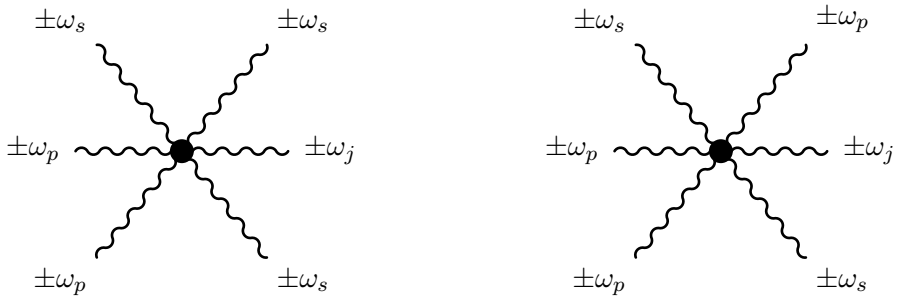

(a) $\omega_j \in \{2\omega_p \mp 3\omega_s, \omega_p + 3\omega_s, 3\omega_s, \omega_s\}$ (b) $\omega_j \in \{3\omega_p \mp 2\omega_s, \omega_p \mp 2\omega_s, \omega_p\}$

Figure 2.9: Possible processes that are allowed from pure energy conservation for six-photon scattering. The leg pointing directly to the right is taken for convenience to be the generated signal by the considered process. We note that the generation of the mixed frequencies like $\omega_j = 2\omega_p + 3\omega_s$ is forbidden asymptotically due to further constraints from full energy/momentum conservation as it is explained for the box diagram.

2.5.2 Pump-Probe Setup with Quasi-constant Backgrounds

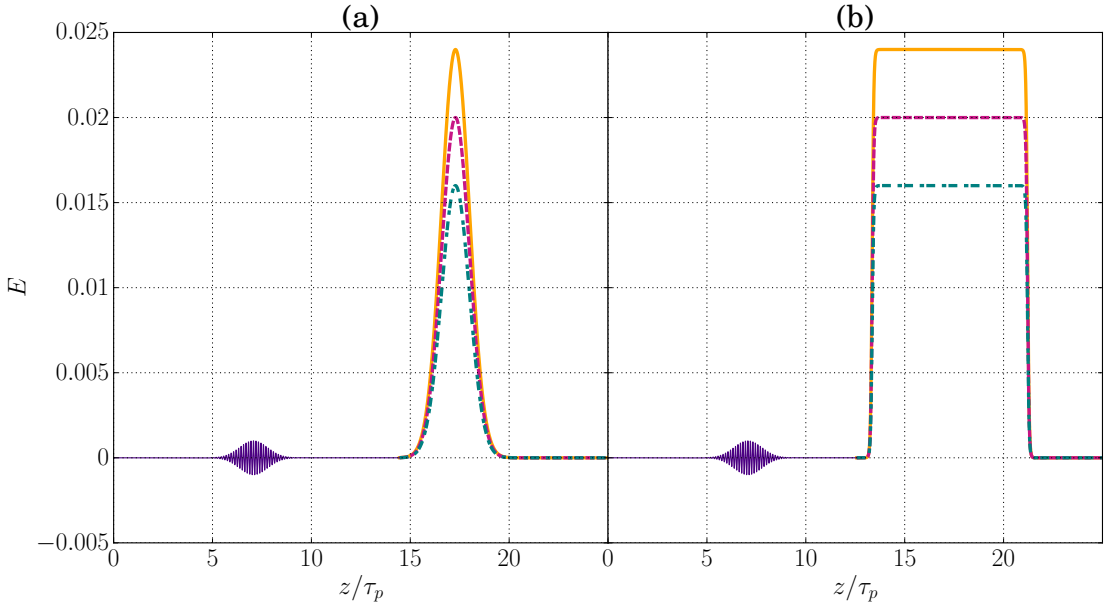

Figure 2.10: Shown are the two main pump-probe setups considered in this thesis. **(a)**: An optical probe pulse collides with a strong Gaussian background. **(b)**: An optical probe pulse collides with a constant-crossed background. The different line styles indicate different amplitudes $\mathcal{E}_s$ of the background field. The typical box length is $L = 3.2 \cdot 10^{-3}$ cm.

Throughout the thesis, we take the probe pulse to have a Gaussian envelope

$$f_p(x^-/\tau_p) = \mathrm{e}^{-\left(\frac{x^-}{\tau_p}\right)^2} ,$$

such that (2.82) is given by

$$\mathbf{E}_p^{(0)}(x^-) = \boldsymbol{\varepsilon}_p E_p^{(0)}(x^-) = \mathcal{E}_p \boldsymbol{\varepsilon}_p \mathrm{e}^{-\left(\frac{x^-}{\tau_p}\right)^2} \cos\left(\omega_p x^-\right)$$

and $E_p^{(0)}(x^-) = \mathcal{E}_p \mathrm{e}^{\left(\frac{x^-}{\tau_p}\right)^2} \cos(\omega_p x^-)$. The specific choices for the strong background envelope functions differ for the two main parts of the thesis. For the simulations of the overlap signal in section 4.1, the strong field is given by a Gaussian background

$$\mathbf{E}_s^{(0)}(x^+) = \mathcal{E}_s \boldsymbol{\varepsilon}_s \mathrm{e}^{-\left(\frac{x^+}{\tau_s}\right)^2} . \tag{2.90}$$

This corresponds to setting $f_s(x^+/\tau_s) = \mathrm{e}^{-\left(\frac{x^+}{\tau_s}\right)^2}$ and $\omega_s = 0$ in (2.84). A snapshot of this simulational setup is shown in panel **(a)** in Fig. 2.10.
For the main analysis of the generation of higher harmonics in section 4.2, the background is chosen to be a rectangular pulse profile

$$f_s(x^+/\tau_s) = \mathrm{Rect}(x^+/\tau_s) , \tag{2.91}$$

where

$$\mathrm{Rect}(x^+/\tau_s) := \theta(x^+/\tau_s + 1/2) - \theta(x^+/\tau_s - 1/2) \tag{2.92}$$

and $\theta(x)$ is the Heaviside step function. Thereby, most of the time, ω_s is approximated with $\omega_s = 0$ as it is shown in panel **(b)** of 2.10.
As it will be further explained in section 3.2 for the numerical method, infinite gradients as in (2.92) are difficult to treat numerically, therefore in the simulation we approximate the rectangular pulse by some mirrored Fermi-Dirac potential

$$\mathrm{Rect}(x^+/\tau_s) \approx \mathrm{FD}(x^+) := \frac{1}{1+\exp\left(\frac{|x^+|-z_m}{z_b}\right)} ,$$

where the parameter z_b and z_m play the role of the "temperature" and "chemical potential". They control the steepness and width of the strong pulse and are always chosen to be $z_b = 5 \cdot 10^{-5}$ cm and $z_m = 100 \cdot z_b$. The definition of the pulse duration τ_s is given by (4.25) and defined by the analytical result for the generation of the second harmonic. As we now commented on all possible lowest order processes from the box- and hexagon diagram and gave the explicit expressions for the strong background, we now further introduce dressed diagrams for the forward-scattered probe which are useful in the interpretation of the analytical, iterative solution of the wave equation in section 3.1.4.

2.5.3 Dressed Diagrams for Four- and Six-photon Scattering

When we consider high harmonic generation in section 3.1.4, the frequency of the strong pulse is approximated as $\omega_s = 0$ and we want to neglect the back-reaction of the probe pulse on the strong pulse. This corresponds to treating the strong pulse as a classical source and it is convenient to introduce dressed photon lines where we omit all external legs from the strong pulse. In the next chapter we solve the wave equation analytically using an iterative ansatz and the diagrams are useful to illustrate the different steps in the iteration. Since the effect of pure four-photon and six-photon scattering with a classical source is of a different nature for the plane wave setup considered, we introduce two different types of „dressing“ in the following.

Effective Four-photon Scattering

For four-photon scattering the two possible processes are shown in Fig. 2.7 and we note again, that the assumption of plane waves forbids the asymptotic generation of mixed frequencies like $\omega_p + 2\omega_2$, as explained in section 2.5.1. In section 4.1 we see, that Fig. 2.7a asymptotically only generates the output frequency $\omega_j = \omega_s$ and can therefore be seen as a change in the strong pulse and is therefore left-travelling. For Fig. 2.7b it is similar and only a $\omega_j = \omega_p$ signal is generated, which is a change in the probe field and therefore forward scattered. As explained above, we neglect the back-reaction of the probe on the strong field, so the relevant dressed diagram is shown in Fig. 2.11, where the interaction vertex with the classical background has been replaced by a square.

Effective Six-photon Scattering

The asymptotic forward scattered signal from the hexagon diagram, which is generated by the process shown in Fig. 2.9b, consists of a signal with frequency $2\omega_p$ and a dc component which travel along the probe light cone as it is shown in section 4.1. The other process in Fig. 2.9a is backward scattered and has again to be interpreted as an

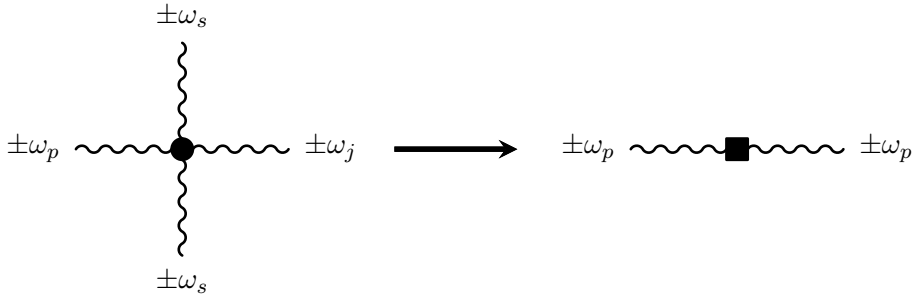

Figure 2.11: Dressed vertices for four-photon scattering of the probe where the pump pulse is treated as a classical source. The interaction with the external field is replaced by a black box as a new effective vertex. The right line indicates the generated signal.

action on the strong pulse. The effective vertex for the generation of the asymptotic second harmonic together with a dc component of six-photon scattering is be denoted by an empty circle and the dressed diagram for Fig. 2.9b is shown in Fig. 2.12:

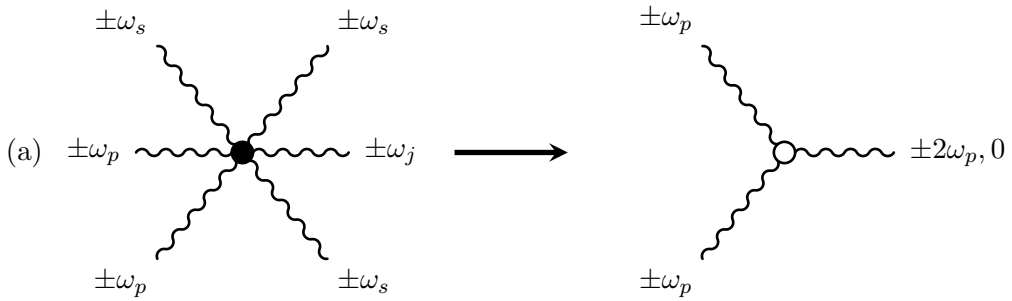

Figure 2.12: Dressed diagrams for the asymptotic generation of the second harmonic and a dc component. The effective vertex which incorporates the interactions with the classical background is denoted by an empty circle. The horizontal right line is thereby the generated signal of the process.

In the next chapter we are going to solve the wave equation analytically and explain the numerical solution of the corresponding Maxwell equations.

Chapter 3

Solution of the Nonlinear Equations of Motion

In the first part of this chapter we derive the solution of the wave equation for the electric field from an iterative ansatz using the Green's function in $(1+1)$ dimensions. From a suitable integration by parts, the forward- and backward scattered fields are introduced and afterwards a surface term is derived which we call the "overlap" field. This term appears in the first iteration as soon as there is any kind of inhomogeneity in the strong field and it vanishes identically in homogenous constant backgrounds. Afterwards, higher iterations for the change in the probe field without taking the back-reaction on the strong pulse are derived and the iterative solution is illustrated using the dressed diagrams introduced in the previous chapter.
In the second part we treat the alternative formulation as coupled nonlinear Maxwell equations, which are first order in time and space. For the case of (1+1) dimensions, the linear Maxwell equations can be written in a simple matrix form. The nonlinearities due to vacuum polarisation are then matrices that extend the linear case. The system is discretised in space using the "Pseudo-characteristic Method of Lines" and spatial derivatives are approximated with finite differences. Using matrix inversion, the equations are then converted to a system of ordinary differential equations (ODEs) and integrated in time using the ODE-solver CVODE.

3.1 Analytical Solution of the Wave Equation

We want to solve the inhomogeneous wave equation

$$\Box \mathbf{E} = \mathbf{T}[\mathbf{E}, \mathbf{B}] \ , \tag{3.1}$$

where $\mathbf{E} = \mathbf{E}_p + \mathbf{E}_s$ and the source term is given by (2.79). In the following we restrict ourselves to fields which only depend only on one temporal dimension (t) and one spatial dimension (z) which means translational invariance in the x- and y-direction. Therefore, the wave equation reduces to

$$(\partial_t^2 - \partial_z^2)\mathbf{E}(t,z) = \mathbf{T}[\mathbf{E}(t,z), \mathbf{B}(t,z)] \ .$$

The inital probe $\mathbf{E}_p^{(0)}$ and the strong pulse $\mathbf{E}_s^{(0)}$ both satisfy the homogenous wave equation

$$(\partial_t^2 - \partial_z^2)\mathbf{E}_p^{(0)}(t,z) = (\partial_t^2 - \partial_z^2)\mathbf{E}_s^{(0)}(t,z) = 0$$

independently. Since all solutions to the homogeneous wave equation in $(1+1)$ dimensions are plane waves, the separate field invariants vanish identically with $\mathcal{G}_p^{(0)} = \mathcal{G}_s^{(0)} = \mathcal{F}_s^{(0)} = \mathcal{F}_p^{(0)} = 0$. Therefore, we can express their magnetic fields $\mathbf{B}_p^{(0)}$ and $\mathbf{B}_s^{(0)}$ via their electric fields, $\mathbf{B}_p^{(0)} = \hat{k}_p \wedge \mathbf{E}_p^{(0)}$ and $\mathbf{B}_s^{(0)} = \hat{k}_s \wedge \mathbf{E}_s^{(0)}$. We also assume that the solution to (3.1) is also a plane wave propagating along the same axis as the pump and the strong pulse. Therefore, we can write $\mathbf{T}[\mathbf{E},\mathbf{B}] = \mathbf{T}[\mathbf{E}]$. Since the nonlinear corrections due to vacuum polarisation depend on the field invariants $\mathcal{G}$ and $\mathcal{F}$, we have

$$\mathbf{T}[\mathbf{E}_s^{(0)}] = 0 \ , \qquad \mathbf{T}[\mathbf{E}_p^{(0)}] = 0 \ .$$

However, for an electromagnetic field $\mathbf{E}$ that consists of two counter-propagating plane waves $\mathbf{E} = \mathbf{E}_p + \mathbf{E}_s$, these invariants do not vanish and we therefore have the wave equation

$$(\partial_t^2 - \partial_z^2)(\mathbf{E}_p + \mathbf{E}_s) = \mathbf{T}[\mathbf{E}_p + \mathbf{E}_s] \ . \tag{3.2}$$

To solve (3.2), we employ an iterative procedure

$$(\partial_t^2 - \partial_z^2)(\mathbf{E}_p^{(n+1)} + \mathbf{E}_s^{(n+1)}) = \mathbf{T}[\mathbf{E}_p^{(n)} + \mathbf{E}_s^{(n)}] \ . \tag{3.3}$$

We set $\mathbf{E} = \mathbf{E}_p + \mathbf{E}_s$ in the following, such that (3.3) becomes

$$(\partial_t^2 - \partial_z^2)\mathbf{E}^{(n+1)} = \mathbf{T}[\mathbf{E}^{(n)}] \ . \tag{3.4}$$

The iterative solution is then given by

$$\mathbf{E}^{(n+1)}(t,z) = \mathbf{E}^{(0)}(t,z) + \Delta\mathbf{E}^{(n)}(t,z) \tag{3.5}$$

with

$$\Delta\mathbf{E}^{(n)}(t,z) = \int \mathrm{d}t'\mathrm{d}z' G_R(t-t', z-z')\mathbf{T}^{(n)}(z',t') \ , \tag{3.6}$$

where $\mathbf{T}^{(n)} := \mathbf{T}[\mathbf{E}^{(n)}]$ and $G_R(t,z)$ is the retarded Green's function for the wave equation in $(1+1)$ dimensions (see App. D for a derivation)

$$G_R(t,z) = \frac{1}{2}\theta(t)\theta(t-|z|) \ . \tag{3.7}$$

3.1.1 Forward and Backward Scattering

The source term $\mathbf{T}^{(n)}$ is given by the sum

$$\mathbf{T}^{(n)}(t,z) = \sum_{i=1}^{\infty} \mathbf{T}_i \left[\mathbf{E}^{(n)}(t,z)\right] \ , \tag{3.8}$$

where the index i denotes the order in the weak-field expansion and $\mathbf{E}^{(n)} := \mathbf{E}_p^{(n)} + \mathbf{E}_s^{(n)}$. It is remarkable, that the charge density, which is given by $-\nabla \cdot \mathbf{P}$ and also appears in $\mathbf{T}$ (see (2.79)) vanishes identically in $(1+1)$ dimensions. Therefore, we have the relation

$$\mathbf{T} = -4\pi\partial_t\mathbf{J} = -\mathbf{4}\pi(\nabla \wedge \partial_t\mathbf{M} + \partial_t^2\mathbf{P}) \ .$$

In analogy to (3.8), we write

$$\mathbf{J}^{(n)}(t,z) = \sum_{i=1}^{\infty} \mathbf{J}_i \left[\mathbf{E}^{(n)}(t,z)\right] \ . \tag{3.9}$$

Now we integrate by parts in (3.6), which leads to

$$\begin{aligned}\Delta\mathbf{E}^{(n)}(t,z) = &-2\pi \int \mathrm{d}z'\mathrm{d}t' \ \delta(t-t')\theta(t-t'-|z-z'|)\mathbf{J}^{(n)}(t',z') \\ &-2\pi \int \mathrm{d}z'\mathrm{d}t' \ \theta(t-t')\delta(t-t'-|z-z'|)\mathbf{J}^{(n)}(t',z') \ .\end{aligned} \tag{3.10}$$

Evaluating the integral over the Delta-distribution in (3.10) yields

$$\Delta\mathbf{E}^{(n)}(t,z) = -2\pi \int_{-\infty}^{z} \mathrm{d}z' \ \mathbf{J}^{(n)}(t-z+z',z') - 2\pi \int_{z}^{\infty} \mathrm{d}z' \ \mathbf{J}^{(n)}(t+z-z',z') \ . \tag{3.11}$$

For a better interpretation of the two terms in (3.11) we now transform to light cone coordinates $x^{\pm} = t \pm z$. In general, the current depends on z and t in the specific combinations $\mathbf{J}^{(n)}(t,z) = \mathbf{J}^{(n)}(t-z,t+z) = \mathbf{J}^{(n)}(x^-,x^+)$. So the transformed currents are given by

$$\mathbf{J}^{(n)}(t,z)\Big|_{t=t-z+z',z=z'} = \mathbf{J}^{(n)}(x^-,x^+ + 2(z'-z))$$

and

$$\mathbf{J}^{(n)}(t,z)\Big|_{t=t+z-z',z=z'} = \mathbf{J}^{(n)}(x^- - 2(z'-z),x^+) \ .$$

Now we substitute $y = 2(z'-z)$ in (3.11) and obtain the general formula for the nth iteration

$$\Delta\mathbf{E}^{(n)}(x^-,x^+) = -\pi \int_{-\infty}^{0} \mathrm{d}y \ \mathbf{J}^{(n)}(x^-,x^+ + y) - \pi \int_{0}^{\infty} \mathrm{d}y \ \mathbf{J}^{(n)}(x^- - y,x^+) \ . \tag{3.12}$$

This allows us to interpret the two different terms

$$\Delta\mathbf{E}^{(n)}(x^-,x^+) = \Delta\overrightarrow{\mathbf{E}}^{(n)}(x^-,x^+) + \Delta\overleftarrow{\mathbf{E}}^{(n)}(x^-,x^+) \tag{3.13}$$

as a sum of a forward and a backward scattered contribution, where

$$\Delta\overrightarrow{\mathbf{E}}^{(n)}(x^-,x^+) = -\pi \int_{-\infty}^{0} \mathrm{d}y \ \mathbf{J}^{(n)}(x^-,x^+ + y) \tag{3.14}$$

is the forward-scattered (or right-scattered) field and

$$\Delta\overleftarrow{\mathbf{E}}^{(n)}(x^-,x^+) = -\pi \int_{0}^{\infty} \mathrm{d}y \ \mathbf{J}^{(n)}(x^- - y,x^+). \tag{3.15}$$

is the backward-scattered (or left-scattered) field. In the next section we see that both terms in (3.12) consist of two different contributions which we call the “asymptotic field” and the “overlap field”.

3.1.2 Overlap and Asymptotic Field

The current $\mathbf{J}^{(n)}(t,z)$ we are interested in consists of two parts

$$\begin{aligned}\mathbf{J}^{(n)}(x^-,x^+) &= \left(\partial_t \mathbf{P}^{(n)}(x^-,x^+) + \nabla \wedge \mathbf{M}^{(n)}(x^-,x^+)\right) \\ &= \left(\partial_t \mathbf{P}^{(n)}(x^-,x^+) + \hat{\mathbf{k}}_p \wedge \partial_z \mathbf{M}^{(n)}(x^-,x^+)\right) ,\end{aligned}$$

where $\mathbf{P}^{(n)}(x^-,x^+) := \mathbf{P}[\mathbf{E}^{(n)}(x^-,x^+)]$ and $\mathbf{M}^{(n)}(x^-,x^+) := \mathbf{M}[\mathbf{E}^{(n)}(x^-,x^+)]$. Let us first calculate the contribution from $\partial_t \mathbf{P}^{(n)}$ to the first integral in (3.12), the forward scattered field

$$\begin{aligned}\Delta\overrightarrow{\mathbf{E}}^{(n)}[\mathbf{P}^{(n)}(x^-,x^+)] &= -\pi \int_{-\infty}^{0} \mathrm{d}y\ \partial_t \mathbf{P}^{(n)}(x^-,x^+ + y) \\ &= -\pi \int_{-\infty}^{0} \mathrm{d}y\ \left[\frac{\partial}{\partial x^-}\mathbf{P}^{(n)}(x^-,x^+ + y) + \frac{\partial}{\partial y}\mathbf{P}^{(n)}(x^-,x^+ + y)\right] \\ &= -\pi \int_{-\infty}^{0} \mathrm{d}y\ \left[\frac{\partial}{\partial x^-}\mathbf{P}^{(n)}(x^-,x^+ + y)\right] \\ &\quad - \pi \left(\mathbf{P}^{(n)}(x^-,x^+) - \lim_{y\to-\infty}\mathbf{P}^{(n)}(x^-,y)\right) . \qquad (3.16)\end{aligned}$$

To illustrate the meaning of the two terms in (3.16), let us consider the case $n = 0$ and $i = 1$ in the weak-field expansion, so we consider only four photon scattering. If we just focus on the term which is proportional to the probe squared, then $\mathbf{P}^{(0)}$ is of the form

$$\mathbf{P}^{(0)}(x^-,x^+) = \boldsymbol{\varepsilon}\ [E_p^{(0)}(x^-)]^2 E_s^{(0)}(x^+) ,$$

where we absorbed all constants in $\boldsymbol{\varepsilon}$. The contribution from the polarisation $\mathbf{P}$ to the forward scattered field of the first iteration is then given by

$$\begin{aligned}\Delta\overrightarrow{\mathbf{E}}^{(0)}[\mathbf{P}^{(0)}(x^-,x^+)] &= -\pi \int_{-\infty}^{0} \mathrm{d}y\ \left[\frac{\partial}{\partial x^-}\mathbf{P}^{(0)}(x^-,x^+ + y)\right] \\ &\quad - \pi \left(\mathbf{P}^{(0)}(x^-,x^+) - \lim_{y\to-\infty}\mathbf{P}^{(0)}(x^-,y)\right) \\ &= -\pi\,\boldsymbol{\varepsilon}\ \frac{\partial}{\partial x^-}[E_p^{(0)}(x^-)]^2 \int_{-\infty}^{0} \mathrm{d}y\ E_s(x^+ + y) \\ &\quad - \pi\boldsymbol{\varepsilon}\ [E_p^{(0)}(x^-)]^2 \left(E_s^{(0)}(x^+) - \lim_{y\to-\infty} E_s^{(0)}(y)\right) . \qquad (3.17)\end{aligned}$$

We first consider the term involving the integral, for example, on the probe light cone with $x^- = 0$. Let us further assume that the integral over the strong probe is non-vanishing and we consider the limit $t, z \to \infty$ such that the pulses are again well separated after the scattering. Therefore, the integral gives a constant value and we refer to this term as the *asymptotic* scattered field. In general we define the asymptotic iterated field as

$$\begin{aligned}\Delta\overrightarrow{\mathbf{E}}^{(n)}_{\mathrm{as}}(x^-) &:= \lim_{x^+\to\infty} \Delta\overrightarrow{\mathbf{E}}^{(n)}(x^-,x^+) , \\ \Delta\overleftarrow{\mathbf{E}}^{(n)}_{\mathrm{as}}(x^+) &:= \lim_{x^-\to\infty} \Delta\overleftarrow{\mathbf{E}}^{(n)}(x^-,x^+) .\end{aligned} \qquad (3.18)$$

The second term in (3.17) is a direct product of the probe and the strong pulse. We note that this term is only present if there is some inhomogeneity in the background,

but not in homogeneous constant crossed or constant magnetic backgrounds as they do not vanish at infinity. An analysis of inhomogeneities in the background was recently carried out in [HH14] and it is shown in section 4.1 to correspond to the overlap signals studied in this thesis. A similar effect in non-constant backgrounds also appeared as a similar surface term in the analysis of the polarisation flip in four-photon scattering in [Din+14b].
If not mentioned otherwise, we assume that all fields vanish at $t = \pm\infty$. Therefore, the first iteration for the polarisation reduces to

$$\Delta\overrightarrow{\mathbf{E}}^{(0)}[\mathbf{P}^{(0)}(x^-,x^+)] = -\pi\,\boldsymbol{\varepsilon}\,\frac{\partial}{\partial x^-}[E_p^{(0)}(x^-)]^2\int_{-\infty}^{0}\mathrm{d}y\;E_s^{(0)}(x^+ + y) \\ -\pi\,\boldsymbol{\varepsilon}\,[E_p^{(0)}(x^-)]^2 E_s^{(0)}(x^+)\;. \quad (3.19)$$

Since the probe and the strong pulse depend on $x^\pm = t \pm z$ respectively and have a finite envelope function, the product of both pulses is maximal if the pulses overlap directly with $x^+ = x^- = 0$. At this point also the field invariants $\mathcal{F}$ and $\mathcal{G}$ take their maximal values. In the limit when both pulses are well separated again, this contribution tends to zero. Therefore, this signal is referred to as *overlap* scattered field.

Similar to the calculation that led to (3.16), we can now calculate the contribution of $\mathbf{M}^{(n)}$ to the forward scattered field

$$\Delta\overrightarrow{\mathbf{E}}^{(n)}[\mathbf{M}^{(n)}(x^-,x^+)] = \widehat{\mathbf{k}}_p \wedge \pi\int_{-\infty}^{0}\mathrm{d}y\;\left[\frac{\partial}{\partial x^-}\mathbf{M}^{(n)}(x^-,x^+ + y)\right] \\ -\pi\widehat{\mathbf{k}}_p \wedge \mathbf{M}^{(n)}(x^-,x^+)\;.$$

For the backward scattered field contribution from the polarisation $\mathbf{P}$ we obtain

$$\Delta\overleftarrow{\mathbf{E}}^{(n)}[\mathbf{P}^{(n)}(x^-,x^+)] \;=\; -\pi\int_0^{\infty}\mathrm{d}y\;\left[\frac{\partial}{\partial x^+}\mathbf{P}^{(n)}(x^- - y,x^+)\right] \;-\; \pi\mathbf{P}^{(n)}(x^-,x^+)\;.$$

The contribution from $\widehat{\mathbf{k}}_p \wedge \partial_z\mathbf{M}$ is given by

$$\Delta\overleftarrow{\mathbf{E}}^{(n)}[\mathbf{M}^{(n)}(x^-,x^+)] = -\widehat{\mathbf{k}}_p\wedge\pi\int_0^{\infty}\mathrm{d}y\;\left[\frac{\partial}{\partial x^+}\mathbf{M}^{(n)}(x^- - y,x^+)\right] + \pi\widehat{\mathbf{k}}_p\wedge\mathbf{M}^{(n)}(x^-,x^+)\,.$$

So the analytical expressions for the overall asymptotic forward and backward scattered signal are

$$\Delta\overrightarrow{\mathbf{E}}^{(n)}_{\mathrm{as}}(x^-,x^+) = -\int_{-\infty}^{0}\mathrm{d}y\frac{\partial}{\partial x^-}\mathbf{U}^{(n)}(x^-,x^+ + y)\;, \quad (3.20)$$

$$\Delta\overleftarrow{\mathbf{E}}^{(n)}_{\mathrm{as}}(x^-,x^+) = -\int_{0}^{\infty}\mathrm{d}y\frac{\partial}{\partial x^+}\mathbf{V}^{(n)}(x^- - y,x^+)\;. \quad (3.21)$$

The vectorial functions are given by

$$\mathbf{U}^{(n)}(x^-,x^+) = \pi(\mathbf{P}^{(n)}(x^-,x^+) - \widehat{\mathbf{k}}_p \wedge \mathbf{M}^{(n)}(x^-,x^+))\;, \quad (3.22)$$

$$\mathbf{V}^{(n)}(x^-,x^+) = \pi(\mathbf{P}^{(n)}(x^-,x^+) + \widehat{\mathbf{k}}_p \wedge \mathbf{M}^{(n)}(x^-,x^+))\;. \quad (3.23)$$

The total overlap field reads

$$\Delta\mathbf{E}^{(n)}_{\mathrm{o}}(x^-,x^+) = -2\pi\mathbf{P}^{(n)}(x^-,x^+)\;, \quad (3.24)$$

where the vectorial part of $\mathbf{P}$ consists of the sum of the electric fields of the probe and the strong pulse. This then defines the direction in which the signal travels. And we note again that the overlap signal vanishes in the asymptotic limit of infinite separation of the pulses

$$\lim_{x^{\pm}\to\infty} \Delta\mathbf{E}_{\mathrm{o}}^{(n)}(x^-, x^+) = 0 \ .$$

Further, we note that if one considers the setup where a probe is evolved from the infinite past into a constant background, the appearance of the overlap signal is different from the one in ever-present constant fields, where the overlap vanishes identically.

3.1.3 Lowest Order Iterations

In this section we calculate the first iteration

$$\Delta\mathbf{E}^{(0)}(t,z) = \Delta\overrightarrow{\mathbf{E}}_{\mathrm{as}}^{(0)}(x^-, x^+) + \Delta\overleftarrow{\mathbf{E}}_{\mathrm{as}}^{(0)}(x^-, x^+) + \Delta\mathbf{E}_{\mathrm{o}}^{(0)}(x^-, x^+) \ . \tag{3.25}$$

for the box and the hexagon diagram. We write the electric fields as $\mathbf{E}_p^{(0)} = \boldsymbol{\varepsilon}_p E_p^{(0)}$ and $\mathbf{E}_s^{(0)} = \boldsymbol{\varepsilon}_s E_s^{(0)}$ which yields the field invariant

$$\mathcal{F}^{(0)} = \frac{1}{2} E_s^{(0)} E_p^{(0)} (\boldsymbol{\varepsilon}_p \cdot \boldsymbol{\varepsilon}_s - (\widehat{\mathbf{k}}_p \wedge \boldsymbol{\varepsilon}_p) \cdot (\widehat{\mathbf{k}}_s \wedge \boldsymbol{\varepsilon}_s)) \ . \tag{3.26}$$

Using the Lagrange identity [AWH12]

$$(\mathbf{a} \wedge \mathbf{b}) \cdot (\mathbf{c} \wedge \mathbf{d}) = (\mathbf{a} \cdot \mathbf{c})(\mathbf{b} \cdot \mathbf{c}) - (\mathbf{b} \cdot \mathbf{c})(\mathbf{a} \cdot \mathbf{d}) \ , \tag{3.27}$$

(3.26) can be further simplified to

$$\mathcal{F}^{(0)} = E_s^{(0)} E_p^{(0)} \ \rho \ , \tag{3.28}$$

where $\rho := 2\ \boldsymbol{\varepsilon}_s \cdot \boldsymbol{\varepsilon}_p$ holds. For the second invariant we can write

$$\mathcal{G} = E_p^{(0)} E_s^{(0)} \sigma \ , \tag{3.29}$$

with $\sigma := 2\boldsymbol{\varepsilon}_s \cdot (\widehat{\mathbf{k}}_p \wedge \boldsymbol{\varepsilon}_p)$.

Box Diagram

For four-photon scattering the effective Lagrangian is given by

$$\mathcal{L}_1 = \frac{\mu_1}{4\pi} \left[4\mathcal{F}^2 + 7\mathcal{G}^2 \right] \ , \tag{3.30}$$

where $\mu_1 = \frac{\alpha}{90\pi}$.
To calculate the polarisation and magnetisation, we first observe the following identities

$$\frac{\partial \mathcal{F}}{\partial \mathbf{E}} = \frac{\partial \mathcal{G}}{\partial \mathbf{B}} = \mathbf{E} \ ,$$
$$\frac{\partial \mathcal{F}}{\partial \mathbf{B}} = -\frac{\partial \mathcal{G}}{\partial \mathbf{E}} = -\mathbf{B} \ .$$

Furthermore, we have

$$\widehat{\mathbf{k}}_p \wedge \mathbf{B}^{(0)} = -\mathbf{E}_p^{(0)} + \mathbf{E}_s^{(0)} \ , \tag{3.31}$$

$$\widehat{\mathbf{k}}_p \wedge \mathbf{E}^{(0)} = \mathbf{B}_p^{(0)} - \mathbf{B}_s^{(0)} \ . \tag{3.32}$$

The polarisation for four-photon scattering is in general

$$\mathbf{P}_1 = \frac{\partial \mathcal{L}_1}{\partial \mathbf{E}} = \frac{\mu_1}{4\pi}\big[8\mathcal{F}\ \mathbf{E} + 14\mathcal{G}\ \mathbf{B}\big] \ , \tag{3.33}$$

which can be written for the lowest order iteration in terms of the probe and strong field as

$$\mathbf{P}_1^{(0)} = \frac{\mu_1}{4\pi}\big[8\mathcal{F}^{(0)}(\mathbf{E}_p^{(0)} + \mathbf{E}_s^{(0)}) + 14\mathcal{G}^{(0)}(\mathbf{B}_p^{(0)} + \mathbf{B}_s^{(0)})\big] \ .$$

In analogy, the magnetisation for the box diagram is

$$\mathbf{M}_1 = \frac{\partial \mathcal{L}_1}{\partial \mathbf{B}} = \frac{\mu_1}{4\pi}\big[- 8\mathcal{F}\mathbf{B} + 14\mathcal{G}\mathbf{E}\big] \ . \tag{3.34}$$

Using (3.31), we obtain

$$\widehat{\mathbf{k}}_p \wedge \mathbf{M}_1^{(0)} = \frac{\mu_1}{4\pi}\big[8\mathcal{F}^{(0)}(\mathbf{E}_p^{(0)} - \mathbf{E}_s^{(0)}) + 14\mathcal{G}^{(0)}(\mathbf{B}_p^{(0)} - \mathbf{B}_s^{(0)})\big] \ .$$

Then the vectorial quantities $\mathbf{U}$ from (3.22) and $\mathbf{V}$ from (3.23) for the forward- and backward scattered field are given by

$$\mathbf{U}_1^{(0)} = \mu_1\big[4\mathcal{F}^{(0)}\mathbf{E}_s^{(0)} + 7\mathcal{G}^{(0)}\mathbf{B}_s^{(0)}\big] \ , \tag{3.35}$$

$$\mathbf{V}_1^{(0)} = \mu_1\big[4\mathcal{F}^{(0)}\mathbf{E}_p^{(0)} + 7\mathcal{G}^{(0)}\mathbf{B}_p^{(0)}\big] \ . \tag{3.36}$$

Introducing two (constant) vectors

$$\mathbf{u}_1 := (4\ \rho\ \boldsymbol{\varepsilon}_s - 7\ \sigma\ \widehat{\mathbf{k}}_p \wedge \boldsymbol{\varepsilon}_s) \ , \tag{3.37}$$

$$\mathbf{v}_1 := (4\ \rho\ \boldsymbol{\varepsilon}_p + 7\ \sigma\ \widehat{\mathbf{k}}_p \wedge \boldsymbol{\varepsilon}_p) \ , \tag{3.38}$$

this can be written in a more compact way as

$$\mathbf{U}_1^{(0)}(x^-, x^+) = \mu_1 [E_s^{(0)}(x^+)]^2 E_p^{(0)}(x^-)\mathbf{u}_1 \ ,$$
$$\mathbf{V}_1^{(0)}(x^-, x^+) = \mu_1 E_s^{(0)}(x^+)[E_p^{(0)}(x^-)]^2\mathbf{v}_1 \ .$$

From (3.20) and (3.21) we know the asymptotic field from the first iteration

$$\Delta\overrightarrow{\mathbf{E}}_{\mathrm{as},1}^{(0)}(x^-, x^+) = -\int_{-\infty}^{0} \mathrm{d}y \frac{\partial}{\partial x^-}\mathbf{U}_1^{(0)}(x^-, x^+ + y) \ ,$$
$$\Delta\overleftarrow{\mathbf{E}}_{\mathrm{as},1}^{(0)}(x^-, x^+) = -\int_{0}^{\infty} \mathrm{d}y \frac{\partial}{\partial x^+}\mathbf{V}_1^{(0)}(x^- - y, x^+) \ ,$$

and therefore

$$\Delta\overrightarrow{\mathbf{E}}_{\mathrm{as},1}^{(0)}(x^-, x^+) = -\mu_1 \frac{\partial}{\partial x^-} E_p^{(0)}(x^-) \int_{-\infty}^{0} \mathrm{d}y\ [E_s^{(0)}(x^+ + y)]^2\ \mathbf{u}_1 \ , \tag{3.39}$$

$$\Delta\overleftarrow{\mathbf{E}}_{\mathrm{as},1}^{(0)}(x^-, x^+) = -\mu_1\ \frac{\partial}{\partial x^+} E_s^{(0)}(x^+) \int_{0}^{\infty} \mathrm{d}y\ [E_p^{(0)}(x^- - y)]^2\ \mathbf{v}_1 \ .$$

The overlap signal is calculated to

$$\begin{aligned}\Delta\mathbf{E}_{1,\mathrm{o}}^{(0)}(x^-, x^+) &= -2\pi\mathbf{P}_1^{(0)}(x^-, x^+) \ , \\ &= -\mu_1 [E_p^{(0)}(x^-)]^2 E_s^{(0)}(x^+)\ \mathbf{v}_1 - \mu_1 [E_s^{(0)}(x^+)]^2 E_p^{(0)}(x^-)\ \mathbf{u}_1 \ .\end{aligned} \tag{3.40}$$

Six-Photon Scattering

For six-photon scattering, the calculation is similar to the one for four-photon scattering, so we state only the results.
The polarisation and magnetisation are given by

$$\mathbf{P}_2 = \frac{\mu_2}{4\pi}\big[(48\mathcal{F}^2 + 26\mathcal{G}^2)\mathbf{E} + 52\mathcal{F}\mathcal{G}\mathbf{B}\big] \ , \tag{3.41}$$

$$\mathbf{M}_2 = \frac{\mu_2}{4\pi}\big[- (48\mathcal{F}^2 + 26\mathcal{G}^2)\mathbf{B} + 52\mathcal{F}\mathcal{G}\mathbf{E}\big] \ . \tag{3.42}$$

The asymptotic fields for the first iteration of six-photon scattering are then

$$\Delta\overrightarrow{\mathbf{E}}^{(0)}_{2,\mathrm{as}}(x^-,x^+) = -\mu_2\frac{\partial}{\partial x^-}[E_p^{(0)}(x^-)]^2\int_{-\infty}^{0}\mathrm{d}y\ [E_s^{(0)}(x^+ + y)]^3\ \mathbf{u}_2 \ , \tag{3.43}$$

$$\Delta\overleftarrow{\mathbf{E}}^{(0)}_{2,\mathrm{as}}(x^-,x^+) = -\mu_2\frac{\partial}{\partial x^+}[E_s^{(0)}(x^+)]^2\int_{0}^{\infty}\mathrm{d}y\ [E_p^{(0)}(x^- - y)]^3\ \mathbf{v}_2 \ ,$$

where we defined

$$\mathbf{u}_2 := (24\rho^2 + 13\sigma^2)\boldsymbol{\varepsilon}_s - 26\rho\sigma(\widehat{\mathbf{k}}_p \wedge \boldsymbol{\varepsilon}_s) \ , \tag{3.44}$$

$$\mathbf{v}_2 := (24\rho^2 + 13\sigma^2)\varepsilon_p + 26\rho\sigma(\widehat{\mathbf{k}}_p \wedge \varepsilon_p) \ . \tag{3.45}$$

The overlap signal is given by

$$\Delta\mathbf{E}^{(0)}_{2,\mathrm{o}}(x^-,x^+) = -\mu_2[E_s^{(0)}(x^-)]^3[E_p^{(0)}(x^+)]^2\ \mathbf{u}_2 - \mu_2[E_s^{(0)}(x^+)]^2[E_p^{(0)}(x^-)]^3\ \mathbf{v}_2 \ .$$

Eight-Photon Scattering

Although we do not consider eight-photon scattering explicitly in this thesis it is useful to identify a corresponding nonlinearity parameter later for the effect on high-harmonic generation and when eight-photon scattering can be neglected. As the calculation is similar to the ones for four- and six-photon scattering, we only give the results. The asymptotic fields are given by

$$\Delta\overrightarrow{\mathbf{E}}^{(0)}_{3,\mathrm{as}}(x^-,x^+) = -\mu_2\frac{\partial}{\partial x^-}[E_p^{(0)}(x^-)]^3\int_{-\infty}^{0}\mathrm{d}y\ [E_s^{(0)}(x^+ + y)]^4\ \mathbf{u}_3 \ , \tag{3.46}$$

$$\Delta\overleftarrow{\mathbf{E}}^{(0)}_{3,\mathrm{as}}(x^-,x^+) = -\mu_2\frac{\partial}{\partial x^+}[E_s^{(0)}(x^+)]^3\int_{0}^{\infty}\mathrm{d}y\ [E_p^{(0)}(x^- - y)]^4\ \mathbf{v}_3 \ ,$$

where we defined

$$\mathbf{u}_3 = (96\rho^3 + 88\rho\sigma^2)\boldsymbol{\varepsilon}_s - (88\rho^2\sigma + 38\sigma^3)(\widehat{\mathbf{k}}_p \wedge \boldsymbol{\varepsilon}_s) \ ,$$

$$\mathbf{v}_3 = (96\rho^3 + 88\rho\sigma^2)\boldsymbol{\varepsilon}_p + (88\rho^2\sigma + 38\sigma^3)(\widehat{\mathbf{k}}_p \wedge \boldsymbol{\varepsilon}_p) \ ,$$

and the overlap signal is given by

$$\Delta\mathbf{E}^{(0)}_{2,\mathrm{o}}(x^-,x^+) = -\mu_3[E_s^{(0)}(x^-)]^4[E_p^{(0)}(x^+)]^3\ \mathbf{u}_3 - \mu_3[E_s^{(0)}(x^+)]^3[E_p^{(0)}(x^-)]^4\ \mathbf{v}_3 \ .$$

3.1.4 Higher Iterations

In the second part of this work, we are interested in solutions which include self-interaction of the probe that lead to a plasma-like vacuum instability and corresponding electromagnetic shock. For that we adopt the iterative procedure (3.3) to solve the wave equation that ignores the changes in the stronger background

$$(\partial_t^2 - \partial_z^2)\mathbf{E}_p^{(n+1)} = \mathbf{T}[\mathbf{E}_p^{(n)} + \mathbf{E}_s^{(0)}] \tag{3.47}$$

with the iterative solution

$$\mathbf{E}_p^{(n+1)} = \mathbf{E}_p^{(0)} + \Delta\mathbf{E}_p^{(n)} \ .$$

The change of the probe field is then given by

$$\Delta\mathbf{E}_p^{(n)}(t,z) = \int \mathrm{d}t' \, \mathrm{d}z' G_R(t-t', z-z')\mathbf{T}^{(n)}(t',z')$$

and in general

$$\mathbf{T}^{(n)}(t,z) = \sum_{i=1}^{\infty} \mathbf{T}_i \left[\mathbf{E}_p^{(n)}(x^-) + \mathbf{E}_s^{(0)}(x^+)\right],$$

where the subscript i is again the order of the weak-field expansion and the retarded Green's function is given by (3.7). The wave equation (3.47), which neglects the back reaction of the probe on the strong pulse, simplifies the calculation of higher iterations and should be justified as we always assume $\mathcal{E}_p \ll \mathcal{E}_s$. And indeed, the numerical solution of Maxwell's equations, which is explained later, does not use this simplification and the results show that this treatment is justified.
We first consider higher iterations for four-photon scattering.

Box Diagram

For simplicity and later use we only focus on the parallel setup with $\boldsymbol{\varepsilon}_p = \boldsymbol{\varepsilon}_s$ in this section.
From (3.35), we know that the vectorial part responsible for the forward scattered signal depends only on the strong pulse. Therefore, we only need to replace

$$\mathbf{E}_p^{(0)}(x^-) \to \mathbf{E}_p^{(1)}(x^-, x^+)$$

in the field invariant $\mathcal{F}$ to obtain the second iteration.
If one defines the auxiliary functions

$$\begin{aligned} o_1(x) &= \int_{-\infty}^{x} \mathrm{d}y \ [E_s^{(0)}(y)]^2 \ , \\ p_1(x) &= \int_{-\infty}^{x} \mathrm{d}y \ [E_s^{(0)}(y)]^2 o_1(y) \ , \end{aligned} \tag{3.48}$$

then the first two iterations of the asymptotic probe field can be written as

$$\begin{aligned} \Delta\mathbf{E}_p^{(0)}(x^-,x^+) &= -8\mu_1 E_p'^{(0)}(x^-) o_1(x^+)\boldsymbol{\varepsilon}_s \ , \\ \Delta\mathbf{E}_p^{(1)}(x^-,x^+) &= -8\mu_1 E_p'^{(0)}(x^-) o_1(x^+)\boldsymbol{\varepsilon}_s + 64\mu_1^2 E_p''^{(0)}(x^-) p_1(x^+)\boldsymbol{\varepsilon}_s \ , \end{aligned}$$

where the prime "$'$" indicates the derivative with respect to x^-.

To get a better understanding of this expression, we insert the explicit expression for the probe pulse

$$\mathbf{E}_p^{(0)}(x^-) = \mathcal{E}_p \boldsymbol{\varepsilon}_p f_p(\varphi_p)\cos(\varphi_p) \tag{3.49}$$

and neglect the derivatives of the envelope function $f_p(\varphi_p)$. Thus we obtain the asymptotic signal

$$\mathbf{E}_p^{(2)}(x^-, x^+) = \mathcal{E}_p \boldsymbol{\varepsilon}_p f_p(\varphi_p)\Big(\cos(\varphi_p) + 8\mu_1\omega_p \sin(\varphi_p) o_1(x^+) - 64\mu_2^2\omega_p^2 \cos(\varphi_p) p_1(x^+)\Big) \,. \tag{3.50}$$

We used that both probe and strong polarisations are parallel to combine the result in one expression and we note that the functions $o_1(x^+)$ and $p_1(x^+)$ yield constant factors in (3.50) in the asymptotic limit $x^+ \to \infty$. Using the dressed diagrams introduced in section 2.5.3, Fig. 3.1 illustrates the general iteration of the wave equation.

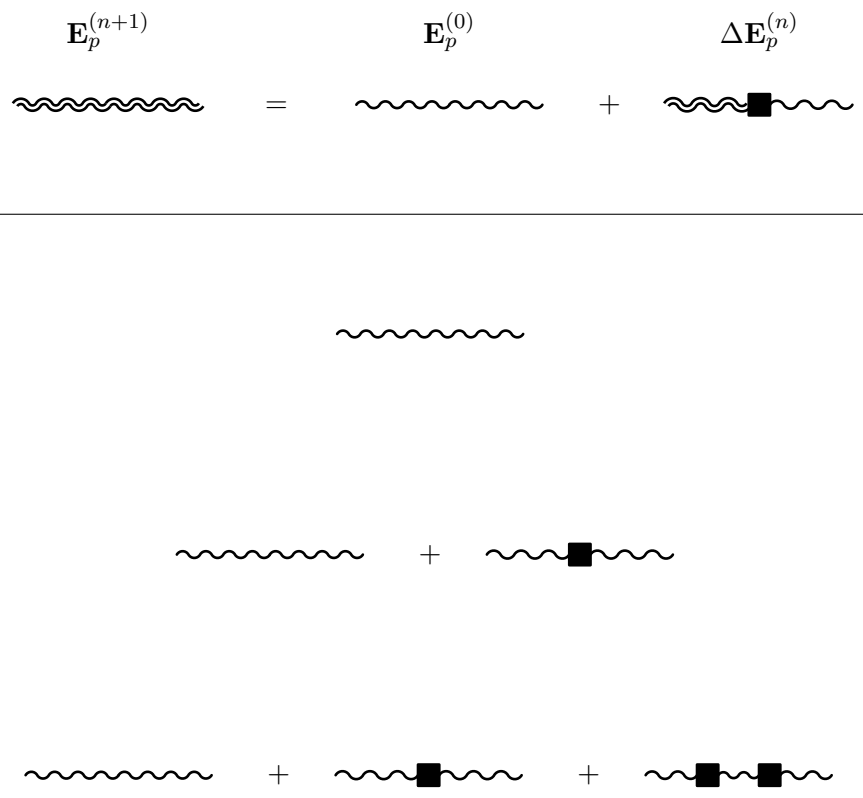

Figure 3.1: Shown is the iterative solution of the wave equation for the probe for four-photon scattering with the first two iterations given explicitly.

Hexagon Diagram

The calculation of the second iteration of the forward-scattered field for the hexagon diagram is more involved than the one for the box diagram, so we also focus only on the case of parallel probe and strong polarisations with $\boldsymbol{\varepsilon}_p = \boldsymbol{\varepsilon}_s$. In analogy to four-photon scattering, we define similar auxiliary functions as integrals over the strong field

$$\begin{aligned} o_2(x) &= \int_{-\infty}^{x} \mathrm{d}y\ [E_s^{(0)}(y)]^3\ , \\ p_2(x) &= \int_{-\infty}^{x} \mathrm{d}y\ [E_s^{(0)}(y)]^3 o_2(y)\ , \\ q_2(x) &= \int_{-\infty}^{x} \mathrm{d}y\ [E_s^{(0)}(y)]^3 [o_2(y)]^2\ . \end{aligned} \tag{3.51}$$

Then the first two iterations can be written as

$$\Delta\mathbf{E}_p^{(0)}(x^-, x^+) = -192\mu_2\ E_p'^{(0)}(x^-) o_2(x^+) \boldsymbol{\varepsilon}_s\ , \tag{3.52}$$

$$\begin{aligned} \Delta\mathbf{E}_p^{(1)}(x^-, x^+) = -\boldsymbol{\varepsilon}_s \Big(& 192\mu_2 E_p^{(0)}(x^-) E_p'^{(0)}(x^-) o_2(x^+) \\ & - (192\mu_2)^2 \big(2E_p^{(0)}(x^-)[E_p'^{(0)}(x^-)]^2 + [E_p^{(0)}(x^-)]^2 E_p''^{(0)}(x^-)\big) p_2(x^+) \\ & + (192\mu_2)^3 E_p^{(0)}(x^-) E_p'^{(0)}(x^-) ([E_p'^{(0)}(x^-)]^2 + E_p^{(0)}(x^-) E_p''^{(0)}(x^-)) q_2(x^+)\big)\ . \end{aligned} \tag{3.53}$$

Again, we can insert the explicit form of the probe pulse

$$\mathbf{E}_p^{(0)}(x^-) = \mathcal{E}_p \boldsymbol{\varepsilon}_p f_p(\varphi_p) \cos(\varphi_p)$$

and neglect the derivative of the envelope function to obtain

$$\begin{aligned} \mathbf{E}_p^{(2)}(x^-, x^+) = \mathcal{E}_p \boldsymbol{\varepsilon}_p f(\varphi_p) \Big(& \cos(\varphi_p) - \frac{1}{4}(192\mu_2)^2 \mathcal{E}_p^2 \omega_p^2 p_2(x^+) f_p^2(\varphi_p) \cos(\varphi) \\ & + 96\mu_2 \mathcal{E}_p \omega_p f_p^2(\varphi_p) o_2(x^+) \sin(2\varphi_p) - \frac{3}{4}(192\mu_2)^2 \mathcal{E}_p^2 \omega_p^2 f_p(\varphi_p)^2 p_2(x^+) \cos(3\varphi_p) \\ & - \frac{1}{4}(192\mu_2)^3 \mathcal{E}_p^3 \omega_p^3 q_2(x^+) f_p^3(\varphi_p) \sin(4\varphi_p)\Big)\ . \end{aligned} \tag{3.54}$$

As the functions (3.51) yield finite values in the asymptotic limit $x^+ \to \infty$ in the main setups considered in this thesis, we see from (3.54) that the second iteration of the wave equation generates up to the fourth harmonic. The diagrammatic iterative solution with the processes involved in the second iteration are shown in Fig. 3.2.

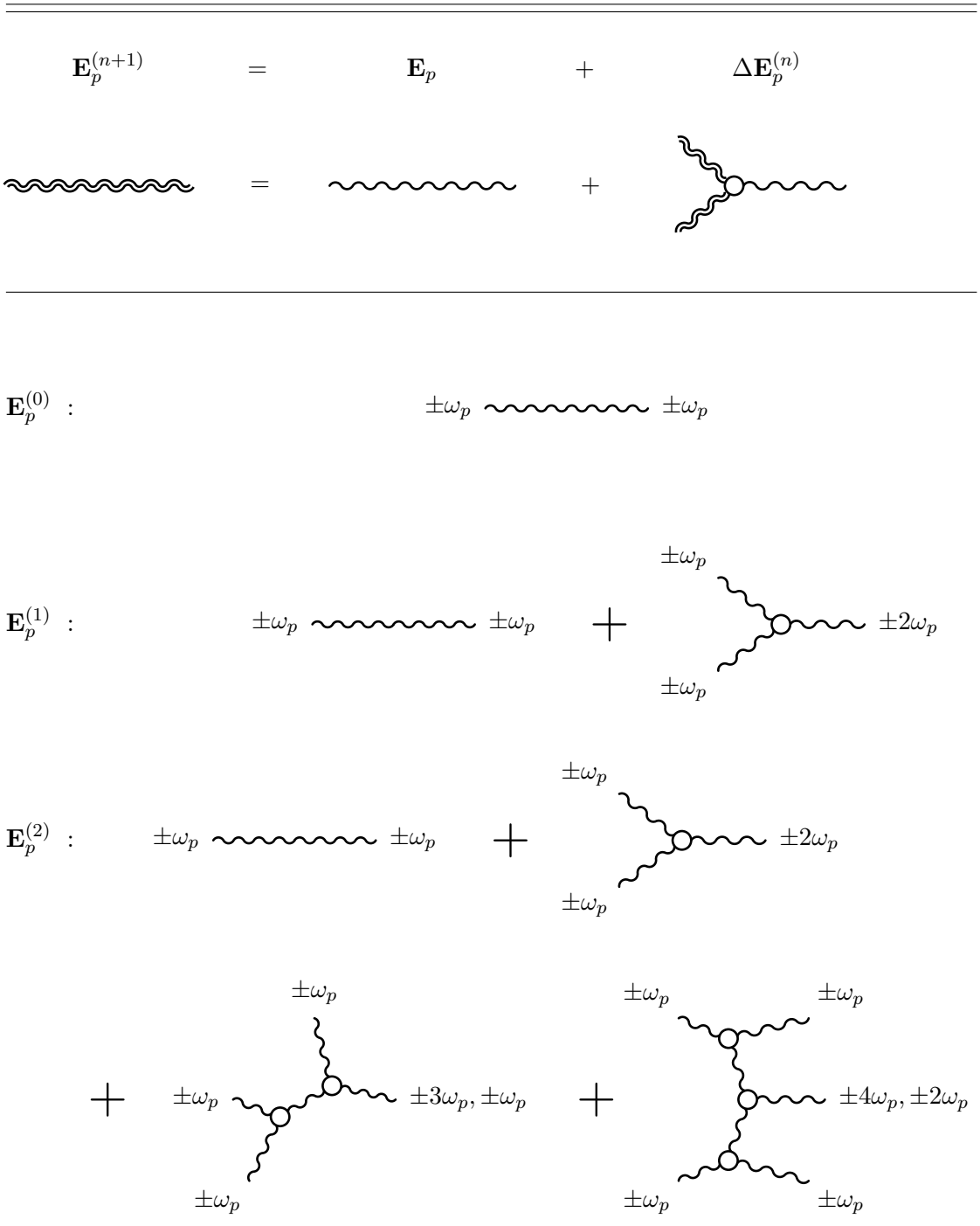

Figure 3.2: Shown is the diagrammatic iteration of the solution of the wave equation for the probe field for pure six-photon scattering together with the processes and resulting signals from the first two iterations.

3.2 Numerical Solution of Maxwell's Equations

For the scenario of two colliding plane wave pulses, the modified Maxwell equations in (2.74) and (2.75) can be written in matrix form:

$$(\mathbb{1}_4 + \mathbf{X})\,\partial_t \mathbf{f} + (\mathbf{Q} + \mathbf{Y})\,\partial_z \mathbf{f} = 0, \tag{3.55}$$

where $\mathbf{f} = (E_x, E_y, B_x, B_y)^T$, $\mathbb{1}_4$ is the identity matrix in four dimensions, $\mathbf{Q}$ is an anti-diagonal matrix with $\mathbf{Q} = \mathrm{adiag}(1, -1, -1, 1)$ and $\mathbf{X}$ and $\mathbf{Y}$ are the perturbations due to the vacuum interaction given in a general form in App. E.2.

Our numerical method, which is explained in more detail in the following, is based on inverting the matrix $(\mathbb{1}_4 + \mathbf{X})$ to convert (3.55) to a system of ordinary differential equations (ODEs), discretising in space using the "Pseudo-characteristic Method of Lines" (PCMOL) [Car80] and integrating the equations of motion using the ODE solver CVODE [Hin+05].

3.2.1 Linear Case

Let us first consider (3.55) with $\mathbf{X} = \mathbf{Y} = \mathbf{0}$, which is the $\hbar \to 0$ limit. This system is hyperbolic [Str04], which means that we can find a basis $\mathbf{u} := \mathbf{S}\,\mathbf{f}$ such that the matrix $\mathbf{\Lambda} = \mathbf{S}\mathbf{Q}\mathbf{S}^{-1} = \mathrm{diag}(-1, -1, 1, 1)$ is diagonal with real eigenvalues:

$$\mathbf{S} = \frac{1}{\sqrt{2}} \begin{pmatrix} -1 & 0 & 0 & 1 \\ 0 & 1 & 1 & 0 \\ 1 & 0 & 0 & 1 \\ 0 & -1 & 1 & 0 \end{pmatrix}, \quad \mathbf{u} := \mathbf{S}\,\mathbf{f} = \frac{1}{\sqrt{2}} \begin{pmatrix} B_y - E_x \\ E_y + B_x \\ E_x + B_y \\ B_x - E_y \end{pmatrix}. \tag{3.56}$$

In this new basis, we have an uncoupled system of advection equations

$$\partial_t \mathbf{u}(t, z) + \mathbf{\Lambda}\,\partial_z \mathbf{u}(t, z) = 0\ .$$

The diagonal elements λ_i of $\mathbf{\Lambda}$ are called the "characteristic speeds" the system, where $\lambda_i = \pm 1$ corresponds to a component travelling along the characteristics $x^{\pm}$ with the speed of light. We proceed by introducing a co-located grid for the components u_i with N grid points. The field components u_i on the grid are arranged block wise in a large $4N$-dimensional vector $\tilde{\mathbf{u}} = (\ldots u_4^{l-1} u_1^l u_2^l u_3^l u_4^l u_1^{l+1} \ldots)$, where $u_i^l = u_i(l\Delta z)$ and $0 < l \leq N$ is the index of the grid point. The PCMOL uses biased differencing for each component u_i according to the sign of the corresponding characteristic speed λ_i, where the component u_i with $\lambda_i > 0$ ($\lambda_i < 0$) is thereby differentiated using backward (forward) finite differences using fourth-order accuracy. In [Sch91] it is argued that this biased differencing using five-point-stencils is an effective fixed grid method for first order hyperbolic partial differential equations because it shows a good balance between introducing minimal numerical diffusion and oscillations in the solution where steep gradients are present. The derivatives at the boundary are also approximated using only field values inside the box. Instead of transforming the system back to $\tilde{\mathbf{f}}$ (the tilde in this section indicates the discretised version on the grid), which is normally done in the PCMOL, the system is solved for $\tilde{\mathbf{u}}$. This has the advantage of having open boundary conditions since the components u_i are only allowed to flow in one direction. If we take the system to be of size L and a spatial resolution of N grid points, then distance is measured in units of $\Delta z = {}^{L}/_{(N-1)}$, where $N - 1$ corresponds to the boundary conditions being taken into account. We are

left with a system of ODEs $\tilde{\mathbf{u}}'(t) = \mathbf{g}[\tilde{\mathbf{u}}(t), t]$, where $\mathbf{g}[\tilde{\mathbf{u}}(t), t] = -\tilde{\mathbf{\Lambda}}\,\mathbf{D}\,\tilde{\mathbf{u}}$, with the 4×4 matrix $\mathbf{\Lambda}$ being mapped onto a $4N \times 4N$ dimensional block-diagonal one, $\tilde{\mathbf{\Lambda}} = \mathbb{1}_N \otimes \mathbf{\Lambda}$ ($\otimes$ is the Kronecker product [LT85]) and $\mathbf{D}$ being the $4N \times 4N$ matrix representing the biased differencing explained above. For the detailed action of $\mathbf{D}$ on $\tilde{\mathbf{u}}$ see Appendix E.1.

The initial conditions are set up in $\tilde{\mathbf{f}}$, the system is integrated in $\tilde{\mathbf{u}}$ using CVODE and transformed back for output. CVODE is an ODE-solver that offers variable-order, variable-step multi-step methods. Initially, we supply the "right-hand-side function" $\mathbf{g}[\tilde{\mathbf{u}}(t), t]$ as above. Since both the linear and nonlinear cases are non-stiff (no rapidly-damped modes are expected), we apply the Adams-Moulton-Methods together with the variational method to solve the resulting linear system. This provides higher accuracy with less computational effort compared to the offered Newton iterations, since neither approximations nor an analytical expression for the Jacobian have to be provided. We always use the parallel implementation of CVODE together with "extended" (long double) precision. The simulations were also confirmed to be independent of the boundary conditions as periodic boundary conditions yield the same results.

3.2.2 Nonlinear Case

By discretising the full nonlinear system (3.55), the matrices $\mathbf{X}$ and $\mathbf{Y}$ also become $4N \times 4N$ dimensional. The system then can also be brought into ODE form $\tilde{\mathbf{u}}'(t) = \mathbf{g}[\tilde{\mathbf{u}}(t), t]$ by inverting the matrix $(\mathbb{1}_{4N} + \tilde{\mathbf{X}})$. Since $\mathbf{X}$ depends only on local field values, it is of block diagonal form:

$$\tilde{\mathbf{X}} = \bigoplus_{l=1}^{N} \mathbf{X}^l \ ,$$

where $\bigoplus$ is the direct sum and $\mathbf{X}^l$ are the matrices $\mathbf{X}$ evaluated at grid point l. This can be used to reduce the inversion of $\tilde{\mathbf{X}}$ to N times the inversion of a 4×4 matrix. The structure of $\mathbf{X}^l$ allows us to rewrite $\mathbf{X}^l$ as $\mathbf{X}^l = \mathbf{G}\,\mathbf{H}^l$ with

$$\mathbf{G} = \begin{pmatrix} 1 & 0 \\ 0 & 1 \\ 0 & 0 \\ 0 & 0 \end{pmatrix}, \qquad \mathbf{H}^l = \begin{pmatrix} x^l_{11} & x^l_{12} & x^l_{13} & x^l_{14} \\ x^l_{21} & x^l_{22} & x^l_{23} & x^l_{24} \end{pmatrix} \ , \tag{3.57}$$

where the x^l_{ij} are the values of the non-vanishing matrix elements of $\mathbf{X}$ given in App. E.2, evaluated at position l. Then we can apply the Woodbury Formula [GVL12],

$$(\mathbb{1}_4 + \mathbf{X}^l)^{-1} = \mathbb{1}_4 - \mathbf{G}(\mathbb{1}_2 + \mathbf{H}^l\mathbf{G})^{-1}\mathbf{H}^l \ , \tag{3.58}$$

to further reduce the inversion to one of the 2×2 matrix

$$(\mathbb{1}_2 + \mathbf{H}^l\mathbf{G}) = \begin{pmatrix} 1 + x^l_{11} & x^l_{12} \\ x^l_{21} & 1 + x^l_{22} \end{pmatrix} \ .$$

which is done via a LU-factorisation for all grid points using an LU-factorisation at each evaluation of the function $\mathbf{g}[\tilde{\mathbf{u}}(t), t]$.
For the parameters considered, the nonlinear corrections $\mathbf{X}$ and $\mathbf{Y}$ do not change the signs of the characteristic speeds, so we use the same biased differencing as in the linear case. The nonlinear ODE-system is then given by

$$\tilde{\mathbf{u}}'(t) = -\tilde{\mathbf{S}}(\mathbb{1}_{4N} + \tilde{\mathbf{X}})^{-1}(\tilde{\mathbf{Q}} + \tilde{\mathbf{Y}})\tilde{\mathbf{S}}^{-1}\mathbf{D}\tilde{\mathbf{u}} \ ,$$

where $\tilde{\mathbf{S}} = \mathbb{1}_N \otimes \mathbf{S}$, $\tilde{\mathbf{Q}} = \mathbb{1}_N \otimes \mathbf{Q}$,

$$\tilde{\mathbf{Y}} = \bigoplus_{l=1}^{N} \mathbf{Y}^l \ , \tag{3.59}$$

in analogy to $\tilde{\mathbf{X}}$ and the inverse matrix

$$(\mathbb{1}_{4N} + \tilde{\mathbf{X}})^{-1} = \bigoplus_{l=1}^{N} (\mathbb{1}_4 + \mathbf{X}^l)^{-1} \tag{3.60}$$

is calculated block wise as in (3.58). All fields are normalised by E_{cr}. The parameters for CVODE are the same as in the linear case. The signals are analysed under the assumption $\omega = |\mathbf{k}|$ using a spatial Fourier transform in *Wolfram Mathematica* [WR12]. As we later analyse harmonic spectra of the forward scattered probe field that are normalised to the initial probe intensity, we give the conventions for the Fourier transform:

$$\widehat{\mathbf{E}}_p(\omega) = \int_{-\infty}^{\infty} \mathrm{d}x^- \ \mathbf{E}_p(x^-)\, \mathrm{e}^{i\omega x^-}. \tag{3.61}$$

The initial probe intensity is defined as

$$I_p^{(0)}(\omega_p) = |\widehat{E}_p^{(0)}(\omega_p)|^2 \tag{3.62}$$

and the intensity of the forward-scattered field is then

$$I_p(\omega) = |\widehat{E}_p(\omega)|^2 \tag{3.63}$$

such that

$$\frac{I(\omega)}{I_p^{(0)}(\omega_p)} = \left[\frac{|\widehat{E}_p(\omega)|}{|\widehat{E}_p^{(0)}(\omega_p)|} \right]^2 \ .$$

Chapter 4

Harmonic-Generation and Shockwaves

The first part of this chapter focuses on the time-resolved analysis of the processes that arise from the first iteration of the wave equation (including the overlap signal) for four- and six-photon scattering. The setup is chosen as two colliding plane waves pulses where the strong background is Gaussian. The main effects are birefringence, harmonic generation (also called photon merging) and the back reaction of the probe on the strong background. We also identify a certain parameter regime where the overlap can possibly dominate the asymptotic signal. Finally, a comparison between the harmonic generation considered and other vacuum processes like photon splitting and pair-creation is made.

The second part investigates vacuum high harmonic generation (VHHG) due to multiple consecutive scattering events in a quasi-constant, rectangular background with vanishing frequency. The nonlinear wave equation of the probe pulse for the box- and hexagon-diagram is solved to all orders for the case of parallel probe and strong polarisations. For six-photon scattering, this solution can be written as a probe-dependent refractive index that leads to generation of high harmonics and eventually to the development of a discontinuity in the wavefront. This shocking appears after a characteristic propagation length in the background that is quantified and the solution is compared to those solutions known for the inviscid Burger's equation. Further, the polarisation-dependency of the harmonic generation is studied numerically and an outlook on ultra-short probe pulses and the effect of inhomogeneities in the background is given. We conclude with a discussion of similarities to harmonic generation in real plasmas, comment on the measurability of the effects studied and on the validity of the approach.

4.1 Overlap Dynamics

4.1.1 Simulational Setup

In this part of the thesis we analyse the predictions from the lowest order iteration of the wave equation leading to the nonlinear response (3.25) for four- and six-photon

scattering. The strong background is thereby chosen to be a Gaussian as it is shown in panel (**a**) of Fig. 2.10:

$$\mathbf{E}_s^{(0)}(x^+) = \mathcal{E}_s \boldsymbol{\varepsilon}_s \mathrm{e}^{-\left(\frac{x^+}{\tau_s}\right)^2} .$$

Since we only consider the first iteration, we drop the iteration index n in this section. To analyse the different frequency components, we simulate the same setup once with linear propagation, once with only four-photon scattering, with only six-photon and with both four-and-six-photon scattering included. The corresponding numerical signal is transformed at each time step to k-space via a spatial Fourier transform using *Wolfram Mathematica* [WR12]. Then the same step with only linear propagation is also transformed to k-space and the linear spectrum substracted from the nonlinear one. This allows for the analysis of the contributions to the fundamental harmonic and the slowly varying *dc* component, since one needs to separate it from the linear probe and strong background. The different frequency components are filtered under the assumption $\omega = |k|$ and then transformed back to coordinate space. In all figures the solid lines are the theoretical predictions, the dashed lines represent the numerical signal. Since the simulation gives only the sum of all contributions, we extract each different component of a harmonic via substraction of the dominant analytical expression from the numerical signal. All signals shown are in units of the probe amplitude $\mathcal{E}_p$.
Although both the analytical solution and the numerical simulation are able to treat arbitrary relative polarisations of the strong and probe fields, we mainly focus on the cases with parallel and perpendicular relative polarisations. The labels $\Delta\mathbf{E}^{\parallel}$ and $\Delta\mathbf{E}^{\perp}$ represent the two cases $\boldsymbol{\varepsilon}_p \cdot \boldsymbol{\varepsilon}_s = 1$ (parallel setup) and $\boldsymbol{\varepsilon}_p \cdot \boldsymbol{\varepsilon}_s = 0$ (perpendicular setup). The full angular dependency of the phase shift resulting from four-photon scattering and the asymptotic generation of higher harmonics, which involve higher iterations in the analytical solution of the wave equation, will be analysed in section 4.2.
The parameters for the simulations shown in this chapter were $N = 4{\cdot}10^5$ grid points, the box length $L = 3.2 \cdot 10^{-5}$ cm, the amplitude of the strong and probe pulse $\mathcal{E}_s = 2 \cdot 10^{-2}$ and $\mathcal{E}_p = 5 \cdot 10^{-3}$. The probe wave length is $\lambda_p = 2.5 \cdot 10^{-8}$ cm corresponding to a frequency $\omega_p = 2.5 \cdot 10^8 \, \frac{1}{\mathrm{cm}} = 0.6$ eV. The pulse durations are $\tau_p = 5 \cdot \lambda_p$ and $\tau_s = 9/7 \cdot \tau_p$.
For a clearer arrangement, we separate each frequency and begin with the fundamental probe frequency ω_p, continue with the analysis of the second harmonic, followed by the dc component and conclude with the third harmonic which is the only further higher harmonic generated from four- and six-photon scattering within the lowest order iteration of the wave equation. Afterwards, we compare under which circumstances photon merging in a magnetic field background resulting in the $2\omega_p$-signal might be prevalent compared to other vacuum polarisation effects like photon splitting and thermally induced electron-positron pair-creation.

4.1.2 Fundamental Harmonic

One of the most prominent dispersive effects predicted from vacuum polarisation is *vacuum birefringence*. The birefringence manifests itself as an alternation of the refractive index which is to lowest order independent of the amplitude of the probe field and depends only on the strength of the strong background and the relative polarisation of the probe and strong field. We see shortly how this effect arises in the asymptotic signal of our analytical treatment. But first we consider the overlap signal.
Evaluating (3.24) for the overlap scattered field from the box diagram, we have the

following contribution to the first harmonic ω_p:

$$\Delta\mathbf{E}_{1,\mathrm{o},\omega_p}(x^-,x^+) = -\mu_1\mathcal{E}_p\mathcal{E}_s^2\mathrm{e}^{-2\left(\frac{x^+}{\tau_s}\right)^2}\mathrm{e}^{-\left(\frac{x^-}{\tau_p}\right)^2}\cos\left(\omega_p x^-\right)\mathbf{u}_1\ . \tag{4.1}$$

The asymptotic change in the fundamental frequency is given by (see (3.39))

$$\Delta\vec{\mathbf{E}}_{1,\mathrm{as},\omega_p}(x^-,x^+) = \frac{1}{2}\mu_1\sqrt{\frac{\pi}{2}}\mathcal{E}_p\mathcal{E}_s^2\omega_p\tau_s\mathrm{e}^{-\left(\frac{x^-}{\tau_p}\right)^2}\left(1+\mathrm{erf}\left(\frac{\sqrt{2}x^+}{\tau_s}\right)\right)\sin\left(\omega_p x^-\right)\mathbf{u}_1\ . \tag{4.2}$$

The time development of the overlap (4.1) and asymptotic field (4.2) for different times of the interaction in the parallel and the perpendicular setups is shown in Fig. 4.1 and Fig. 4.2. One sees that the asymptotic signal dominates the overlap field.

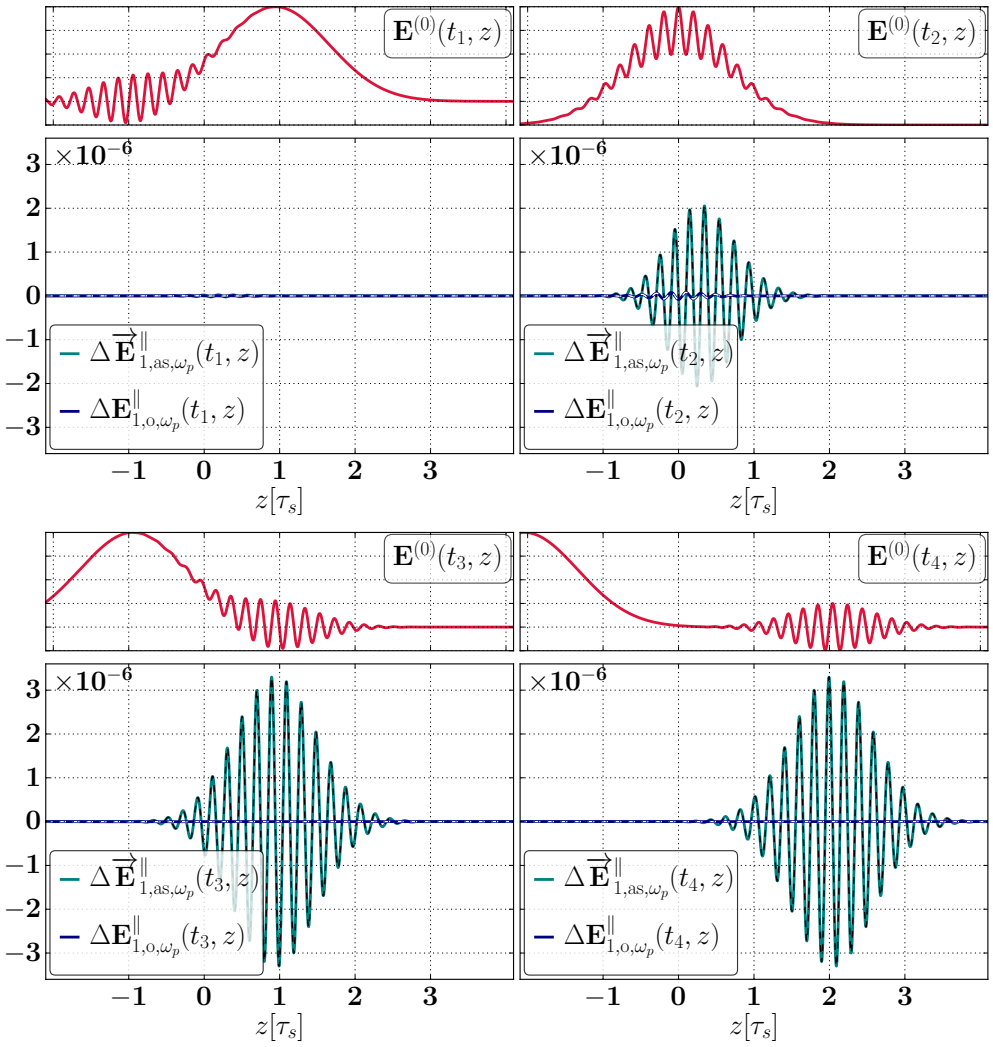

Figure 4.1: Time evolution in the parallel setup of the nonlinear response in the fundamental frequency ω_p at four different times $t_4 > t_3 > t_2 > t_1$. The upper panels show the position of the probe and strong pulse in the simulation box. The lower panels show the overlap and asymptotic fundamental harmonic ω_p from four-photon scattering. Solid lines are the analytical expressions and the dashes show the numerical signal. All fields are in units of the probe amplitude $\mathcal{E}_p$.

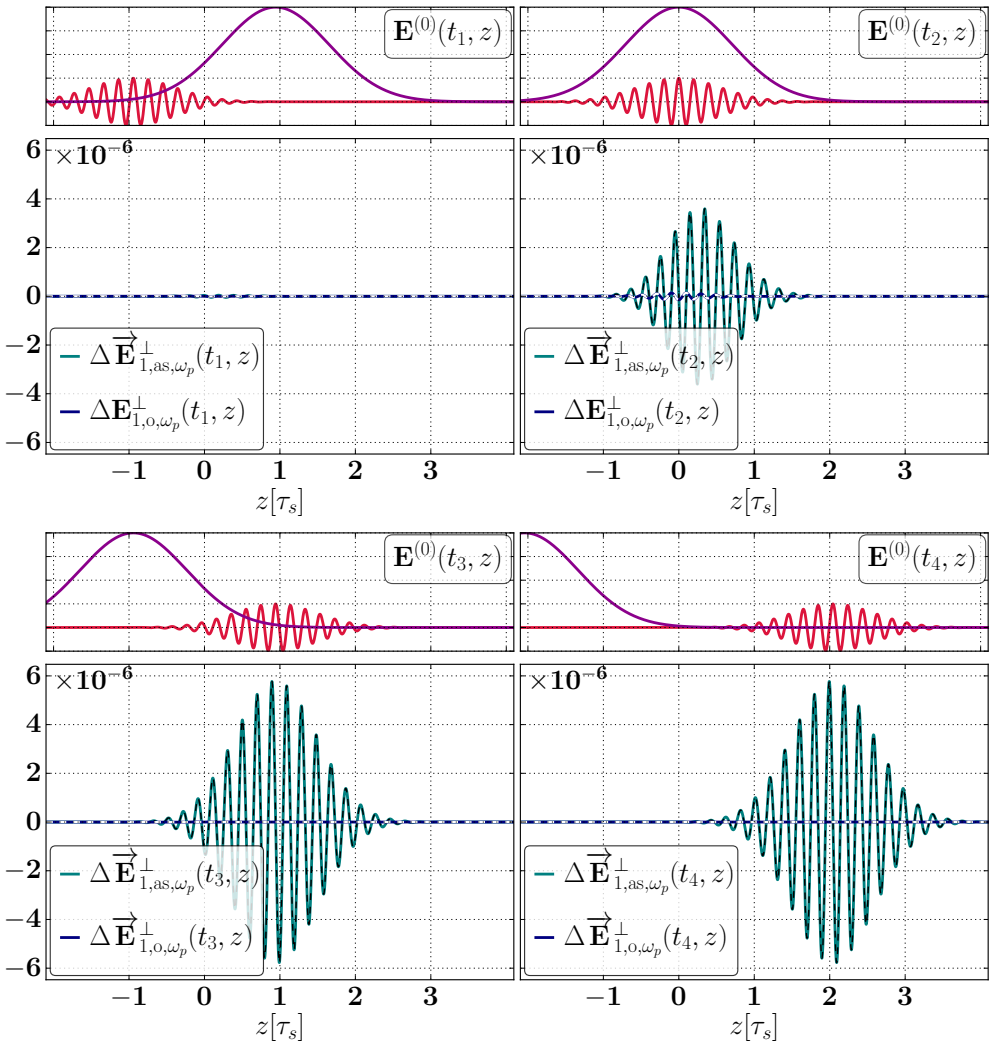

Figure 4.2: Time evolution of the change in the fundamental harmonic ω_p for four-photon scattering in the perpendicular setup. The upper panels show the positions of the different polarisation components of the initial probe and strong pulse at different times $t_4 > t_3 > t_2 > t_1$. The dashes indicate the numerical signal. All fields are normalised to $\mathcal{E}_p$.

As already mentioned, it is a well-known result that four-photon scattering in constant crossed field backgrounds causes vacuum birefringence and as such it can be seen as a change in the refractive index $\mathsf{n} = 1 \to \mathsf{n} = 1 + \delta\mathsf{n}_1$ for the probe while passing through the background. The change in the refractive index is given by [BB67b; DG00]

$$\delta\mathsf{n}_1 = 4\mu_1\mathcal{E}_s^2\left[4\left(\boldsymbol{\varepsilon}_p\cdot\boldsymbol{\varepsilon}_s\right)^2 + 7\left(\boldsymbol{\varepsilon}_p\wedge\boldsymbol{\varepsilon}_s\right)^2\right]. \tag{4.3}$$

We write n_1 where the index 1 indicates that this effect is caused by four photon scattering. This change of the refractive index causes a phase shift in the carrier phase of the probe field, $\cos(\varphi_p) \to \cos(\varphi_p - \delta\varphi_p)$.
For parallel and perpendicular polarisations, the asymptotic change in the probe field (4.2) is always parallel to the probe field, so we can write

$$\mathbf{E}_p^{(1)}(x^-, x^+) = \mathcal{E}_p\boldsymbol{\varepsilon}_p\mathrm{e}^{-\left(\frac{x^-}{\tau_p}\right)^2}\Big(\cos(\varphi_p) + \delta\varphi_p(x^+)\sin\big(\omega_p x^-\big)\Big)$$

for $\delta\varphi_p(x^+) \ll 1$. The phase shift $\delta\varphi_p(x^+)$ is then given by

$$\delta\varphi_p(x^+) = \frac{\omega_p}{2}\int_{-\infty}^{x^+} \mathrm{d}y\ \mathsf{n}_1^{\parallel,\perp}(y)\ , \tag{4.4}$$

for the parallel and perpendicular case and the phase-dependent refractive index is defined as

$$\delta\mathsf{n}_1^{\parallel,\perp}(y) = 2\mu_1[E_s(y)]^2\,(11 \mp 3)\ . \tag{4.5}$$

We note that this phase-shift is in agreement with (4.2). The integral (4.4) over the strong pulse is a measure for the energy density in the strong background and numerical experiments showed that the expression for the phase shift is valid for all kinds of slowly-varying backgrounds. This agrees with the observation in [Din+14b], where it is shown that birefringence signals are dominated by the energy content of the strong pulse and not by the specific shape. We note that the refractive index is, to lowest order in α, independent of the probe amplitude. So after passing the strong pulse, the whole pulse is shifted by the overall phase $\delta\varphi_p$:

$$\delta\varphi_p := \lim_{x^+\to\infty}\delta\varphi_p(x^+) = \frac{\omega_p}{2}\int_{-\infty}^{\infty} \mathrm{d}y\ \mathsf{n}_1^{\parallel,\perp}(y)\ . \tag{4.6}$$

If one also wants to interpret the overlap signal (4.1) as a refractive index different from unity, one obtains

$$\delta\varphi_{p,\mathrm{o}}(x^+) = \frac{\omega_p}{2}\int_{-\infty}^{x^+} \mathrm{d}y\ \mathsf{n}_{1,\mathrm{o}}^{\parallel,\perp}(y)\ , \tag{4.7}$$

where the refractive index for the overlap signal is defined as [KBR16]

$$\delta\mathsf{n}_{1,\mathrm{o}}^{\parallel,\perp}(x^+) = 2\mu_1(11 \mp 3)\frac{E_p(\varphi_p)}{\partial_- E_p(\varphi_p)}\partial_+[E_s(x^+)]^2\ . \tag{4.8}$$

If one takes a plane wave probe with $\tau_p \to \infty$, this agrees with eqs. (28) and (29) of [HH14] for the parallel and perpendicular setup with the identifications $\omega_\phi = \omega_s$, $\omega = \omega_p$, $\xi(\varphi) = E_p(\varphi_p)$, $\omega_s\Gamma_2 = \frac{\partial_+ E_s(x^+)}{E_s(x^+)}$. But since the overlap signal is in phase with the probe and contains the derivative of the strong field, the interpretation as a pure refractive index needs further investigation including higher order processes of four-photon scattering.
For the parameters considered, the asymptotic field exceeds the overlap signal. Only for $\omega_p\tau_s \ll 1$ the overlap signal dominates over the asymptotic one.

Although we made the assumption $\omega_p\tau_p \gg 1$, the numerical analysis also shows the contribution from the derivative of the Gaussian envelope-function:

$$\Delta\vec{\mathbf{E}}_{1,\mathrm{d},\omega_p}(x^-,x^+) = \mu_1\sqrt{\frac{\pi}{2}}\mathcal{E}_p\mathcal{E}_s^2\frac{\tau_s}{\tau_p}\frac{x^-}{\tau_p}\mathrm{e}^{-\left(\frac{x^-}{\tau_p}\right)^2}\left(1+\mathrm{erf}\left(\frac{\sqrt{2}x^+}{\tau_s}\right)\right)\cos\big(\omega_p x^-\big)\mathbf{u}_1\ . \tag{4.9}$$

Since we always assume $\omega_p\tau_p \gg 1$, the derivative of the envelope function only contributes comparable to the overlap field for the current parameters ($\omega_p\tau_p \approx 25$). This is shown in Fig. 4.3.

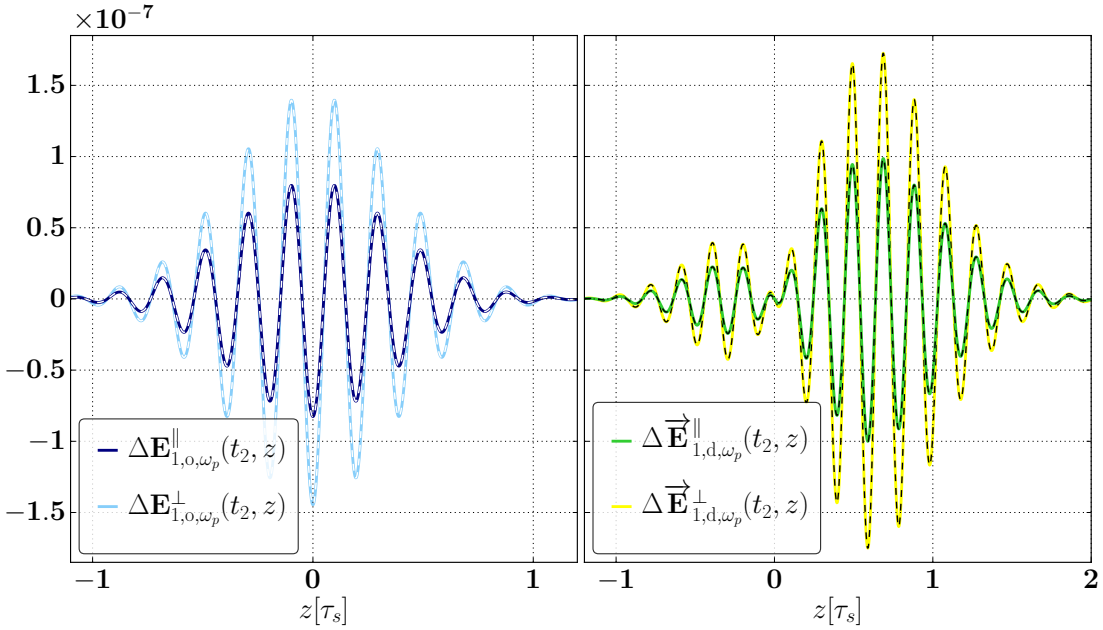

Figure 4.3: Comparison of the maximal overlap signal with the derivative of the envelope function for the fundamental harmonic ω_p from four-photon scattering. The dashes show the numerical signal.

From six-photon scattering we also obtain a contribution to the first harmonic which is much smaller than the one from the box diagram since $\mathcal{E}_p, \mathcal{E}_s \ll 1$. For the overlap signal this is given by

$$\Delta\mathbf{E}_{2,\mathrm{o},\omega_p}(x^-,x^+) = -\frac{3}{4}\mu_2\mathcal{E}_p^3\mathcal{E}_s^2 \mathrm{e}^{-3\left(\frac{x^-}{\tau_p}\right)^2} \mathrm{e}^{-2\left(\frac{x^+}{\tau_s}\right)^2} \cos\left(\omega_p x^-\right)\mathbf{v}_2 \ . \tag{4.10}$$

For the asymptotic signal, we see from $(\cos\varphi_p)^3 = \frac{1}{4}(3\cos\varphi_p + \cos 3\varphi)$ that the ω_p contribution stems from the current $\mathbf{J}_2$ where the vectorial part is of the probe and is therefore left-travelling:

$$\begin{aligned}\Delta\overleftarrow{\mathbf{E}}_{2,\mathrm{as},\omega_p}(x^-,x^+) = \frac{1}{4}\mu_2\sqrt{3\pi}\mathcal{E}_p^3\mathcal{E}_s^2 \ \mathrm{e}^{-\frac{1}{12}\tau_p^2\omega_p^2} \ \mathrm{e}^{-2\left(\frac{x^+}{\tau_s}\right)^2} \ \frac{\tau_p}{\tau_s}\frac{x^+}{\tau_s} \\ \cdot\left(2+\mathrm{erf}\left(\frac{\sqrt{3}x^-}{\tau_p}-\frac{\mathrm{i}\tau_p\omega_p}{2\sqrt{3}}\right)+\mathrm{erf}\left(\frac{\sqrt{3}x^-}{\tau_p}+\frac{\mathrm{i}\tau_p\omega_p}{2\sqrt{3}}\right)\right)\mathbf{v}_2 \ .\end{aligned} \tag{4.11}$$

We note that the ω_p-dependence in (4.11) disappears asymptotically as the integral over the probe pulse gives a constant (small) value, which is due to the absence of wave mixing as explained in section 2.5.1. Snapshots of both signals for the maximal overlap of the strong pulse and the probe pulse are shown in Fig. 4.4.

4.1.3 Second Harmonic

We note that there is no lowest order, forward-scattered signal of the second harmonic from four-photon scattering since in this $(1+1)$ dimensional setup as the generation is suppressed for kinematical reasons [Adl71]. This is also in agreement with our observation that the forward scattered signal from four-photon scattering only gives a

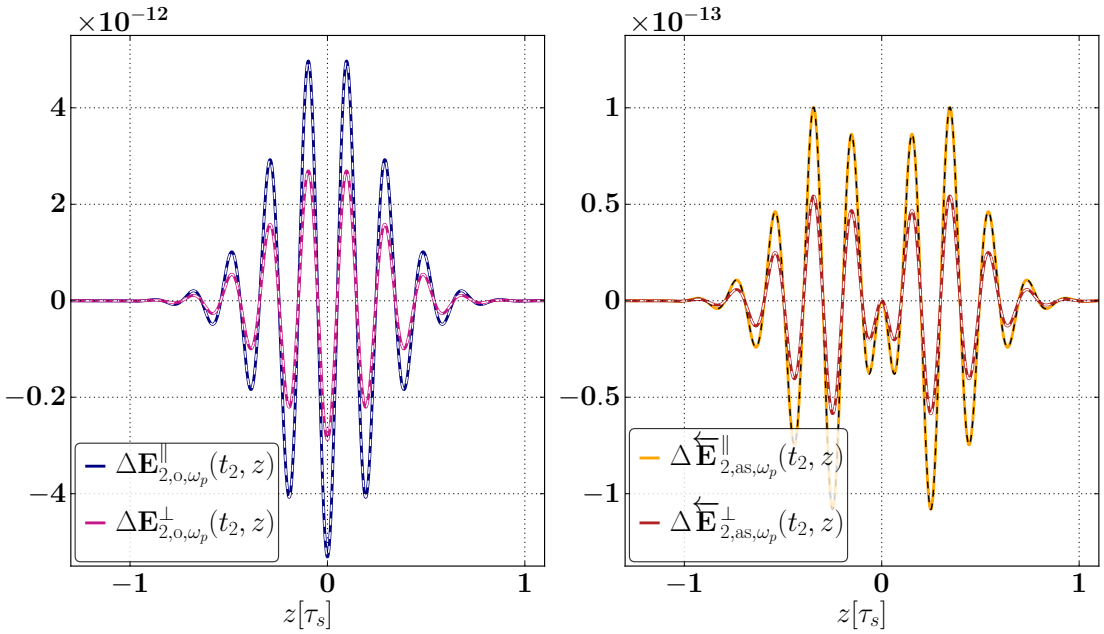

Figure 4.4: Overlap and left-travelling signal for the fundamental harmonic from six-photon scattering. The dashes show the numerical signal.

contribution to the fundamental harmonic. But the $2\omega_p$ signal can be generated as an overlap signal from pure four-photon scattering:

$$\Delta\mathbf{E}_{1,\mathrm{o},2\omega_p}(x^-,x^+) = -\frac{1}{2}\mu_1\mathcal{E}_p^2\mathcal{E}_s \mathrm{e}^{-2\left(\frac{x^-}{\tau_p}\right)^2}\mathrm{e}^{-\left(\frac{x^+}{\tau_s}\right)^2}\cos\left(2\omega_p x^-\right)\mathbf{v}_1\ . \tag{4.12}$$

The asymptotic generation of the right-travelling asymptotic field is given by the hexagon diagram:

$$\Delta\overrightarrow{\mathbf{E}}_{2,\mathrm{as},2\omega_p}(x^-,x^+) = \frac{1}{2}\mu_2\mathcal{E}_p^2\mathcal{E}_s^3\sqrt{\frac{\pi}{3}}\omega_p\tau_s\mathrm{e}^{-2\left(\frac{x^-}{\tau_p}\right)^2}\left(1+\mathrm{erf}\left(\frac{\sqrt{3}x^+}{\tau_s}\right)\right) \cdot\sin\left(2\omega_p x^-\right)\mathbf{u}_2\ . \tag{4.13}$$

A direct comparison of these two signals is shown in Fig. 4.5 and Fig. 4.6 for different interaction times and the time development of the maximum of the overlap and asymptotic field in the parallel setup is plotted in Fig. 4.7.

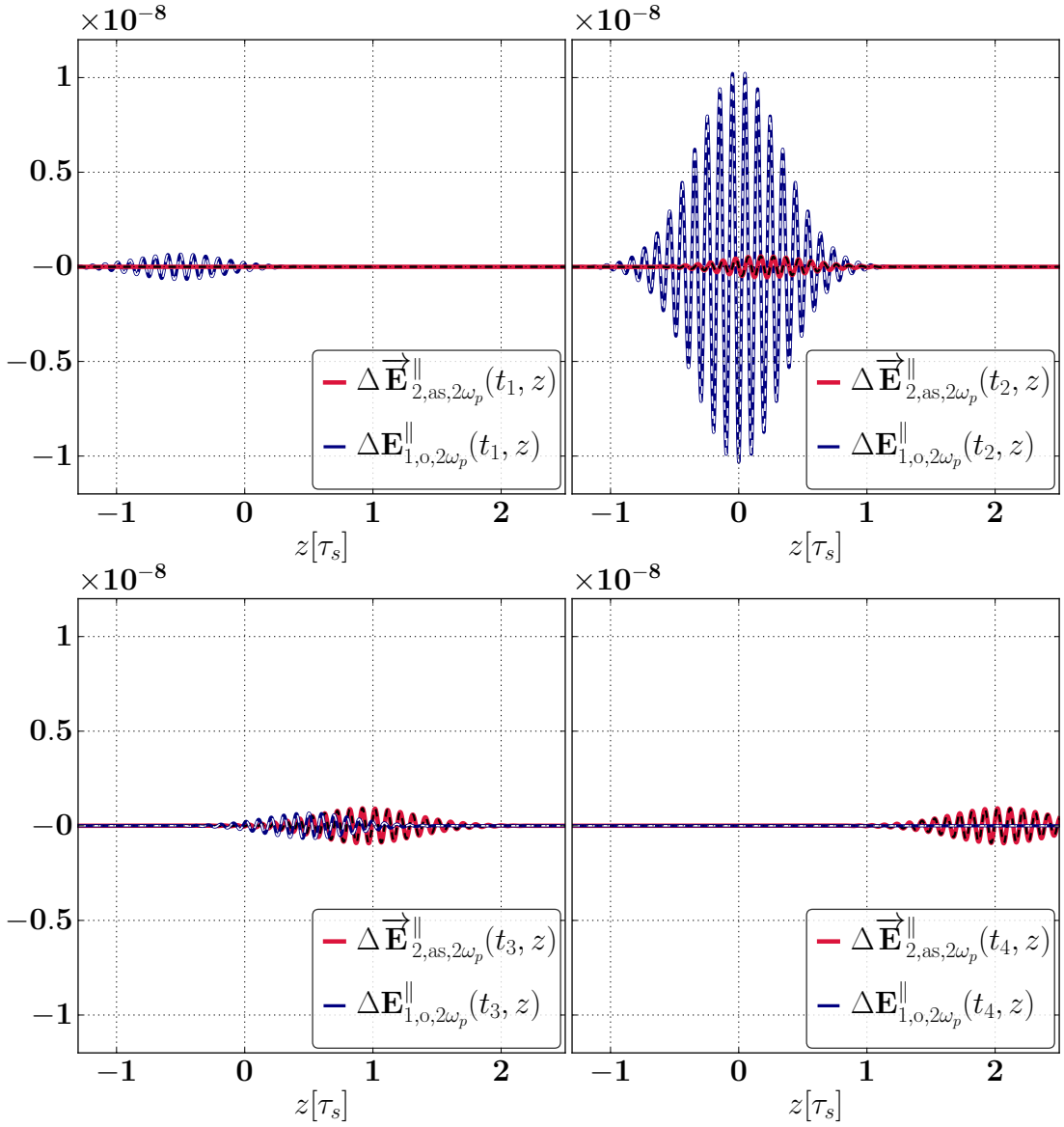

Figure 4.5: Time evolution in the parallel setup of the second harmonic $2\omega_p$ for the overlap signal stemming from four-photon scattering and the asymptotic signal from six-photon scattering. The dashes show the numerical signal. The overlap field signal exceeds the asymptotic one.

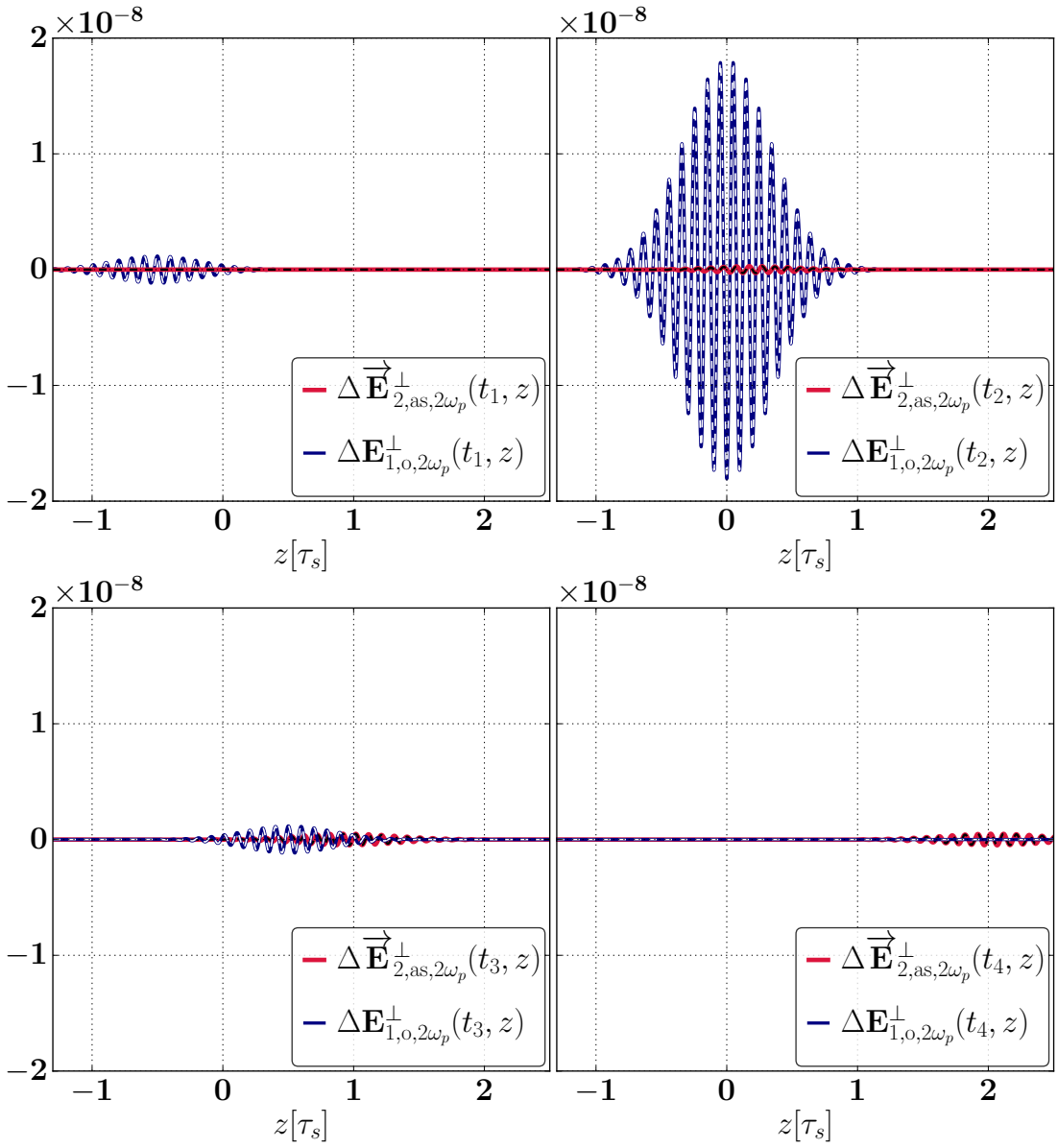

Figure 4.6: Time evolution in the perpendicular setup of the second harmonic $2\omega_p$ for the overlap signal stemming from four-photon scattering and the asymptotic signal from six-photon scattering. The dashes show the numerical signal.

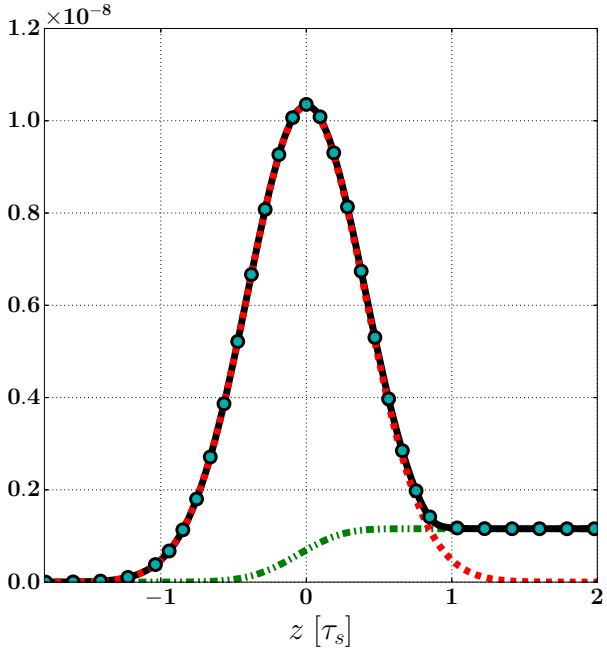

Figure 4.7: Shown is the maximum of the amplitude of the second harmonic for the overlap field (red dashed), the asymptotic field (green dashed-dotted) and the sum field. The turquoise-black dots show the numerical results.

We see that the overlap field dominates over the asymptotic signal for our parameters. To get a better qualitative understanding when this is the case, let us define a nonlinearity parameter

$$\zeta = \frac{1}{\eta}\int_{-\infty}^{\infty} \mathrm{d}\varphi_s \; \chi(\varphi_s)^2 \; , \tag{4.14}$$

where

$$\chi(\varphi_s) = \frac{\sqrt{|k_p \cdot F_s|}}{m} \tag{4.15}$$

is the *quantum efficiency parameter* [Rit85] for the probe photons and $\eta := \frac{k_p k_s}{m^2}$. The overlap field does not include any explicit integral of the strong field or the derivative of the probe pulse, whereas the factor $\omega_p \tau_s$ in ζ (and the asymptotic signal) is a measure for how many probe oscillations „fit“ into the strong background. For the current setup $\chi = \sqrt{2\pi}\mathcal{E}_s^2 \omega_p \tau_s \approx 3 \cdot 10^{-2}$ and one sees that for $\zeta \ll 1$, the overlap field can dominate. Apart from the two dominant overlap and asymptotic signals (4.12) and (4.13), there is also a backward-scattered signal where the vectorial part of $\mathbf{J}_1$ is of the probe pulse:

$$\Delta\overleftarrow{\mathbf{E}}_{1,\mathrm{as},2\omega_p}(x^-,x^+) = \frac{1}{16}\mu_1\sqrt{\frac{\pi}{2}}\frac{\tau_p}{\tau_s}\frac{x^+}{\tau_s}\mathcal{E}_s\mathcal{E}_p^2 \mathrm{e}^{-\left(\frac{x^+}{\tau_s}\right)^2} \mathrm{e}^{-\frac{1}{2}\omega_p^2\tau_p^2}\left(2 + \mathrm{erf}\left(\frac{2x^- - i\omega_p\tau_p^2}{\sqrt{2}\tau_p}\right) + \mathrm{erf}\left(\frac{2x^- + i\omega_p\tau_p}{\sqrt{2}\tau_p}\right)\right)\mathbf{v}_1 \; .$$

As we already had for the left-travelling first harmonic from six-photon scattering, the interpretation of $\Delta\overleftarrow{\mathbf{E}}_{1,\mathrm{as},2\omega_p}(x^-,x^+)$ as an asymptotic $2\omega_p$ signal is not completely correct as the integral of the probe field squared,

$$\int_{-\infty}^{\infty} \mathrm{d}y \; [E_p^{(0)}(y)]^2 = \frac{1}{2}\sqrt{\frac{\pi}{2}}\mathcal{E}_p^2\tau_p\left(1 + \mathrm{e}^{-\frac{1}{2}\tau_p^2\omega_p^2}\right) \; ,$$

yields a fixed value and therefore any dependence on $2\omega_p$ disappears in the limit of asymptotically separated pulses due to the absence of wave mixing. A snapshot of this signal is shown in Fig. 4.8:

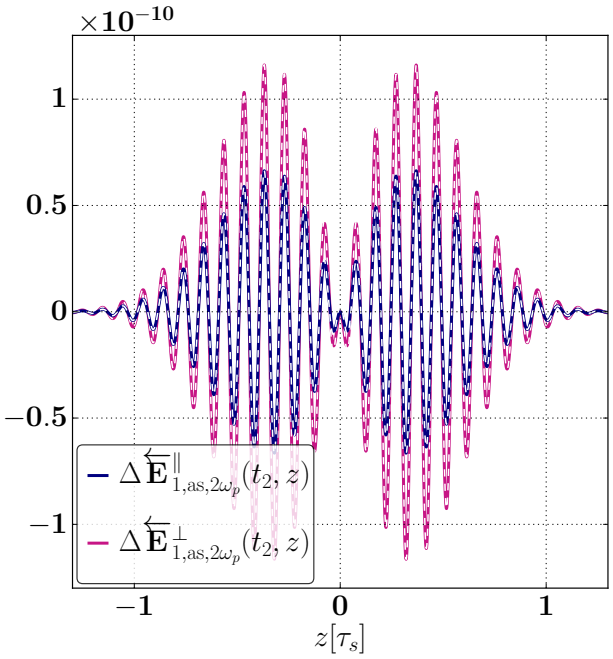

Figure 4.8: Snapshot of the left-travelling asymptotic second harmonic of the box diagram when probe and strong pulse show maximal overlap.

There are two further signals from the hexagon, the overlap field and the contribution from the derivative of the envelope function:

$$\Delta\mathbf{E}_{2,\mathrm{o},2\omega_p}(x^-,x^+) = -\frac{1}{2}\mu_2\mathcal{E}_s^3\mathcal{E}_p^2\mathrm{e}^{-2\left(\frac{x^-}{\tau_p}\right)^2}\mathrm{e}^{-3\left(\frac{x^+}{\tau_s}\right)^2}\cos\left(2\omega_p x^-\right)\mathbf{u}_2\ ,$$

$$\Delta\overrightarrow{\mathbf{E}}_{2,\mathrm{d},2\omega_p}(x^-,x^+) = \mu_2\mathcal{E}_p^2\mathcal{E}_s^3\sqrt{\frac{\pi}{3}}\frac{\tau_s}{\tau_p}\frac{x^-}{\tau_p}\mathrm{e}^{-2\left(\frac{x^-}{\tau_p}\right)^2}\left(1+\mathrm{erf}\left(\frac{\sqrt{3}x^+}{\tau_s}\right)\right)$$
$$\cdot\cos\left(2\omega_p x^-\right)\mathbf{u}_2\ . \quad (4.16)$$

A space-time plot of both fields is shown in Fig. 4.9 and we see that both signals are negligible as $\omega_p\tau_p \gg 1$ and $\mathcal{E}_s \gg \mathcal{E}_p$.

4.1.4 DC Component

For both four- and six-photon scattering there are signals which are quadratic in the probe pulse

$$[E_p^{(0)}(x^-)]^2 = \frac{1}{2}\mathcal{E}_p^2\left(\mathrm{e}^{-2\left(\frac{x^-}{\tau_p}\right)^2} + \mathrm{e}^{-2\left(\frac{x^-}{\tau_p}\right)^2}\cos\left(2\omega_p x^-\right)\right)\ .$$

The signal therefore consists of two parts, one which contains only the envelope function of the probe alone and one that contributes potentially to the second harmonic, as we already encountered above. The first one is a signal which is peaked around $\omega = 0$ and we therefore refer to it as the *zeroth harmonic*, *dc component* or *rectification*.

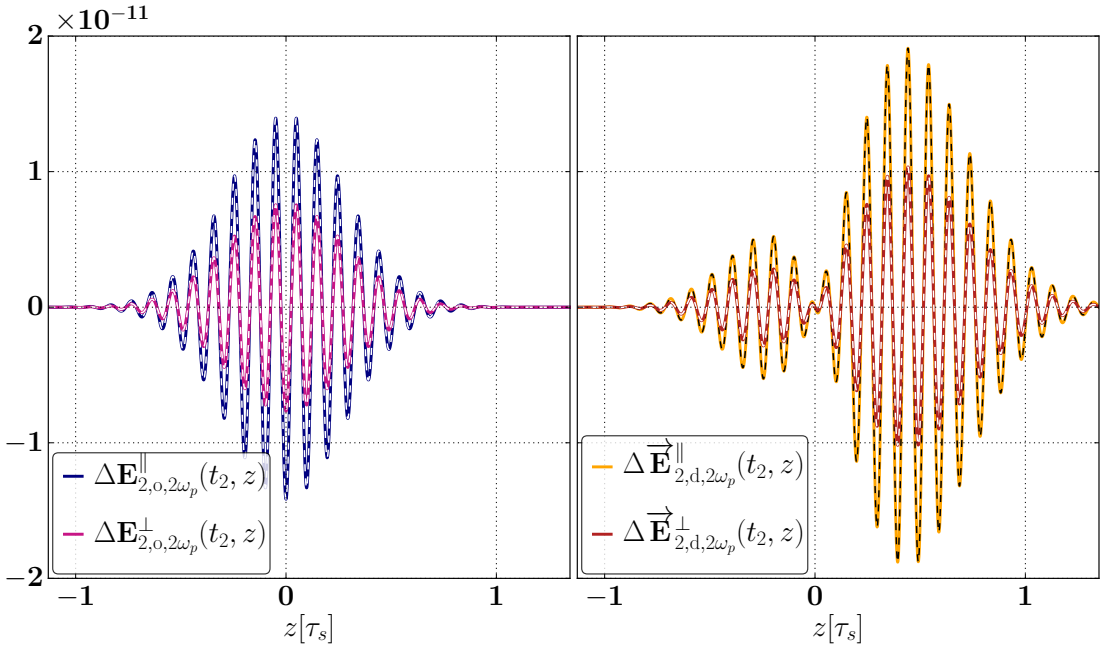

Figure 4.9: The left panel shows the overlap field of the second harmonic from six-photon scattering, the right panel shows the asymptotic field where the derivative acts on the envelope function of the probe. Since $\omega_p\tau_p \gg 1$, the signal is much smaller than the asymptotic signal shown in Fig. 4.5 and Fig. 4.6. The dashes show the numerical signal.

For four-photon scattering, this signal stems from the process in Fig. 2.7 (a) and since the vectorial part in $\mathbf{J}_1$ is here of the probe pulse, it is left-travelling and can be interpreted as a change in or back reaction on the strong background caused by the probe pulse. The lowest order contribution of the overlap and asymptotic signal is given by

$$\begin{aligned}\Delta\mathbf{E}_{1,\mathrm{o,dc}}(x^-,x^+) =& -\frac{1}{2}\mu_1\mathcal{E}_s\mathcal{E}_p^2\mathrm{e}^{-2\left(\frac{x^-}{\tau_p}\right)^2}\mathrm{e}^{-\left(\frac{x^+}{\tau_s}\right)^2}\mathbf{v}_1\ ,\\ \Delta\overleftarrow{\mathbf{E}}_{1,\mathrm{as,dc}}(x^-,x^+) =& \frac{1}{2}\mu_1\sqrt{\frac{\pi}{2}}\frac{\tau_p}{\tau_s}\frac{x^+}{\tau_s}\mathcal{E}_s\mathcal{E}_p^2\mathrm{e}^{-\left(\frac{x^+}{\tau_s}\right)^2}\left(1+\mathrm{erf}\left(\frac{\sqrt{2}x^-}{\tau_p}\right)\right)\mathbf{v}_1\ .\end{aligned} \tag{4.17}$$

The time-development of the amplitudes and the space-time evolution for (4.17) are shown in Fig. 4.10 and Fig. 4.11 and we see again that the overlap dominates the asymptotic signal.

For six-photon scattering, the dc component can not be interpreted as a change in background as the vectorial part in $\mathbf{J}_2$ is of the strong pulse and the signal is right-travelling. Since it contains frequencies of order $\approx \frac{1}{\tau_p} \ll \omega_p$, the contribution only comes from the derivative of the envelope function and if $\omega_p\tau_p \gg 1$, the right-travelling zeroth harmonic mostly only show a small contribution to the overall dynamics. The analytical expressions for the overlap and asymptotic field are

$$\begin{aligned}\Delta\mathbf{E}_{2,\mathrm{o,dc}}(x^-,x^+) =& -\frac{1}{2}\mu_2\mathcal{E}_s^3\mathcal{E}_p^2\mathrm{e}^{-2\left(\frac{x^-}{\tau_p}\right)^2}\mathrm{e}^{-3\left(\frac{x^+}{\tau_s}\right)^2}\mathbf{u}_2\ ,\\ \Delta\overrightarrow{\mathbf{E}}_{2,\mathrm{as,dc}}(x^-,x^+) =& \mu_2\sqrt{\frac{\pi}{3}}\mathcal{E}_s^3\mathcal{E}_p^2\frac{\tau_s}{\tau_p}\frac{x^-}{\tau_p}\mathrm{e}^{-\left(\frac{x^-}{\tau_p}\right)^2}\left(1+\mathrm{erf}\left(\frac{\sqrt{3}x^+}{\tau_s}\right)\right)\mathbf{u}_2\ .\end{aligned} \tag{4.18}$$

A space-time plot is shown in Fig. 4.12.

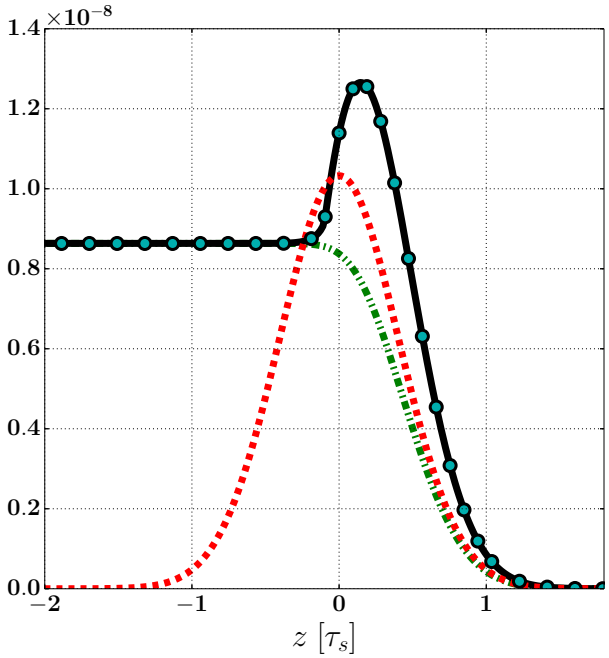

Figure 4.10: Shown is the maximal amplitude of the dc component in the parallel case from the box diagram as it travels leftwards with the strong probe. The red dashed line is the overlap, the green dashed-dotted line the asymptotic and the black solid the sum field. We see that also here the overlap signal dominates the asymptotic one.

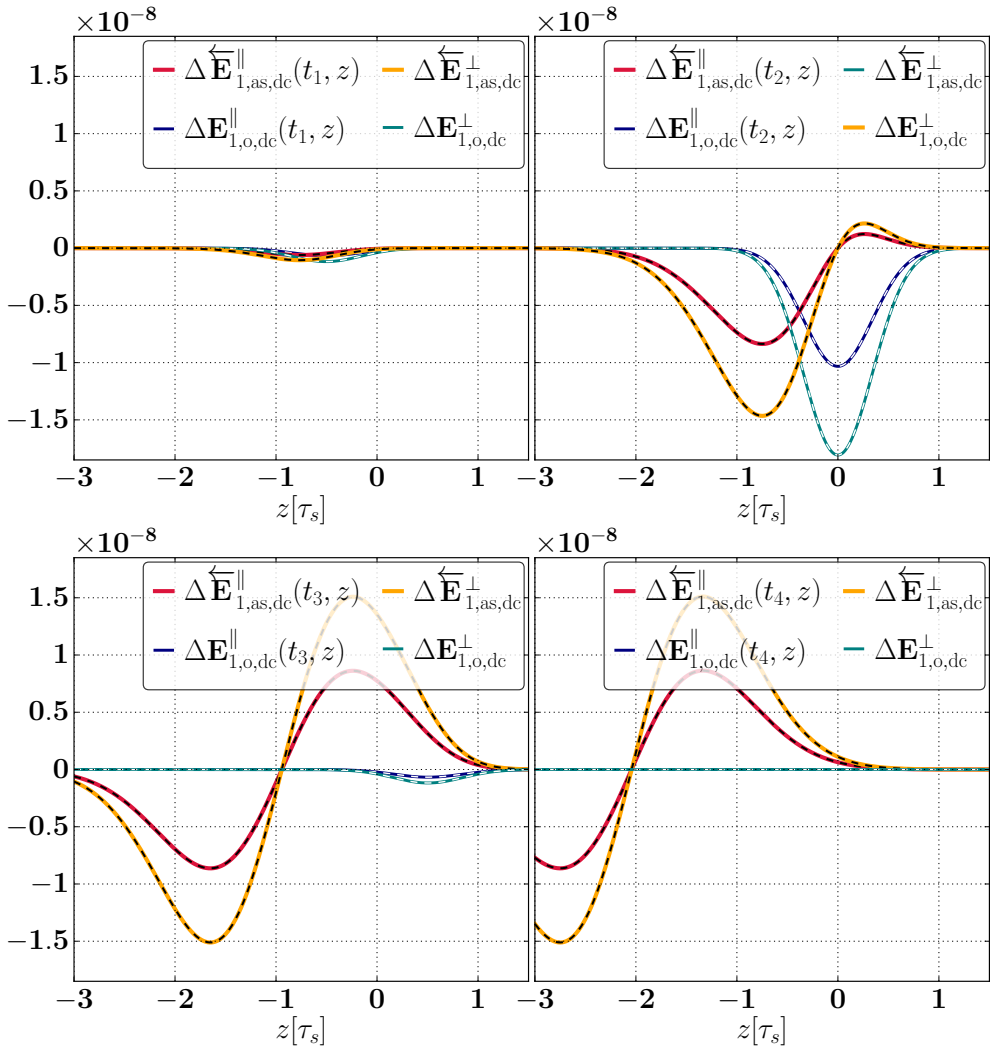

Figure 4.11: Time evolution of the left-travelling rectification from four-photon scattering.

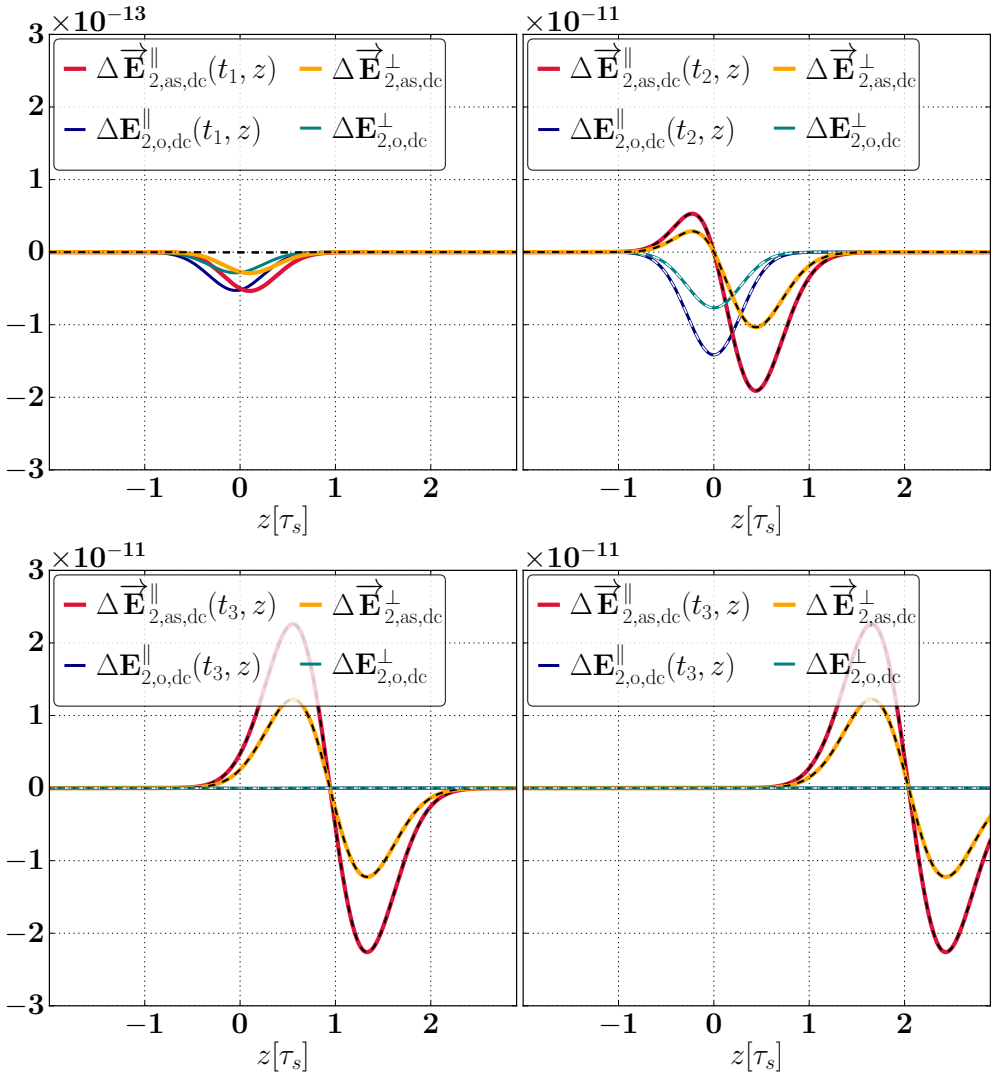

Figure 4.12: Different snapshots of the parallel and perpendicular right-travelling dc component from six-photon scattering.

4.1.5 Higher Harmonics

The next higher harmonic would be $3\omega_p$, but the direct asymptotic generation of a $3\omega_p$ signal for the scattering of plane waves appears only in eight-photon scattering, as it is shown in section 3.1.3 since the forward-scattered current $\mathbf{J}_3$ involves the probe cubed and $\cos(x)^3 = \frac{1}{4}(3\cos(x) + \cos(3x)$. To lowest order, there is no right-travelling third harmonic from four- and six-photon scattering. But if the vectorial part of $\mathbf{J}_2$ is from the probe field, the third harmonic is generated as an overlap and asymptotic left-travelling signal:

$$\Delta\mathbf{E}_{2,\mathrm{o},3\omega_p}(x^-,x^+) = -\frac{1}{4}\mu_2\mathcal{E}_p^3\mathcal{E}_s^2\mathrm{e}^{-3\left(\frac{x^-}{\tau_p}\right)^2}\mathrm{e}^{-2\left(\frac{x^+}{\tau_s}\right)^2}\cos\left(3\omega_p x^-\right)\mathbf{v}_2\ ,$$

$$\Delta\overleftarrow{\mathbf{E}}_{2,\mathrm{as},3\omega_p}(x^-,x^+) = \frac{1}{4}\mu_2\mathcal{E}_p^3\mathcal{E}_s^2\sqrt{\frac{\pi}{3}}\frac{\tau_p}{\tau_s}\frac{x^+}{\tau_s}\mathrm{e}^{-2\left(\frac{x^+}{\tau_s}\right)^2}\mathrm{e}^{-\frac{3}{4}\tau_p^2\omega_p^2}\left(2+\mathrm{erf}\left(\frac{\sqrt{3}(x^- + \frac{i}{2}\tau_p^2\omega_p)}{\tau_p}\right)\right.$$
$$\left.+\,\mathrm{erf}\left(\frac{\sqrt{3}(x^- - \frac{i}{2}\tau_p^2\omega_p)}{\tau_p}\right)\right)\mathbf{v}_2\ . \quad (4.19)$$

Two snapshots of both fields for the maximal overlap of the probe and strong field are shown in Fig. 4.13. We note again that the $3\omega_p$-dependence of the asymptotic signal disappears in the limit $x^- \to \infty$ due to the absence of wave mixing.

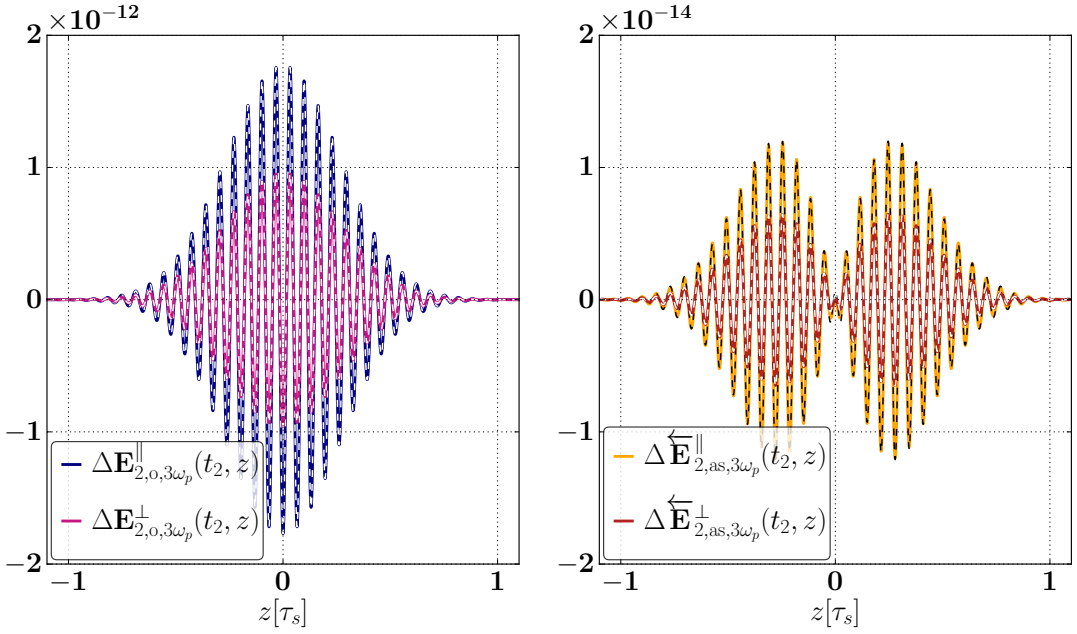

Figure 4.13: The third harmonic $3\omega_p$ is generated as an overlap signal (left panel) and as a left-travelling asymptotic signal (right panel) in six photon scattering. The perpendicular generation is less efficient than the parallel case.

In general, the asymptotic n-th harmonic involves $2(n+1)$-photon scattering amplitudes for plane waves and can be directly calculated from the weak-field expansion (2.64) of the Heisenberg-Euler Lagrangian. Both the overlap and the asymptotic field originate from an integration of a single term in the wave equation. But since the overlap field appears as a boundary term, it shows a different space-time dynamics compared to the

asymptotic field. Nevertheless, they show the same selection rules for the polarisation of the scattered photons of the higher harmonic. In the parallel setup, all harmonics are generated in the parallel mode

$$l\gamma_{\parallel} \to \gamma'_{\parallel} \,,$$

where $\gamma_{\parallel}$ is an incoming probe photon with a polarisation parallel to the strong pulse, $l \in \mathbb{N}^+$ and γ' the scattered photon. For the perpendicular setup with $\boldsymbol{\varepsilon}_p \cdot \boldsymbol{\varepsilon}_s = 0$, the incoming probe photons $\gamma_{\perp}$ generate the even harmonics parallel to the strong field and the odd harmonics parallel to the probe:

$$2l\gamma_{\perp} \to \gamma'_{\parallel} \,, \qquad (2l-1)\gamma_{\perp} \to \gamma'_{\perp} \,.$$

For the direct generation from the corresponding weak-field expansion, the n-th harmonic has a dependence $E_n \sim \mathcal{E}_s^{n+1}\mathcal{E}_p^n\omega_p\tau_s$ following from the explanation above. But since we are in a regime $\mathcal{E}_p, \mathcal{E}_s \ll 1$, the higher harmonics are strongly suppressed. In the second part of this thesis we analyse a different mechanism for high harmonic generation, which involves only the box and hexagon diagram, but requires longer propagation lengths $\Phi = \omega_p\tau_s$.

4.1.6 Discussion

We saw from (3.17) that the overlap signal depends on the past of the background field as it is a surface term stemming from an integral over the derivative of the background. As a consequence, it disappears for fields which are completely homogeneous like homogeneous constant-crossed and constant, homogeneous magnetic fields. For the overlap signal to appear, some inhomogeneity in the background is needed. Therefore, it makes a difference whether one considers forever-constant fields or the propagation of the photons into a background which is evolved from the past. We saw for quasi-constant backgrounds that it is valid to integrate the change of the refractive index due to four-photon scattering (see (4.3)) over the shape of the background since the effect is only dependent on the energy density of the strong field. But as most of current and future experiments use high-power lasers to measure vacuum polarisation effects, the background can not be treated as constant. Therefore, it might be necessary to include the overlap signal into this notion for recent and future experiments trying to measure vacuum birefringence as it was analysed in [HH14]. Strong inhomogeneities in the magnetic fields in the atmospheres of astrophysical objects like neutron stars might also influence calculations which rely on locally constant field approximations such as the so-called „vacuum resonance“ [HL01; HL04]. Such signals might be investigated with missions similar to GEMS [Gho+13] or telescopes like NuSTAR [Har+10].

The strongest magnetic fields available appear at neutron stars like Soft Gamma Repeater and X-Ray Pulsars. The field strengths surrounding such magnetars are close or also above the critical field E_{cr} and therefore the emitted radiation is very likely to be subjected to photon-photon scattering effects while passaging the magnetosphere. Polarisation measurements of the emitted X-Rays could be therefore very well suited to study the nonlinear properties of the vacuum [Gho+13; Tav+13]. In such extreme environments also the process of photon splitting $\gamma \to 2\gamma'$ of one photon into two photons of lower frequency is expected to be of particular importance. In the following we compare the number of photons per unit volume which are merged into the second harmonic from the overlap and the asymptotic field with the number of photons that are split in

a quasi-constant magnetic background. The photon splitting density was calculated in [PR72] and is given by

$$\rho_{\gamma\to 2\gamma'} = \frac{\alpha^3}{10}\left[\frac{19}{315\pi}\right]^2 \frac{L}{\lambda\!\!\!^{-}} B^6 \left(\frac{\omega}{m}\right)^5 \rho \ . \tag{4.20}$$

$\lambda\!\!\!^{-} = 2\pi/m$ is the reduced Compton wavelength, L is the propagation length, ρ is the density of incoming photons of the probe with frequency ω and B is the magnetic field strength. We note that the splitting density (4.20) has strong dependence on $(\omega/m)^5$ and in our case, where the magnetic field is perpendicular to the propagation direction of the probe photons, also dispersion has to be taken into account. To compare this expression with the result for photon merging, we take the plane wave limit of the probe with $\tau_p \to \infty$, the constant field limit for the background, $\tau_s \to \infty$ and set the electric fields to zero. To quantify the effect of the overlap signal, we define the relative field variation $\Delta = \Delta B/B$ of the background where ΔB is the difference in the magnetic field over the propagation distance L of the probe. From (4.12) and (4.13) we then have the following photon densities for the overlap and the asymptotic processes:

$$\begin{aligned}
\rho^{\mathrm{o}}_{2\gamma\to\gamma'} &= 2\alpha^3\left[\frac{11\mp 3}{180\pi}\right]^2 B^2\Delta^2\frac{\omega}{m}(\rho\pi\lambda\!\!\!^{-3})\rho \ , \\
\rho_{2\gamma\to\gamma'} &= 8\alpha^3\left[\frac{37\pm 11}{315\pi}\right]^2 B^2\zeta^2\frac{\omega}{m}(\rho\pi\lambda\!\!\!^{-3})\rho \ .
\end{aligned} \tag{4.21}$$

ζ is defined by $\zeta = B^2\omega L$ and the $\pm$ is for the probe photon polarisation being parallel or perpendicular to the magnetic background. Although the dependence of the generation of the second harmonic on ω/m is only linear compared to (4.20), for photon merging a high density of probe photons in a cylinder of radius and height $\lambda\!\!\!^{-}$ along the probe light cone is needed as it can be seen from (4.21). To get a more qualitative understanding when harmonic generation is more dominant than splitting, let us consider a photon gas in contact with a thermal bath at temperature T. The number of photons per unit volume with a certain energy in the interval $[\omega, \omega+\delta\omega]$, where $\delta\omega \ll \omega$, is then given by a Bose-Einstein distribution

$$\rho \ \sim \ \frac{\omega^2\delta\omega}{\exp\!\left(\frac{\omega}{k_B T}\right)-1} \ ,$$

where k_B is the Boltzmann constant. Using this expression in (4.20) and (4.21) yields the following ratios for photon splitting and merging:

$$\begin{aligned}
\frac{\rho^{\mathrm{o}}_{2\gamma\to\gamma'}}{\rho_{\gamma\to 2\gamma'}} &\sim \left(\frac{m}{\omega}\frac{\Delta}{B^2}\right)^2 \frac{\lambda\!\!\!^{-}}{L}\frac{\delta\omega}{m}\frac{1}{\exp\!\left(\frac{\omega}{k_B T}\right)-1} \ , \\
\frac{\rho_{2\gamma\to\gamma'}}{\rho_{\gamma\to 2\gamma'}} &\sim \frac{L\delta\omega}{\exp\!\left(\frac{\omega}{k_B T}\right)-1} \ .
\end{aligned}$$

Apart from dispersive effects also dissipative effects like e^+e^- pair-creation can take place. In [KDG12; KGDP13] two different mechanisms of thermal pair-creation were considered. The first one is the scattering of two photons off each other with an internal fermion propagator, which is then summed over the ensemble of the thermal photon gas yielding a number density

$$\rho_{2\gamma\to e^+e^-} \sim 2m^4\left(\frac{\alpha}{2\pi}\right)^2\left(\frac{k_B T}{m}\right)^3 \mathrm{e}^{-\frac{2m}{k_B T}}, \tag{4.22}$$

which is valid for $k_B T/m \ll 1$. As this result originates from the integration over a rectangular volume, the adjusted version for a propagation distance is given by

$$\rho_{2\gamma\to e^+e^-} \sim 2\frac{1}{\lambda\!\!\!^{-3}}\frac{L}{\lambda\!\!\!^{-}}\left(\frac{\alpha}{2\pi}\right)^2\left(\frac{k_B T}{m}\right)^3 \mathrm{e}^{-\frac{2m}{k_B T}} \ .$$

The second process considered is based on the interaction of the thermal photons with the background photons via the polarisation operator. The rate of pairs produced via this mechanism is then obtained via the optical theorem and given by

$$\rho_{\gamma\to e^+e^-} \sim \frac{3^{3/4}\alpha}{4\sqrt{2}\pi^{3/2}}\frac{1}{\lambda\!\!\!^{-3}}\frac{L}{\lambda\!\!\!^{-}}\left(\frac{k_B T}{m}\right)^2 \delta^{1/4}\mathrm{e}^{-\frac{4}{\sqrt{3\delta}}} \ . \tag{4.23}$$

Again, the length L was introduced in (4.23) and the result adapted for a constant magnetic background with

$$\delta = \left(\frac{k_B T}{2m}\right) B$$

and $\delta \ll 1$. Both pair-creation rates (4.22) and (4.23) are exponentially suppressed for $k_B T \ll m$, whereas the splitting and merging rates are perturbative in $k_B T/m$. As the temperature of most observable neutron stars is about $T = 10^5 K$ [HL06], this leads to a ratio $k_B T/m \approx 10^{-4}$, so thermal pair-creation is exponentially suppressed compared to photon merging and splitting.
After the analysis of the first iteration of the wave equation including the overlap signal and a comparison between harmonic generation and other dispersive and dissipative vacuum polarisation effects in this chapter, we now consider high harmonic generation based on higher iterations of the wave equation.

4.2 Higher-order Processes and VHHG

In this section we analyse a certain mechanism for *vacuum high harmonic generation* (VHHG) which is based on multiple consecutive scattering events. As we have seen in the previous chapter, four-photon scattering generates to lowest order a first harmonic forward scattered signal in the scattering of two plane wave pulses. Six-photon scattering then generated an asymptotic second harmonic and in general $2(n+1)$ photon scattering leads to an asymptotic nth harmonic. But as we consider the case of $\mathcal{E}_p, \mathcal{E}_s \ll 1$, this direct harmonic generation is strongly suppressed as the nth harmonic scales as $\mathcal{E}_s^{n+1}\mathcal{E}_p^{n-1}$, leading to extremely small intensities. This type of vacuum high harmonic generation has been investigated using the full polarisation operator in [DHK05; FN07] and using the lowest order of the weak-field expansion in [Lun+06; KK12; KBR14; GKS13].

If the fields' spacetime extent is much larger than a single scattering length, multiple scattering events can occur as we have already seen in Fig. 3.1 for four-photon scattering and Fig. 3.2 for six-photon scattering. But also combined processes like four-photon followed by six-photon scattering can occur. Usually it is assumed that the probability for multiple scattering events is much lower than single scattering events and multiple events are neglected. However, if the extent of the field is large enough, then the probability for multiple scattering increases with the propagation length so that all orders of chained processes have to be taken into account. This is the approach we take in the following for high harmonic generation.

If a large number of higher harmonics are generated in the spectrum, the shape of the electromagnetic plane waves also changes and this leads to the possibility of shock wave generation. In the "shock regime" (which is quantified later), as all orders of scattering can play a role in the generation, the spectrum is expected to be qualitatively different from the perturbative case of having only a single scattering event, where four-photon scattering is the most probable and higher harmonics are exponentially suppressed. Such a type of shock generation is also known from nonlinear optics [AL83] and often compared to the optical Kerr effect [Mar10].
There have been several studies of the consequences of this self-interaction. Lutzky and Toll [LT59] showed that if $\mathcal{G} = 0$, a current that depends nonlinearly on the invariant $\mathcal{F} = -F^2/4E_{\text{cr}}^2 = (E^2 - B^2)/2$ leads to the generation of an electromagnetic discontinuity or "shock". After identifying an application in magnetised neutron stars, shocks were analysed in a constant magnetic field background using a first- [Roz93], second- [ZF82] and several- [HH98; HH99] order weak-field expansion of the Heisenberg-Euler Lagrangian with an all-order analysis performed by Bialynicka-Birula [BB81]. An astrophysical environment was further modelled by introducing nonlinear vacuum effects into equations of relativistic magnetohydrodynamics [HH99] and into a dusty plasma [MSE05].

The outline of our analysis in this section is as follows:
First, we introduce the simulational setup, then we derive an all-order solution to the phase shift arising from pure four-photon scattering in a constant crossed electromagnetic background for the probe having parallel and perpendicular polarisations to the strong field. This analysis allows us a to identify nonlinearity parameter which quantifies when four-photon scattering is of importance in the generation of higher harmonics.
Afterwards, higher iterations of the wave equation for pure six-photon scattering in the parallel setup are calculated and an all-order solution for the scattered field is given which depends on another nonlinearity parameter that quantifies the transition from

the perturbative regime to the "shock regime". Then high harmonic generation from chained pure four-photon scattering and from higher order weak-field terms are shown to be negligible. This is followed by an extensive analysis of the transition into the shock regime for the parallel case as the nonlinearity parameter approaches unity. The angular dependency of the harmonics, the corresponding shockwaves and their interplay with dispersive effects are studied. In the discussion, an outlook on ultra-short probe pulses and harmonic generation in inhomogeneous backgrounds is given. This is followed by a comparison of VHHG with harmonic generation in real plasmas and we comment on the validity of the approach chosen in this thesis.

4.2.1 Simulational Setup

In this chapter we mainly focus on a pump-probe setup where the strong pulse is a constant plane wave background. The analytical expression of the strong pulse is thereby given by

$$\mathbf{E}_s^{(0)}(x^+) = \boldsymbol{\varepsilon}_s \mathcal{E}_s \mathrm{Rect}(x^+) \ ,$$

where $\mathrm{Rect} = \theta(x^+/\tau_s + 1/2) - \theta(x^-/\tau_s - 1/2)$ and $\theta(x)$ is the Heaviside step-function. The simulational setup is depicted in Fig. 2.10 (**b**). As explained in section 3.2, for the numerical simulation, we approximate the constant background as a mirrored Fermi-Dirac-Pulse to avoid infinite gradients:

$$\mathrm{Rect}(x^+) \approx \mathrm{FD}(x^+) := \frac{1}{1 + \exp\left(\frac{|x^+| - z_m}{z_b}\right)} \ . \tag{4.24}$$

To define a proper effective pulse duration τ_s for the Rect- and the Fermi-Dirac-function, we consider the asymptotic generation of the second harmonic of the hexagon diagram in the parallel case with $\boldsymbol{\varepsilon}_p \cdot \boldsymbol{\varepsilon}_s = 0$. The analytical expression is then given by (3.43):

$$\begin{aligned}\Delta\mathbf{E}^{(1)}_{2,p,as}(x^-) &= \lim_{x^+\to\infty} 96\mu_2 \, \boldsymbol{\varepsilon}_s \, \mathcal{E}_p^2 \mathrm{e}^{-2\left(\frac{x^-}{\tau_p}\right)} o_2(x^+) \sin\left(2\omega_p x^-\right) \\ &= 96\mu_2 \boldsymbol{\varepsilon}_s \mathcal{E}_p^2 \mathcal{E}_s^3 \mathrm{e}^{-2\left(\frac{x^-}{\tau_p}\right)} \tau_s \sin\left(2\omega_p x^-\right) \ ,\end{aligned}$$

where o_2 is given by (compare (3.51))

$$o_2(x^+) = \mathcal{E}_s^3 \int_{-\infty}^{0} \mathrm{d}y [\mathrm{FD}(x^+ + y)]^3 \ .$$

The analytic expression for the pulse duration is then

$$\tau_s = \frac{1}{\mathcal{E}_s^3} \lim_{x^+\to\infty} o_2(x^+) = z_b \left(\frac{4}{1 + \mathrm{e}^{\frac{z_m}{z_b}}} - \frac{1}{\left(1 + \mathrm{e}^{\frac{z_m}{z_b}}\right)^2} + 2\log\left(1 + \mathrm{e}^{\frac{z_m}{z_b}}\right) - 3 \right) \ . \tag{4.25}$$

Simulation Parameters

Our analysis is valid when $\mathcal{E}_s, \mathcal{E}_p \ll 1$ and we see shortly that the single parameter relevant to high harmonic generation in the shock regime is $\nu_2 = 192\mu_2 \mathcal{E}_s^3 \mathcal{E}_p \Phi$ with $\Phi = \omega_p \tau_s$ (see (4.31)). Now we wish to simulate the occurrence of a shock wave, for which $\nu_2 \to 1$, implying Φ must be very large in order to compensate for the weak

field strengths. However, a large Φ is computational expensive to simulate. To compare analytical and numerical results, we therefore extrapolate the theoretical result to values of $\mathcal{E}_s \not\ll 1$, allowing a simulation for smaller Φ to be performed, with the condition that the physical prediction is only valid for a particular value of ν_2 when $\mathcal{E}_s \ll 1$. For this reason, we often quote simulation parameters in terms of shock parameters rather than absolute field strengths and spatial extent.
If no other parameters are given, the probe amplitude was taken as $\mathcal{E}_p = 0.01$ and $\Phi = 387$ with $\lambda_p = 1.6 \cdot 10^{-4}$ cm for all simulations shown. $\tau_s = 9.85 \cdot 10^{-3}$ cm is always given by (4.25) with $z_b = 5 \cdot 10^{-5}$ cm and $z_m = 100 \cdot z_b$. Then the corresponding amplitude of the strong field is given by the relation

$$\mathcal{E}_s = \left(\frac{\nu_2}{192 \mu_2 \mathcal{E}_p \Phi} \right)^{1/3} .$$

Most simulations were carried out with $N = 10^6$ grid points in this chapter to properly resolve the high harmonics and it was checked that the results are robust against change in the resolution.
The parameters for the simulations in section 4.2.6 were the same as for the parallel case, except of the simulation in Fig. 4.28 and the left panel of Fig. 4.29 where we used $\mathcal{E}_p = 0.2$, $\mathcal{E}_s = 1.44$, $\lambda_p = 5.33 \cdot 10^{-7}$ cm, for Fig. 4.30 and the right panel of Fig. 4.29 $\mathcal{E}_p = 0.01$, $\mathcal{E}_s = 5.67$ and $\lambda_p = 1.6 \cdot 10^{-4}$ cm and for the simulations in Fig. 4.31 $\mathcal{E}_p = 2 \cdot 10^{-4}$, $\mathcal{E}_s = 14.4$ and $\lambda_p = 5.33 \cdot 10^{-7}$ cm.

4.2.2 All-order Phase Shift from Four-photon Scattering

In section 4.1.2 the phase shift from the box-diagram for parallel and perpendicular polarisations was given. Now we analyse the phase shift for arbitrary relative polarisations and explain why the parallel and perpendicular setup have a distinct role. The dependency of the phase shift of the probe on arbitrary relative polarisation of the strong and probe pulse for the current setup with a square pulse is shown in Fig. 4.14. To obtain the difference of the phases the same setup is simulated once without any nonlinearities and once with four-photon scattering turned on. When both pulses are well-separated again, each probe is transformed to Fourier space and the absolute phase is determined by

$$\varphi = \arctan \frac{\operatorname{Im} \tilde{E}(\omega_p)}{\operatorname{Re} \tilde{E}(\omega_p)} ,$$

where the Fourier transform is defined in (3.61). The phase-shift is then simply given by the difference of the absolute phases of the linear and the nonlinear probe pulse. The theoretical prediction is given by (cf. (4.4) and (4.3))

$$\delta\varphi_p = \frac{\omega_p}{2} \int_{-\infty}^{\infty} \mathrm{d}y \; \mathsf{n}_1(y) \tag{4.26}$$

where

$$\delta \mathsf{n}_1 = 4 \mu_1 \mathcal{E}_s^2 \left[4 \left(\boldsymbol{\varepsilon}_p \cdot \boldsymbol{\varepsilon}_s \right)^2 + 7 \left(\boldsymbol{\varepsilon}_p \wedge \boldsymbol{\varepsilon}_s \right)^2 \right] . \tag{4.27}$$

If one takes an arbitrary relative polarisation, a certain ellipticity is introduced in the probe field. This is a result of the two different refractive indices that act on the probe. The part of the probe that is parallel to the strong field travels at a different velocity

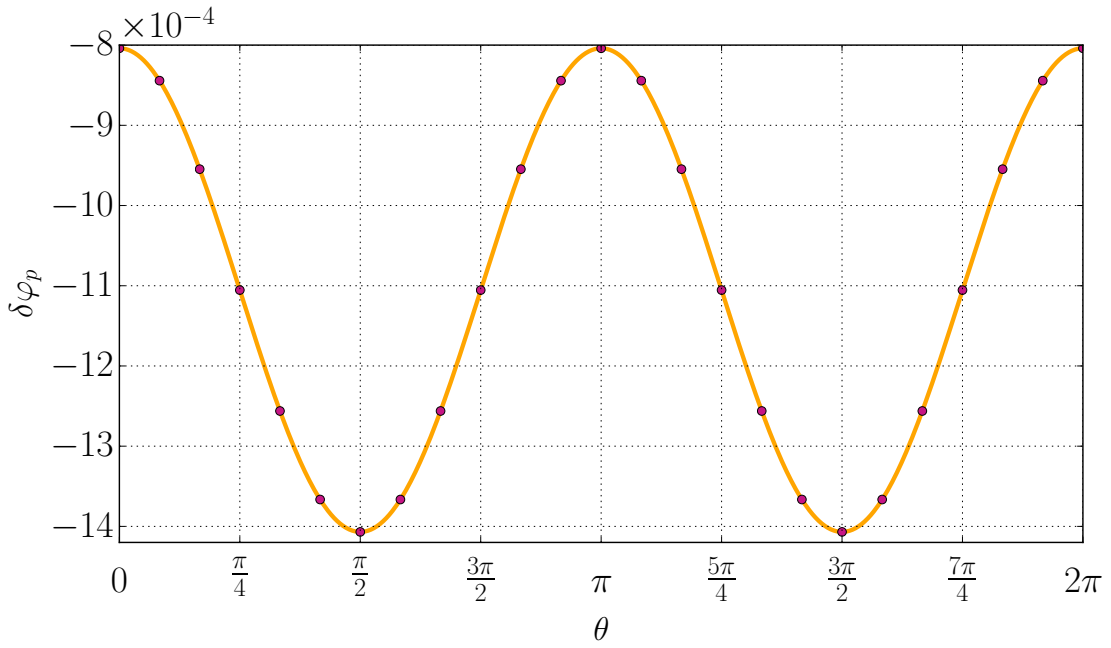

Figure 4.14: Shown is the angular dependency of the relative phase-shift due to four-photon scattering of the probe pulse after passing the strong pulse. The solid line is the theoretical prediction, the dots show the numerical result. θ is the relative angle between the polarisations of both pulses with $\boldsymbol{\varepsilon}_p \cdot \boldsymbol{\varepsilon}_s = \cos\theta$. The parameters for the simulations were $\lambda_p = 1.6 \cdot 10^{-4}$ cm, $\mathcal{E}_p = 5 \cdot 10^{-3}, \mathcal{E}_s = 0.1$ and $N = 1.12 \cdot 10^4$.

than the part which is perpendicular to the strong field. So both parts get a different phase shift. The situation is different if the probe is in one of the states with $\boldsymbol{\varepsilon}_p \cdot \boldsymbol{\varepsilon}_s = 0$ or $\boldsymbol{\varepsilon}_p \cdot \boldsymbol{\varepsilon}_s = 1$. Then the expression for the higher iterations simplify since for $\mathcal{G} = 0$ (parallel) or $\mathcal{F} = 0$ (perpendicular) the polarisation vectors (3.35) and their higher iterated versions only contribute to the same polarisation and there is no interaction between both modes which simplifies the iterations. In both cases the nonlinear response is always parallel to the probe field and the first two iterations in the limit $x^+ \to \infty$ and the parallel setup are then given by

$$\Delta\mathbf{E}^{(0)}_{1,\omega_p,\mathrm{as}}(x^-) = 16\mu_1\mathcal{E}_s^2\mathcal{E}_p\boldsymbol{\varepsilon}_p \mathrm{e}^{-\left(\frac{x^-}{\tau_p}\right)^2} \sin\left(\omega_p x^-\right) ,$$

$$\Delta\mathbf{E}^{(1)}_{1,\omega_p,\mathrm{as}}(x^-) = 16\mu_1\mathcal{E}_s^2\mathcal{E}_p\boldsymbol{\varepsilon}_p \mathrm{e}^{-\left(\frac{x^-}{\tau_p}\right)^2} \left(\sin\left(\omega_p x^-\right) - 8\mu_1\mathcal{E}_s^2\mathcal{E}_p\boldsymbol{\varepsilon}_p \cos\left(\omega_p x^-\right)\right)$$

and a similar expression is obtained for the perpendicular setup. Further analysis of the next two iterations reveals the following pattern illustrated on the fourth iteration:

$$\mathbf{E}^{(4)}_{1,\omega_p,\mathrm{as}}(x^-) = \mathcal{E}_p\boldsymbol{\varepsilon}_p \mathrm{e}^{-\left(\frac{x^-}{\tau_p}\right)^2} \cdot \left(\cos\left(\omega_p x^-\right) + \upsilon_1 \sin\left(\omega_p x^-\right) - \frac{(\upsilon_1)^2}{2!}\cos\left(\omega_p x^-\right) - \frac{(\upsilon_1)^3}{3!}\sin\left(\omega_p x^-\right) + \frac{(\upsilon_1)^4}{4!}\cos\left(\omega_p x^-\right)\right) ,$$

where we defined the multi-scale-parameter $\upsilon_1 = \upsilon_1^{\parallel,\perp}$ for the parallel and perpendicular setup of four-photon scattering as

$$\upsilon_1^{\parallel,\perp} = (11 \mp 3)\mu_1\mathcal{E}_s^2\Phi = \frac{1}{2}\delta\mathsf{n}_1^{\parallel,\perp}\Phi , \tag{4.28}$$

$\Phi = \omega_p\tau_s$ and $\delta\mathsf{n}_1$ is the well-known vacuum refractive index (4.3):

$$\delta\mathsf{n}_1^{\parallel,\perp} = 2(11 \mp 3)\mu_1\mathcal{E}_s^2 .$$

The first two iterations are depicted diagrammatically in Fig. 3.1. If we make a transformation of variables,

$$\frac{\partial}{\partial x^-} = \omega_p \frac{\partial}{\partial \varphi_p} \ ,$$

one finds in general for the summation of all diagrams for the forward scattered field

$$\mathbf{E}_{1,\omega_p}(\varphi_p) = \sum_{n=0}^{\infty} \frac{(-\upsilon_1)^n}{n!} \frac{\partial^n}{\partial \varphi_p^n} \mathbf{E}_p^{(0)}(\varphi_p) \ .$$

We note again that we always neglect the derivative of the envelope function of the probe. Interpreting this infinite sum as a shift operator yields the final result

$$\mathbf{E}_{1,\omega_p}(\varphi_p) = \mathrm{e}^{-\upsilon_1 \frac{\partial}{\partial \varphi_p}} \mathbf{E}_p^{(0)}(\varphi_p) = \mathbf{E}_p^{(0)}(\varphi_p - \upsilon_1) \ . \tag{4.29}$$

Expression (4.29) is valid for the parallel setup with $\upsilon_1^{\parallel}$ and the perpendicular setup with $\upsilon_1^{\perp}$ as in both cases the nonlinear corrections are parallel to the probe field. The interpretation of (4.29) is the summation of all possible graphs of the higher iterations in Fig. 3.1, giving a fully dressed electromagnetic field solution for the probe pulse where all interactions with the external classical source (the strong pulse) are taken into account.

This all-order solution to the phase shift in a plane wave propagating through a constant background derived from the Heisenberg-Euler Lagrangian complements a recent example solution of the phase shift derived from the Schwinger-Dyson equation applied to the polarisation operator [Meu+15].

4.2.3 All-order Solution for Six-photon Scattering

As we already discussed in section 4.1, the direct asymptotic generation of the nth harmonic involves the process of $2(n+1)$-photon scattering for $E \ll 1$. So for the second harmonic, six-photon scattering is the dominant process, but we also saw that higher iterations generated higher harmonics. For the parallel case, the first two iterations of the wave equations in our setup are given by

$$\begin{aligned}
\mathbf{E}_p^{(0)} &= \mathcal{E}_p \boldsymbol{\varepsilon}_p \mathrm{e}^{-\left(\frac{x^-}{\tau_p}\right)^2} \cos(\varphi_p) \ , \\
\mathbf{E}_p^{(1)} &= \mathcal{E}_p \boldsymbol{\varepsilon}_p \mathrm{e}^{-\left(\frac{x^-}{\tau_p}\right)^2} \left[\cos(\varphi_p) + \frac{\upsilon_2}{2} \sin(2\varphi_p)\right] \ , \\
\mathbf{E}_p^{(2)} &= \mathcal{E}_p \boldsymbol{\varepsilon}_p \mathrm{e}^{-\left(\frac{x^-}{\tau_p}\right)^2} \left[\left(1 - \frac{1}{2}\left(\frac{\upsilon_2}{2}\right)^2\right) \cos(\varphi_p) + \frac{\upsilon_2}{2} \sin(2\varphi_p) \right. \\
&\qquad \left. - \frac{3}{2}\left(\frac{\upsilon_2}{2}\right)^2 \cos(3\varphi_p) - \frac{2}{3}\left(\frac{\upsilon_2}{2}\right)^3 \sin(4\varphi_p)\right] \ ,
\end{aligned} \tag{4.30}$$

where the quantity $\upsilon_2 = \nu_2 \mathrm{e}^{-\left(\frac{x^-}{\tau_p}\right)^2}$ is what we refer to as „shock parameter“ for six-photon scattering with

$$\nu_2 = 192 \mu_2 \mathcal{E}_s^3 \mathcal{E}_p \Phi \ . \tag{4.31}$$

For the case with $\boldsymbol{\varepsilon}_p \cdot \boldsymbol{\varepsilon}_s = 1$, each iteration only contributes a term which is parallel to the probe pulse as the field invariants $\mathcal{G} = \mathcal{G}^{(n)} = 0$ vanish identically and are not affected by higher iterations. So all harmonics are generated parallel to the probe field. The first two iterations are shown diagrammatically in Fig. 3.2. Analysing higher iterations as in the case of the box-diagram leads to the all-order solution for the forward scattered probe pulse:

$$\mathbf{E}_p(\varphi_p) = 2\mathcal{E}_p \boldsymbol{\varepsilon}_p \sum_{j=1}^{\infty} (-1)^{j+1} \left[\frac{J_{2j}\big(2j\upsilon_2\big)}{2j\upsilon_2} \sin(2j\varphi_p) + \frac{J_{2j-1}\big((2j-1)\upsilon_2\big)}{(2j-1)\upsilon_2} \cos((2j-1)\varphi_p) \right] \tag{4.32}$$

Here $J_l(\cdot)$ is the lth-order Bessel function of the first kind [GR07].
It is really remarkable that the all-order-solution (4.32) resembles the Bessel-Fubini solution [FG35; Bla66] to Burger's equation which describes the propagation of lossless finite-amplitude planar acoustic waves in inviscid fluids [Ros07; Péc12],

$$u_{\mathrm{BF}}(t,z) = 2u_0 \sum_{j=1}^{\infty} \frac{J_j(j\nu_{\mathrm{BF}})}{j\nu_{\mathrm{BF}}} \sin\big(j\omega_0(t-z)\big) \,, \tag{4.33}$$

where the initial profile is given by a sinusoidal

$$u_{\mathrm{BF}}(t=0,z) = u_0 \sin(\omega_0 z)$$

and $0 \leq \nu_{\mathrm{BF}} \leq 1$ is a normalised propagation distance of the wave from the point of excitation. Although the physics and the nonlinearities are of completely different origin, ν_{BF} plays the same role as the shock parameter ν_2 and many known behaviours of (4.33) will be recovered in section 4.2.5 where the generation of shockwaves is analysed and the similarities are shown explicitly.
We note that for the perpendicular setup, the first iteration is parallel to the strong pulse and therefore the higher iterations mix. This can be seen from the vacuum current for the hexagon diagram consisting of the polarisation (3.41) and magnetisation (3.42). In the first iteration for the perpendicular case, the field invariant $\mathcal{F}^{(0)} = 0$. Now since the first iteration gives a probe component parallel to the strong pulse, both quantities $\mathcal{G}^{(n)}$ and $\mathcal{F}^{(n)}$ become non-zero and develop a much more complicated space-time-dependency compared to the parallel case. Both the parallel and perpendicular components therefore interact via the $\mathcal{FG}$ term in the current.
The selection rules are the same as we found in section 4.1 although the mechanism here is different from considering the direct harmonic generation. The even harmonics are generated parallel to the strong field and the odd ones parallel to the probe field.
The analysis of arbitrary relative polarisations turns out to be particularly difficult and the harmonic generation is also seen to be highly suppressed in general compared to the parallel case. In section 3.1.4 we derived a formula for the second iteration in the parallel case and already the second iteration for arbitrary relative polarisations is quite complicated and therefore even higher iterations become more and more involved.

4.2.4 Other Processes in Vacuum Harmonic Generation

VHHG from Higher Order Four-photon Scattering

As the calculation in section 3.1.3 shows, there is no generation of the second harmonic as a lowest order process as the field invariants of the probe and strong field vanish

separately. But this does not completely exclude the generation of the second harmonic from four-photon scattering as it can be generated via a higher-order process. When the probe and strong pulse overlap, their field invariants $\mathcal{F}_{p,s}, \mathcal{G}_{p,s}$ do not vanish separately anymore and this signal can be used as an input for a chained process as it is shown in Fig. 4.15. To get a qualitative estimate for the intensity of the merged $2\omega_p$-field, we

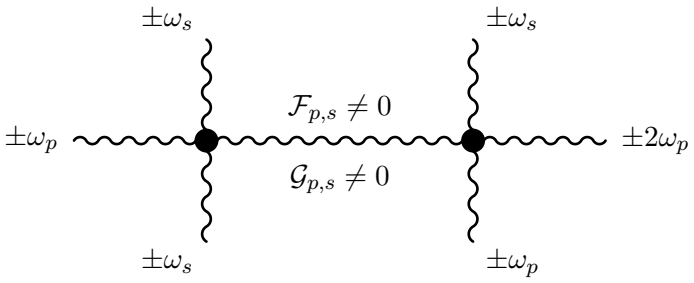

Figure 4.15: Chained vertices for the asymptotic generation of the second harmonic from four-photon scattering in the plane wave pump-probe setup.

assume that the incoming probe photon scatters once which leads to a change $\delta\mathsf{n}_1 = 16\mu_1\mathcal{E}_s^2$ in the probe field and therefore in the field invariants $\mathcal{F}, \mathcal{G}$. This scattered signal then scatters with an additional single probe photon as it is shown in Fig. 4.15, which contributes an additional contribution $\upsilon_1 = 8\mu_1\mathcal{E}_s\mathcal{E}_p\Phi$ and results in a combined contribution of

$$\nu_1 = 2(8\mu_1)^2\mathcal{E}_s^3\mathcal{E}_p\Phi \ . \tag{4.34}$$

Since $\upsilon_2 = \nu_2 \exp\big[-(x^-/\tau_p)^2\big]$ is bounded from above, $\upsilon_2 \leq \nu_2$, we quantify the effect of six-photon scattering to VHHG by ν_2. To compare the effectivity of the generation of the second harmonic from four- and six-photon scattering, we therefore consider the ratio

$$\frac{\nu_1}{\nu_2} = \frac{7}{17145\pi} \approx 2.6 \cdot 10^{-4} \ . \tag{4.35}$$

So the generation of the second harmonic from the box diagram is always suppressed by a factor of 10^{-4} compared to the asymptotic signal from the hexagon diagram, independent of the chosen parameters. This is also observed in the numerical simulations where the ratio of the amplitudes of the second harmonic from the box- and hexagon-diagram is given by

$$\sqrt{\frac{I_{\mathrm{box}}(2\omega_p)}{I_{\mathrm{hex}}(2\omega_p)}} = 1.8 \cdot 10^{-4} \ ,$$

which is close to the estimate (4.35). One can now even go further with the analogy to the generation of higher harmonics and use the calculation of the hexagon diagram with ν_1 as shock parameter. From (4.30) we then infer the relative intensities

$$\begin{aligned}
\frac{I(2\omega_p)}{I_p^{(0)}(\omega_p)} &= \left(\frac{\nu_1}{2}\right)^2 = 10^{-7.6} \ , \\
\frac{I(3\omega_p)}{I_p^{(0)}(\omega_p)} &= \left(\frac{3\nu_1^2}{8}\right)^2 = 10^{-14.8} \ , \\
\frac{I(4\omega_p)}{I_p^{(0)}(\omega_p)} &= \left(\frac{\nu_1^3}{12}\right)^2 = 10^{-23.0} \ .
\end{aligned}$$

A comparison with a numerical simulation in which $\nu_1 = 3.3 \cdot 10^{-4}$ ($\mathcal{E}_s = 5, \mathcal{E}_p = 10^{-2}, \Phi = 1550$) is shown in Fig. 4.16. We see that the estimate (4.34) predicts the numerical intensities correctly within one order of magnitude. The generation of higher harmonics is less effective in the perpendicular setup than in the parallel one. This is also common to six-photon scattering. As a comparison, the shock parameter for pure six-photon scattering for this scenarios exceeds ν_1 by several orders of magnitude since $\nu_2 = 2.7 \gg \nu_1$.

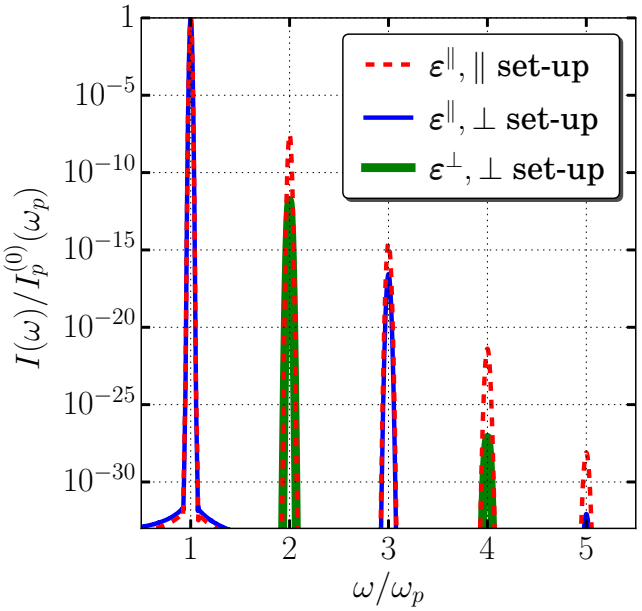

Figure 4.16: High harmonic generation from multiple four-photon scattering for $\nu_1 = 3.3 \times 10^{-4}$. $\varepsilon^{\parallel}$ ($\varepsilon^{\perp}$) denotes the component parallel (perpendicular) to the probe field.

Dispersive Effects

Although we argued in the last section that the box-diagram gives only a negligible (direct) contribution to harmonic generation, the dispersive effect with one incoming and one outgoing probe photon might potentially influence the generated harmonic spectra. Since we also introduced a parameter υ_1 (see (4.28) and we set $\upsilon_1 = \upsilon_1^{\parallel}$) to quantify the dispersive effects, the ratio

$$\frac{\upsilon_1}{\nu_2} = \frac{7}{24\mathcal{E}_s\mathcal{E}_p}$$

indicates when it should be a good approximation to only consider the hexagon diagram. But for this ratio to be small, we would require

$$\mathcal{E}_p\mathcal{E}_s \gg \frac{7}{48} \approx 0.15 \,, \tag{4.36}$$

which is not justified. We therefore study the cases without any ($\upsilon_1 \ll 1$), with weak ($\upsilon_1 \approx 1$) and with strong ($\upsilon_1 \gg 1$) dispersive effects separately.

Higher-order Weak-field Expansion

As we have seen in section 4.1.5, using the next term in the weak-field-expansion of the Heisenberg-Euler Lagrangian, also the third harmonic can be directly produced as

an asymptotic signal. Since we quantified six-photon scattering with ν_2 in the parallel setup, we use the same argument to quantify the effect of eight-photon scattering using the shock-parameter $\nu_3 = 1536\mu_3\mathcal{E}_s^4\mathcal{E}_p^2\Phi$ which is obtained from (3.46). To justify when higher-orders in the expansion can be neglected, the quantity

$$\frac{\nu_3}{\nu_2} = \frac{32\mathcal{E}_s\mathcal{E}_p}{3}$$

must be small. Therefore, the condition for the hexagon diagram being the dominant process in Harmonic generation is given by

$$\mathcal{E}_p\mathcal{E}_s \ll \frac{32}{3} ,$$

which is fulfilled since we always consider $\mathcal{E}_p \ll 1$ and $\mathcal{E}_s \ll 1$. Since higher terms in the weak-field expansion introduce further factors of $\mathcal{E}_p$ and $\mathcal{E}_s$, we take this as an indicator that only considering six-photon scattering as the dominant process in vacuum harmonic generation should be a justified approximation.

4.2.5 VHHG and Electromagnetic Shockwave

It turns out that the most effective setup for high harmonic generation is the parallel case with $\boldsymbol{\varepsilon}_p \cdot \boldsymbol{\varepsilon}_s = 1$ (leading to $\mathcal{G} = 0$), whereas all cases where $\mathcal{G} \neq 0$ are substantially suppressed compared to the case with vanishing $\mathcal{G}$.
Therefore, we first consider only high-harmonic generation from pure six-photon scattering in the parallel setup for different parameter regimes.

Perturbative Regime for VHHG (Parallel Case)

It was shown in section 4.2.3 that the all-order solution for the forward-scattered probe field for $\nu_2 \leq 1$ is given by a certain combination of Bessel functions (cf. (4.32)) that depends on the shock-parameter ν_2 which also serves as a perturbative parameter if $\nu_2 \ll 1$. This parameter range is what we call „perturbative - “ or „pre-shock regime“.
To get a better qualitative understanding of the solution in this regime, one can expand the Bessel-function $J_j(j\nu_2)$ in (4.32) as [Wat51]

$$J_j(j\nu_2) = \frac{1}{\Gamma(j+1)}\left(\frac{j\nu_2}{2}\right)^j + \mathcal{O}\Big((j\nu_2)^{j+1}\Big)$$

for $0 < j\nu_2 \ll \sqrt{j+1}$. Let us define the coefficients $a_l(\nu)$ of the scattered field (4.32) as

$$a_j(\nu_2) = \frac{2J_j(j\nu_2)}{j\nu_2} . \tag{4.37}$$

Then in the pre-shock regime with $\nu_2 \ll 1$, the coefficients satisfy

$$|a_l(\nu_2)| = \frac{1}{\Gamma(j+1)}\left(\frac{j\nu_2}{2}\right)^{j-1} + \mathcal{O}(\nu_2^{j+1}) . \tag{4.38}$$

Now for the higher harmonics with $l \gg 1$, we can use the Stirling formula [AWH12]

$$\Gamma(1+j) \approx \sqrt{2\pi j}\left(\frac{j}{\mathrm{e}}\right)^j$$

to approximate the Gamma-Function and obtain

$$|a_l(\nu_2)| = \frac{(\nu_2 \mathrm{e})^j}{\nu_2 j^{3/2}\sqrt{2\pi}} + \mathcal{O}(\nu_2^{j+1}) \ .$$

The ratio of two succeeding coefficients is then given by

$$\left|\frac{a_{j+1}(\nu_2)}{a_j(\nu_2)}\right| \approx \nu_2$$

from which we infer that the $(n+1)$th harmonic is exponentially suppressed compared to the nth harmonic.
This exponential suppression is also seen in the *log-log*-plot Fig. 4.17 of the normalised intensity $I(\omega)/I_p^{(0)}(\omega_p)$ and shows the excellence agreement of the perturbative expansion (4.38) with the numerical simulation for $\nu_2 = 0.05 \ll 1$, where the red dots indicate the theoretically predicted peak intensity. We note that assuming $\nu_2 \ll 1$ corresponds to considering only the lowest order chained process to generate a given harmonic. Since already the probability for two probe photons to generate the second harmonic is very small, the merging of this signal into a third (or even higher) harmonic is exponentially suppressed. If one gradually increases ν_2 such that $\nu_2 \ll 1$ is no longer fulfilled, one could expect a change in the exponential behaviour of the spectrum since more and more different processes can contribute to a given harmonic and ν_2 can no longer be seen as a perturbative parameter. This is what we call the „shock regime“ and is analysed in the next section.

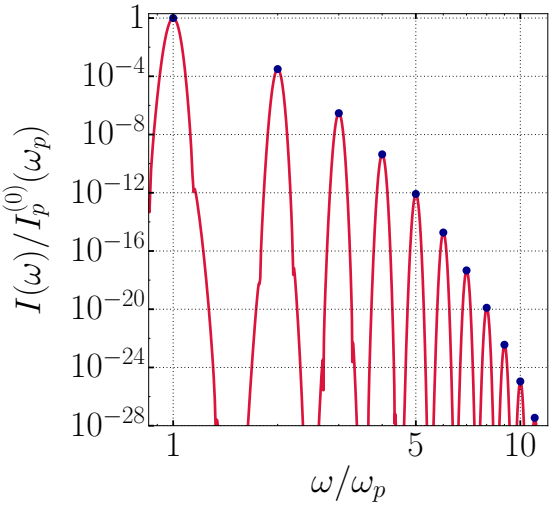

Figure 4.17: Normalised intensities of the harmonics generated in the perturbative regime with $\nu_2 = 0.05$. The higher harmonics are exponentially suppressed.

Shock Regime $\nu_2 \to 1$ (Parallel Case)

As we have seen in the previous section, the pre-shock regime was characterised by the nonlinearity parameter being small, $\nu_2 \ll 1$ and the generated harmonics in the probe pulse are highly suppressed. As this parameter is increased from zero towards one, a qualitatively different behaviour of the harmonic spectrum is observed as it is shown in Fig. 4.18 for different values from $\nu_2 = 0.05$ up to $\nu_2 = 1$.

Starting at approximately $\nu_2 = 0.6$, parts of the spectrum are no longer exponentially

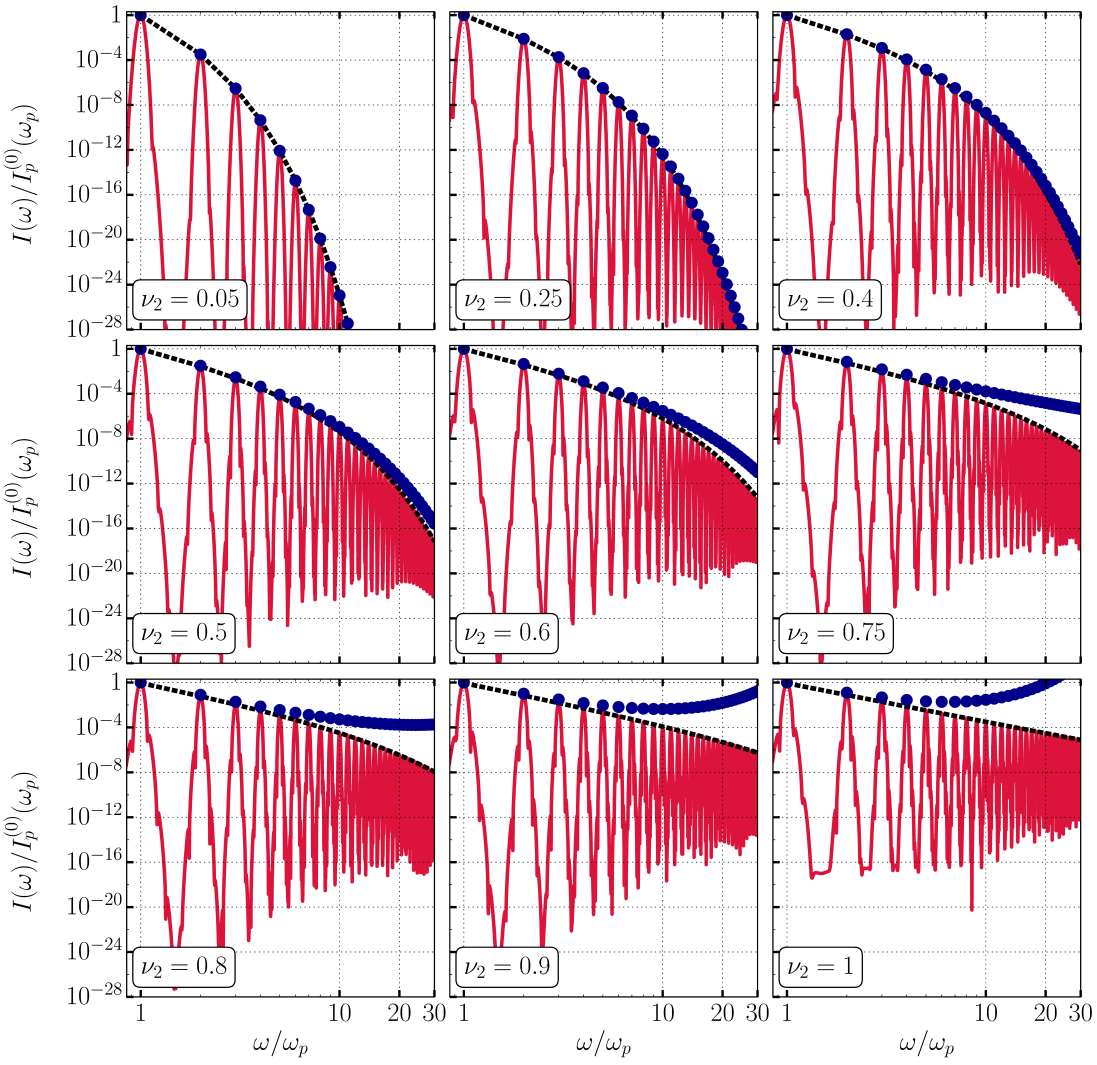

Figure 4.18: Harmonic spectra in the parallel setup for different values of ν_2. The dots show the leading-order perturbative term, the dashed line is the all-order analytical solution and the solid line is from numerical simulation. The harmonics start showing at approximately $\nu_2 \approx 0.6$ a transition from exponential suppression to a power-law behaviour.

suppressed but rather show the behaviour of a power law. This is the parameter range which we call "shock regime". Approaching $\nu_2 \to 1$, the intensities of all shown harmonics obey

$$I(j\omega_p) \sim j^{\gamma(\nu_2)} \ , \tag{4.39}$$

where j is the number of the harmonic and $\gamma(\nu_2)$ is a increasing function of ν_2. From numerical results the exponent satisfies $\gamma(\nu_2) < -3.4$. From a physical point of view this corresponds to summing all possible contributions to a given harmonic.
This can also be understood from the iterations of the wave equation. For example, the third iteration of the wave equation also gives a contribution to the second harmonic, but is suppressed by an additional factor of ν_2. But since also the coefficients of the higher iterations grow with the order of the iteration, in the shock regime all the higher terms can no longer be neglected. The perturbative expansion (4.38) is not even suitable to reproduce the correct qualitative behaviour of the spectrum for ν_2 approaching one.

Another consequence of the fact that a perturbative expansion is no longer valid comes from the all-order solution (4.32) which depends not only on the parameter ν_2 but on quantity $v_2 = \nu_2 \exp\bigl(-(x^-/\tau_p)^2\bigr)$. To obtain the correct theoretical peak intensities that match the numerical simulations for higher values of ν_2, one has to transform the Bessel-functions with the envelope function taken into account. This is done numerically using *Wolfram Mathematica*.
Similar to the analysis of the perturbative case where we obtained the exponential suppression of the higher harmonics, we can also observe the qualitative power-law from the behaviour of the Bessel-functions. To do so, we take the infinite-plane-wave limit $\tau_p \to \infty$ for the probe pulse which corresponds to setting the envelope function to one and $v_2 = \nu_2$. The relative intensity of two consecutive harmonics is then given by

$$\left|\frac{a_{j+1}(\nu_2)}{a_j(\nu_2)}\right|^2 = \left|\frac{J_{j+1}[(j+1)\nu_2]}{J_j(j\nu_2)}\right|^2 \left(\frac{j}{j+1}\right)^2 . \tag{4.40}$$

Considering the higher harmonics with $j\nu_2 \gg 1$, the absolute values of the Bessel-functions can be approximated as [Wat51]

$$|J_j(j\nu_2)| \sim (2\pi j)^{-\frac{1}{2}} ,$$

where phase terms were neglected. The coefficients therefore obey

$$|a_j(\nu_2)| \sim \frac{1}{\nu_2\, j^{\frac{3}{2}}}\sqrt{\frac{2}{\pi}} \tag{4.41}$$

and from (4.40) follows

$$\left|\frac{a_{j+1}(\nu_2)}{a_j(\nu_2)}\right|^2 \sim \left(\frac{j}{j+1}\right)^3 , \tag{4.42}$$

which correctly predicts a power-law dependence of the harmonics. For the normalised intensity $I_p(j\omega_p)/I_p^{(0)}(\omega_p)$, it follows from (4.41) that for $\nu_2 = 1$, the gradient in a log-log-plot is given by

$$\log\left(\frac{I_p(j\omega_p)}{I_p^{(0)}(\omega_p)}\right) \sim \log\left|\frac{a_j}{a_0}\right|^2 \underset{jv\to\infty}{\sim} -\log\frac{2}{\pi} - 3\log j .$$

The -3 is probably an overestimate, since $v_2 = \nu_2 \exp\bigl(-(x^-/\tau_p)^2\bigr)$ and for most parts of the probe, $v_2 < 1$. The numerical and theoretical exponent for the spectrum in the last pane of Fig. 4.18 with $\nu_2 = 1$ is found to be $\gamma = -3.4$ which can be likely traced back to the influence of the finite pulse duration τ_p. A space-time plot of the deformed probe field with $\nu_2 = 1$ is shown in Fig. 4.19.

We note that the all-order solution (4.32) can also be derived from a probe-dependent refractive index $\mathsf{n} = 1 + \delta\mathsf{n}_2$ with a phase-dependent refractive index for six-photon scattering with $\nu_2 = \delta\mathsf{n}_2\Phi$, where

$$\delta\mathsf{n}_2[E_p, E_s] = 192\mu_2 E_s^3 E_p . \tag{4.43}$$

Then the asymptotic scattered field can be written as

$$E_p(\varphi_p) = E_p^{(0)}(\varphi_p - \nu_2[E_p]) .$$

The solution shows that the parts of the probe with a higher (positive) amplitude travel with slower phase velocity whereas the parts with smaller (negative) amplitude are accelerated compared to the linear propagation where all parts travel with the same phase

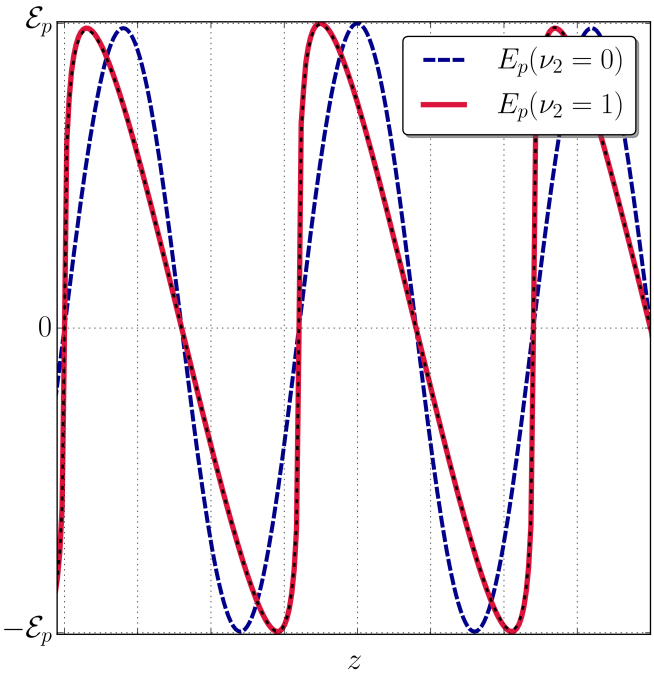

Figure 4.19: In the parallel setup the probe pulse develops a significant steepening while passing a strong electromagnetic background which eventually leads to a discontinuity if $\nu_2 \to 1$. The short black dashes show the analytical solution (4.32).

velocity. The effect is also typical of a second-order susceptibility [Rad+08]. Finally, the steepening of the wavefronts becomes so high that a discontinuous shock is introduced in the solution. Also the Bessel-Fubini solution (4.33) develops such a discontinuity as $\nu_{\mathrm{BF}} \to 1$ which is shown in Fig. 4.20.
In the left panel both expressions are evaluated for the same arguments and the right panel shows that both graphs are related by a reflection $z \to -z$ and a phase shift of $-\pi/2$. Using the established relation between both solutions, the critical value $\nu_2 = 1$ corresponds to the situation where the solution develops a discontinuous shock. Following the argumentation from the inviscid flow, then dissipative effects need to be taken into account. For our scenario this would correspond to electron-positron pair-creation. Further, since so many high harmonics are generated in the spectrum, the condition $j\omega_p \ll m$ is no longer valid, which questions the applicability of the Heisenberg-Euler Lagrangian to effectively describe the light-light interaction due to the nonlinear quantum vacuum.

Although we just argued that the predictions of $\nu_2 > 1$ might be unphysical without taking any further modifications into account, we study now the regime with $\nu_2 > 1$ for completeness and the results are useful for the analysis of the influence of dispersion relative polarisations on the generated spectrum for $\nu_2 = 1$.
From the theory of the solution to Burger's equation it is also known that the infinite sum of Bessel-functions (4.33) becomes divergent for $\nu_2 > 1$ and does not yield the proper physical solution to the differential equation. The theoretical prediction for the pulse shape from (4.32) for several values of $\nu_2 > 1$ are shown in Fig. 4.21, which show a drastically different behaviour than the solution for $\nu_2 = 1$. We note that the graphs in Fig. 4.21 agree with those for the Bessel-Fubini solution shown in [She91].

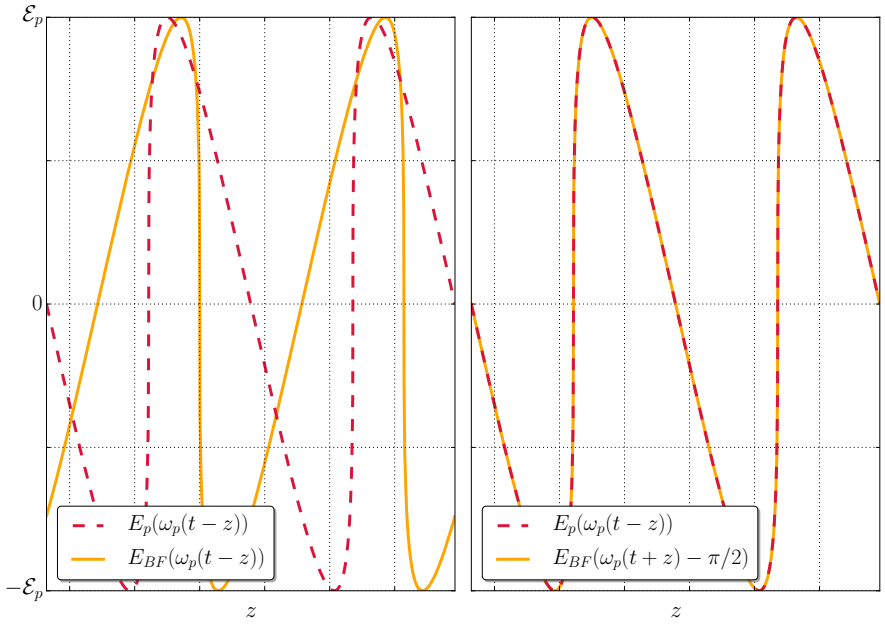

Figure 4.20: The left panel shows a comparison between the scattered probe field (4.32) with $\nu_2 = 1$ and the adapted Bessel-Fubini solution (4.33) with $\nu_{\mathrm{BF}} = 1$. Both graphs show a similar steepening of the wavefronts, but the shock fronts appear on different sides of the pulse different direction. The right panel shows that both solutions are related to each other by $z \to -z$ and $\delta\varphi_p = \pi/2$.

There exist several extensions of the Bessel-Fubini solution for Burger's equation for an infinite plane wave as initial condition. The general solution is thereby given by the Cole-Hopf transformation [Whi11] as a quotient between two Fourier series [EH04], where one limit gives the Bessel-Fubini solution for $\nu_{\mathrm{BF}} < 1$ and the other one is known as the Fay solution, valid for $\nu_{\mathrm{BF}} \gg 1$. In [EH99] a linear system of equations is found, from which the coefficients in a series expansion of each Fourier coefficient can be derived one by one for regions where both the Bessel-Fubini and the Fay solution yield wrong solutions.
Since a similar analysis for our pump-probe setup is out of the scope of this thesis, we only state the result that coefficients of the solution for $\nu_2 \gg 1$ finally [EH04] approach those of a pure saw-tooth-profile [Rud95] in the probe field as $\nu_2 \to \infty$:

$$\mathbf{E}(\varphi) = \boldsymbol{\varepsilon}\mathcal{E} \sum_{j=1}^{\infty} (-1)^{j+1} \left[\frac{\cos(2j-1)\varphi}{2j-1} + \frac{\sin 2j\varphi}{2j} \right]. \tag{4.44}$$

We note that only in the asymptotic limit $\nu_2 \to \infty$ all harmonics are generated with a power-law dependence $I(\omega) \sim \omega^{-2}$, for finite ν_2 the exponent γ is less, $\gamma < -2$, and there exists some kind of cut-off for the generation of high harmonics. In the numerical solution, one might think that this is due to a finite grid resolution, but since we use 5000 grid points per wavelength in all relevant simulations and the theoretical limit to resolve a given frequency is two points per corresponding wavelength given by the Nyquist-Shannon-theorem [Nyq28; Sha49; PFT], frequencies up to $\omega_p \sim 500$ should be properly resolved and propagated. The result also turns out to be insensitive to higher resolutions.
The qualitative behaviour of the spectrum with a power-law-exponential-transition with a cut-off was also discovered using a simple-wave analysis of the propagation of a plane wave in a strong magnetic field in [HH98].

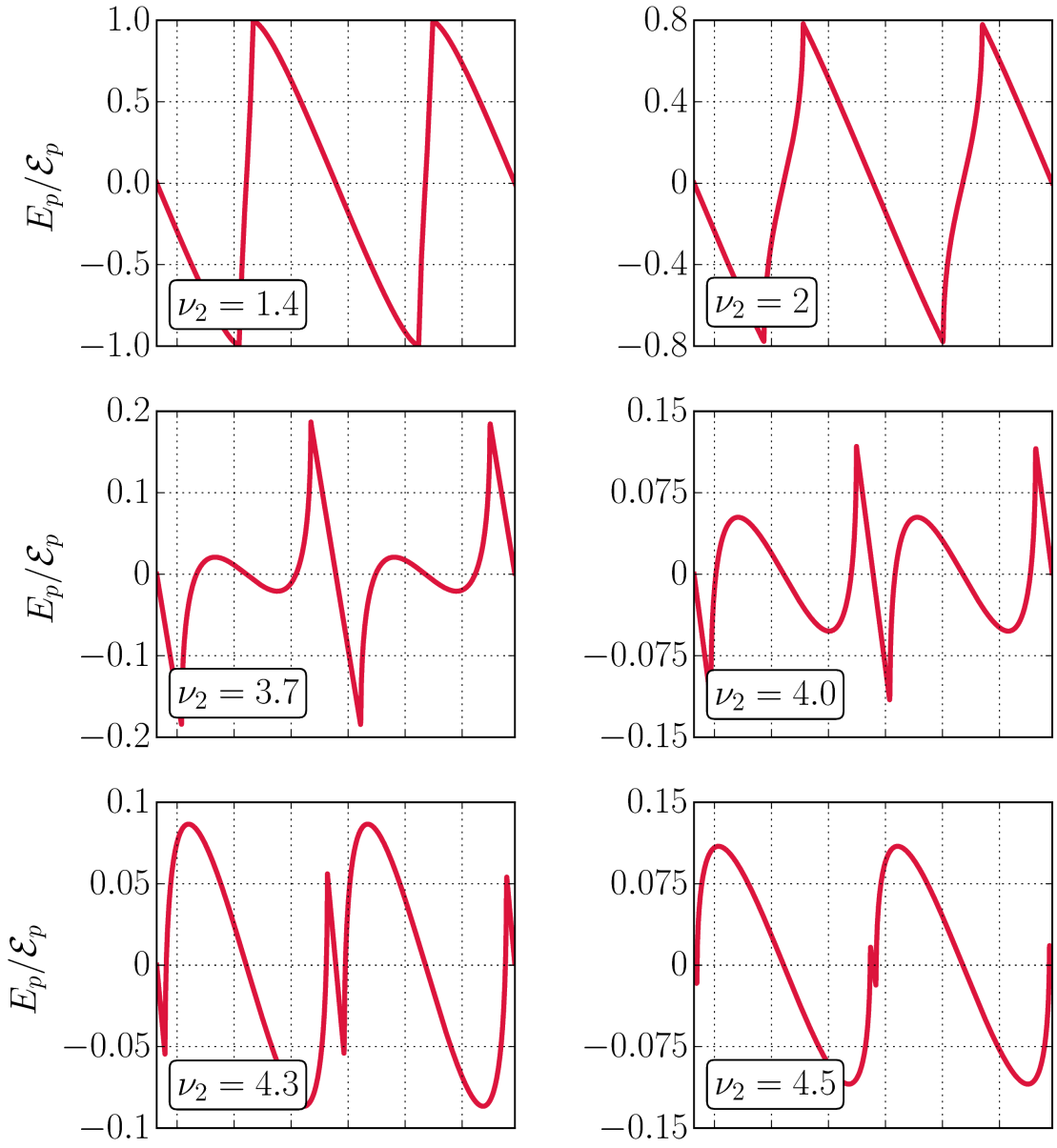

Figure 4.21: The behaviour of the all-order solution (4.32) changes drastically for $\nu_2 > 1$ which shows that the infinite sum of Bessel-functions is not convergent anymore, leading to unphysical behaviour.

Several numerical spectra for $\nu_2 > 1$ are shown in Fig. 4.22. The highest ν_2 that we were able to achieve numerically was $\nu_2 = 1.4$. The corresponding asymptotic probe is shown in Fig. 4.23. For higher values of ν_2, the ODE-Solver did not show convergence in the numerical solution, which indicates that higher resolutions would be needed. But this leads to problems with the desired accuracy in the solution corelated with much more computational effort. An alternative would be to adapt numerical "shock-capturing" methods [LLV92; Tor13] or use "adaptive-mesh-refinement" [BC89; BO84; ER15].

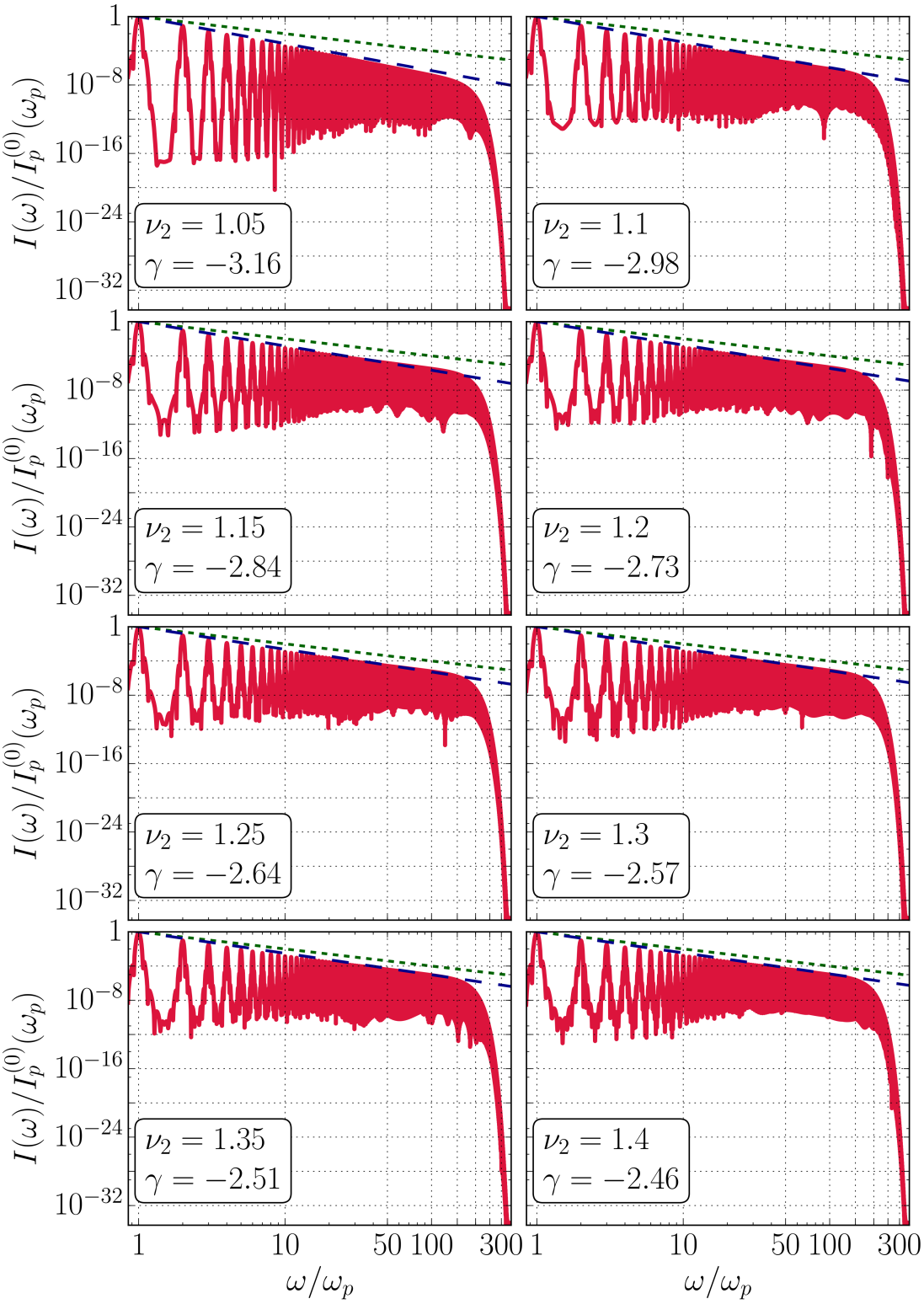

Figure 4.22: The numerical solution develops a shallower power law dependence as the shock parameter ν_2 is increased above one. The universal exponent as predicted by the analytical solution for Burger's equation is thereby $\gamma(\nu_2 \to \infty) = 2$, which is indicated by the green short-dashed line. The power law with exponent given in the lower-left corner is given by the long blue dashed.

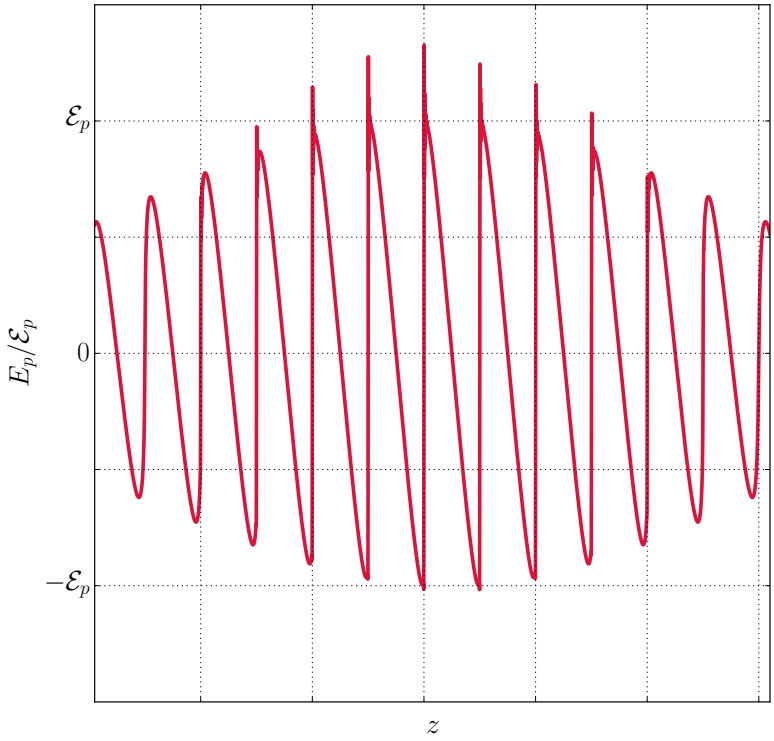

Figure 4.23: The numerical simulation of the probe after passing a strong field with $\nu_2 = 1.4$ has such steep gradients that it introduces spurious oscillations in the numerical solution.

Up to now we only considered six-photon scattering as single source of VHHG. But as it was argued in section 4.2.4, the effect of a modified refractive index on harmonic generation can not be neglected since we consider a parameter regime with $\mathcal{E}_p, \mathcal{E}_s \ll 1$. For general arbitrary relative polarisations, the two different refractive indices lead to complicated phase relations between the different harmonics. The case of parallel polarisations is special since there all harmonics are generated parallel to the probe pulse and are therefore exposed to the same change of refractive index. Since this change is, to lowest order, independent of the frequency [Adl+70], the phase lag is common to all harmonics and the generated spectra are essentially unaffected by four-photon scattering. The spectra for $\nu_2 = 1$ of pure-six- and combined four-and-six-photon scattering are shown in Fig. 4.24 together with the absolute value of their difference. As we already estimated in (4.35), the effect is of the order $10^{-4} - 10^{-5}$ for the intensity of the second harmonic. Although the spectra do not differ significantly, the dispersive nature of four-photon scattering can be observed. In Fig. 4.25 a space-time plot of both asymptotic signals reveals that the box-diagram causes a clearly visible phase-shift of the entire probe pulse, without affecting its shape.

For arbitrary relative polarisations, the two different refractive indices introduce different phase relations between the generated harmonics. As a consequence, the prevention of a synchronous interplay between the frequency components lead to a suppression of VHHG and also the nature of the deformation of the probe pulse in the shock regime shows a strong dependence on the relative polarisations.
These effects are studied in the next section for different parameter regimes.

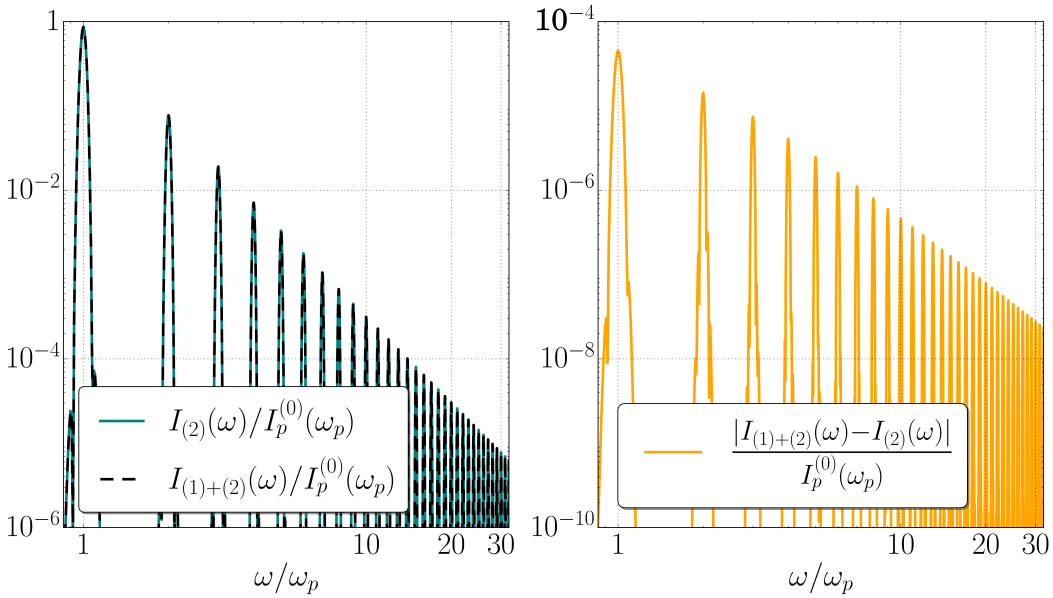

Figure 4.24: The left panel shows the spectra for pure six- and combined four- and six-photon scattering in the parallel case with $\nu_2 = 1$. The right panel shows the difference between the two spectra.

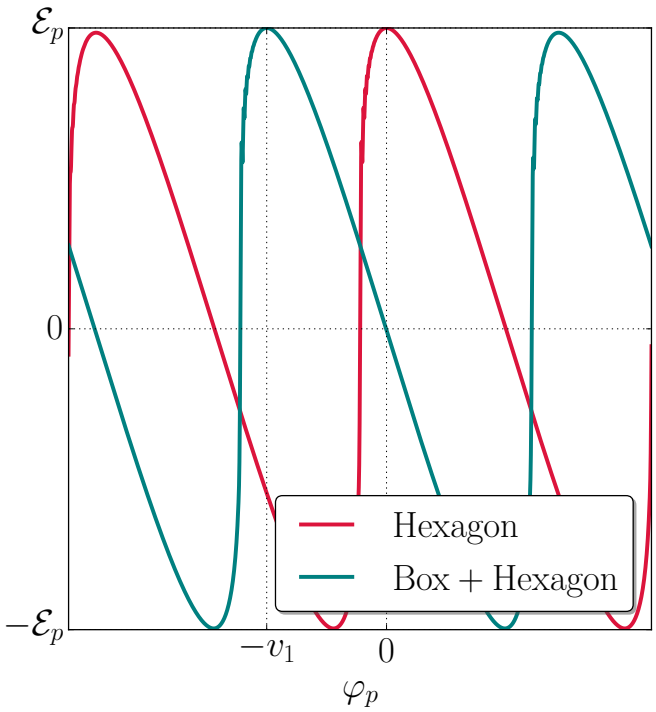

Figure 4.25: Shockwave with $v_1 = 2.57$ and $\nu_2 = 1$ for the hexagon diagram and combined box and hexagon. The only clearly visible influence is the induced phase shift by v_1.

4.2.6 Polarisation Dependency

So far our discussion was for parallel probe and strong polarisations and we saw that four-photon scattering does not contribute significantly to the generation of the shockwave. We split the discussion of how dispersive effects on relative polarisations influence the

generation of higher harmonics into three parameter regimes which are quantified using the shock-parameter $\upsilon_1 := \upsilon_1^{\parallel}$ (cf. (4.28)) for pure four-photon scattering. First we consider the limiting case of absence of dispersion with $\upsilon_1 \ll \nu_2$, then the influence of the dispersive vacuum with $\upsilon_1 \approx \nu_2$ followed by an analysis of the strong dispersive regime with $\upsilon_1 \gg \nu_2$.

Dispersionless Vacuum: $\upsilon_1 \ll \nu_2$

In the non-parallel case with arbitrary relative polarisation between the probe and strong pulse, the shock-behaviour of the pulse and the generated spectra are already different from the parallel case for only six-photon scattering. This is demonstrated for the perpendicular setup for the values $\nu_2 = 0.05, 0.6, 1$ of the parallel shock-parameter in Fig. 4.26 where the different line styles indicate the relative polarisations of the harmonic to the probe pulse. For the parallel setup, all higher harmonics were generated parallel to the probe pulse. In the perpendicular case, all even harmonics are generated parallel to the strong background while all odd harmonics are parallel to the probe pulse.

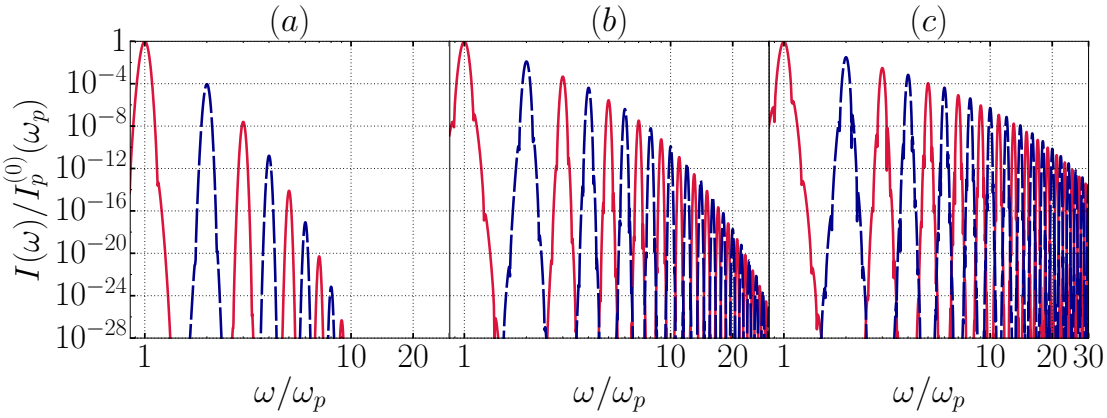

Figure 4.26: Harmonic spectra from numerical simulation of the perpendicular setup for different regimes of solution: (a) $\nu_2 = 0.05, (b)$ $\nu_2 = 0.6, (c)$ $\nu_2 = 1$. The red solid lines (blue dashed) peaks are harmonics parallel to the probe (strong) pulse.

The solution shows a much more complicated behaviour due to the asynchronous interaction of the different harmonics which eventually leads to a suppression to VHHG in this case. One might be tempted to think the form of the polarisation (3.41) and the magnetisation (3.42) for the hexagon diagram that a similar analysis with another shock parameter $\nu_2^{\perp} = 104\mathcal{E}_s^3\mathcal{E}_p\Phi$ might be valid. But this is not the case due to the complicated interaction of the different harmonics in different polarisations via the $\mathcal{GF}$ mixing term in the current.
Although the all-order solution (4.32) is only valid for the parallel case, we use it to explain the qualitative behaviour in the perpendicular setup. Therefore, we state the solution again and split it into even and odd frequencies:

$$\mathbf{E}_p(\varphi_p, \nu_2) = \mathbf{E}_p^{\text{even}}(\varphi_p, \nu_2) + \mathbf{E}_p^{\text{odd}}(\varphi_p, \nu_2) \ , \tag{4.45}$$

where

$$\begin{aligned}\mathbf{E}_p^{\text{even}}(\varphi_p,\nu_2) &= 2\mathcal{E}_p\boldsymbol{\varepsilon}_p\sum_{j=1}^{\infty}(-1)^{j+1}\frac{J_{2j}\big(2j\upsilon_2\big)}{2j\upsilon_2}\sin(2j\varphi_p)\ ,\\ \mathbf{E}_p^{\text{odd}}(\varphi_p,\nu_2) &= 2\mathcal{E}_p\boldsymbol{\varepsilon}_p\sum_{j=1}^{\infty}(-1)^{j+1}\frac{J_{2j-1}\big((2j-1)\upsilon_2\big)}{(2j-1)\upsilon_2}\cos((2j-1)\varphi_p)\ .\end{aligned} \tag{4.46}$$

and again $\upsilon_2 = \nu_2\ \mathrm{e}^{-\left(\frac{x^-}{\tau_p}\right)^2}$ includes the envelope function of the probe. A space-time plot of the corresponding numerical shock-wave for $\nu_2 = 1$ in the perpendicular setup is shown in the left panel of Fig. 4.27. The component perpendicular to the probe pulse shows a similar behaviour as in parallel case, the development of a saw-tooth-profile, but with double the probe frequency. In contrast, the superposition of harmonics with polarisation parallel to the probe pulse show a different behaviour and tend to develop a rectangular pulse shape. The split solution for the parallel case with $\nu_2 = 1$ is shown in the upper right panel of Fig. 4.27 which qualitatively explains the generated shockwave form due to the selection rules for the polarisation of even and odd harmonics. The even harmonics are generated parallel to the strong pulse such that this behaviour is similar to $\mathbf{E}_p^{\text{even}}(\varphi_p,1)$, the odd frequencies generate a pulse shape similar to $\mathbf{E}_p^{\text{odd}}(\varphi_p,1)$.
As in the parallel case, we expect both components to attend an asymptotic spectral intensity $I(\omega) \sim \omega^{-2}$ as $\nu_2 \to \infty$, leading the following expressions for the scattered field:

$$\begin{aligned}\mathbf{E}_{\text{rect}}(\varphi) &= \mathcal{E}\sum_{j=1}^{\infty}(-1)^{j+1}\,\frac{\cos(2j-1)\varphi}{2j-1}\ ,\\ \mathbf{E}_{\text{saw}}(\varphi) &= \mathcal{E}\sum_{j=1}^{\infty}(-1)^{j+1}\,\frac{\sin 2j\varphi}{2j}\ .\end{aligned} \tag{4.47}$$

The corresponding graphs of these asymptotic pulse shapes are shown in the lower right panel of Fig. 4.27. As in the parallel case, both components develop a shock front.

In the next section we investigate the effect of a background with $\upsilon_1 \approx \nu_2$.

Dispersive Vacuum $\upsilon_1 \approx \nu_2$

For the parallel case, dispersive effects from four-photon scattering did not influence the shape of the generated shockwave since all harmonics were objected to the same dispersion relation and therefore gained the same asymptotic phase shift. For the perpendicular setup, the different refractive indices lead to different phase relations between the harmonics and therefore might potentially influence the shape of the generated shockwave. For weak dispersion with $\upsilon_1 = 0.5$ and $\nu_2 = 1$ the resulting shockwave is shown in Fig. 4.28.
Apart from a phase shift by $-\upsilon_1$, the the pulse shows a similar shape as in the non-dispersive case shown in the left panel of Fig. 4.27 where only six-photon scattering was considered. The corresponding spectrum for $\upsilon_1 = 0.5$ is depicted in the left panel of Fig. 4.29.
Further increasing the shock parameter υ_1 leads to a significant change in the deformation of the probe pulse. This is shown for $\upsilon_1 = 2.5$ in Fig. 4.30.
The asymptotic component parallel to the probe pulse for $\upsilon_1 = 2.5$ develops a similar

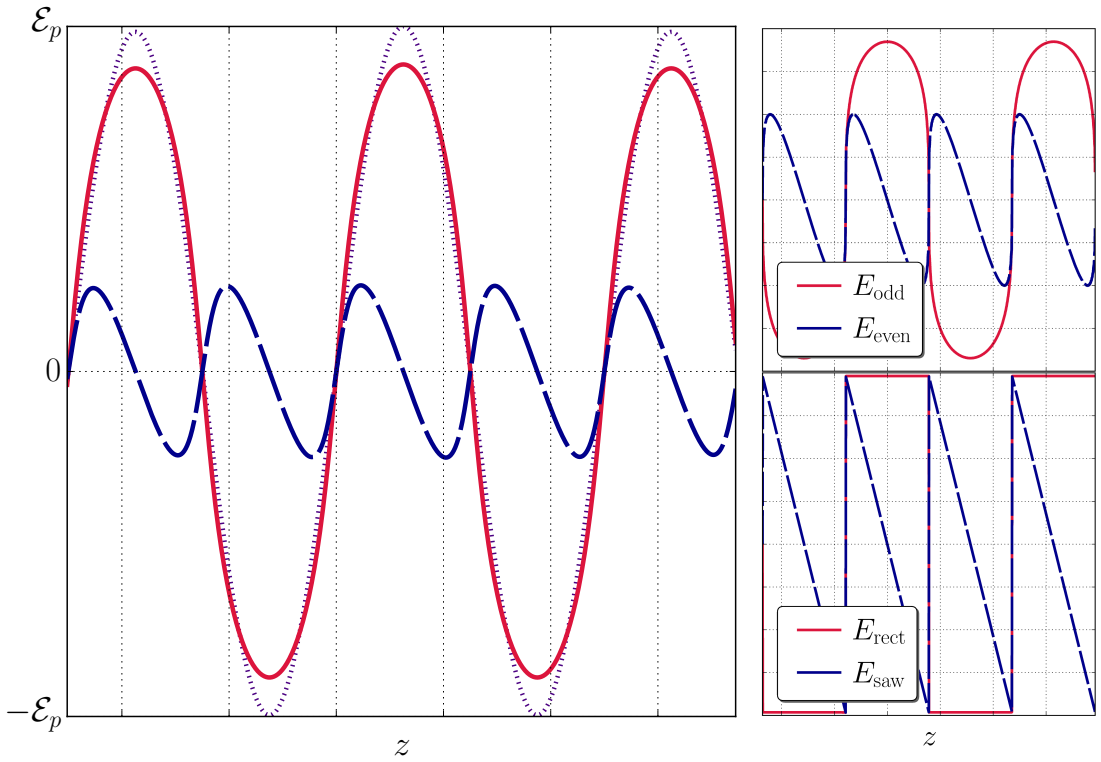

Figure 4.27: The left panel shows a space-time plot of the shockwave generated in the perpendicular setup for $\nu_2 = 1$ from pure six-photon scattering. The red solid line is the shape of the component parallel to the probe pulse consisting only of odd harmonics. The blue line with long dashes is the newly generated component parallel to the strong field which is only formed from even frequencies. The short dashed line indicate the initial probe profile. The upper right panel shows the split solution (4.46) of the parallel case with $\nu_2 = 1$ and the lower right panel show the limit of $\nu_2 \to \infty$ (4.47) as a comparison.

deformation as it is observed for a pulse propagating in an optical Kerr medium, for which the polarisation has the form

$$P_i = \chi^{(1)}_{ij} E_j + \chi^{(3)}_{ijkl} E_j E_k E_l \ , \tag{4.48}$$

where $\chi^{(j)}$ is the jth susceptibility tensor. In this case, the refractive index depends on the modulus of the electric field of the probe [MN04], $\mathsf{n} = 1 + \delta\mathsf{n}(|E_p|^2)$, and as a result, the parts of the probe with higher amplitude travel with a smaller phase velocity than those with a smaller amplitude. As we have seen, the parallel component of the probe contains only the odd harmonics and therefore the behaviour described by (4.48) is consistent, since the highest nonlinear term stems from E_p^3 and all higher powers are suppressed since $\mathcal{E}_p \ll 1$. The perpendicular component does not show any particular deformation.

The corresponding spectrum is shown in the right panel of (4.29) and we observe that the ordering of the harmonics is no longer monotone and the higher even harmonics are more suppressed that the odd one. This is due to the refractive index being smaller by a factor of 4/7 for the component parallel to the probe and the perpendicular component is objected to higher dispersive effects, leading to a more complicated phase relation between the harmonics. In the parallel setup each generated harmonic experiences the same dispersion relation and therefore the interaction of all generated signals can add

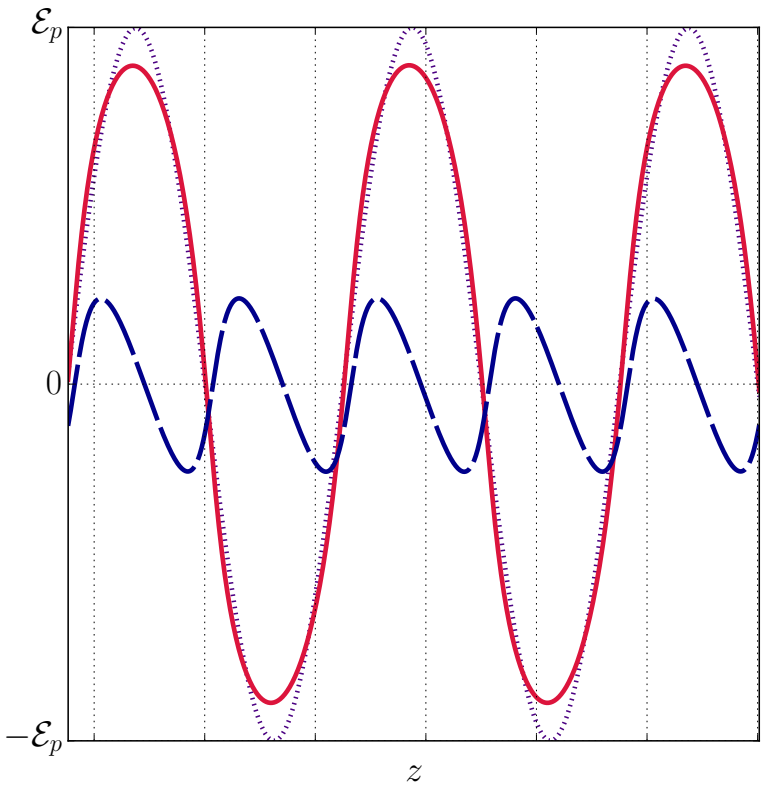

Figure 4.28: Shockwave in the weakly dispersive, perpendicular setup with $\nu_2 = 1$ and $\upsilon_1 = 0.5$. The red solid line indicates the component parallel to the probe field, the long blue dashes field parallel to the strong pulse and the short dashes show the initial pulse profile. Although both components are objected to different refractive indices, the behaviour is still similar to the case of pure-six-photon scattering.

up synchronously.
For the perpendicular setup, the odd (even) harmonics are generated perpendicular (parallel) to the strong pulse and thus the different refractive indices induce different phase lags between the harmonics. Each scattered signal, which might be the input for another chained process, obtains a different phase. In contrast to the parallel case, these phase mismatches lead to an incoherent summation of all possible processes. Therefore, the generation of high harmonics is less effective and the development of shocks suppressed.

The problem and influence of different refractive indices on the generation of higher harmonics is also common to nonlinear optics and known as "phase-matching" problem [Trä07]. The mismatch of phase relations between the interacting waves can lead to a large suppression of the conversion into higher frequencies in nonlinear media. Our observations of carrier-wave shocking are similar to those in reported in [Kin+07], where numerical studies using a pseudospectral spatial-domain technique [TKN05] were used to model nonlinear light propagation and showed excellent agreement with theory in the dispersionless limit. The authors also observed that a nonlinear refractive index has potentially a large influence on the effectiveness of carrier-wave steepening due to the phase mismatch.
In the next section even higher dispersive effects are studied and we will see that the phase mismatch explained above leads to so heavy suppression of harmonic generation that also the derivative of the envelope function become visible.

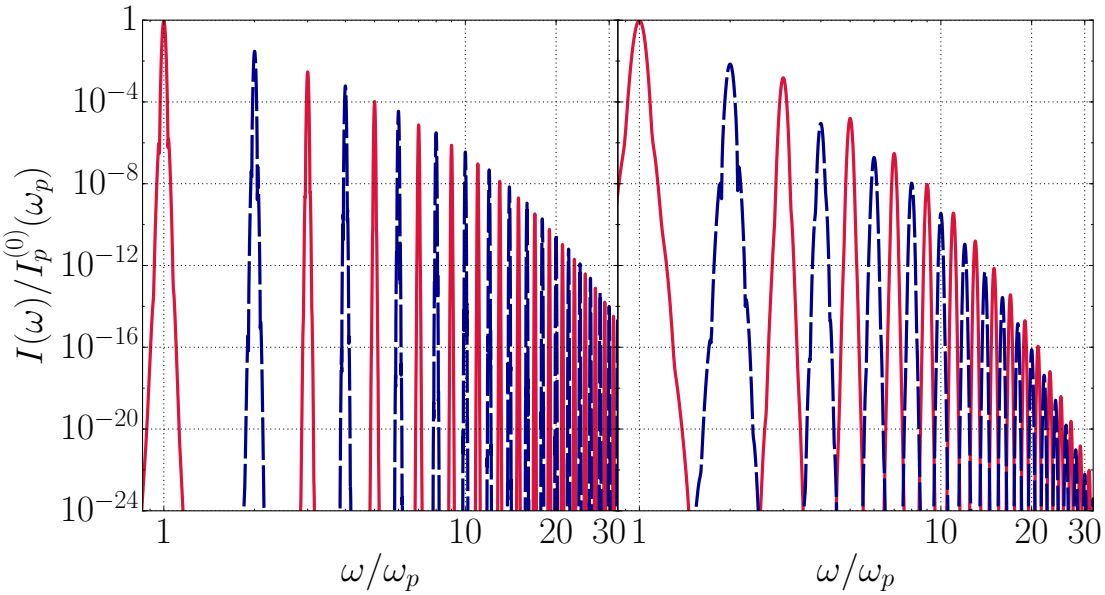

Figure 4.29: Small dispersion (left panel with $v_1 = 0.5$) does not influence the harmonic generation in perpendicular setup significantly. As dispersive effects become stronger (right panel with $v_1 = 2.5$), the ordering of the harmonics is changed and the generation of the perpendicular harmonics (blue dashed line) becomes higher suppressed compared to the parallel component (red solid line).

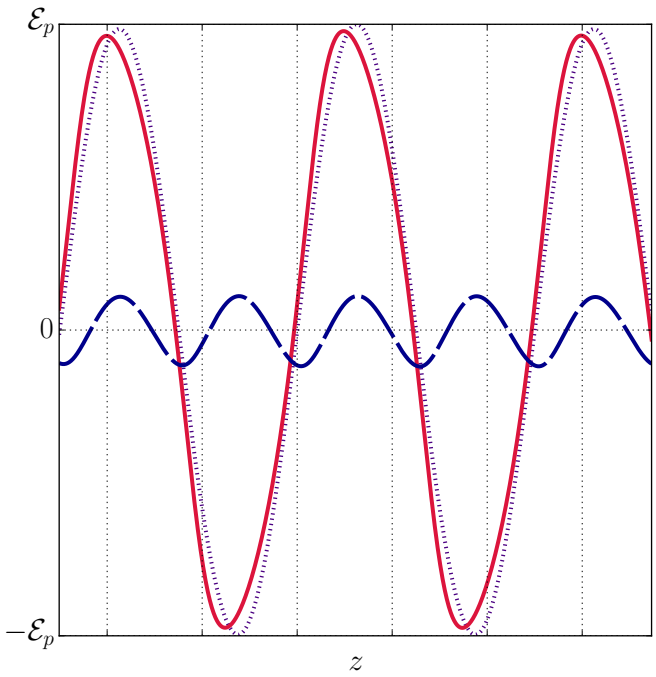

Figure 4.30: The shape of the generated shock wave changes significantly in the parallel component (red solid) as dispersive effects become stronger ($v_1 = 2.5$, $\nu_2 = 1$). The perpendicular field (blue long dashes) is also generated, but the steepening is suppressed. The initial pulse profile is indicated by the short dashes.

4.2.7 Strongly-dispersive Vacuum $\upsilon_1 \gg \nu_2$

For the regime where four-photon scattering is much more prevalent than six-photon scattering, a comparison of the different harmonic spectra for shock parameters $\upsilon_1 = 25$ and $\nu_2 = 1$ is shown in Fig. 4.31 for the perpendicular setup with comparison four–, six- and four-and-six photon scattering.

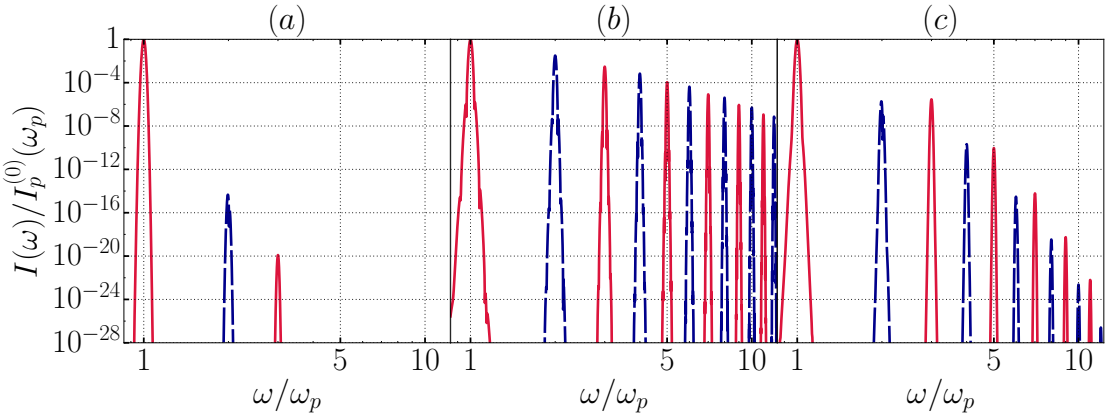

Figure 4.31: We consider strong dispersive effects with $\upsilon_1 = 25$ and $\nu_2 = 1$ in the perpendicular setup. The left pane shows the harmonic spectra generated from pure four-photon scattering, the middle pane from just six-photon scattering and the right pane for when both are combined. The red solid (blue dashed) peaks are harmonics parallel to the probe (strong) pulse.

Again, the harmonic generation is highly suppressed due to the highly distorted phase relations of the generated frequencies. Up to now we always assumed that the derivative of the envelope function of the probe pulse can be neglected (cf. (2.83)), which turned out to be a good approximation. In the numerical simulation, the derivative of the envelope also appeared as it was analysed in section 4.1 in the discussion of the overlap signal. But as we always treated the case $\omega_p \tau_p \gg 1$, the effect was never directly visible but only after filtering the corresponding component. Now in the strongly dispersive case the phase mismatch of the higher harmonics in the perpendicular setup is so high that already the generation of the second harmonic is strongly suppressed and the deformation of the probe pulse becomes clearly visibly. A space-time plot of the deformed component parallel to the strong pulse is shown in Fig. 4.32.

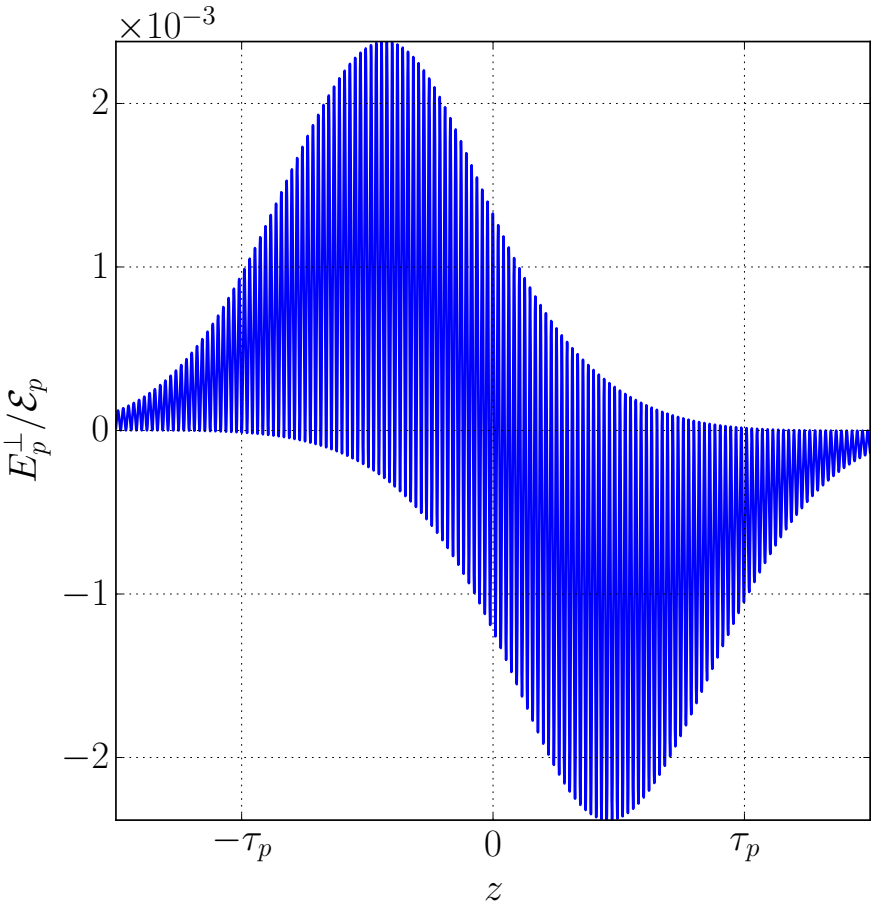

Figure 4.32: Shown is the probe component parallel to the strong pulse for the perpendicular setup in the presence of strong dispersion with $\upsilon_1 = 25$ with $\nu_2 = 1$. The effect of high harmonic generation is strongly suppressed by dispersion and the deformation of the envelope becomes visible.

4.3 Discussion for VHHG

4.3.1 Ultra-short Probe Pulses

As we saw in the previous section, in the case of strong dispersion, the effect of the derivative of the envelope function can also be directly observed. Up to now, we have taken $\omega_p\tau_p \gg 1$ such that neglecting the envelope was a good approximation. If one relaxes this condition and considers very short pulses, the all-order solution (4.32) could possibly become invalid as $\omega_p\tau_p \gg 1$ was used in the derivation. Therefore, we simulated a few-cycle-pulse with $\omega_p\tau_p = 5$ in the $\nu_2 = 1$ parallel setup. The inital profile together with the generated shockwave is shown in Fig. 4.33.

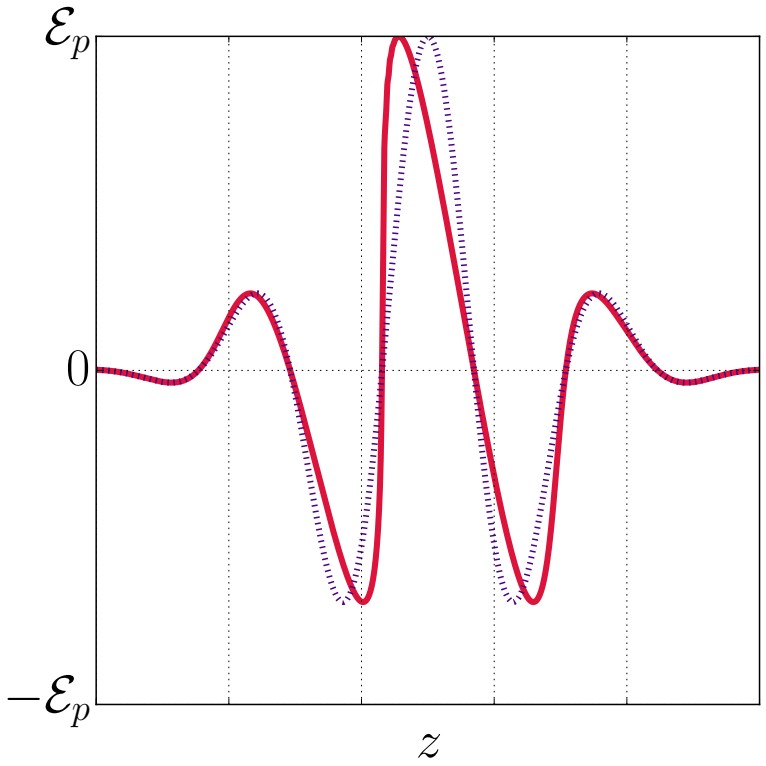

Figure 4.33: Shock wave induced in a few-cycle pulse with $\omega_p\tau_p = 5$ (red solid line) together with the inital probe profile (blue dashed) in the parallel setup after passing a constant background with $\nu_2 = 1$. The effect of pulse steepening is similar to the case analysed in section 4.2.5 for long pulses with $\omega_p\tau_p \gg 1$.

The resulting spectrum together with the initial probe spectrum and a long pulse with $\nu_2 = 1$ is shown in Fig. 4.34. The initial spectrum of the probe is much broader as the pulse is shorter in position space. Again, the inclusion of four-photon scattering has a negligible effect on the spectrum as it only causes a phase shift. As we see, the spectrum of the shocked short pulse is much smoother than that of the long pulse, but obeys essentially the same power law as the long probe. This can be understood from the inital spectrum. In the long-pulse case, the initial spectrum is peaked strongly around ω_p with the limit of a δ-peak for the plane wave limit $\tau_p \to \infty$. Therefore, the nth harmonic is sharply peaked around the well-defined frequency $n\omega_p$. As the width of the initial spectrum scales with $\sim \frac{1}{\tau_p}$, for the shorter pulse a much broader range of frequencies

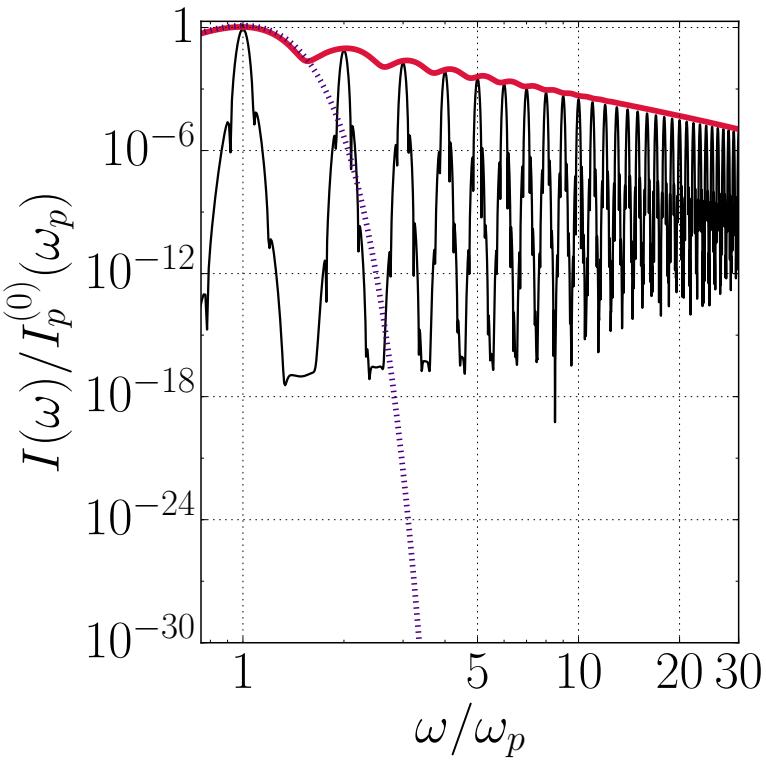

Figure 4.34: The spectrum of the few-cycle shock wave shown in Fig. 4.33 (red thick line) compared to the spectrum of a long pulse (thin black line) in the parallel $\nu_2 = 1$ case. The spectra show the same power-law-scaling, but the peaks of the short pulse spectrum are much more smoothened out compared to long pulse. This results from the initial probe spectrum (blue dashed) containing much more frequencies which merge into less sharply peaked sum frequencies.

can merge together into higher harmonics. So for n photons with individual frequencies $\omega_{p,l}$ from this larger spectrum, the resulting signal has a frequency at $\sum_{l=1}^{n} \omega_{p,l}$. The similarity of the power-law-behaviour of the spectrum is an indication that our original analysis is also valid in the few-cycle case, but the extensive analysis of this case is beyond the scope of this thesis.

4.3.2 VHHG in Inhomogeneous Backgrounds

As constant fields comparable to the critical field are very hard to generate in terrestrial experiments, mainly focused laser beams are used to study vacuum polarisation effects. Therefore, the assumption of a constant background, often assumed to be a "constant-crossed-field" with $|\mathbf{E}| = |\mathbf{B}| = const.$ and $\mathbf{E} \cdot \mathbf{B} = 0$, is questionable. To study more realistic scenarios, at least one single cycle in the background has to be considered. To give an outlook on the study of inhomogeneities in the background, we have included a single sinusoidal oscillation in the background as it is shown in Fig. 4.35. As we have seen in (4.30), the second harmonic scales to lowest order in ν_2 with $\nu_2 \sim \mathcal{E}_s^3 \mathcal{E}_p$, the third one with $(\nu_2)^2$ and in general the nth harmonic with $(\mathcal{E}_s^3 \mathcal{E}_p)^{n-1}$. So the even harmonics originate from integrals over odd powers of the strong field, the odd ones from even powers of the strong field. As we included a sinusoidal oscillation in the background, one would expect the even harmonics to be heavily suppressed as opposed to the odd ones because the integration over odd powers of a sinusoid vanishes. For the analysis of

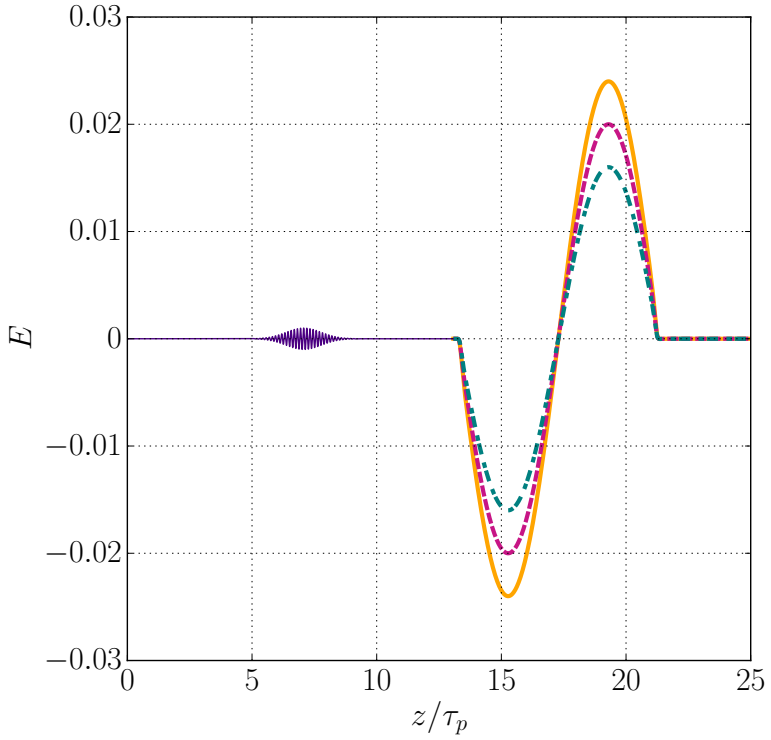

Figure 4.35: Simulational setup to study the effect of inhomogeneities in the background on VHHG. The otherwise constant background now includes a single sinusoidal oscillation. The different line styles indicate different field strengths.

the odd harmonics, let us consider the third harmonic for simplicity. As we have seen, the third harmonic scales with $(\nu_2)^2 \sim \mathcal{E}_s^6$, so it originates from an integral over $\sin^6 \varphi_s$. From the identity

$$\sin^6 \varphi_s = \frac{5}{16} - \frac{15}{32}\cos 2\varphi_s + \frac{3}{16}\cos 4\varphi_s - \frac{1}{32}\cos 6\varphi_s$$

we see that $\sin^6 \varphi_s$ also has a constant contribution. One could now think that only the constant term with $\frac{5}{16}$ is relevant to reach the same intensity for the third harmonic as in the constant background. If this were the case, then a simulation with $\nu_2 = (\frac{16}{5})^{1/2}$ with the oscillating strong field should lead to the same intensity of the third harmonic as $\nu_2 = 1$ with a constant background. The $\frac{16}{5}$ would then compensate for the $\frac{5}{16}$ in the $\sin^6 \varphi_s$ to yield the same "effective" ν_2 for the generation of third harmonic. The resulting spectrum for pure six-photon and combined four- and six-photon scattering is shown in Fig. 4.36. We see that the harmonic generation is strongly suppressed compared to the constant case although we adjusted the relevant value ν_2 to compensate for the inhomogeneity. This suggests that the shape of the background introduces a much more complicated interplay of the harmonics and cannot be compensated by a power scaling. Also for the setup of a Gaussian background one might naively think that an "effective" pulse duration τ_s can be defined and the all-order solution (4.32) would apply. But there was no numerical indication that this is the case.

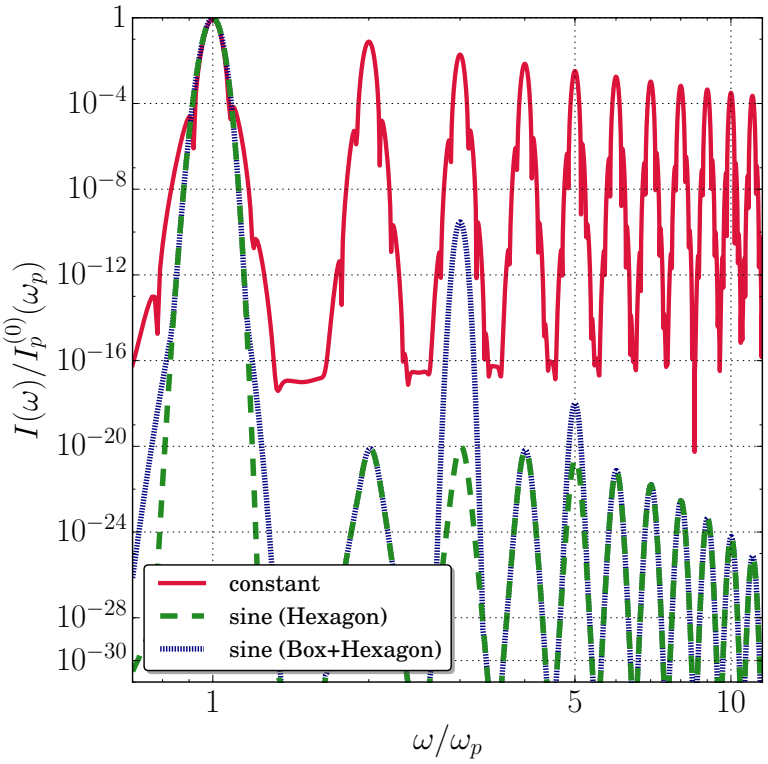

Figure 4.36: The red solid line is the generated spectrum for an optical probe after passing a constant background with $\nu_2 = 1$. The green long dashed line is the spectrum of the probe with only six-photon scattering included after passing a sinusoidal background as it is shown in Fig. 4.35 with an adjusted value $\nu_2 \to \nu_2(\frac{16}{5})^{1/2}$. The blue short dashes are the probe spectrum with the additional inclusion of four-photon scattering in the simulation. The generation of harmonics is heavily suppressed in both cases of a non-constant strong pulse.

4.3.3 Comparison with Harmonic Generation in Laser-irradiated Plasmas

The results obtained in this thesis suggest a certain similarity of VHHG via the virtual electron-positron "plasma" to the generation of high harmonics in laser-irradiated foils. There are no nonlinear effects of light propagation for plane waves as the nonlinearity only depends on the field invariants $\mathcal{F}$ and $\mathcal{G}$ and they vanish identically for plane waves. In this sense, the quantum vacuum also shows a certain transparency to light propagation similar to the one of a plasma which is a linear medium for photon frequencies above the plasma frequency [Bit13]. Unlike the plasma in a laser-irradiated foil, where one assumes complete ionisation as the laser hits the target, the vacuum first has to be "activated" by a strong background, which is similar to pump-probe experiments in spectroscopy (see e.g. [SBN04; Lup+14]).
The rectangular function used to model the constant background in the current chapter on VHHG is also used as an initial profile function for the electron density of a target in a laser-experiment [McK+13] and for the laser profile used in capillary discharge waveguides to produce Multi-GeV electron beams [Lee+14]. Another similarity is the selection rules for harmonic generation, which are also present in the relativistic oscillating mirror (ROM) model [Gor+05]. In our parallel pump-probe setup, all harmonics were generated parallel to the probe pulse, while in the perpendicular case the even harmonics were gen-

erated parallel and the odd ones perpendicular to the strong pulse. In the ROM-model, selection rules for the generated harmonics for oblique incident of the laser on the target are also found. Odd harmonics are generated in the p-polarisation (where p stands for "parallel" to the plane of incidence) and the even ones in the s-polarisation ("senkrecht", so perpendicular to the plane of incidence [LJP96]). The more effective generation of harmonics parallel to the probe pulse is also reminiscent of nonlinear Compton scattering [Kin14] where the emission of photons with polarisation parallel to the background is preferred.
The power-law behaviour for the intensity of lower harmonics together with the exponential suppression of higher harmonics is also observed for the real plasma present in laser-foil experiments. In the ROM-model, theoretical predictions with $I(\omega) \sim \omega^{-5/2}$[Gor+04] and a universal exponent of $I(\omega) \sim \omega^{\gamma}$ with with $\gamma = -8/3$ [BGP06] have been derived. Experimental values for such exponents were found for solid-state targets to be intensity dependent with ranges from -5.50 to -3.38 [Nor+96]. For our vacuum high harmonic generation, the power-law behaviour in the numerical and analytical spectra first appears evidently at shock parameters of $\nu_2 \approx 0.85$. We found that the exponent increases as a function $\gamma = \gamma(\nu_2)$ and yields similar values of $-4.5 \lesssim \gamma < -2$.
The existence of a cutoff harmonic for finite values of ν_2 is also found for photon merging, but unlike the ROM-model, no scaling behaviour for the cutoff frequency could be determined from the numerical results as higher values with $\nu_2 > 1.4$ were not feasible to simulate.
The theoretical value $\gamma = -2$ corresponds to the case $\nu_2 \to \infty$ and would only be obtained for an infinite propagation distance. But this value is never reachable because of the production of real electron-positron pairs from seeded pair-creation [Rei62; NR64]. Another possibility is the multi-photon Breit-Wheeler processes [BW34; Pik+14] for which a probe photon γ_p with four-wave vector k_p would have to interact with n photons from the background with wave vector k_{bg} satisfying [Sei+16]

$$s = (k + n\, k_{\mathrm{bg}})^2 = 2\omega n \omega' \left(1 - \cos \sphericalangle(\vec{k}_p, \vec{k}_{\mathrm{bg}})\right) > 4m \ ,$$

where s is the Mandelstam variable [PS95], m is the mass of the electron and $\cos\sphericalangle(\vec{k}, \vec{k}_{\mathrm{bg}}) = -1$ corresponds to our setup of counter-propagating pulses. Such relaxation effects would likely lead to a depletion of the higher harmonics and therefore prevent the generation of extremely high gradients in the probe. Further alternative possible mechanisms to prevent the probe wave from developing a shock front are explained in the next section on the validity of the approach chosen in this thesis. Also taking transverse pulse dimensions into account leads naturally to dispersive effects [MN04] that can possibly dominate the vacuum nonlinearities.

The spectra of high harmonics generated in laser-gas and laser-liquid interactions shows a qualitatively different behaviour, namely the development of a "plateau" region in the spectrum which is not present in VHHG. The effect observed in these experiments is the three-step recombination mechanism [Trä07; WSG08]. The gas or liquid is used as a target for a laser pulse whose amplitude is comparable to the Coulomb field experienced by the electrons due to the nucleus. The electron can then tunnel outside the binding potential of the nucleus (which is lowered by the laser) and additionally gets accelerated by the external field. A recombination of the electron and the nucleus then leads to the emission of high harmonics. As this effect is of completely different fundamental nature, no such "plateau" region is observed in vacuum high harmonic generation as studied in the present work.

Harmonic generation in the parallel setup was only minimally effected by dispersive effects due to the non-unitary refractive index induced by the strong background. This

is because all modes obtain the same phase lag and therefore the interaction lead to a coherent summation of higher order processes, leading to a monotonic increase of the higher harmonics with the propagation distance.

The perpendicular setup did not show such an effective harmonic generation since the different harmonics interacted in a complicated, non-phase-synchronous way since the possible chains leading to a given harmonic experienced different refractive indices for different propagation distances. The summation of this incoherent, complicated phase relation leads to an overall phase mismatch resulting in a suppression of harmonic generation. A similar effect is found for nonlinear optical materials in [Kin+07] which eventually leads to an attenuation of pulse-steepening effects.

4.3.4 Validity of Approach

With the generation of very high harmonics, the assumption that the variation of the field inhomogeneity does not vary significantly over a Compton wavelength also becomes invalid such that the applicability of the Heisenberg-Euler Lagrangian is questionable. Extensions to the Heisenberg-Euler Lagrangian including derivatives of the field invariants $\mathcal{F}$ and $\mathcal{G}$ also exist in the literature [MME81; GS96; GS99; DH99]. Let us follow the analogy from section 4.2.5 that the all-order solution of the scattered field for a Lagrangian can be obtained as a solution to a nonviscid Burger's equation. We start from a Lagrangian containing only polynomials of the field invariants $\mathcal{F}$ and $\mathcal{G}$ and obtain schematically an equation

$$\partial_t E_p(t,z) + c\, E_p(t,z)\partial_z E_p(t,z) = 0 \tag{4.49}$$

with some constant c. Then such a derivative term in the Lagrangian would naturally introduce a second order derivative term in (4.49) possibly acting as a dissipative (viscous) term [Tho13] which might prevent the wave from developing infinite gradients.
Similarly, also dispersive effects from the frequency dependent refractive index in a strong external field as it was found by Toll in [Tol52], can be used to introduce a third derivative [ZF82] into Burger's equation for constant magnetic backgrounds, finally leading to a Korteweg-de-Vries-type equation. The Korteweg-de-Vries equation is known for allowing Soliton-type solutions such that also dispersive effects might finally prevent the wave from shocking. The detailed study of these effects is outside the scope of this thesis, but may inform future research.

In the pump-probe setup considered in this thesis the effect of transverse directions and therefore longitudinal polarisations was ignored. We note that the invariants $\mathcal{F}$ and $\mathcal{G}$ also remain small for single focused laser pulses that have additional longitudinal field components E_z and B_z opposed to counter-propagating pulses. For example, a radially polarised Gaussian beam with amplitude E_0, frequency ω and wave vector $\vec{k} = k\hat{e}_z$ along the z-axis exhibits $\mathcal{G} = 0$, but

$$\mathcal{F} = \frac{1}{2}(E^2 - B^2) \approx \frac{1}{2}\theta_0^2 E_0^2 \sin^2(\omega t - kz)$$

close to the focus [McD00], where

$$\theta_0 = \frac{2}{kw_0} \tag{4.50}$$

is the diffraction angle and w_0 the width of the pulse in the transverse plane of the beam. Then the limit $w_0 \to \infty$ corresponds to the plane wave case with $\theta_0 \to 0$ and therefore $\mathcal{F} \to 0$. To see in which parameter range the assumption of plane waves is justified, we define the diffraction parameter

$$l = \frac{w_0^2}{\lambda_p \tau_s} \,, \tag{4.51}$$

where w_0 is the again the "waist" of the probe pulse. If one assumes that the extension of the probe pulse in the directions perpendicular to the propagation is smaller than the one of the strong background, then $l \ll 1$ represents the "far zone" in which diffractive effects play an important role whereas the "near zone" is characterised by $l \gg 1$ and in this regime neglecting diffraction should be a good approximation [Lev68].
Another effect of transverse dimensions would be the enhancement of self-focusing [cS00; KT07]. For six-photon scattering, the scattered field is a function of the field itself leading to the generation of higher harmonics and an increase of intensities and some relaxation effects, such as real electron-positron-pair creation might more relevant.
Neglecting transverse dimensions also leads to the vanishing of an asymptotic second harmonic from pure four-photon scattering. In [KK12] it was shown that for non-parallel probe and strong pulse wave vectors, elastic four-photon scattering (which corresponds to four-wave mixing which is forbidden as explained in the last chapter) is permitted and the scattered field obtains an additional factor $1 - \cos(\theta)$ from non-parallel probe and strong wave vectors. θ is thereby the angle between the k-vector of the probe and strong pulse such that $\theta = 0$ corresponds to parallel propagation and therefore vanishing of all nonlinearities.
It is also shown that for long pulses with $\tau \gg w_0$, the scattered field is dominated by the focusing of the beam while for short pulses ($\tau \ll w_0$) the scattered field is dominated by the longitudinal pulse shape.
Polarisation effects from heavier Standard Model particles like muons with mass $m_{mu} \approx 200m$ were neglected as this would correspond to a change in the critical field $E_{\text{cr}} \to 200E_{\text{cr}}$ and therefore these effects are heavily suppressed since all fields are normalised by this factor.
Corrections from scattering with even heavier particles like pions (which comprise a quark-anti-quark pair) or closed quark loops, were shown to be relevant only at much higher energy scales than considered in this thesis [FD08]. Therefore, considering effects of vacuum polarisation due to virtual electron-positron pairs should be a good approximation.

4.3.5 Measurability

The analysis of high harmonic generation showed that the probe develops a discontinuity as the shock-parameter $\nu_2 = 192\mu_2\mathcal{E}_s^3\mathcal{E}_p\Phi \approx 1$ in the parallel setup whereas in the perpendicular case the generation of the high frequency components was suppressed and also strongly sensitive to dispersion.
So in the ideal case one would consider six-photon scattering in the parallel setup (which is insensitive to the leading-order vacuum refractive index). The current highest electric field of a laser pulse produced in a laboratory is of the order $E = 3 \times 10^{-4} E_{\text{cr}}$ [Yan+08]. Assuming both probe and strong field are of this order of magnitude, $\nu_2 \sim E^4$ and the limit $\nu_2 \to 1$ would require extremely high pulse durations and/or frequencies. And as the coefficient $\mu_2 = \alpha/315\pi \ll 1$, it is clear that the shock regime is currently well out of the reach of optical laser-based experiments.

Vacuum induced electromagnetic shock waves are more likely to be important in astrophysical contexts like the the evolution of X-ray pulsars and strongly-magnetised neutron stars or "magnetars" [Maz+79; CCY92; HL03].
The surrounding magnetic fields of these objects are comparable to E_{cr} or even higher and are assumed to have a depth of 0.1-10 cm [HL06]. The current results were derived for a constant crossed field background, but can be generalised to a constant magnetic field, which should be a good approximation to the local field in strongly-magnetic pulsars, which is expected to be that of a dipole [HL06] on the stellar scale. But also there, the assumption of a completely homogeneous background is questionable and we have seen that VHHG is strongly sensitive to shape of the strong field.
In laser-based experiments, vacuum polarisation will more likely be measured as elastic photon-photon scattering [Men+06; Hei+06; Fer+07; TM10; KPK10; KDK10; KH11; MK11; Din+14b; Din+14a; HH14; GKS13; KS15] or lowest-order photon merging [BMS01; Lun+06; KK12; GKS14] . The current best experimental limits for photon-photon scattering in an all-optical laser setup [Ber+00] and in setups combining magnetic fields with resonant optical cavities [Zav+12; Cad+14] are still a few orders of magnitude above the QED prediction.

Chapter 5

Conclusions and Outlook

5.1 Conclusions

Many predictions of vacuum polarisation effects are obtained for constant, homogeneous backgrounds, but the analysis becomes difficult as soon as one considers fields that are non-uniform in space and time.

This thesis is dedicated to the study of the propagation of optical radiation in electromagnetic backgrounds where the photon wavelength is much shorter than the typical variation of the background. The main effects considered here are a probe-dependent refractive index experienced by the probe due to the background and the generation of higher harmonics.

After a short introduction to the notion of vacuum polarisation and a derivation of the Heisenberg-Euler Lagrangian in **chapter 2**, the simulational setup of two plane wave pulses, where a probe pulse collides with a strong "background", has been introduced and possible allowed processes for this setup in the case of weak fields have been discussed.

In **chapter 3**, the analytical, iterative solution to the wave equation in (1+1) dimensions for the electric field has been introduced. The first iteration has led to the dynamically-generated "overlap" signals that do not arise in standard scattering theory. Neglecting the back-reaction of the probe on the strong pulse, further iterations have been calculated and for six-photon scattering interpreted as processes that generate higher harmonics in the probe spectrum.
In the second part of the chapter, a numerical method has been adopted to solve the Maxwell equations that include the weak-field corrections from the Heisenberg-Euler Lagrangian. This allows, to the best of our knowledge, the first direct numerical time integration of the full quantum-modified Maxwell equations.

In **chapter 4**, both methods have been applied to pump-probe setups. In the first part, the strong background has been a pure Gaussian envelope and the time-resolved dynamics of the collision of both pulses has been studied. A complete analysis of all processes from four- and six-photon scattering that arise from the first iteration of the wave equation has been carried out with theory and simulation showing excellent agreement. The main effects here have been birefringence, harmonic generation and also the back reaction of the probe on the background. As the overlap signal can potentially dominate the asymptotic signal in the presence of inhomogeneities, the question of the validity of locally-constant-field-approximations arises and indicates the need of a more

careful analysis of their applicability.
The second part of this chapter then has been dedicated to the study of the influence of higher order processes. The strong pulse has been chosen to be a square pulse with vanishing frequency. For this setup with parallel pulse polarisations, the wave equation can be solved explicitly for four- and six-photon scattering and two analytical all-order-solutions for the scattered probe pulse has been derived. One leads to an integrated phase shift of the entire probe which originates from a linear refractive index independent of the probe field. The other one can be compactly written as a refractive index depending on the probe amplitude, leading to vacuum high harmonic generation in the interaction region. Based on the weak-field expansion of the Heisenberg-Euler model, the probe-dependent phase eventually leads to the development of a "shock" after a characteristic propagation length. The process of high harmonic generation turns out to be very sensitive to relative non-parallel polarisations and to dispersive effects similar to the problem of "phase-matching" in quantum optics.
In the last part of chapter 4, a brief outlook on ultra-short pulses and the study of high harmonic generation in inhomogeneous backgrounds based on the numerical method has been given. In the discussion, a comparison with plasma physics has been made and the validity of the approach using plane waves has been discussed.

5.2 Outlook

There are several experiments like PVLAS [PV] and the two upcoming ELI-NP [EL] and HIBEF [HI] experiments that are designed to finally measure real photon-photon scattering for the first time. Due to the smallness of the effect, extremely high intensities and/or large field extents are required and hence many experiments rely on tightly-focused lasers. We saw that in this case the assumption of plane waves becomes invalid and deviations are expected. Therefore, generalisations of the methods used in this thesis to more than $(1 + 1)$ dimensions are desirable to connect to these experiments. For the Green's function approach, this has already been done successfully by several authors, but only for the first iteration of the wave equation. The generalisation of the numerical method to higher dimensions has already been developed with the advantage to treat arbitrary pulse shapes and collision geometries which could be used to optimise experimental setups. A further improvement will demand the inclusion of real electron-positron pair-production, but up to now, no self-consistent model that includes dispersive and dissipative vacuum polarisation effects has been developed.

There have been many different proposals to measure vacuum polarisation over the last decades such that experimental data is much desired and needed. The experiments will help to confirm a more than 80 years old prediction considered untestable at the time when it was made. Additionally, the search can also lead to indicators of physics "Beyond the Standard Model". This could be the existence of new particles like "weakly interacting sub-eV/massive particles" (WISPs and WIMPs), axion-like particles or gauge bosons of a hidden $U(1)$-factor that extends the gauge group of the Standard Model. Therefore, independent of the observation of light-by-light scattering, such experiments will give insights, at least in terms of experimental bounds, on the existence of new physics.

Publications

This thesis is based on the following publications:

- **"Interaction of photons traversing a slowly varying electromagnetic background"**
  B. King, P. Böhl and H. Ruhl
  Phys. Rev. D 90 (6 2014) p. 065018
  DOI: 10.1103/PhysRevD.90.065018

- **"Vacuum high-harmonic generation in the shock regime"**
  P. Böhl, B. King, and H. Ruhl
  Phys. Rev. A 92 (2015), p. 032115
  DOI: 10.1103/PhysRevA.92.032115
  This article was selected as "Editors' Suggestion" in *Phys. Rev. A* and as "Research Highlight" in *Nature Photonics* in Nov. 2015 [Won15].
  Figure 16 was selected for "Kaleidoscope" in *Phys. Rev. A* in Sep. 2015:
  `https://journals.aps.org/pra/kaleidoscope/pra/92/3/032115`

- **"Vacuum high-harmonic generation in the shock regime and photon-photon scattering dynamics"**
  B. King, P. Böhl and H. Ruhl
  Journal of Physics: Conference Series 691.1 (2016), p. 012022
  URL: `http://stacks.iop.org/1742-6596/691/i=1/a=012022`

- **"Vacuum high-harmonic generation and electromagnetic shock"**
  P. Böhl, B. King and H. Ruhl
  Journal of Plasma Physics 82 (02 Apr. 2016). issn:1469-7807
  DOI: 10.1017/S0022377816000210

Other publications by the author not included in this thesis are:

- **"Particle-In-Cell simulation of laser irradiated two-component microspheres in 2 and 3 dimensions"**
  V. Pauw and T. M. Ostermayr and K.-U. Bamberg and P. Böhl and F. Deutschmann and D. Kiefer and C. Klier and N. Moschüring and H. Ruhl
  Nuclear Instruments and Methods in Physics Research Section A: Accelerators, Spectrometers, Detectors and Associated Equipment (2016), pp. . issn: 0168-9002
  DOI: 10.1016/j.nima.2016.02.012

Appendices

Appendix A

Conventions and Notation

A.1 Conventions

Apart from the second chapter with the derivation of the propagator for arbitrary quadratic Hamiltonians, Greek indices like μ, ν, α take values in $0, 1, 2, 3$. Small latin indices like i, j, k take the values $1, 2, 3$. The metric tensor is defined as

$$g^{\mu\nu} = g_{\mu\nu} = \mathrm{diag}(1, -1, -1, -1) \ . \tag{A.1}$$

Scalar products are then defined as $kx := g_{\mu\nu} k^\mu x^\mu = k^0 x^0 - \mathbf{k} \cdot \mathbf{x}$ with the Einstein summation convention that summation over repeated indices is implicit.
If not written explicitly, we chose natural units with $h = c = 1$.
The field strength or Faraday tensor is given by

$$F^{\mu\nu} = \begin{pmatrix} 0 & -E_1 & -E_2 & -E_3 \\ E_1 & 0 & -B_3 & B_2 \\ E_2 & B_3 & 0 & -B_1 \\ E_3 & -B_2 & B_1 & 0 \end{pmatrix} \ . \tag{A.2}$$

The dual field strength is defined as

$$\star F^{\mu\nu} = \frac{1}{2!} \epsilon^{\mu\nu\sigma\rho} F_{\sigma\rho} \ ,$$

where $\epsilon^{\mu\nu\sigma\rho}$ is total anti-symmetric in all indices with $\epsilon^{1234} = 1$. In components, $\star F^{\mu\nu}$ is given by

$$\star F^{\mu\nu} = \begin{pmatrix} 0 & -B_1 & -B_2 & -B_3 \\ B_1 & 0 & E_3 & -E_2 \\ B_2 & -E_3 & 0 & E_1 \\ B_3 & E_2 & -E_1 & 0 \end{pmatrix} \ . \tag{A.3}$$

The following identities hold:

$$F^{i0} = E^i \ , \qquad \star F^{i0} = B^i \ , \tag{A.4}$$

$$F^{ij} = -\varepsilon^{ijk} B^k \ , \qquad \star F^{ij} = \varepsilon^{ijk} E^k \ . \tag{A.5}$$

The field invariants are defined as

$$\mathcal{F} = -\frac{1}{4} F_{\mu\nu} F^{\mu\nu} = \frac{1}{2}(E^2 - B^2) \ ,$$

$$\mathcal{G} = -\frac{1}{4} F_{\mu\nu} \star F^{\mu\nu} = \mathbf{E} \cdot \mathbf{B} \ .$$

The secular invariants are then defined in terms of $\mathcal{F}$ and $\mathcal{G}$ as

$$a := \sqrt{\sqrt{\mathcal{F}^2 + \mathcal{G}^2} + \mathcal{F}} \,,$$
$$b := \sqrt{\sqrt{\mathcal{F}^2 + \mathcal{G}^2} - \mathcal{F}}$$

and satisfy

$$ab = \mathcal{G} \,, \tag{A.6}$$
$$a^2 - b^2 = 2\mathcal{F} \,. \tag{A.7}$$

A.2 List of Symbols

Chapter 1

$\mathbf{D}$, $\mathbf{H}$	Electric displacement and magnetising field, first appearing in (1.2).
$\mathbf{P}$, $\mathbf{M}$	Polarisation and magnetisation, appearing for the first time in (1.3) and (1.4), properly defined in in (1.15).
$\chi^{(n)}_{\mathrm{e,m}}$	n-th electric/magnetic susceptibility tensors, first appearing in (1.5).
$\hbar$, c	Planck's constant, speed of light in vacuum.
e^-, e^+	Electrons and positrons.
m, e	Mass of the electron and the charge of the electron is $-e < 0$.
E_{cr}, B_{cr}	Critical field strength defined in (1.6) and below (1.6).
λ_{C}	Compton wavelength of the electron define on Page 3
$\sigma_{\gamma\gamma}$	Cross section for light-by-light scattering, given by (1.7).
$\lambda\!\!\!^{-}_{\mathrm{C}}, t_{\mathrm{C}}$	Reduced Compton-wavelength and Compton-time defined on Page 3.
$F_{\mu\nu}$, $\star F_{\mu\nu}$	Electromagnetic field strength or Faraday Tensor defined in (A.2) and (A.3).
$g^{\mu\nu}$, $g_{\mu\nu}$	Minkowski metric defined in (A.1).
$\mathcal{F}$, $\mathcal{G}$	Electromagnetic field invariants defined in (1.14).
$J^{\mu}_{\mathrm{matter}}$	Matter four-current $J^{\mu}_{\mathrm{matter}} = (\rho_{\mathrm{matter}}, \mathbf{J}_{\mathrm{matter}})$ introduced on Page 5.
$\mathcal{L}_{\mathrm{MW}}$	Maxwell-Lagrangian $\mathcal{L}_{\mathrm{MW}}$ introduced on Page 5.
γ^{μ}	γ-matrices satisfying $\gamma^{\mu}\gamma^{\nu} + \gamma^{\mu}\gamma^{\nu} = 2g^{\mu\nu}$.
$\sigma^{\mu\nu}$	Spin matrices defined in (2.12).
D_{μ}, Π_{μ}	Covariant derivative defined on Page 5 and canonical momentum given by (2.13).
$\not{A}$	Feynman-slash notation with $\not{A} := \gamma^{\mu} A_{\mu}$.
Ψ, $\bar{\Psi}$	Dirac spinor and its Dirac conjugate with $\bar{\Psi} := \Psi^{\dagger}\gamma^0$
S_{QED}, $\mathcal{L}_{\mathrm{QED}}$	QED action and QED Lagrangian defined in (1.11) and (1.13).
$\mathcal{L}_{\mathrm{int}}(\mathcal{F}, \mathcal{G})$	Interaction Lagrangian for effective photon-photon interaction, explained on Page 6.

Chapter 2

$\phi(x)$	Scalar field satisfying the Klein-Gordon-equation (2.1).

∇, Δ	Nabla operator and Laplacian with $\Delta = \nabla^2$.
$\Box$	d'Alembert operator defined by $\Box := g^{\mu\nu}\partial_\mu\partial_\nu = \partial_t^2 - \Delta$.
$Z[j]$	Generating functional for n-point correlation functions in presence of a source j, defined in (2.2).
$W[j]$	Generating functional for the connected n-point correlation functions in presence of a source j, defined in (2.5).
$S_\mathrm{F}(x, x')$	Feynman propagator defined by (2.4).
$\Gamma[A]$, $\mathcal{L}_\mathrm{eff}$	Effective action and effective Lagrangian for the photon field, defined in (2.9) and (2.11).
$\mathcal{H}_\mathrm{pt}$	Proper-time Hamiltonian defined in (2.15).
$\mathcal{H}$	General quadratic Hamiltonian defined in (2.20) with constant metric G on phase space.
$\hat{X} := (\hat{x}, \hat{p})$	Coordinate operator $\hat{X} := (\hat{x}, \hat{p})$ on phase space consisting of the position operator $\hat{x}$ and position operator $\hat{p}$, defined on Page 17
$\langle , \rangle$	Standard Euclidean scalar product on $2n$-dimensional phase space defined in (2.21).
$\psi_y^t(x)$	Wave function of $\lvert\psi(y,t\rangle$ with $\psi_y^t(x) = \langle x\lvert\psi(y,t)\rangle$ and
$\lvert\psi(y,t)\rangle$	$\psi(y,t) := \mathrm{e}^{-i\mathcal{H}t}\lvert y\rangle$ is the time-evolved state of $\lvert y\rangle$ defined in (2.22).
$\hat{x}(t)$	Time-evolved operator $\hat{x}$ defined in (2.25).
Ω	Standard symplectic matrix given by (2.27).
$\mathbb{1}_n$	n-dimensional identity matrix.
$S^t := \mathrm{e}^{-t\Lambda}$	Symplectic flow defined in (2.36) and its generator Λ defined in (2.32).
S_i^t	Blocks of the symplectic flow S^t, defined in (2.40).
$f(y, S^t)$	Function used to define $\psi_y^t(x)$ in (2.45).
$N(S^t)$	Function to further refine the expression of $\psi_y^t(x)$ in (2.50) with
Φ_y^t	given by (2.51).
$N(S^t)$	Another function defined by (2.54) further refining $\psi_y^t(x)$.
a, b	Secular invariants defined in (B.15).
$\mathcal{L}_\mathrm{HE}$	Heisenberg-Euler Lagrangian given by (2.63), the $\mathcal{L}_\mathrm{eff}$ for constant fields with $F_{\mu\nu} = const.$
$\mathcal{L}_i$, μ_i	i-th term in the weak-field expansion (2.64) of $\mathcal{L}_\mathrm{HE}$ with coefficient μ_i given in (2.68).
C_i	Coefficients in the covariant nonlinear Maxwell equations (2.70) which are derived in App. C.3.
$\mathbf{J}[\mathbf{E}, \mathbf{B}]$	Vacuum current in the Maxwell equations (2.75) defined by (2.76) and (2.77).
$\mathbf{T}[\mathbf{E}, \mathbf{B}]$	Vacuum source term in the inhomogeneous wave equation (2.78) defined in (2.79).
$\mathbf{J}_i[\mathbf{E}, \mathbf{B}]$,	Source terms for the ith-order weak-field expansion, defined in
$\mathbf{T}_i[\mathbf{E}, \mathbf{B}]$	(2.80).
$\mathbf{M}_i, \mathbf{P}_i$	Magnetisation and polarisation for the ith-order weak-field expansion, defined in (2.81).
x^+, x^-	Light cone coordinates defined on Page 27.
$\mathbf{E}_p^{(0)}(x^-)$	Analytic expression for the initial electric field of the probe pulse given by (2.82).
$\boldsymbol{\varepsilon}_p$, ω_p, k_p, τ_p	Polarisation vector, carrier frequency, wave vector of the probe and probe pulse duration, defined on Page 27.
$E_p^{(0)}(x^-)$,	Amplitude function and envelope function of the probe pulse de-
$f_p(x^-)$	fined on Page 27.

φ_p	Lorentz-invariant phase of the probe pulse, introduced Page 27.
$\mathbf{E}_s^{(0)}(x^+)$	Analytic expression for the initial strong pulse given by (2.84).
$\boldsymbol{\varepsilon}_s$, ω_s, k_s, τ_s	Polarisation vector, carrier frequency, wave vector of the strong pulse and pulse duration, defined on Page 27.
$E_s^{(0)}(x^+)$, $f_s(x^+)$	Amplitude function and envelope function of the strong pulse defined on Page 27.
φ_s	Lorentz-invariant phase of the probe pulse, introduced Page 27.
$\mathbf{B}_{p,s}^{(0)}$	Initial magnetic fields of the pulses given by (2.87).

Chapter 3

$\mathbf{E}^{(n)}$, $\mathbf{E}_p^{(n)}$, $\mathbf{E}_s^{(n)}$	Iterative solution to the wave equation for the electric field (3.3), where n is the iteration index given by (3.5). In general, upper right indices in parentheses indicate iterated quantities.
$\Delta\mathbf{E}^{(n+1)}(t,z)$	Nonlinear correction in the iterative solution containing the inhomogeneity of the wave equation, defined in (3.6).
$G_R(t,z)$	Retarded Green's function for the wave equation defined in (3.7).
$\mathbf{T}^{(n)}(t,z)$	Source term for the wave equation depending on the nth iteration of the electric field, defined in (3.8).
$\mathbf{J}^{(n)}(t,z)$	Current in Maxwell equations and the integrated version of the iterated wave equation, depending on the nth iterated fields, defined in (3.9).
$\Delta\mathbf{E}^{(n)}(x^-,x^+)$	Iterated electric field with arguments transformed to light cone coordinates. Defined in (3.12).
$\Delta\overrightarrow{\mathbf{E}}^{(n)}(x^-,x^+)$	Forward or right scattered field defined in (3.14).
$\Delta\overleftarrow{\mathbf{E}}^{(n)}(x^-,x^+)$	Backward- or left scattered field defined in (3.15).
$\mathbf{P}^{(n)}$, $\mathbf{M}^{(n)}$	Polarisation and magnetisation which depend on the nth iteration of the fields, defined on Page 38.
$\Delta\overrightarrow{\mathbf{E}}_{\text{as}}^{(n)}(x^-)$	Asymptotic forward scattered field defined by (3.18).
$\Delta\overleftarrow{\mathbf{E}}_{\text{as}}^{(n)}(x^+)$	Asymptotic backward scattered fields defined by (3.18).
$\mathbf{U}^{(n)}$, $\mathbf{V}^{(n)}$	Vectorial functions appearing in the asymptotic forward and backward scattered fields, defined in (3.22) and (3.23).
$\Delta\mathbf{E}_{\text{o}}^{(n+1)}$	Overlap field defined in (3.24).
σ, ρ	Geometric factors depending on the relative polarisations of the probe and strong pulse, defined in (3.28) and (3.29).
$\mathbf{P}_1$, $\mathbf{M}_1$	Polarisation and magnetisation for the box diagram, defined in (3.33) and (3.34).
$\mathbf{P}_i^{(n)}$, $\mathbf{M}_i^{(n)}$	Polarisation and magnetisation for the ith term in the weak-field expansion, depends on the n-th iteration of the electric and magnetic fields. In general, lower right indices refer to the order of the weak-field expansion in this chapter.
$\mathbf{u}_1, \mathbf{v}_1$	Constant polarisation vectors for $\mathbf{U}_1$ and $\mathbf{V}_1$ defined in (3.37) and (3.38).
$\mathbf{u}_i, \mathbf{v}_i$	Constant polarisation vectors for $\mathbf{U}_i$ and $\mathbf{V}_i$.
$'$	A prime indicates the derivative with respect to x^-.
$o_i(x), p_i(x), q_i(x)$	Integrals over certain powers of the strong pulse defined for the box diagram in (3.48) and in (3.51) for the hexagon diagram.
$\mathbf{Q}$, $\mathbf{X}$, $\mathbf{Y}$	Matrices appearing in the numerical formulation of Maxwell's equations defined on Page 47.

$\mathbf{f}$	Vector consisting of the electric and magnetic fields, defined on Page 47.
$\mathbf{u}$	Electric and Magnetic fields in the eigenbasis of $\mathbf{Q}$, defined in (3.56).
$\mathbf{S}$	Transformation matrix between $\mathbf{f}$ and $\mathbf{u}$, defined in (3.56).
$\mathbf{\Lambda}$	Diagonal matrix with the eigenvalues λ_i of $\mathbf{Q}$, defined on Page 47.
$\tilde{\mathbf{u}}$	Discretised version of $\mathbf{u}$ on the grid. In general, tilde indicate the discretised quantities on the numerical grid.
L, N, Δz	Box-length, number of grid points and spacing on the grid, introduced on Page 47.
$\mathbf{g}[\tilde{\mathbf{u}}, t]$	Right-hand side function of the ODEs in the numerical method, introduced on Page 47.
$\mathbf{X}^l$, $\mathbf{Y}^l$	The values of $\mathbf{X}$ and $\mathbf{Y}$ at grid point l, see Page 47.
$\mathbf{G}$, $\mathbf{H}^l$	Matrices to factorise $\mathbb{1}_4 + \mathbf{X}^l$, defined in (3.57).
$\widehat{\mathbf{E}}_p(\omega)$	Fourier transform of the probe field, defined in (3.61).
$I_p^{(0)}(\omega_p)$	Intensity of the initial probe, defined in (3.62).
$I_p(\omega)$	Intensity spectrum of the forward-scattered probe field, defined in (3.63).

Chapter 4

$\Delta\mathbf{E}^{\parallel}$, $\Delta\mathbf{E}^{\perp}$	Components of the nonlinear field response in the parallel ($\boldsymbol{\varepsilon}_p \cdot \boldsymbol{\varepsilon}_s = 1$) and in the perpendicular ($\boldsymbol{\varepsilon}_p \cdot \boldsymbol{\varepsilon}_s = 0$) setup, introduced on Page 52.
$\Delta\mathbf{E}_{i,\mathrm{as},\omega}(x^-, x^+)$	Nonlinear asymptotic scattered field of the ith weak-field expansion with a frequency ω, first used in (4.2).
$\Delta\mathbf{E}_{i,\mathrm{o},\omega}(x^-, x^+)$	Nonlinear overlap field, first used in (4.1).
$\Delta\mathbf{E}_{i,\mathrm{d},\omega}(x^-, x^+)$	Nonlinear field from a derivative function, i is again the order of the weak-field expansion and ω the frequency of the signal.
$\delta\mathsf{n}_1$	Non-trivial refractive index from four-photon scattering in constant crossed backgrounds, defined in (4.3).
$\delta\varphi_p$	Phase-shift due to $\delta\mathsf{n}_1$ introduced on Page 54.
$\delta\varphi_{p,\mathrm{o}}$	Phase shift due to the overlap signal, given by (4.7).
ζ	Nonlinearity parameter for the overlap signal, defined by (4.14).
χ	Quantum efficiency parameter, defined by (4.15).
Φ	Propagation length introduced on Page 67.
$\mathrm{Rect}(x^+)$	Rectangular function, defined on Page 71.
$\mathrm{FD}(x^+)$	Mirrored Fermi-Dirac-potential defined in (4.24).
$\upsilon_1^{\parallel,\perp}$	Multi-scale-parameter for four-photon scattering defined in (4.28).
υ_2	Shock parameter for six-photon scattering which includes the probe envelope function $f_p(x^-)$, defined on Page 74 with
ν_2	Pure shock parameter for six-photon scattering, defined in (4.31).
$J_l(\cdot)$	lth order Bessel function of the first kind, introduced on Page 75.
$u_{\mathrm{BF}}(t, z)$	Bessel-Fubini solution to Burger's equation, defined in (4.33).
ν_{BF}	Normalised propagation distance appearing in the Bessel-Fubini solution (4.33).
ν_1	Shock parameter for chained four-photon scattering to generate a second harmonic, defined in (4.34).
ν_3	Shock parameter for eight-photon scattering, defined of Page 78.
$a_j(\nu)$	Coefficients appearing in the all-order solution (4.32), defined in (4.37).

$\gamma(\nu)$	Variable exponent in the intensity of the harmonics, introduced in (4.39).
$\delta\mathsf{n}_2$	Non-trivial refractive index from six-photon scattering, defined in (4.43).
$\mathbf{E}_p^{\text{even}}$, $\mathbf{E}_p^{\text{odd}}$	Even and odd frequency components of (4.32), defined in (4.46)
E_{square}, E_{saw}	Square and Saw-tooth function, defined in (4.47).
θ_0	Diffraction angle for a Gaussian pulse, defined in (4.50).
l	Diffraction parameter for a Gaussian pulse, defined in (4.51).
w_0	Width of the Gaussian pulse in the transverse plane, introduced on Page 101.

Appendix B

Details for the HE Lagrangian

B.1 Uniqueness of Flows on a Manifold

We want to show that (cf. (2.34) and (2.35))

$$\mathrm{e}^{-it\mathcal{H}}\hat{X}\mathrm{e}^{it\mathcal{H}} = S^t\hat{X} \ . \tag{B.1}$$

Now both sides of (B.1) define a flow, where a flow on a manifold M is a map

$$\varphi : \mathbb{R} \times M \to M$$

such that

$$\begin{aligned} \varphi(0,p) &= p \ , \\ \varphi(t,\phi(s,p)) &= \varphi(t+s,p) \ . \end{aligned}$$

Suppose we have two flows φ_1 and φ_2 and their derivatives at the origin are identical:

$$\frac{\mathrm{d}}{\mathrm{d}t}\varphi_1(t,p)\Big|_{t=0} = \frac{\mathrm{d}}{\mathrm{d}t}\varphi_2(t,p)\Big|_{t=0} \quad \forall p \in M \ .$$

Then it follows that both flows are identical, $\varphi_1 \equiv \varphi_2$.
In order to prove this, we first want to show that every flow φ satisfies an ordinary differential equation of the form

$$\frac{\mathrm{d}}{\mathrm{d}t}\varphi(t,p) = X(\varphi(t,p)) \ ,$$

which is not automatic since X could also be dependent on t and p. If we define X through

$$X(p) := \frac{\mathrm{d}}{\mathrm{d}t}\varphi(t,p)|_{t=0}$$

we have

$$\begin{aligned} \frac{\mathrm{d}}{\mathrm{d}t}\varphi(t,p) &= \frac{\mathrm{d}}{\mathrm{d}s}\varphi(t+s,p)\Big|_{s=0} \\ &= \frac{\mathrm{d}}{\mathrm{d}s}\varphi(s,\varphi(t,p))\Big|_{s=0} \\ &= X(\varphi(t,p)) \ , \end{aligned}$$

which is what we wanted to show. Now we see that for a fixed point $p \in M$, we have an ordinary differential equation with initial condition $\varphi(0,p) = p$. Since the differential equation is completely specified by X, which is the derivative at $t = 0$, we have shown that if $X_1(p) = X_2(p)$ for arbitrary p, then $\varphi_1 = \varphi_2$ which follows from the uniqueness of the solution to ordinary differential equations [CA92]. And since we have (cf. (2.37))

$$\frac{\mathrm{d}}{\mathrm{d}t}\varphi_2(t,\hat{X})\Big|_{t=0} = -i[\mathcal{H},\hat{X}] = \frac{\mathrm{d}}{\mathrm{d}t}\varphi_1(t,\hat{X})\Big|_{t=0} \tag{B.2}$$

(B.1) follows.

B.2 Relations Between the Matrix Blocks of S^t

We want to obtain certain relations of the symplectic flow (2.36) $S^t = \mathrm{e}^{-t\Lambda}$ where $\Lambda = \Omega^{-1}G$. Since Λ is an element of $sp(2n)$, $S^t = \mathrm{e}^{-t\Lambda}$ is a symplectic matrix where the defining property of the symplectic group $Sp(2n)$ is leaving the standard skew-symmetric matrix Ω invariant:

$$P^T\Omega P = \Omega \tag{B.3}$$

for $P \in Sp(2n)$. We will denote the $n \times n$-blocks of S^t as

$$S^t =: \begin{pmatrix} S_1^t & S_2^t \\ S_3^t & S_4^t \end{pmatrix} .$$

The relation (B.3) gives the following conditions on the blocks S_i^t:

$$\begin{aligned} (S_3^t)^T S_1^t &= (S_1^t)^T S_3^t \ , \\ (S_4^t)^T S_2 &= (S_2^t)^T S_4^t \ , \\ (S_1^t)^T S_4^t - (S_3^t)^T S_2^t &= \mathbb{1}_n \ , \\ (S_4^t)^T S_1^t - (S_2^t)^T S_3^t &= \mathbb{1}_n \ . \end{aligned}$$

The transpose of (B.3) yields the other relations

$$\begin{aligned} S_1^t (S_2^t)^T &= S_2^t (S_1^t)^T \ , \\ S_3^t (S_4^t)^T &= S_4^t (S_3^t)^T \ , \\ S_1^t (S_4^t)^T - S_2^t (S_3^t)^T &= \mathbb{1}_n \ , \\ S_4^t (S_1^t)^T - S_3^t (S_2^t)^T &= \mathbb{1}_n \ . \end{aligned} \tag{B.4}$$

Using these relations one can easily write down the inverse matrix

$$(S^t)^{-1} = S^{-t} = \begin{pmatrix} S_1^{-t} & S_2^{-t} \\ S_3^{-t} & S_4^{-t} \end{pmatrix} = \begin{pmatrix} (S_4^t)^T & -(S_2^t)^T \\ (-S_3^t)^T & (S_1^t)^T \end{pmatrix}$$

from which it follows that

$$\begin{aligned} S_1^{-t} &= (S_4^t)^T \ , & S_2^{-t} &= -(S_2^t)^T \ , \\ S_3^{-t} &= (S_3^t)^T \ , & S_4^{-t} &= -(S_1^t)^T \ . \end{aligned} \tag{B.5}$$

B.3 Proof of $R(S^t) = 1\ \forall t$

In the derivation of the propagator for an arbitrary Hamiltonian, we were able to derive the explicit form up to an unknown function $R(S^t)$ which appears in (2.54). In the following we will show that $R(S^t) = 1\ \forall t$ by demanding that the solution must satisfy explicitely the Schrödinger equation.
In terms of $R(S^t)$ the unitarity condition (2.46) becomes

$$R(S^{-t}) = \overline{R(S^t)}$$

from which we infer

$$R(S^t)R(S^{-t}) = R(S^t)\overline{R(S^t)} = R(1) = 1$$

and therefore

$$|R(S^t)| = 1\ .$$

So $R(S^t)$ is only a phase. To finally fix this phase, we now require

$$\left(\frac{\mathrm{d}}{\mathrm{d}t} + i\mathcal{H}\right)\psi_y^t(x) = 0\ .$$

The time-derivative of $\psi_y^t(x)$ will contribute a term involving a trace as the derivative of a determinant of one-parameter family of matrices $A(t)$ is given by [Bel97]

$$\frac{\mathrm{d}}{\mathrm{d}t}\det A(t) = \det A(t)\,\mathrm{Tr}\left(A^{-1}(t)\frac{d}{dt}A(t)\right)\ . \tag{B.6}$$

Since $\psi_y^t(x)$ is a solution to the Schrödinger equation by construction, it is enough to compare this term to the trace part stemming from $i\mathcal{H}\psi_y^t(x)$ to finally fix $R(S^t)$.
Therefore, we need

$$\begin{aligned}\frac{\mathrm{d}}{\mathrm{d}t}S_2^t &= \left(\frac{\mathrm{d}}{\mathrm{d}t}S^t\right)_2 \\ &= -\left(\mathrm{e}^{-\Lambda t}\Lambda\right)_2 \\ &= -\left(S^t\Lambda\right)_2\end{aligned}$$

and so

$$\begin{aligned}\left(S_2^t\right)^{-1}\frac{\mathrm{d}}{\mathrm{d}t}S_2^t &= -(S_2^t)^{-1}(S_1^t\Lambda_2 + S_2^t\Lambda_4) \\ &= -(S_2^t)^{-1}S_1^t\Lambda_2 - \Lambda_4\ .\end{aligned}$$

Inserting these relations into (B.6) gives

$$\frac{\mathrm{d}}{\mathrm{d}t}(\det S_2^t)^{-1/2} = \frac{1}{2}(\det S_2^t)^{-1/2}\,\mathrm{Tr}\left[(S_2^t)^{-1}S_1^t\Lambda_2 + \Lambda_4\right]\ . \tag{B.7}$$

Now we look for this expression from $i\mathcal{H}\psi_y^t(x)$. We started with a Hamiltonian (2.20) such that

$$\mathcal{H} = \frac{1}{2}\left(\langle x, G_1 x\rangle + \langle x, G_2 p\rangle + \langle p, G_3 x\rangle + \langle p, G_4 p\rangle\right)\ .$$

Now Λ is defined as $\Lambda = \Omega^{-1}G$ and therefore the components are related by

$$\Lambda = \begin{pmatrix} \Lambda_1 & \Lambda_2 \\ \Lambda_3 & \Lambda_4 \end{pmatrix} = \begin{pmatrix} G_3 & G_4 \\ -G_1 & -G_2 \end{pmatrix} .$$

There are two trace-terms in $\mathcal{H}$. The first one is

$$\begin{aligned} \frac{i}{2}\langle p, G_3 x\rangle &= \frac{1}{2}\operatorname{Tr} G_3 + \frac{i}{2}\langle G_3 x, p\rangle \\ &= \frac{1}{2}\operatorname{Tr} G_2 + \frac{i}{2}\langle G_3 x, p\rangle \\ &= -\frac{1}{2}\operatorname{Tr}\Lambda_4 + \frac{i}{2}\langle G_3 x, p\rangle , \end{aligned}$$

where we used $[x^i, p_j] = i\delta^i_j$ and that G as a metric is symmetric and therefore $G_2 = G_3$. The second term stems from $\langle p, p\rangle$, therefore we need the spatial derivatives of $\varphi^t_y(x)$:

$$\begin{aligned} \frac{\partial}{\partial x^j}\exp\Big[-\frac{i}{2}\langle y, S^t_4 (S^t_2)^{-1} y\rangle - \frac{i}{2}\langle x, (S^t_2)^{-1} S^t_1 x\rangle + i\langle (S^t_2)^{-1} y, x\rangle\Big] \\ = \exp[\,]\Big(-i\left((S^t_2)^{-1} S^t_1 x\right) + i\left((S^t_2)^{-1} y\right)\Big)_j . \end{aligned}$$

The second derivative is then given by

$$\begin{aligned} &\frac{\partial^2}{\partial x^j x^k}\exp\Big[-\frac{i}{2}\langle y, S^t_4 (S^t_2)^{-1} y\rangle - \frac{i}{2}\langle x, (S^t_2)^{-1} S^t_1 x\rangle + i\langle (S^t_2)^{-1} y, x\rangle\Big] \\ &= -\exp[\,]\Big[\Big(\left((S^t_2)^{-1} S^t_1 x\right) - \left((S^t_2)^{-1} y\right)\Big)_k \Big(\left((S^t_2)^{-1} S^t_1 x\right) - \left((S^t_2)^{-1} y\right)\Big)_j + i\left((S^t_2)^{-1} S^t_1\right)_{jk}\Big] \end{aligned}$$

and so

$$\begin{aligned} \frac{i}{2}\langle p, G_4 p\rangle &= \frac{i}{2}\exp[\,]\langle \left((S^t_2)^{-1} S^t_1 x\right) - \left((S^t_2)^{-1} y\right), G_4\left((S^t_2)^{-1} S^t_1 x\right) - \left((S^t_2)^{-1} y\right)\rangle \\ &\qquad - \frac{1}{2}\operatorname{Tr}\big(G_4 (S^t_2)^{-1} S^t_1\big) \\ &= \frac{i}{2}\exp[\,]\langle \left((S^t_2)^{-1} S^t_1 x\right) - \left((S^t_2)^{-1} y\right), \Lambda_2\left((S^t_2)^{-1} S^t_1 x\right)\big) - \left((S^t_2)^{-1} y\right)\rangle \\ &\qquad - \frac{1}{2}\operatorname{Tr}\big(\Lambda_2 (S^t_2)^{-1} S^t_1\big) . \end{aligned} \tag{B.8}$$

Using the cyclicity of the trace, it follows from (B.8) and (B.7) that $R(S^t)$ is independent of t and therefore

$$R(S^t) = 1 \quad \forall t \quad .$$

B.4 Symplectic Flow for Constant Electromagnetic Fields

To derive the Heisenberg-Euler Lagrangian as a special case of the propagator for arbitrary Hamiltonians, we need the blocks of the symplectic flow $S^t = \mathrm{e}^{-t\Lambda}$ where $\Lambda = \Omega^{-1}G$

is given by (see (2.57))

$$\begin{aligned}\Lambda = \Omega^{-1}G &= \begin{pmatrix} 0 & \mathbb{1}_4 \\ -\mathbb{1}_4 & 0 \end{pmatrix} \begin{pmatrix} \tilde{F}^T g^{-1}\tilde{F} & \tilde{F}^T g^{-1} \\ g^{-1}\tilde{F} & g^{-1} \end{pmatrix} \\ &= \begin{pmatrix} g^{-1}\tilde{F} & g^{-1} \\ -\tilde{F}^T g^{-1}\tilde{F} & -\tilde{F}^T g^{-1} \end{pmatrix} \\ &= \begin{pmatrix} g^{-1}\tilde{F} & g^{-1} \\ \tilde{F}g^{-1}\tilde{F} & \tilde{F}g^{-1} \end{pmatrix} ,\end{aligned}$$

where $\tilde{F} := \frac{e}{2}F$. To calculate the symplectic flow (2.36), we observe

$$\Lambda^2 = 2 \begin{pmatrix} (g^{-1}\tilde{F})^2 & (g^{-1}\tilde{F})g^{-1} \\ \tilde{F}(g^{-1}F)^2 & (\tilde{F}g^{-1})^2 \end{pmatrix}$$

and in general we have

$$\Lambda^n = 2^{n-1} \begin{pmatrix} (g^{-1}\tilde{F})^n & (g^{-1}\tilde{F})^{n-1}g \\ \tilde{F}(g^{-1}\tilde{F})^n & (\tilde{F}g^{-1})^n \end{pmatrix} .$$

Therefore:

$$S^t = \exp(-t\Lambda) = \begin{pmatrix} \mathbb{1} & 0 \\ 0 & \mathbb{1} \end{pmatrix} + \sum_{n=1}^{\infty} \frac{(-t)^n}{n!} 2^{n-1} \begin{pmatrix} (g^{-1}\tilde{F})^n & (g^{-1}\tilde{F})^{n-1}g^{-1} \\ \tilde{F}(g^{-1}\tilde{F})^n & (\tilde{F}g^{-1})^n \end{pmatrix}$$

with

$$\begin{aligned} S_1^t &= \mathbb{1} + \frac{1}{2}\sum_{n=1}^{\infty} \frac{(-2t)^n}{n!}(g^{-1}\tilde{F})^n \\ &= \frac{1}{2}\left(\mathbb{1} + \sum_{n=0}^{\infty} \frac{(-2t)^n}{n!}(g^{-1}\tilde{F})^n\right) \\ &= \frac{1}{2}\left(\mathbb{1} + \exp\left(-2tg^{-1}\tilde{F}\right)\right) \\ &= \exp\left(-tg^{-1}\tilde{F}\right)\cosh\left(g^{-1}\tilde{F}\right) , \end{aligned}$$

$$\begin{aligned} S_2^t &= \frac{1}{2}\sum_{n=1}^{\infty} \frac{(-2t)^n}{n!}(g^{-1}\tilde{F})^{n-1}g^{-1} \\ &= \frac{1}{2}\left(\sum_{n=1}^{\infty} \frac{(-2t)^n}{n!}(g^{-1}F)^n\right)\tilde{F}^{-1} \\ &= \frac{1}{2}\left(\exp\left(-2tg^{-1}\tilde{F}\right) - \mathbb{1}\right)\tilde{F}^{-1} \\ &= -\exp\left(-tg^{-1}\tilde{F}\right)\sinh\left(tg^{-1}\tilde{F}\right)\tilde{F}^{-1} \end{aligned} \tag{B.9}$$

and by observing that

$$\tilde{F}((g^{-1}\tilde{F})^{n-1}g^{-1})\tilde{F} = \tilde{F}(g^{-1}\tilde{F})^n \ ,$$
$$\tilde{F}((g^{-1}\tilde{F})^n)\tilde{F}^{-1} = (\tilde{F}g^{-1})^n$$

one finds

$$S_3^t = \tilde{F}S_2^t\tilde{F} \ ,$$
$$S_4^t = \tilde{F}S_1^t\tilde{F}^{-1} \ .$$

So we know from (B.9) we know that

$$S_2^t = -\sinh\Big(g^{-1}\tilde{F}t\Big)\exp\Big(-g^{-1}\tilde{F}t\Big)\tilde{F}^{-1} \ .$$

Therefore, the inverse is given by

$$\begin{aligned}(S_2^t)^{-1} &= -\tilde{F}\exp\Big(g^{-1}\tilde{F}t\Big)\sinh\Big(g^{-1}\tilde{F}t\Big)^{-1} \\ &= -\tilde{F}(\sinh\Big(g^{-1}\tilde{F}t\Big) + \cosh\Big(g^{-1}\tilde{F}t\Big))\sinh\Big(g^{-1}\tilde{F}t\Big)^{-1} \\ &= -\tilde{F}\left(1+\coth\Big(g^{-1}\tilde{F}t\Big)\right) \ . \end{aligned} \tag{B.10}$$

To calculate the propagator, we need the following matrix products:

$$\begin{aligned}S_4^t(S_2^t)^{-1} &= -\tilde{F}\cosh\Big(g^{-1}\tilde{F}t\Big)\exp\Big(-g^{-1}\tilde{F}t\Big)\tilde{F}^{-1}\tilde{F}\exp\Big(g^{-1}\tilde{F}\Big)\sinh\Big(g^{-1}\tilde{F}t\Big)^{-1} \\ &= -\tilde{F}\coth\Big(g^{-1}\tilde{F}t\Big) \ , \end{aligned}$$

$$\begin{aligned}(S_2^t)^{-1}S_1^t &= -\tilde{F}\exp\Big(g^{-1}\tilde{F}t\Big)\sinh\Big(g^{-1}\tilde{F}t\Big)^{-1}\cosh\Big(g^{-1}\tilde{F}t\Big)\exp\Big(-g^{-1}\tilde{F}t\Big) \\ &= -\tilde{F}\coth\Big(g^{-1}\tilde{F}t\Big) \ . \end{aligned}$$

So for the exponential in (2.55) we have

$$\begin{aligned}\Phi_y^t(x) &= \exp\Big[\frac{i}{2}\Big(\langle y,\tilde{F}\coth\Big(g^{-1}\tilde{F}t\Big)y\rangle + \langle x,\tilde{F}\coth\Big(g^{-1}\tilde{F}t\Big)x\rangle \\ &\qquad - 2\langle\tilde{F}y,x\rangle - 2\langle\tilde{F}\coth\Big(g^{-1}\tilde{F}t\Big)y,x\rangle\Big)\Big] \\ &= \exp\Big[\frac{i}{2}\langle(y-x),\tilde{F}\coth\Big(g^{-1}\tilde{F}t\Big)(y-x)\rangle - i\langle x,\tilde{F}y\rangle\Big)\Big] \ , \end{aligned} \tag{B.11}$$

where we used that $\tilde{F}\coth\Big(g^{-1}\tilde{F}t\Big)$ is symmetric. From (B.11) we infer that $\Phi(x,x)=0$ since $\tilde{F}$ is antisymmetric.

B.5 $\det\exp\big(-g^{-1}Ft\big)$ and $\det\big(\frac{e}{2}F/\sinh\big(\frac{e}{2}g^{-1}Ft\big)\big)$

To finally calculate the Heisenberg-Euler Lagrangian, we saw from (2.59) that we need the two quantities $\det\exp\big(-g^{-1}Ft\big)$ and $\det\big(\frac{e}{2}F/\sinh\big(\frac{e}{2}g^{-1}Ft\big)\big)$ which we now calculate. If we define an operator

$$M^t := \exp\big(g^{-1}Ft\big)$$

it follows that

$$(M^t)^T = M^{-t} = (M^t)^{-1}$$

and therefore

$$(\det M^t)^2 = 1 \ .$$

Since M is path-wise connected to the identity and the determinant in continuous in t, we have

$$\det M^t = 1 \ .$$

To calculate the object

$$\det \sinh \frac{e}{2} g^{-1} F t \tag{B.12}$$

we need the eigenvalues of

$$g^{-1}F = \begin{pmatrix} 0 & E_x & E_y & E_z \\ E_x & 0 & -B_z & B_y \\ E_y & B_z & 0 & -B_x \\ E_z & -B_y & B_x & 0 \end{pmatrix} \ . \tag{B.13}$$

We need the characteristic polynomial which is given by

$$\begin{aligned} P(\lambda) = &-\lambda \begin{pmatrix} -\lambda & -B_z & B_y \\ B_z & -\lambda & -B_x \\ -B_y & B_x & -\lambda \end{pmatrix} - E_x \det \begin{pmatrix} E_x & -B_z & B_y \\ E_y & -\lambda & -B_x \\ E_z & B_x & -\lambda \end{pmatrix} \\ &+ E_y \begin{pmatrix} E_x & -\lambda & B_y \\ E_y & B_z & -B_x \\ E_z & -B_y & -\lambda \end{pmatrix} - E_z \begin{pmatrix} E_x & -\lambda & -B_z \\ E_y & B_z & -\lambda \\ E_z & -B_y & B_x \end{pmatrix} \ . \end{aligned}$$

The subdeterminants are given by

$$\begin{aligned} &\det \begin{pmatrix} -\lambda & -B_z & B_y \\ B_z & -\lambda & -B_x \\ -B_y & B_x & -\lambda \end{pmatrix} \\ &= -\lambda(\lambda^2 + B_x^2) + B_z(-B_z\lambda - B_xB_y) + B_y(B_zB_x - \lambda B_y) \\ &= -\lambda^3 + \lambda(-B_x^2 - B_z^2 - B_y^2) \\ &= -\lambda(\lambda^2 + B_x^2 + B_y^2 + B_z^2) \\ &= -\lambda(\lambda^2 + |\mathbf{B}|^2) \ , \end{aligned}$$

$$\begin{aligned} &\det \begin{pmatrix} E_x & -B_z & B_y \\ E_y & -\lambda & -B_x \\ E_z & B_x & -\lambda \end{pmatrix} \\ &= E_x(\lambda^2 + B_x^2) + B_z(-E_y\lambda + B_xE_z) + B_y(E_yB_x + \lambda E_z) \\ &= \lambda^2 E_x + \lambda(-E_yB_z + E_zB_y) + E_xB_x^2 + E_zB_xB_z + E_yB_xB_y \\ &= \lambda^2 E_x + \lambda(-E_yB_z + E_zB_y) + B_x(E_xB_x + E_zB_z + E_yB_y) \\ &= \lambda^2 E_x + \lambda(-E_yB_z + E_zB_y) + B_x(\mathbf{E}\cdot\mathbf{B}) \ , \end{aligned}$$

$$
\begin{aligned}
&\det \begin{pmatrix} E_x & -\lambda & B_y \\ E_y & B_z & -B_x \\ E_z & -B_y & -\lambda \end{pmatrix} \\
&= E_x(-\lambda B_z - B_x B_y) + \lambda(-\lambda E_y + B_x E_z) + B_y(-E_y B_y - E_z B_z) \\
&= -\lambda^2 E_y + \lambda(-E_x B_z + B_x E_z) - E_x B_x B_y - E_y B_y B_y - B_y E_z B_z \\
&= -\lambda^2 E_y + \lambda(-E_x B_z + B_x E_z) - B_y(\mathbf{E}\cdot\mathbf{B}) \ ,
\end{aligned}
$$

$$
\begin{aligned}
&\det \begin{pmatrix} E_x & -\lambda & -B_z \\ E_y & B_z & -\lambda \\ E_z & -B_y & B_x \end{pmatrix} \\
&= E_x(B_z B_x - \lambda B_y) + \lambda(E_y B_x + \lambda E_z) - B_z(-E_y B_y - E_z B_z) \\
&= \lambda^2 E_z + \lambda(E_y B_x - E_x B_y) + B_z(\mathbf{E}\cdot\mathbf{B}) \ .
\end{aligned}
$$

Therefore:

$$
\begin{aligned}
P(\lambda) &= \lambda^2(\lambda^2 + |\mathbf{B}|^2) - E_x(\lambda^2 E_x + \lambda(-E_y B_z + E_z B_y) + B_x(\mathbf{E}\cdot\mathbf{B})) \\
&\quad + E_y(-\lambda^2 E_y + \lambda(-E_x B_z + B_x E_z) - B_y(\mathbf{E}\cdot\mathbf{B})) \\
&\quad - E_z(\lambda^2 E_z + \lambda(E_y B_x - E_x B_y) + B_z(\mathbf{E}\cdot\mathbf{B})) \\
&= \lambda^4 + \lambda^2(|\mathbf{B}|^2 - |\mathbf{E}|^2) + \lambda(\mathbf{E}\cdot\mathbf{E}\wedge\mathbf{B}) - (\mathbf{E}\cdot\mathbf{B})^2 \\
&= \lambda^4 + \lambda^2(|\mathbf{B}|^2 - |\mathbf{E}|^2) - (\mathbf{E}\cdot\mathbf{B})^2 \\
&= \lambda^4 - 2\lambda^2\mathcal{F} - \mathcal{G}^2
\end{aligned}
$$

and the eigenvalues of $g^{-1}F$ are therefore given by

$$
\begin{aligned}
\lambda_{F,1} &= \sqrt{\mathcal{F} - \sqrt{\mathcal{F}^2 + \mathcal{G}^2}} \qquad & \lambda_{F,2} &= -\lambda_{F,1} \ , \\
\lambda_{F,3} &= \sqrt{\mathcal{F} + \sqrt{\mathcal{F}^2 + \mathcal{G}^2}} \qquad & \lambda_{F,4} &= -\lambda_{F,3} \ .
\end{aligned}
\tag{B.14}
$$

Now we express the eigenvalues using the secular invariants

$$
\begin{aligned}
a &= \lambda_{F,1} = \sqrt{\sqrt{\mathcal{F}^2 + \mathcal{G}^2} + \mathcal{F}} \ , \\
b &= i\lambda_{F,3} = \sqrt{\sqrt{\mathcal{F}^2 + \mathcal{G}^2} - \mathcal{F}} \ .
\end{aligned}
\tag{B.15}
$$

Therefore,

$$
\det g^{-1}F = \prod_i \lambda_{F,i} = -a^2 b^2
$$

and

$$
\det F = \det g \det g^{-1}F = a^2 b^2 \ .
$$

Now we diagonalise $g^{-1}F$ with an orthogonal matrix U such that $UFU^{-1} = \Lambda = \mathrm{diag}(\lambda_{F,1}, \lambda_{F,2}, \lambda_{F,3}, \lambda_{F,4})$ is diagonal. Then

$$
\det \sinh\Big(\frac{e}{2} g^{-1} F t\Big) = \det\Big(U^{-1} \sinh\Big(\frac{e}{2}\Lambda t\Big) U\Big) = \prod_i \sinh\Big(\frac{e}{2}\lambda_i t\Big) \tag{B.16}
$$

$$
= -\sinh^2(\tfrac{e}{2} a t)\sin^2(\tfrac{e}{2} b t) \tag{B.17}
$$

and therefore

$$
\det\left(\frac{\frac{e}{2}F}{\sinh\frac{e}{2}g^{-1}Ft}\right)^{1/2} = i\frac{e^2 ab}{4\sinh\frac{e}{2}at\sin\frac{e}{2}bt} \ . \tag{B.18}
$$

B.6 $\mathrm{tr}\exp\left(\mathrm{i}\frac{e}{4}t\sigma^{\mu\nu}F_{\mu\nu}\right)$

We want to calculate $\mathrm{tr}\exp\left[it\frac{e}{4}\sigma^{\mu\nu}F_{\mu\nu}\right]$ as it appears in (2.14) and (2.17), so it is useful to find the eigenvalues of $\sigma^{\mu\nu}F_{\mu\nu}$. As the eigenvalues of a matrix squared are only the eigenvalues squared of the original matrix, we make use the identity

$$\begin{aligned}(\sigma F)^2 &= \frac{1}{2}F_{\mu\nu}F_{\lambda\kappa}\left\{\sigma^{\mu\nu},\sigma^{\lambda\kappa}\right\}\\ &= 2\left(F_{\mu\nu}F^{\mu\nu}+i\gamma^5 F_{\mu\nu}\star F^{\mu\nu}\right)\\ &= -8\left(\mathcal{F}+i\gamma_5\mathcal{G}\right)\ ,\end{aligned}$$

where we used [DG00]

$$\frac{1}{2}\left\{\sigma^{\mu\nu},\sigma^{\lambda\kappa}\right\} = \delta^{\mu\lambda}\delta^{\nu\kappa}-\delta^{\mu\kappa}\delta^{\nu\lambda}+i\epsilon^{\mu\nu\lambda\kappa}\gamma^5 \tag{B.19}$$

and $\gamma^5 := i\gamma^0\gamma^1\gamma^2\gamma^3$ with $(\gamma^5)^2 = 1$. Since $(\gamma^5)^2 = 1$, its eigenvalues are given by ± 1. Let $X_\pm$ be the eigenvectors of γ^5, then we have

$$(\sigma F)^2 X = -8\left(\mathcal{F}+i\gamma_5\mathcal{G}\right)X = -8\left(\mathcal{F}\pm i\mathcal{G}\right)X_\pm$$

and therefore the eigenvalues are given by $-8(\mathcal{F}\pm i\mathcal{G})$ and since the eigenvalues of a matrix squared are simply the eigenvalues squared, the eigenvalues of (σF) are given by $\lambda_i = \pm\sqrt{-8(\mathcal{F}\pm i\mathcal{G})}$ with $i = 1,2,3,4$. For later convenience, we express these eigenvalues by the secular invariants:

$$\lambda_i = \pm\sqrt{-8(\mathcal{F}\pm i\mathcal{G})} = \pm\sqrt{-4(a\pm ib)^2} = \mp 2\mathrm{i}(a\pm \mathrm{i}b)\ . \tag{B.20}$$

The trace evaluates then to

$$\mathrm{tr}\,\mathrm{e}^{\mathrm{i}t\frac{e}{4}\sigma F} = \sum_i \mathrm{e}^{i\frac{e}{4}t\lambda_i} = 4\cosh\left(\frac{e}{2}at\right)\cos\left(\frac{e}{2}bt\right)\ . \tag{B.21}$$

Appendix C

Maxwell and Wave Equations in Polarisable Vacuum

C.1 Nonlinear Maxwell Equations from an Interaction Lagrangian $\mathcal{L}_{\text{int}}(\mathcal{F},\mathcal{G})$

In the following we show that an interaction Lagrangian $\mathcal{L}_{\text{int}}(\mathcal{F},\mathcal{G})$ for pure photon-photon scattering leads to contributions to Maxwell equations that can be interpreted as polarisation $\mathbf{P}$ and magnetisation $\mathbf{M}$ similar to a nonlinear medium.
We start with a general Lagrangian (where we do not specify the kinetic term for the fermions):

$$\mathcal{L} = \mathcal{L}_{\text{matter}} + \mathcal{L}_{\text{Maxwell}} + \mathcal{L}_{\text{int}} + \mathcal{L}_{\text{cur}} \tag{C.1}$$

with

$$\begin{aligned}\mathcal{L}_{\text{Maxwell}} &= -\frac{1}{16\pi}F_{\mu\nu}F^{\mu\nu}\ ,\\ \mathcal{L}_{\text{int}} &= \mathcal{L}_{\text{int}}(\mathcal{F},\mathcal{G})\\ \mathcal{L}_{\text{cur}} &= -A_\mu J^\mu_{\text{matter}}\ .\end{aligned}$$

The Euler-Lagrange equations with respect to the gauge field are given by

$$\partial_\mu \frac{\partial\mathcal{L}}{\partial(\partial_\mu A_\nu)} - \frac{\partial\mathcal{L}}{\partial A_\nu} = 0\ .$$

Therefore:

$$-\frac{1}{4\pi}\partial_\mu F^{\mu\nu} - \partial_\mu\left(\frac{\partial\mathcal{L}_{\text{int}}}{\partial\mathcal{F}}F^{\mu\nu} + \frac{\partial\mathcal{L}_{\text{int}}}{\partial\mathcal{G}}\star F^{\mu\nu}\right) + J^\nu_{\text{matter}} = 0 \tag{C.2}$$

and we note in the case of $\mathcal{L}_{\text{int}} = 0$ this yields Maxwell equations in vacuum

$$\partial_\mu F^{\mu\nu} = 4\pi J^\mu_{\text{matter}}\ .$$

If one sets $\nu = 0$ in (C.2), one obtains

$$\frac{1}{4\pi}\partial_i F^{i0} + \partial_i\left(\frac{\partial\mathcal{L}_{\text{int}}}{\partial\mathcal{F}}F^{i0} + \frac{\partial\mathcal{L}_{\text{int}}}{\partial\mathcal{G}}\star F^{i0}\right) = J^0_{\text{matter}}$$

or written in **E**- and **B**-fields:

$$\frac{1}{4\pi}\partial_i E^i + \partial_i \left(\frac{\partial \mathcal{L}_{\text{int}}}{\partial \mathcal{F}} E^i + \frac{\partial \mathcal{L}_{\text{int}}}{\partial \mathcal{G}} B^i \right) = \rho_{\text{matter}} \ . \tag{C.3}$$

We observe

$$\left(\frac{\partial \mathcal{L}_{\text{int}}}{\partial \mathcal{F}} \mathbf{E} + \frac{\partial \mathcal{L}_{\text{int}}}{\partial \mathcal{G}} \mathbf{B} \right) = \frac{\partial \mathcal{L}_{\text{int}}}{\partial \mathbf{E}}$$

such that (C.3) is given by

$$\nabla \cdot \mathbf{E} = 4\pi \rho_{matter} - 4\pi \nabla \cdot \frac{\partial \mathcal{L}_{\text{int}}}{\partial \mathbf{E}}$$

and a comparison with (1.2) suggests the identification

$$\mathbf{P} := \frac{\partial \mathcal{L}_{\text{int}}}{\partial \mathbf{E}} \ .$$

Now we take the spatial components $\nu = j$ of (C.2):

$$\frac{1}{4\pi}\left(\partial_t F^{0j} + \partial_i F^{ij}\right) + \partial_t \left(\frac{\partial \mathcal{L}_{\text{int}}}{\partial \mathcal{F}} F^{0j} + \frac{\partial \mathcal{L}_{\text{int}}}{\partial \mathcal{G}} \star F^{0j} \right) + \partial_i \left(\frac{\partial \mathcal{L}_{\text{int}}}{\partial \mathcal{F}} F^{ij} + \frac{\partial \mathcal{L}_{\text{int}}}{\partial \mathcal{G}} \star F^{ij} \right) = J^j_{\text{matter}}$$

which translates into

$$(-\partial_t \mathbf{E} + \nabla \wedge \mathbf{B}) = 4\pi \mathbf{J}_{\text{matter}} + 4\pi(\partial_t \mathbf{P} + \nabla \wedge \mathbf{M}) \ ,$$

where we defined

$$\mathbf{M} = \frac{\partial \mathcal{L}_{\text{int}}}{\partial \mathbf{B}} \ .$$

We thereby observed that

$$\partial_i \left(\frac{\partial \mathcal{L}_{\text{int}}}{\partial \mathcal{F}} F^{ij} + \frac{\partial \mathcal{L}_{\text{int}}}{\partial \mathcal{G}} \star F^{ij} \right) = \partial_i \left(\frac{\partial \mathcal{L}_{\text{int}}}{\partial \mathcal{F}} \epsilon^{jik} B^k - \frac{\partial \mathcal{L}_{\text{int}}}{\partial \mathcal{G}} \epsilon^{jik} E^k \right)$$

can be written as

$$\partial_i \left(\frac{\partial \mathcal{L}_{\text{int}}}{\partial \mathcal{F}} F^{ij} + \frac{\partial \mathcal{L}_{\text{int}}}{\partial \mathcal{G}} \star F^{ij} \right) = -(\nabla \wedge \mathbf{M})^j \ ,$$

where we used

$$\frac{\partial \mathcal{L}_{\text{int}}}{\partial \mathcal{F}} \mathbf{B} - \frac{\partial \mathcal{L}_{\text{int}}}{\partial \mathcal{G}} \mathbf{E} = -\frac{\partial \mathcal{L}_{\text{int}}}{\partial \mathbf{B}} \quad .$$

C.2 Wave Equation with Source Terms

In the following we will derive the wave equation for the magnetic field **B** and electric field **E**. We start with the Maxwell equations

$$\nabla \wedge \mathbf{B} - \partial_t \mathbf{E} = 4\pi \mathbf{J}_{\text{matter}} + 4\pi \mathbf{J}[\mathbf{E}, \mathbf{B}] \ , \tag{C.4}$$

$$\nabla \wedge \mathbf{E} + \partial_t \mathbf{B} = \mathbf{0} \ , \tag{C.5}$$

$$\nabla \cdot \mathbf{D} = 4\pi \rho_{\text{matter}} \ , \tag{C.6}$$

$$\nabla \cdot \mathbf{B} = 0 \ , \tag{C.7}$$

where we defined

$$\mathbf{J}[\mathbf{E},\mathbf{B}] := (\partial_t \mathbf{P} + \nabla \wedge \mathbf{M}) \ .$$

To derive the wave equation for $\mathbf{B}$, we take the curl of (C.4) and obtain

$$\partial_t^2 \mathbf{B} - \Delta \mathbf{B} = 4\pi \nabla \wedge \mathbf{J}_{\text{matter}} + 4\pi \nabla \wedge \mathbf{J}[\mathbf{E},\mathbf{B}] \ ,$$

where we used

$$\nabla \wedge (\nabla \wedge \mathbf{B}) = \nabla(\nabla \cdot \mathbf{B}) - \Delta \mathbf{B}$$

together with (C.5) and (C.7).
For the wave equation for $\mathbf{E}$ we take the curl of (C.5) and obtain

$$\nabla(\nabla \cdot \mathbf{E}) - \Delta \mathbf{E} + \partial_t^2 \mathbf{E} + 4\pi \partial_t \mathbf{J}[\mathbf{E},\mathbf{B}] + 4\pi \partial_t \mathbf{J}_{\text{matter}} = 0$$

where we used (C.4). Now we know from (C.6) that

$$\nabla \cdot \mathbf{E} = 4\pi \rho_{\text{matter}} - 4\pi \nabla \cdot \mathbf{P}$$

and therefore

$$\partial_t^2 \mathbf{E} - \Delta \mathbf{E} = \mathbf{T}[\mathbf{E},\mathbf{B}] - 4\pi \nabla \rho_{\text{matter}}$$

with the field-dependent source

$$\mathbf{T}[\mathbf{E},\mathbf{B}] := -4\pi(\partial_t^2 \mathbf{P} + \nabla \wedge \partial_t \mathbf{M} - \nabla(\nabla \cdot \mathbf{P}))$$

and we note that $\mathbf{J}[\mathbf{E},\mathbf{B}]$ and $\mathbf{T}[\mathbf{E},\mathbf{B}]$ are related via

$$\mathbf{T}[\mathbf{E},\mathbf{B}] = -4\pi \partial_t \mathbf{J}[\mathbf{E},\mathbf{B}] + 4\pi \nabla(\nabla \cdot \mathbf{P}) \ .$$

C.3 Covariant Maxwell Equations with Coefficients C_i

In the previous section we considered a general Lagrangian (C.1) of the form

$$\mathcal{L} = \mathcal{L}_{\text{matter}} + \mathcal{L}_{\text{Maxwell}} + \mathcal{L}_{\text{int}} + \mathcal{L}_{\text{cur}} \ .$$

Since we do not consider any massive particles in this thesis, we set $\mathcal{L}_{\text{matter}} = \mathcal{L}_{\text{cur}} = 0$. In the following we will derive the Maxwell equations for a general Lagrangian $\mathcal{L} = \mathcal{L}_{\text{Maxwell}} + \mathcal{L}_{\text{int}}(a,b)$, which is equivalent to $\mathcal{L} = \mathcal{L}_{\text{Maxwell}} + \mathcal{L}_{\text{int}}(\mathcal{F},\mathcal{G})$ as we have the relations

$$a = \left(\sqrt{\mathcal{F}^2 + \mathcal{G}^2} + \mathcal{F}\right)^{1/2} , \tag{C.8}$$

$$b = \left(\sqrt{\mathcal{F}^2 + \mathcal{G}^2} - \mathcal{F}\right)^{1/2} , \tag{C.9}$$

$$ab = \mathcal{G} \ , \tag{C.10}$$

$$a^2 - b^2 = 2\mathcal{F} \ . \tag{C.11}$$

In the following we only consider the contributions from $\mathcal{L}_{\text{int}}$ and install the free propagation from $\mathcal{L}_{\text{Maxwell}}$ in the final result. Before we proceed, we need the following definitions and identities:

$$r^2 := a^2 + b^2 = 2\sqrt{\mathcal{F}^2 + \mathcal{G}^2} \ , \tag{C.12}$$

$$2\mathcal{F} + r^2 = 2a^2 \ , \tag{C.13}$$

$$2\mathcal{F} - r^2 = -2b^2 \ , \tag{C.14}$$

$$\mathcal{F} + r^2 = \tfrac{1}{2}(3a^2 + b^2) \ , \tag{C.15}$$

$$\frac{\partial \mathcal{F}}{\partial(\partial_\mu A_\nu)} = -F^{\mu\nu} \ , \tag{C.16}$$

$$\frac{\partial \mathcal{G}}{\partial(\partial_\mu A_\nu)} = -\star F^{\mu\nu} \ . \tag{C.17}$$

For the Euler-Lagrange equations we need

$$\begin{aligned}
\frac{\partial \mathcal{L}_{\text{int}}}{\partial(\partial_\mu A_\nu)} &= \frac{\partial \mathcal{L}_{\text{int}}}{\partial a}\frac{\partial a}{\partial(\partial_\mu A_\nu)} + \frac{\partial \mathcal{L}_{\text{int}}}{\partial b}\frac{\partial b}{\partial(\partial_\mu A_\nu)} \\
&= \frac{\partial \mathcal{L}_{\text{int}}}{\partial a}\Big(\frac{\partial a}{\partial \mathcal{G}}\frac{\partial \mathcal{G}}{\partial(\partial_\mu A_\nu)} + \frac{\partial a}{\partial \mathcal{F}}\frac{\partial \mathcal{F}}{\partial(\partial_\mu A_\nu)}\Big) \\
&\quad + \frac{\partial \mathcal{L}_{\text{int}}}{\partial b}\Big(\frac{\partial b}{\partial \mathcal{G}}\frac{\partial \mathcal{G}}{\partial(\partial_\mu A_\nu)} + \frac{\partial b}{\partial \mathcal{F}}\frac{\partial \mathcal{F}}{\partial(\partial_\mu A_\nu)}\Big) \\
&= -\frac{\partial \mathcal{L}_{\text{int}}}{\partial a}\Big(\frac{\partial a}{\partial \mathcal{G}} \star F^{\mu\nu} + \frac{\partial a}{\partial \mathcal{F}} F^{\mu\nu}\Big) \\
&\quad - \frac{\partial \mathcal{L}_{\text{int}}}{\partial b}\Big(\frac{\partial b}{\partial \mathcal{G}} \star F^{\mu\nu} + \frac{\partial b}{\partial \mathcal{F}} F^{\mu\nu}\Big) \\
&= -\left(\frac{\partial \mathcal{L}_{\text{int}}}{\partial a}\frac{\partial a}{\partial \mathcal{G}} + \frac{\partial \mathcal{L}_{\text{int}}}{\partial b}\frac{\partial b}{\partial \mathcal{G}}\right)\star F^{\mu\nu} \\
&\quad - \left(\frac{\partial \mathcal{L}_{\text{int}}}{\partial a}\frac{\partial a}{\partial \mathcal{F}} + \frac{\partial \mathcal{L}_{\text{int}}}{\partial b}\frac{\partial b}{\partial \mathcal{F}}\right) F^{\mu\nu} \ ,
\end{aligned}$$

where we used (C.16) and (C.17) in the third equality. We note that a derivative acts only on the expression directly on the right and we write brackets when it acts on products of functions. The equations of motion are given by

$$\begin{aligned}
\partial_\mu \frac{\partial \mathcal{L}_{\text{int}}}{\partial(\partial_\mu A_\nu)} &= -\partial_\mu\left[\left(\frac{\partial \mathcal{L}_{\text{int}}}{\partial a}\frac{\partial a}{\partial \mathcal{G}} + \frac{\partial \mathcal{L}_{\text{int}}}{\partial b}\frac{\partial b}{\partial \mathcal{G}}\right)\star F^{\mu\nu}\right] \\
&\quad - \partial_\mu\left[\left(\frac{\partial \mathcal{L}_{\text{int}}}{\partial a}\frac{\partial a}{\partial \mathcal{F}} + \frac{\partial \mathcal{L}_{\text{int}}}{\partial b}\frac{\partial b}{\partial \mathcal{F}}\right) F^{\mu\nu}\right] \\
&= -\star F^{\mu\nu}\partial_\mu\left(\frac{\partial \mathcal{L}_{\text{int}}}{\partial a}\frac{\partial a}{\partial \mathcal{G}} + \frac{\partial \mathcal{L}_{\text{int}}}{\partial b}\frac{\partial b}{\partial \mathcal{G}}\right) \\
&\quad - F^{\mu\nu}\partial_\mu\left(\frac{\partial \mathcal{L}_{\text{int}}}{\partial a}\frac{\partial a}{\partial \mathcal{F}} + \frac{\partial \mathcal{L}_{\text{int}}}{\partial b}\frac{\partial b}{\partial \mathcal{F}}\right) \\
&\quad - \left(\frac{\partial \mathcal{L}_{\text{int}}}{\partial a}\frac{\partial a}{\partial \mathcal{F}} + \frac{\partial \mathcal{L}_{\text{int}}}{\partial b}\frac{\partial b}{\partial \mathcal{F}}\right)\partial_\mu F^{\mu\nu} \ ,
\end{aligned} \tag{C.18}$$

where we used the Bianchi-Identity $\partial_\mu \star F^{\mu\nu} = 0$. We proceed by calculating the quantities

$$\frac{\partial a}{\partial \mathcal{G}} \ , \ \frac{\partial a}{\partial \mathcal{F}} \ , \ \frac{\partial b}{\partial \mathcal{F}} \ , \ \frac{\partial b}{\partial \mathcal{G}}$$

and the derivatives

$$\partial_\mu \frac{\partial a}{\partial \mathcal{G}} \ , \ \partial_\mu \frac{\partial a}{\partial \mathcal{F}} \ , \ \partial_\mu \frac{\partial b}{\partial \mathcal{F}} \ , \ \partial_\mu \frac{\partial b}{\partial \mathcal{G}} \ , \ \partial_\mu \frac{\partial \mathcal{L}_{\text{int}}}{\partial a} \ , \ \partial_\mu \frac{\partial \mathcal{L}_{\text{int}}}{\partial b} \ .$$

$$\begin{aligned}\frac{\partial a}{\partial \mathcal{G}} &= \frac{\partial}{\partial \mathcal{G}}(\sqrt{\mathcal{F}^2+\mathcal{G}^2}+\mathcal{F})^{1/2} \\ &= \frac{1}{2a}\frac{\partial}{\partial \mathcal{G}}\sqrt{\mathcal{F}^2+\mathcal{G}^2} \\ &= \frac{1}{2a}\frac{\mathcal{G}}{\sqrt{\mathcal{F}^2+G^2}} \\ &= \frac{b}{r^2}\ ,\end{aligned} \tag{C.19}$$

where we used (C.10) and (C.12) in the last step.

$$\begin{aligned}\frac{\partial b}{\partial \mathcal{G}} &= \frac{\partial}{\partial \mathcal{G}}(\sqrt{\mathcal{F}^2+\mathcal{G}^2}-\mathcal{F})^{1/2} \\ &= \frac{b}{r^2}\ .\end{aligned} \tag{C.20}$$

Similarly, we obtain

$$\begin{aligned}\frac{\partial a}{\partial \mathcal{F}} &= \frac{\partial}{\partial \mathcal{F}}(\sqrt{\mathcal{F}^2+\mathcal{G}^2}+\mathcal{F})^{1/2} \\ &= \frac{1}{2a}\frac{\partial}{\partial \mathcal{F}}(\sqrt{\mathcal{F}^2+\mathcal{G}^2}+\mathcal{F}) \\ &= \frac{1}{2a}\Big(\frac{2\mathcal{F}}{r^2}+1\Big) \\ &= \frac{1}{2ar^2}\Big(2\mathcal{F}+r^2\Big) \\ &= \frac{a}{r^2}\ ,\end{aligned} \tag{C.21}$$

where we used (C.13) in the last step.

$$\begin{aligned}\frac{\partial b}{\partial \mathcal{F}} &= \frac{\partial}{\partial \mathcal{F}}(\sqrt{\mathcal{F}^2+\mathcal{G}^2}-\mathcal{F})^{1/2} \\ &= \frac{1}{2b}\frac{\partial}{\partial \mathcal{F}}(\sqrt{\mathcal{F}^2+\mathcal{G}^2}-\mathcal{F}) \\ &= \frac{1}{2b}\Big(\frac{2\mathcal{F}}{r^2}-1\Big) \\ &= \frac{1}{2br^2}\Big(2\mathcal{F}-r^2\Big) \\ &= -\frac{b}{r^2}\ .\end{aligned} \tag{C.22}$$

The last equality follows from (C.14). To obtain the derivates, we first calculate some useful quantities:

$$\begin{aligned}\partial_\mu a &= \frac{\partial a}{\partial \mathcal{G}}\partial_\mu \mathcal{G}+\frac{\partial a}{\partial \mathcal{F}}\partial_\mu \mathcal{G} \\ &= \frac{1}{r^2}(b\partial_\mu \mathcal{G}+a\partial_\mu \mathcal{F})\ ,\end{aligned} \tag{C.23}$$

which follows from (C.19) and (C.21).

$$\begin{aligned}\partial_\mu b &= \frac{\partial b}{\partial \mathcal{G}}\partial_\mu \mathcal{G}+\frac{\partial b}{\partial \mathcal{F}}\partial_\mu \mathcal{G} \\ &= \frac{1}{r^2}(a\partial_\mu \mathcal{G}-b\partial_\mu \mathcal{F})\ ,\end{aligned} \tag{C.24}$$

where (C.20) and (C.22) were used in the last step. Furthermore, we need:

$$\begin{aligned}\partial_\mu r &= \partial_\mu \left(\tfrac{1}{2}(3a^2+b^2)-\mathcal{F}\right)^{1/2} \\ &= \frac{1}{2r}\left(3a\partial_\mu a + b\partial_\mu b - \partial_\mu \mathcal{F}\right)\end{aligned} \quad , \tag{C.25}$$

where the first equality is from (C.15). With these formulas we can now easily calculate the derivatives:

$$\begin{aligned}\partial_\mu \frac{\partial a}{\partial \mathcal{G}} &= \partial_\mu \left(\frac{b}{r^2}\right) = \frac{1}{r^2}\partial_\mu b - \frac{2b}{r^3}\partial_\mu r \\ &= \frac{1}{r^2}\partial_\mu b - \frac{b}{r^4}(3a\partial_\mu a + b\partial_\mu b - \partial_\mu \mathcal{F}) \\ &= \frac{1}{r^4}\left[(r^2-b^2)\partial_\mu b - 3ab\partial_\mu a - b\partial_\mu \mathcal{F}\right] \\ &= \frac{1}{r^6}\left[a^2(a\partial_\mu \mathcal{G} - b\partial_\mu \mathcal{F}) - 3ab(b\partial_\mu \mathcal{G} + a\partial_\mu \mathcal{F}) - br^2\partial_\mu \mathcal{F}\right] \\ &= \frac{1}{r^6}\left[a(a^2-3b^2)\partial_\mu \mathcal{G} + b(b^2-3a^2)\partial_\mu \mathcal{F}\right] \ ,\end{aligned}$$

$$\begin{aligned}\partial_\mu \frac{\partial a}{\partial \mathcal{F}} &= \partial_\mu \left(\frac{a}{r^2}\right) = \frac{1}{r^2}\partial_\mu a - \frac{2a}{r^3}\partial_\mu r \\ &= \frac{1}{r^2}\partial_\mu a - \frac{a}{r^4}\left[3a\partial_\mu a + b\partial_\mu b - \partial_\mu \mathcal{F}\right] \\ &= \frac{1}{r^4}\left[(r^2-3a^2)\partial_\mu a - ab\partial_\mu b + a\partial_\mu \mathcal{F}\right] \\ &= \frac{1}{r^6}\left[(b^2-2a^2)(b\partial_\mu \mathcal{G} + a\partial_\mu \mathcal{F}) - ab(a\partial_\mu \mathcal{G} - b\partial_\mu \mathcal{F}) + ar^2\partial_\mu \mathcal{F}\right] \\ &= \frac{1}{r^6}\left[b(b^2-3a^2)\partial_\mu \mathcal{G} + a(3b^2-a^2)\partial_\mu \mathcal{F}\right] \ ,\end{aligned}$$

$$\partial_\mu \frac{\partial b}{\partial \mathcal{G}} = \partial_\mu \left(\frac{b}{r^2}\right) = \frac{1}{r^6}\left[a(a^2-3b^2)\partial_\mu \mathcal{G} + b(b^2-3a^2)\partial_\mu \mathcal{F}\right]$$

and

$$\partial_\mu \frac{\partial b}{\partial \mathcal{F}} = -\partial_\mu \frac{\partial a}{\partial \mathcal{G}} = \frac{1}{r^6}\left[a(3b^2-a^2)\partial_\mu \mathcal{G} + b(3a^2-b^2)\partial_\mu \mathcal{F}\right] \ .$$

Additionally, we need

$$\begin{aligned}\partial_\mu \frac{\partial \mathcal{L}_{\text{int}}}{\partial a} &= \frac{\partial^2 \mathcal{L}_{\text{int}}}{\partial a^2}\partial_\mu a + \frac{\partial \mathcal{L}_{\text{int}}}{\partial a \partial b}\partial_\mu b \\ &= \frac{1}{r^2}\left[\mathcal{L}_{aa}(b\partial_\mu \mathcal{G} + a\partial_\mu \mathcal{F}) + \mathcal{L}_{ab}(a\partial_\mu \mathcal{G} - b\partial_\mu \mathcal{F})\right] \\ &= \frac{1}{r^2}\left[(b\mathcal{L}_{aa} + a\mathcal{L}_{ab})\partial_\mu \mathcal{G} + (a\mathcal{L}_{aa} - b\mathcal{L}_{ab})\partial_\mu \mathcal{F}\right] \ ,\end{aligned}$$

where

$$\mathcal{L}_{ab} := \frac{\partial^2 \mathcal{L}_{\text{int}}}{\partial a \partial b}$$

and the other quantities are defined in an analogous way. For the derivative of $\partial \mathcal{L}_{\text{int}}/\partial b$ we have

$$\begin{aligned}\partial_\mu \frac{\partial \mathcal{L}_{\text{int}}}{\partial b} &= \frac{\partial^2 \mathcal{L}_{\text{int}}}{\partial b^2}\partial_\mu b + \frac{\partial \mathcal{L}_{\text{int}}}{\partial a \partial b}\partial_\mu a \\ &= \frac{1}{r^2}\left[\mathcal{L}_{bb}(a\partial_\mu \mathcal{G} - b\partial_\mu \mathcal{F}) + \mathcal{L}_{ab}(b\partial_\mu \mathcal{G} + a\partial_\mu \mathcal{F})\right] \\ &= \frac{1}{r^2}\left[(a\mathcal{L}_{bb} + b\mathcal{L}_{ab})\partial_\mu \mathcal{G} + (a\mathcal{L}_{ab} - b\mathcal{L}_{bb})\partial_\mu \mathcal{F}\right] \ .\end{aligned}$$

So we can finally calculate the quantities in (C.18). Let us begin with

$$\left(\frac{\partial\mathcal{L}_{\text{int}}}{\partial a}\frac{\partial a}{\partial\mathcal{F}}+\frac{\partial\mathcal{L}_{\text{int}}}{\partial b}\frac{\partial b}{\partial\mathcal{F}}\right)=\frac{a\mathcal{L}_a-b\mathcal{L}_b}{r^2}=:-4C_1\ ,$$

where

$$C_1:=-\frac{a\mathcal{L}_a-b\mathcal{L}_b}{4r^2}\ .$$

$$\begin{aligned}
\partial_\mu\left(\frac{\partial\mathcal{L}_{\text{int}}}{\partial a}\frac{\partial a}{\partial\mathcal{F}}+\frac{\partial\mathcal{L}_{\text{int}}}{\partial b}\frac{\partial b}{\partial\mathcal{F}}\right)&=\partial_\mu\frac{\partial\mathcal{L}_{\text{int}}}{\partial a}\frac{\partial a}{\partial\mathcal{F}}+\frac{\partial\mathcal{L}_{\text{int}}}{\partial a}\partial_\mu\frac{\partial a}{\partial\mathcal{F}}+\partial_\mu\frac{\partial\mathcal{L}_{\text{int}}}{\partial b}\frac{\partial b}{\partial\mathcal{F}}+\frac{\partial\mathcal{L}_{\text{int}}}{\partial b}\partial_\mu\frac{\partial b}{\partial\mathcal{F}}\\
&=\frac{1}{r^4}\left[(ab\mathcal{L}_{aa}+a^2\mathcal{L}_{ab})\partial_\mu\mathcal{G}+(a^2\mathcal{L}_{aa}-ab\mathcal{L}_{ab})\partial_\mu\mathcal{F}\right]\\
&\quad+\frac{1}{r^6}\mathcal{L}_a\left[b(b^2-3a^2)\partial_\mu\mathcal{G}+a(3b^2-a^2)\partial_\mu\mathcal{F}\right]\\
&\quad-\frac{1}{r^4}\left[(ab\mathcal{L}_{bb}+b^2\mathcal{L}_{ab})\partial_\mu\mathcal{G}+(ab\mathcal{L}_{ab}-b^2\mathcal{L}_{bb})\partial_\mu\mathcal{F}\right]\\
&\quad+\frac{1}{r^6}\mathcal{L}_b\left[a(3b^2-a^2)\partial_\mu\mathcal{G}+b(3a^2-b^2)\partial_\mu\mathcal{F}\right]\\
&=\frac{1}{r^6}\big[a(3b^2-a^2)\mathcal{L}_a+b((3a^2-b^2)\mathcal{L}_b\\
&\quad+r^2(a^2\mathcal{L}_{aa}-2ab\mathcal{L}_{ab}+b^2\mathcal{L}_{bb})\big]\partial_\mu\mathcal{F}\\
&\quad+\frac{1}{r^6}\big[b(b^2-3a^2)\mathcal{L}_a+a(3b^2-a^2)\mathcal{L}_b\\
&\quad+r^2(ab\mathcal{L}_{aa}+(a^2-b^2)\mathcal{L}_{ab}-ab\mathcal{L}_{bb})\big]\partial_\mu\mathcal{G}\\
&=4C_2\,\partial_\mu\mathcal{F}+4C_4\,\partial_\mu\mathcal{G}\\
&=-C_2\,\partial_\mu(F_{\alpha\beta}F^{\alpha\beta})-C_4\,\partial_\mu(\star F_{\alpha\beta}F^{\alpha\beta})\ ,
\end{aligned}$$

where we defined

$$\begin{aligned}
C_2&:=\frac{1}{4r^6}\big[a(3b^2-a^2)\mathcal{L}_a+b((3a^2-b^2)\mathcal{L}_b\\
&\qquad+r^2(a^2\mathcal{L}_{aa}-2ab\mathcal{L}_{ab}+b^2\mathcal{L}_{bb})\big]\ ,\\
C_4&:=\frac{1}{4r^6}\big[b(b^2-3a^2)\mathcal{L}_a+a(3b^2-a^2)\mathcal{L}_b\\
&\qquad+r^2(ab\mathcal{L}_{aa}+(a^2-b^2)\mathcal{L}_{ab}-ab\mathcal{L}_{bb})\big]\ .
\end{aligned}$$

We further obtain

$$\begin{aligned}
\partial_\mu\left(\frac{\partial\mathcal{L}_{\rm int}}{\partial a}\frac{\partial a}{\partial\mathcal{G}}+\frac{\partial\mathcal{L}_{\rm int}}{\partial b}\frac{\partial b}{\partial\mathcal{G}}\right) &= \partial_\mu\frac{\partial\mathcal{L}_{\rm int}}{\partial a}\frac{\partial a}{\partial\mathcal{G}}+\frac{\partial\mathcal{L}_{\rm int}}{\partial a}\partial_\mu\frac{\partial a}{\partial\mathcal{G}}+\partial_\mu\frac{\partial\mathcal{L}_{\rm int}}{\partial b}\frac{\partial b}{\partial\mathcal{G}}+\frac{\partial\mathcal{L}_{\rm int}}{\partial b}\partial_\mu\frac{\partial b}{\partial\mathcal{G}}\\
&= \frac{1}{r^4}\left[(b^2\mathcal{L}_{aa}+ab\mathcal{L}_{ab})\partial_\mu\mathcal{G}+(ab\mathcal{L}_{aa}-b^2\mathcal{L}_{ab})\partial_\mu\mathcal{F}\right]\\
&\quad\frac{1}{r^6}\mathcal{L}_a\left[a(a^2-3b^2)\partial_\mu\mathcal{G}+b(b^2-3a^2)\partial_\mu\mathcal{F}\right]\\
&\quad\frac{1}{r^4}\left[(a^2\mathcal{L}_{bb}+ab\mathcal{L}_{ab})\partial_\mu\mathcal{G}+(a^2\mathcal{L}_{ab}-ab\mathcal{L}_{bb})\partial_\mu\mathcal{F}\right]\\
&\quad\frac{1}{r^6}\mathcal{L}_b\left[b(b^2-3a^2)\partial_\mu\mathcal{G}+a(3b^2-a^2)\partial_\mu\mathcal{F}\right]\\
&= \frac{1}{r^6}\big[a(a^2-3b^2)\mathcal{L}_a+b(b^2-3a^2)\mathcal{L}_b\\
&\quad+r^2(b^2\mathcal{L}_{aa}+2ab\mathcal{L}_{ab}+a^2\mathcal{L}_{bb})\big]\partial_\mu\mathcal{G}\\
&\quad+\frac{1}{r^6}\big[b(b^2-3a^2)\mathcal{L}_a+a(3b^2-a^2)\mathcal{L}_b\\
&\quad+r^2(ab\mathcal{L}_{aa}+(a^2-b^2)\mathcal{L}_{ab}-ab\mathcal{L}_{bb}\big]\partial_\mu\mathcal{F}\\
&= 4C_3\,\partial_\mu\mathcal{G}+4C_4\,\partial_\mu\mathcal{F}\\
&= -C_3\,\partial_\mu(\star F_{\alpha\beta}F^{\alpha\beta})-C_4\,\partial_\mu(F_{\alpha\beta}F^{\alpha\beta})\ ,
\end{aligned}$$

where

$$\begin{aligned}
C_3 := \frac{1}{4r^6}\big[&a(a^2-3b^2)\mathcal{L}_a+b(b^2-3a^2)\mathcal{L}_b\\
&+r^2(b^2\mathcal{L}_{aa}+2ab\mathcal{L}_{ab}+a^2\mathcal{L}_{bb})\big]\ .
\end{aligned}$$

Using these expressions, we can write the equations of motion as

$$4\pi\partial_\mu\frac{\partial\mathcal{L}_{\rm Maxwell}}{\partial(\partial_\mu A_\nu)}+4\pi\partial_\mu\frac{\partial\mathcal{L}_{\rm int}}{\partial(\partial_\mu A_\nu)}=0$$

which yields

$$\begin{aligned}
&(-1+4\pi C_1)\,\partial_\mu F^{\mu\nu}+4\pi C_2\,F^{\mu\nu}\partial_\mu(F_{\alpha\beta}F^{\alpha\beta})\\
&+4\pi\,C_3\star F^{\mu\nu}\partial_\mu(\star F_{\alpha\beta}F^{\alpha\beta})+4\pi\,C_4\big[\star F^{\mu\nu}\partial_\mu(F_{\alpha\beta}F^{\alpha\beta})+F^{\mu\nu}\partial_\mu(\star F_{\alpha\beta}F^{\alpha\beta})\big]=0 \quad \text{(C.26)}
\end{aligned}$$

or, equivalently,

$$\begin{aligned}
&\partial_\mu F^{\mu\nu}=4\pi\Big((C_1\,\partial_\mu F^{\mu\nu}+C_2\,F^{\mu\nu}\partial_\mu(F_{\alpha\beta}F^{\alpha\beta})\\
&+\ C_3\star F^{\mu\nu}\partial_\mu(\star F_{\alpha\beta}F^{\alpha\beta})+\ C_4\big[\star F^{\mu\nu}\partial_\mu(F_{\alpha\beta}F^{\alpha\beta})+F^{\mu\nu}\partial_\mu(\star F_{\alpha\beta}F^{\alpha\beta})\big]\Big)=0\ . \quad \text{(C.27)}
\end{aligned}$$

For a general scalar φ we have the identities

$$\begin{aligned}
\partial_\mu F^{\mu i} &= (-\partial_t\mathbf{E}+\nabla\wedge\mathbf{B})^i\ ,\\
F^{\mu i}\partial_\mu\varphi &= (-\mathbf{E}\,\partial_t\varphi-\mathbf{B}\wedge\boldsymbol{\nabla}\varphi)^i\ ,\\
\star F^{\mu i}\partial_\mu\varphi &= (-\mathbf{B}\,\partial_t\varphi+\mathbf{E}\wedge\boldsymbol{\nabla}\varphi)^i\ ,
\end{aligned}$$

so we can express the dynamical equations of (C.27) in $\mathbf{E}$ and $\mathbf{B}$-fields:

$$(\nabla\wedge\mathbf{B}-\partial_t\mathbf{E})=4\pi\mathbf{J}[\mathbf{E},\mathbf{B}]\ ,$$

where

$$\begin{aligned}\mathbf{J}[\mathbf{E},\mathbf{B}] := {} & C_1(\partial_t\mathbf{E} - \nabla\wedge\mathbf{B}) + C_2(\mathbf{E}\,\partial_t(F_{\alpha\beta}F^{\alpha\beta}) + \mathbf{B}\wedge\nabla(F_{\alpha\beta}F^{\alpha\beta})) \\ & + C_3(\mathbf{B}\,\partial_t(\star F_{\alpha\beta}F^{\alpha\beta}) - \mathbf{E}\wedge\nabla(\star F_{\alpha\beta}F^{\alpha\beta})) \\ & + C_4(\mathbf{B}\,\partial_t(F_{\alpha\beta}F^{\alpha\beta}) - \mathbf{E}\wedge\nabla(F_{\alpha\beta}F^{\alpha\beta}) + \mathbf{E}\,\partial_t(\star F_{\alpha\beta}F^{\alpha\beta}) \\ & \qquad + \mathbf{B}\wedge\nabla(\star F_{\alpha\beta}F^{\alpha\beta}))\ .\end{aligned}$$

This can be re-arranged to

$$\begin{aligned}\mathbf{J}[\mathbf{E},\mathbf{B}] = {} & \big[C_1\,(\partial_t\mathbf{E} - \nabla\wedge\mathbf{B}) + (C_2\mathbf{E} + C_4\mathbf{B})\,\partial_t(F_{\alpha\beta}F^{\alpha\beta}) \\ & + (C_2\mathbf{B} - C_4\mathbf{E})\wedge\nabla(F_{\alpha\beta}F^{\alpha\beta}) \\ & + (C_4\mathbf{B} - C_3\mathbf{E})\wedge\nabla(F_{\alpha\beta}\star F^{\alpha\beta}) \\ & + (C_3\mathbf{B} + C_4\mathbf{E})\,\partial_t(F_{\alpha\beta}\star F^{\alpha\beta})\big]\ .\end{aligned}$$

Appendix D

Green's Function for the Wave Equation in $(1+1)$ Dimensions

This section is based on [Mah02].
The defining equation for the Green's function of the wave equation in $(1+1)$ dimensions is

$$\left(\frac{\partial^2}{\partial t^2} - \frac{\partial^2}{\partial z^2}\right) G(z,t) = \delta(t)\delta(z) \ . \tag{D.1}$$

Now we introduce the Fourier representation of the δ-distribution and of the Green's function $G(z,t)$:

$$\delta(z) = \frac{1}{2\pi} \int_{-\infty}^{\infty} \mathrm{d}k \ \mathrm{e}^{ikz} \tag{D.2}$$

$$G(z,t) = \frac{1}{2\pi} \int_{-\infty}^{\infty} \mathrm{d}k \ \tilde{G}(k,t) \ \mathrm{e}^{ikz} \tag{D.3}$$

where

$$\tilde{G}(k,t) = \mathrm{FT}[G(z,t)](k,t) = \int_{-\infty}^{\infty} \mathrm{d}z \ G(z,t) \ \mathrm{e}^{-ikz}.$$

Inserting (D.2) and (D.3) in (D.1) yields

$$\frac{1}{2\pi}\left(\frac{\partial^2}{\partial t^2} - \frac{\partial^2}{\partial z^2}\right) \int_{-\infty}^{\infty} \mathrm{d}k \ \tilde{G}(k,t) \ \mathrm{e}^{ikz} = \frac{1}{2\pi} \int_{-\infty}^{\infty} \mathrm{d}k \ \mathrm{e}^{ikz} \ ,$$

which leads to the equation

$$\left(\frac{\partial^2}{\partial t^2} + k^2\right) \tilde{G}(k,t) = \delta(t) \ . \tag{D.4}$$

The homogenous part of (D.4) is just the differential equation for a harmonic oscillator. So we make the ansatz $\tilde{G}_1(k,t) := \tilde{G}_1(\omega,t) = C_1 \cos(\omega t)$ with the dispersion relation $\omega = k$ and a constant C_1. To solve the inhomogeneous equation, we use the „variation of the constant“ [AWH12] and make the ansatz

$$\tilde{G}_1(\omega,t) = C_1(t) \cos \omega t \ . \tag{D.5}$$

The second time derivative of $\tilde{G}$ is therefore given by

$$\frac{\partial^2}{\partial t^2}\tilde{G}(\omega,t) = \ddot{C}_1(t)\cos\omega t - 2\omega\dot{C}_1(t)\sin\omega t - \omega^2 C_1(t)\sin\omega t \ .$$

So we obtain

$$\begin{aligned}\left(\frac{\partial^2}{\partial t^2}+\omega^2\right)\tilde{G}_1(\omega,t) &= \ddot{C}_1(t)\cos\omega t - 2\omega\dot{C}_1(t)\sin\omega t - \omega^2 C_1(t)\cos\omega t + \omega^2\cos\omega t \\ &= \ddot{C}_1(t)\cos\omega t - 2\omega\dot{C}_1(t)\sin\omega t \\ &= -\omega\dot{C}_1(t)\sin\omega t \ ,\end{aligned}$$

where the last equality follows from integration by parts of one time derivative since the equations always have to be understood applied to some test-functions:

$$\ddot{C}_1(t)\cos\omega t = \omega\dot{C}_1(t)\sin\omega t + \text{boundary terms} \ .$$

The boundary terms vanish since we assume the solution to vanish at infinity. So we are left with the equation

$$\dot{C}_1(t)\sin\omega t = -\frac{\delta(t)}{\omega}. \tag{D.6}$$

This suggests the ansatz $C_1(t) = -\frac{\theta(t)}{\omega}$, where $\theta(t)$ is the Heaviside step function with $\frac{\partial}{\partial t}\theta(t) = \delta(t)$ and we obtain

$$\delta(t)\sin\omega t = -\frac{\delta(t)}{\omega} \ . \tag{D.7}$$

But if we multiply (D.7) by an arbitrary test function $f(t)$ and integrate over t, we obtain

$$-\int_{-\infty}^{\infty}\mathrm{d}t\ f(t)\frac{\delta(t)}{\omega}\sin\omega t = -\int_{-\infty}^{\infty}\mathrm{d}t f(t)\frac{\delta(t)}{\omega}$$

Using one of the defining properties of the δ-distribution, namely $\int_{-\infty}^{\infty}\mathrm{d}t\ f(t)\delta(t) = f(0)$, we obtain the contradiction

$$f(0)\sin 0 = f(0),$$

and conclude that $G_1(\omega,t) = -\frac{\theta(t)}{\omega}\cos\omega t$ is not a valid solution to (D.4) and as a consequence, $C_1(t) = 0$.
A second ansatz for the solution to (D.4) is given by $\tilde{G}_2(k,t) := \tilde{G}_2(\omega,t) = C_2\sin(\omega t)$, which yields

$$\begin{aligned}\left(\frac{\partial^2}{\partial t^2}+\omega^2\right)\tilde{G}_2(\omega,t) &= \ddot{C}_2(t)\sin\omega t + 2\omega\dot{C}_2(t)\cos\omega t \\ &= \omega\dot{C}_2(t)\cos\omega t \\ &= \delta(t) \ ,\end{aligned}$$

where we again integrated by parts from the first to the second line. The ansatz $C_2(t) = \frac{\theta(t)}{\omega}$ yields

$$\int_{-\infty}^{\infty}\mathrm{d}t\ f(t)\frac{\delta(t)}{\omega}\cos\omega t = \int_{-\infty}^{\infty}\mathrm{d}t f(t)\frac{\delta(t)}{\omega}$$

from which we obtain, again after multiplying with a test function $f(t)$ and integration over t,

$$f(0)\cos 0 = f(0) \ .$$

So we see that $\tilde{G}(\omega,t) \equiv \tilde{G}_2(\omega,t) = \frac{\theta(t)}{\omega}\sin\omega t$ is the general solution to (D.4). Since we want to have an expression for $G(z,t)$, we need to take the inverse Fourier transform of $\tilde{G}(\omega,t)$:

$$\begin{aligned} G(z,t) &= \frac{\theta(t)}{2\pi}\int_{-\infty}^{\infty} \mathrm{d}k \ \frac{\sin(kt)}{k}\ \mathrm{e}^{-ikz} \\ &= \frac{\theta(t)}{2\pi}\int_{-\infty}^{\infty} \mathrm{d}k \ \left(\frac{\sin(kt)\cos(kz)}{k} - i\frac{\sin(kt)\sin(kz)}{k}\right) \\ &= \frac{\theta(t)}{2\pi}\int_{-\infty}^{\infty} \mathrm{d}k \ \frac{\sin(kt)\cos(kz)}{k} \ , \end{aligned}$$

where we used $e^{-x} = \cos x - i\sin x$ from the first to the second line. From second to the third line, we used the fact that $\frac{\sin(ckt)\sin(kz)}{k}$ is an odd function of k and therefore the integration vanishes. Now we use the trigonometric identity

$$\sin x\cos y = \frac{1}{2}(\sin(x-y)+\sin(x+y))$$

and obtain

$$G(z,t) = \frac{\theta(t)}{4\pi}\int_{-\infty}^{\infty} \mathrm{d}k \ \left(\frac{\sin k(t-z)}{k} + \frac{\sin k(t+z)}{k}\right) \ . \tag{D.8}$$

To calculate the integral

$$\int_{-\infty}^{\infty} \mathrm{d}k \ \frac{\sin\alpha k}{k} \ ,$$

we proceed by introducing the rectangular function

$$\mathrm{Rect}(z/\tau) := \theta(z/\tau + 1/2) - \theta(z/\tau - 1/2) \ ,$$

which is just a square function of length τ with value 1 for $z \in (-\tau/2, \tau/2)$ and zero otherwise. We now take the Fourier transform of $\mathrm{Rect}(z/\tau)$:

$$\int_{\infty}^{\infty} \mathrm{d}z \ \mathrm{Rect}(z/\tau)\ \mathrm{e}^{-ikz} = \int_{\tau/2}^{\tau/2} \mathrm{d}z \ e^{-ikz} = 2\ \frac{\sin\frac{\tau k}{2}}{k} \ . \tag{D.9}$$

If we set $\tau = 2\alpha$ in (D.9), we can write:

$$\begin{aligned} \int_{-\infty}^{\infty} \mathrm{d}k \ \frac{\sin\alpha k}{k} &= \frac{1}{2}\int_{-\infty}^{\infty} \mathrm{d}k \int_{-\infty}^{\infty} \mathrm{d}z \ \mathrm{Rect}\,(z/2\alpha)\, e^{-ikz} \\ &= \alpha\int_{-\infty}^{\infty} \mathrm{d}y \ \mathrm{Rect}(y) \int_{-\infty}^{\infty} \mathrm{d}k \ \mathrm{e}^{-2i\alpha y} \\ &= \pi\frac{\alpha}{|\alpha|}\int_{-\infty}^{\infty} \mathrm{d}y \ \mathrm{Rect}(y)\delta(y) \\ &= \pi\mathrm{sign}(\alpha) \end{aligned}$$

From the second to the third equality sign, we made the substitution $y = z/2\alpha$ and interchanged the order of integrations, from the third to the fourth we used (D.2) and the relation $\delta(ky) = \delta(y)/|k|$. The Green's function (D.8) therefore reads

$$G(z,t) = \frac{\theta(t)}{4}\left[\mathrm{sign}(t-z) + \mathrm{sign}(t+z)\right] \ .$$

To further simplify this expression, we use

$$\frac{1}{2}\left[\operatorname{sign}(t-x)+\operatorname{sign}(t+x)\right]=\theta(t-|x|)$$

and arrive at our final formula:

$$G(z,t)=\frac{\theta(t)}{2}\theta(t-|z|)\ .$$

Appendix E

Numerical Method

E.1 Biased Finite Differences

The action of the matrix $\mathbf{D}$ on the vector $\tilde{\mathbf{u}}$ can be encoded in the use of an adaption of the DSS020 function from [Sch91]:

$$\mathbf{D}\tilde{\mathbf{u}} = \begin{pmatrix} d_-(u_1^1) \\ d_-(u_2^1) \\ d_+(u_3^1) \\ d_+(u_4^1) \\ d_-(u_1^2) \\ d_-(u_2^2) \\ d_+(u_3^2) \\ d_+(u_4^2) \\ \vdots \end{pmatrix},$$

where the function $d_-(u^l)$ is defined as

$$\begin{aligned} d_-(u^l) := & \\ l = 1 : & \\ & q(-25u^1 + 48u^2 - 36u^3 + 16u^4 - 3u^5) \\ l = N-2 : & \\ & q(u^{N-4} - 8u^{N-3} + 8u^{N-1} - u^N) \\ l = N-1 : & \\ & q(-u^{N-4} + 6u^{N-3} - 18u^{N-2} + 10u^{N-1} + 3u^N) \\ l = N : & \\ & q(3u^{N-4} - 16u^{N-3} + 36u^{N-2} - 48u^{N-1} + 25u^N) \\ \text{else} : & \\ & q(-3u^{l-1} - 10u^l + 18u^{l+1} - 6u^{l+2} + u^{l+3}) \end{aligned}$$

with $q = 1/12\Delta z$ and $d_+(u^l)$ as

$$
\begin{aligned}
&d_+(u^l) := \\
&\quad l = 1 : \\
&\qquad q(-25u^1 + 48u^2 - 36u^3 + 16u^4 - 3u^5) \\
&\quad l = 2 : \\
&\qquad q(-3u^1 - 10u^2 + 18u^3 - 6u^4 + u^5) \\
&\quad l = 3 : \\
&\qquad q(u^1 - 8u^2 + 8u^4 - u^5) \\
&\quad l = N : \\
&\qquad q(3u^{N-4} - 16u^{N-3} + 36u^{N-2} - 48u^{N-1} + 25u^N) \\
&\quad \text{else} : \\
&\qquad q(-u^{l-3} + 6u^{l-2} - 18u^{l-1} + 10u^l + 3u^{l+1}).
\end{aligned}
$$

E.2 Matrices X and Y

The Maxwell equations in the plane wave setup can be written in matrix form:

$$(\mathbb{1}_4 + \mathbf{X})\,\partial_t \mathbf{f} + (\mathbf{Q} + \mathbf{Y})\,\partial_z \mathbf{f} = 0, \tag{E.1}$$

where $\mathbf{f} = (E_x, E_y, B_x, B_y)^T$, $\mathbb{1}_4$ is the identity in four dimensions, $\mathbf{Q}$ is an anti-diagonal matrix with $\mathbf{Q} = \mathrm{adiag}(1, -1, -1, 1)$ and $\mathbf{X} = (x_{ij})$, $\mathbf{Y} = (y_{ij})$ are the vacuum perturbation, where the non-zero elements are given by

$$
\begin{aligned}
x_{11} &= 4\pi\,(C_1 - C_2\rho_{11} - C_3\rho_{33} - 2C_4\rho_{13})\ , \\
x_{12} &= 4\pi\,(-C_2\rho_{12} - C_3\rho_{34} - C_4(\rho_{14} + \rho_{23}))\ , \\
x_{13} &= 4\pi\,((C_2 - C_3)\rho_{13} + C_4(\rho_{33} - \rho_{11}))\ , \\
x_{14} &= 4\pi\,(C_2\rho_{14} - C_3\rho_{23} + C_4(\rho_{34} - \rho_{12}))\ , \\
x_{21} &= 4\pi\,(-C_2\rho_{12} - C_3\rho_{34} - C_4(\rho_{14} + \rho_{23}))\ , \\
x_{22} &= 4\pi\,(C_1 - C_2\rho_{22} - C_3\rho_{44} - 2C_4\rho_{24})\ , \\
x_{23} &= 4\pi\,(C_2\rho_{23} - C_3\rho_{14} + C_4(\rho_{34} - \rho_{12}))\ , \\
x_{24} &= 4\pi\,((C_2 - C_3)\rho_{24} + C_4(\rho_{44} - \rho_{22}))\ , \\
y_{11} &= 4\pi\,(-C_2\rho_{14} + C_3\rho_{23} + C_4(\rho_{12} - \rho_{34}))\ , \\
y_{12} &= 4\pi\,(-(C_2 - C_3)\rho_{24} + C_4(\rho_{22} - \rho_{44}))\ , \\
y_{13} &= 4\pi\,(C_2\rho_{34} + C_3\rho_{12} - C_4(\rho_{14} + \rho_{23}))\ , \\
y_{14} &= 4\pi\,(C_1 + C_2\rho_{44} + C_3\rho_{22} - 2C_4\rho_{24})\ , \\
y_{21} &= 4\pi\,((C_2 - C_3)\rho_{13} + C_4(\rho_{33} - \rho_{11}))\ , \\
y_{22} &= 4\pi\,(C_2\rho_{23} - C_3\rho_{14} + C_4(\rho_{34} - \rho_{12}))\ , \\
y_{23} &= 4\pi\,(-C_1 - C_2\rho_{33} - C_3\rho_{11} + 2C_4\rho_{13})\ , \\
y_{24} &= 4\pi\,(-C_2\rho_{34} - C_3\rho_{12} + C_4(\rho_{14} + \rho_{23}))\ ,
\end{aligned}
$$

where we define $\rho_{ij} := 4f_i f_j$ such that e.g. $\rho_{14} = 4E_x B_y$ and the C_i are given by (2.72) and (2.73). .

Acknowledgements

DANK AN...

Meinen Doktorvater, Prof. Dr. Hartmut Ruhl, dafür, dass Du mir die Möglichkeit gegeben hast, mich im Rahmen dieser Arbeit in die mir neuen Gebiete der numerischen Mathematik, Quantenelektrodynamik in starken Feldern und nichtlinearer Differentialgleichungen einzuarbeiten.

Dr. Ben King, für die produktive Zusammenarbeit, die Begeisterung und Ausdauer, die Du bei allen Problemen der Physik an den Tag legst und dafür, dass Du Dir immer die Zeit genommen hast, meine Fragen zu beantworten.

Prof. Dr. Dieter Lüst, Prof. Dr. Otmar Biebel, Prof. Dr. Jörg Schreiber und Prof. Dr. Dieter Braun, für die Einwilligung, in meiner Prüfungskommission mitzuwirken und für die unkomplizierte Terminfindung.

Ute Tobiasch, dafür, dass Du Dich immer um alles Verwaltungstechnische gekümmert hast und dabei immer auf Dich Verlass war.

Claudia Barstorfer, Frederik Hetsch, Michael Kay, Nils Carqueville, Daniel Plencner und Maximilian Imgrund. Die Aufzählung ist dabei nur chronologisch gedacht. Danke für all die interessanten Gespräche und Unterhaltungen (egal, ob fachlicher, allgemeiner oder absurder Natur), das Teilen von vielen Ansichten im Leben und die Unterstützung in den schwierigen Momenten. Und auch für eine gewisse Nachsicht, falls man mal wieder eine Weile nichts mehr von mir gehört hat.

Karl-Ulrich Bamberg, für die Begleitung als treuer Leidensgenosse durch diese Doktorarbeit. Unsere unzähligen, gemeinsamen Mittagessen waren doch immer sehr kurzweilig. Durch Dich habe ich auch viel über Themen wie etwa High-Performance-Computing gelernt.

Matthias und Julia Apel, Peter Patalong, Andreas Deser, Susanne Barisch-Dick, Philipp Reineck, Martin Fuchs, Michael Heinlein und Salvatore Santoro, dafür, dass Ihr mich auch schon eine ganze Zeit begleitet, auch wenn Ihr das in letzter Zeit nicht unbedingt mehr so wahrgenommen habt.

Meine Familie, dabei insbesondere an meine Mutter und meine Schwester, für Eure kompromisslose Unterstützung über die ganzen Jahre.

Bibliography

[Adl+70] Stephen L Adler et al. „Photon splitting in a strong magnetic field“. In: *Physical Review Letters* 25.15 (1970), p. 1061.

[Adl71] S. L. Adler. „Photon splitting and photon dispersion in a strong magnetic field“. In: *Ann. Phys.* 67.2 (1971), pp. 599–647.

[AL83] D. Anderson and M. Lisak. „Nonlinear asymmetric self-phase modulation and self-steepening of pulses in long optical waveguides“. In: *Phys. Rev. A* 27 (3 1983), pp. 1393–1398. URL: http://link.aps.org/doi/10.1103/PhysRevA.27.1393.

[AWH12] G. B. Arfken, H. J. Weber, and F. E. Harris. *Mathematical Methods for Physicists*. seventh. Elsevier, 2012.

[BB67a] R. Baier and P. Breitenlohner. In: *Acta Phys. Austriaca* 25 (1967), p. 212.

[BB67b] R. Baier and P. Breitenlohner. In: *Nuovo Cim. B* 47 (1967), p. 117.

[BB70] Z. Bialynicka-Birula and I. Bialynicka-Birula. „Nonlinear effects in quantum electrodynamics. Photon propagation and photon splitting in an external field“. In: *Phys. Rev. D* 2.10 (1970), pp. 2341–2345.

[BB81] Z. Bialynicka-Birula. „Nonlinear phenomena in the propagation of electromagnetic waves in the magnetized vacuum“. In: *Physica D* 2 (1981), p. 513.

[BC89] Marsha J Berger and Phillip Colella. „Local adaptive mesh refinement for shock hydrodynamics“. In: *Journal of computational Physics* 82.1 (1989), pp. 64–84.

[BC91] Paul N Butcher and David Cotter. *The elements of nonlinear optics*. Vol. 9. Cambridge University Press, 1991.

[Bel97] R. Bellman. *Introduction to Matrix Analysis: Second Edition*. Classics in Applied Mathematics. Society for Industrial and Applied Mathematics, 1997. ISBN: 9780898713992. URL: https://books.google.de/books?id=sP8J4oqwlLkC.

[Ber+00] D. Bernard et al. „Search for stimulated photon-photon scattering in vacuum“. In: *Eur. Phys. J. D* 10 (2000), pp. 141–145.

[BGP06] T. Baeva, S. Gordienko, and A. Pukhov. „Theory of high-order harmonic generation in relativistic laser interaction with overdense plasma“. In: *Phys. Rev. E* 74 (2006), p. 046404. DOI: 10.1103/PhysRevE.74.046404. URL: http://link.aps.org/doi/10.1103/PhysRevE.74.046404.

[Bit13] José A Bittencourt. *Fundamentals of plasma physics*. Springer Science & Business Media, 2013.

[BKR16] P. Böhl, B. King, and H. Ruhl. „Vacuum high-harmonic generation and electromagnetic shock“. In: *Journal of Plasma Physics* 82 (02 Apr. 2016). ISSN: 1469-7807. DOI: 10.1017/S0022377816000210. URL: http://journals.cambridge.org/article_S0022377816000210.

[Bla66] David T Blackstock. „Connection between the Fay and Fubini solutions for plane sound waves of finite amplitude“. In: *The Journal of the Acoustical Society of America* 39.6 (1966), pp. 1019–1026.

[BLP82] V. B. Berestetskii, E. M. Lifshitz, and L. P. Pitaevskii. *Quantum Electrodynamics (second edition)*. Oxford: Butterworth-Heinemann, 1982.

[BMS01] G. Brodin, M. Marklund, and L. Stenflo. „Proposal for Detection of QED Vacuum Nonlinearities in Maxwells Equations by the Use of Waveguides“. In: *Phys. Rev. Lett.* 87.171801 (2001), p. 171801.

[BO84] M. J. Berger and J. Oliger. „Adaptive mesh refinement for hyperbolic partial differential equations“. In: *J. Comput. Phys.* 53 (1984), pp. 484–512.

[Bus08] Paul Busch. „Time in Quantum Mechanics“. In: ed. by J.G. Muga, R. Sala Mayato, and Í.L. Egusquiza. Berlin, Heidelberg: Springer Berlin Heidelberg, 2008. Chap. The Time–Energy Uncertainty Relation, pp. 73–105. ISBN: 978-3-540-73473-4. DOI: 10.1007/978-3-540-73473-4_3. URL: http://dx.doi.org/10.1007/978-3-540-73473-4_3.

[BW34] G. Breit and J. A. Wheeler. In: *Phys. Rep.* 46 (1934), p. 1087.

[CA92] R. Cooke and V.I. Arnold. *Ordinary Differential Equations*. Springer Textbook. Springer Berlin Heidelberg, 1992. ISBN: 9783540548133. URL: https://books.google.de/books?id=JUoyqlW7PZgC.

[Cad+14] A. Cadène et al. „Vacuum magnetic linear birefringence using pulsed fields: status of the BMV experiment“. In: *Eur. Phys. J.* D68 (2014), p. 16. DOI: 10.1140/epjd/e2013-40725-9. arXiv: 1302.5389 [physics.optics].

[Car80] M. B. Carver. „Pseudo characteristic method of lines solution of the conservation equations“. In: *Journal of Computational Physics* 35.1 (1980), pp. 57–76.

[CCY92] C-F. Chang, K. Cheung, and T-C. Yuan. „Formation of Very Strongly Magnetized Neutron Stars: Implications for Gamma-Ray Bursts“. In: *Astron. J.* 392.1 (1992), pp. L9–L13.

[cS00] Marin Soljači ć and Mordechai Segev. „Self-trapping of electromagnetic beams in vacuum supported by QED nonlinear effects“. In: *Phys. Rev. A* 62 (4 2000), p. 043817. DOI: 10.1103/PhysRevA.62.043817. URL: http://link.aps.org/doi/10.1103/PhysRevA.62.043817.

[DG00] W. Dittrich and H. Gies. *Probing the Quantum Vacuum*. Berlin: Springer-Verlag, 2000.

[DH99] G. V. Dunne and T. M. Hall. „Borel summation of the derivative expansion and effective actions“. In: *Phys. Rev. D* 60 (1999), p. 065002.

[DHK05] A. Di Piazza, K. Z. Hatsagortsyan, and C. H. Keitel. „Harmonic generation from laser-driven vacuum“. In: *Phys. Rev. D* 72 (2005), p. 085005.

[DHK06] A. Di Piazza, K. Z. Hatsagortsyan, and C. H. Keitel. „Light Diffraction by a Strong Standing Electromagnetic Wave“. In: *Phys. Rev. Lett.* 97.083603 (2006), p. 083603.

[Din+14a] V. Dinu et al. „Photon polarization in light-by-light scattering: Finite size effects“. In: *Phys. Rev. D* 90 (2014), p. 045025. DOI: 10.1103/PhysRevD.90.045025. URL: http://link.aps.org/doi/10.1103/PhysRevD.90.045025.

[Din+14b] V. Dinu et al. „Vacuum refractive indices and helicity flip in strong-field QED“. In: *Phys. Rev. D* 89 (2014), p. 125003. DOI: 10.1103/PhysRevD.89.125003. URL: http://link.aps.org/doi/10.1103/PhysRevD.89.125003.

[Din16] Michael Dine. *Supersymmetry and string theory: Beyond the standard model*. Cambridge University Press, 2016.

[Dir27] P. A. M. Dirac. „The Quantum Theory of the Emission and Absorption of Radiation“. In: *Proceedings of the Royal Society of London A: Mathematical, Physical and Engineering Sciences* 114.767 (1927), pp. 243–265. ISSN: 0950-1207. DOI: 10.1098/rspa.1927.0039. URL: http://rspa.royalsocietypublishing.org/content/114/767/243.

[Dir31] P. A. M. Dirac. „Quantised Singularities in the Electromagnetic Field“. In: *Proceedings of the Royal Society of London A: Mathematical, Physical and Engineering Sciences* 133.821 (1931), pp. 60–72. ISSN: 0950-1207. DOI: 10.1098/rspa.1931.0130. URL: http://rspa.royalsocietypublishing.org/content/133/821/60.

[Dun12] Gerald V. Dunne. „The Heisenberg-Euler Effective Action: 75 years on“. In: *Int. J. Mod. Phys.* A27 (2012). [Int. J. Mod. Phys. Conf. Ser.14,42(2012)], p. 1260004. arXiv: 1202.1557 [hep-th].

[EH04] B. O. Enflo and C. M. Hedberg. *Theory of Nonlinear Acoustics in Fluids*. 2004. DOI: 10.1007/0-306-48419-6.

[EH99] Bengt Enflo and Claes Hedberg. „Fourier decomposition of a plane nonlinear sound wave and transition from Fubini´ s to Fay´ s solution of Burger´ s equation“. In: *Nonlinear Acoustics at the Turn of the Millenium, Proceedings of 15th International Symposium on Nonlinear Acoustics, Göttingen, Germany,* American Institute of Physics, Melville, New York. 1999.

[EK35] Hans Euler and Bernhard Kockel. „Über die streuung von licht an licht nach der diracschen theorie“. In: *Naturwissenschaften* 23.15 (1935), pp. 246–247.

[EL] *Extreme Light Infrastructure*. http://www.eli-np.ro/.

[ER15] N. Elkina and H. Ruhl. „Reflection-free finite volume Maxwell's solver for adaptive grids“. In: *ArXiv e-prints* (Nov. 2015). arXiv: 1511.04994 [physics.comp-ph].

[FD08] P. C. Ferreira and J. D. de Deus. „QCD corrections to QED vacuum polarization“. In: *Eur. Phys. J. C* 54 (2008), pp. 539–545.

[Fer+07] A. Ferrando et al. „Nonlinear Phase Shift from Photon-Photon Scattering in Vacuum“. In: *Phys. Rev. Lett.* 99.15 (2007), p. 150404. DOI: 10.1103/PhysRevLett.99.150404.

[FG35] E. Fubini-Ghiron. „Anomalie nella propagazione di onde acustiche di grande ampiezza“. In: *Alta Frequenza* 4 (1935), pp. 530–581.

[FN07] A.M. Fedotov and N.B. Narozhny. „Generation of harmonics by a focused laser beam in the vacuum“. In: *Physics Letters A* 362.1 (2007), pp. 1 –5. ISSN: 0375-9601. DOI: http://dx.doi.org/10.1016/j.physleta.2006.09.085. URL: http://www.sciencedirect.com/science/article/pii/S0375960106015271.

[Foc37] Vladimir Aleksandrovich Fock. „Eigen-time in classical and quantum mechanics“. In: *Izv. Akad. Nauk SSSR* 4.5 (1937), p. 551.

[FW63] P. A. Franken and J. F. Ward. „Optical Harmonics and Nonlinear Phenomena“. In: *Rev. Mod. Phys.* 35 (1963), pp. 23–39. DOI: 10.1103/RevModPhys.35.23. URL: http://link.aps.org/doi/10.1103/RevModPhys.35.23.

[Gho+13] Pranab Ghosh et al. „White Paper on GEMS Study of Polarized X-rays from Neutron Stars“. In: (2013). arXiv: 1301.5514 [astro-ph.HE].

[GKS13] H. Gies, F. Karbstein, and N. Seegert. „Quantum reflection as a new signature of quantum vacuum nonlinearity“. In: *New J. Phys.* 15 (2013), p. 083002. URL: http://stacks.iop.org/1367-2630/15/i=8/a=083002.

[GKS14] H. Gies, F. Karbstein, and R. Shaisultanov. In: *Phys. Rev. D* 90 (2014), p. 033007. DOI: 10.1103/PhysRevD.90.033007. URL: http://link.aps.org/doi/10.1103/PhysRevD.90.033007.

[Gor+04] S. Gordienko et al. „Relativistic Doppler Effect: Universal Spectra and Zeptosecond Pulses“. In: *Phys. Rev. Lett.* 93 (11 2004), p. 115002. DOI: 10.1103/PhysRevLett.93.115002. URL: http://link.aps.org/doi/10.1103/PhysRevLett.93.115002.

[Gor+05] S. Gordienko et al. „Coherent Focusing of High Harmonics: A New Way Towards the Extreme Intensities“. In: *Phys. Rev. Lett.* 94 (10 2005), p. 103903. DOI: 10.1103/PhysRevLett.94.103903. URL: http://link.aps.org/doi/10.1103/PhysRevLett.94.103903.

[GR07] I. Gradshteyn and I. Ryzhik. *Table of Integrals, Series, and Products*. Academic Press, San Diego, 2007.

[GR11] H. Gies and L. Roessler. „Vacuum polarization tensor in inhomogeneous magnetic fields“. In: *Phys. Rev. D* 84 (2011), p. 065035.

[GS96] V. P. Gusynin and I. A. Shovkovy. „Derivative expansion for the one-loop effective Lagrangian in QED“. In: *Can. J. Phys.* 74 (1996), p. 282.

[GS99] V. P. Gusynin and I. A. Shovkovy. „Derivative expansion of the effective action for QED in 2+1 and 3+1 dimensions“. In: *J. Math. Phys.* 40 (1999), p. 5406.

[GVL12] G. H. Golub and C. F. Van Loan. *Matrix computations*. Vol. 3. JHU Press, 2012.

[Hal33] O Halpern. „Scattering processes produced by electrons in negative energy states“. In: *Physical Review* 44.10 (1933), p. 855.

[Har+10] Fiona A. Harrison et al. „The Nuclear Spectroscopic Telescope Array (NuSTAR)“. In: *Proc. SPIE* 7732 (2010), 77320S–77320S–8. DOI: 10.1117/12.858065. URL: http://dx.doi.org/10.1117/12.858065.

[HE36] W. Heisenberg and H. Euler. „Folgerungen aus der Diracschen Theorie des Positrons“. In: *Z. Phys.* 98 (1936), p. 714.

[Hei+06] T. Heinzl et al. „On the observation of vacuum birefringence“. In: *Opt. Commun.* 267 (2006), pp. 318–321.

[HH14] Huayu Hu and Jie Huang. „Modified light-cone condition via vacuum polarization in a time-dependent field“. In: *Phys. Rev. A* 90 (2014), p. 062111. DOI: 10.1103/PhysRevA.90.062111. URL: http://link.aps.org/doi/10.1103/PhysRevA.90.062111.

[HH98] J. S. Heyl and L. Hernquist. „Electromagnetic shocks in strong magnetic fields“. In: *Phys. Rev. D* 58 (1998), p. 043005.

[HH99] J. S. Heyl and L. Hernquist. „Nonlinear QED effects in strong-field magnetohydrodynamics“. In: *Phys. Rev. D* 59 (1999), p. 045005.

[HI] *Helmholtz International Beamline for Extreme Fields at the European XFEL*. http://www.hzdr.de/db/Cms?pOid=35325&pNid=3214.

[Hin+05] A. C. Hindmarsh et al. „SUNDIALS: Suite of Nonlinear and Differential/Algebraic Equation Solvers“. In: *ACM Trans. Math. Softw.* 31.3 (Sept. 2005), pp. 363–396. ISSN: 0098-3500. DOI: 10.1145/1089014.1089020. URL: http://doi.acm.org/10.1145/1089014.1089020.

[HL01] W. C. G. Ho and D. Lai. „Atmospheres and spectra of strongly magnetized neutron stars“. In: *Mon. Not. R. Astron. Soc.* 327 (2001), pp. 1081–1096.

[HL03] W. C. G. Ho and D. Lai. „Atmospheres and spectra of strongly magnetized neutron stars - II. The effect of vacuum polarization“. In: *Mon. Not. R. Astron. Soc.* 338 (2003), pp. 233–252.

[HL04] W. C. G. Ho and D. Lai. „SPECTRAL FEATURES IN THE THERMAL EMISSION FROM ISOLATED NEUTRON STARS: DEPENDENCE ON MAGNETIC FIELD STRENGTHS“. In: *Astrophys. J* 607 (2004), pp. 420–425.

[HL06] A. K. Harding and D. Lai. „Physics of strongly magnetized neutron stars“. In: *Rep. Prog. Phys.* 69.9 (2006), pp. 2631–2708.

[Kay16] Michael M. Kay. Private Communication. 2016.

[KBR14] B. King, P. Böhl, and H. Ruhl. „Interaction of photons traversing a slowly varying electromagnetic background“. In: *Phys. Rev. D* 90 (6 2014), p. 065018.

[KBR16] B. King, P. Böhl, and H. Ruhl. „Vacuum high-harmonic generation in the shock regime and photon-photon scattering dynamics“. In: *Journal of Physics: Conference Series* 691.1 (2016), p. 012022. URL: http://stacks.iop.org/1742-6596/691/i=1/a=012022.

[KDG12] B. King, A. Di Piazza, and H. Gies. In: *Phys. Rev. D* 86.125007 (2012), p. 125007.

[KDK10] B. King, A. Di Piazza, and C. H. Keitel. „Double-slit vacuum polarisation effects in ultra-intense laser fields“. In: *Phys. Rev. A* 82 (2010), p. 032114.

[KGDP13] B King, H Gies, and A Di Piazza. „Erratum: Pair production in a plane wave by thermal background photons [Phys. Rev. D 86, 125007 (2012)]“. In: *Phys. Rev. D* 87.6 (2013), p. 069905.

[KH11] G. Y. Kryuchkyan and K. Z. Hatsagortsyan. „Bragg Scattering of Light in Vacuum Structured by Strong Periodic Fields“. In: *Phys. Rev. Lett.* 107 (2011), p. 053604. DOI: 10.1103/PhysRevLett.107.053604.

[KH16] B. King and T. Heinzl. „Measuring vacuum polarization with high-power lasers“. In: *High Power Laser Science and Engineering* 4 (2016), e5 (12 pages). ISSN: 2052-3289. DOI: 10.1017/hpl.2016.1. arXiv: hep-ph/1510.08456 [hep-ph]. URL: http://journals.cambridge.org/article_S2095471916000013.

[Kin+07] P. Kinsler et al. „Optical carrier wave shocking: Detection and dispersion“. In: *Phys. Rev. E* 75 (2007), p. 066603.

[Kin10] B. King. „Vacuum Polarisation Effects in Intense Laser Fields“. PhD thesis. Ruprecht-Karls-Universität Heidelberg http://www.ub.uni-heidelberg.de/archiv/10846, 2010.

[Kin14] B. King. „Double Compton scattering in a constant crossed field“. In: (2014). eprint: arXiv:1410.5478 (hep-th).

[KK12] B King and CH Keitel. „Photonphoton scattering in collisions of intense laser pulses“. In: *New Journal of Physics* 14.10 (2012), p. 103002. URL: http://stacks.iop.org/1367-2630/14/i=10/a=103002.

[KN50] R. Karplus and M. Neuman. „Non-Linear Interactions between Electromagnetic Fields“. In: *Phys. Rev.* 80 (3 1950), pp. 380–385. DOI: 10.1103/PhysRev.80.380.

[KPK10] B. King, A. Di Piazza, and C. H. Keitel. „A matterless double-slit“. In: *Nature Photon.* 4 (2010), pp. 92–94.

[KS15] F. Karbstein and R. Shaisultanov. „Photon propagation in slowly varying inhomogeneous electromagnetic fields“. In: (2015). arXiv: 1503.00532 [hep-ph].

[KT07] Dmitri Kharzeev and Kirill Tuchin. „Vacuum self-focusing of very intense laser beams“. In: *Phys. Rev. A* 75 (4 2007), p. 043807. DOI: 10.1103/PhysRevA.75.043807. URL: http://link.aps.org/doi/10.1103/PhysRevA.75.043807.

[Lee+14] W. P. Leemans et al. „Multi-GeV Electron Beams from Capillary-Discharge-Guided Subpetawatt Laser Pulses in the Self-Trapping Regime“. In: *Phys. Rev. Lett.* 113 (2014), p. 245002.

[Lev68] L. Levi. *Applied Optics*. New York: John Wiley & Sons, Inc., 1968.

[LJP96] R. Lichters, J. Meyer-ter-Vehn, and A. Pukhov. „Shortpulse laser harmonics from oscillating plasma surfaces driven at relativistic intensity“. In: *Physics of Plasmas (1994-present)* 3.9 (1996), pp. 3425–3437. DOI: http://dx.doi.org/10.1063/1.871619.

[LLV92] Randall J LeVeque and Randall J Le Veque. *Numerical methods for conservation laws*. Vol. 132. Springer, 1992.

[LT59] M. Lutzky and J. S. Toll. „Formation of Discontinuities in Classical Nonlinear Electrodynamics“. In: *Phys. Rep.* 113 (1959), p. 1649.

[LT85] Peter Lancaster and Miron Tismenetsky. *The theory of matrices: with applications*. Academic press, 1985.

[Lun+06] E. Lundström et al. „Using High-Power Lasers for Detection of Elastic Photon-Photon Scattering“. In: *Phys. Rev. Lett.* 96 (2006), p. 083602. DOI: 10.1103/PhysRevLett.96.083602. URL: http://link.aps.org/abstract/PRL/v96/e083602.

[Lup+14] Mattia Lupetti et al. „Attosecond Photoscopy of Plasmonic Excitations“. In: *Phys. Rev. Lett.* 113 (11 2014), p. 113903. DOI: 10.1103/PhysRevLett.113.113903. URL: http://link.aps.org/doi/10.1103/PhysRevLett.113.113903.

[Mah02] G. D. Mahan. *Applied Mathematics*. New York: Springer Science+Business Media, 2002.

[Mar10] M. Marklund. „Fundamental optical physics: Probing the quantum vacuum“. In: *Nature Photon.* 4.2 (2010), pp. 72–74.

[Max63] J Clerk Maxwell. „A Dynamical Theory of the Electromagnetic Field.“ In: *Proceedings of the Royal Society of London* 13 (1863), pp. 531–536.

[Maz+79] E. P. Mazets et al. In: *Nature* 282 (1979), p. 687.

[McD00] Kirk T McDonald. *Gaussian laser beams with radial polarization*. 2000. URL: http://www.physics.princeton.edu/~mcdonald/examples/axicon_big.pdf.

[McK+13] P. McKenna et al. *Laser-Plasma Interactions and Applications*. Springer, 2013.

[Men+06] J. T. Mendonca et al. „Photon acceleration in vacuum“. In: *Phys. Lett. A* 359 (2006), pp. 700–704.

[Meu+15] S. Meuren et al. „Polarization-operator approach to pair creation in short laser pulses“. In: *Phys. Rev. D* 91 (2015), p. 013009.

[MK11] Y. Monden and R. Kodama. „Enhancement of Laser Interaction with Vacuum for a Large Angular Aperture“. In: *Phys. Rev. Lett.* 107 (2011), p. 073602.

[MME81] SG Mamaev, VM Mostapanenko, and MI Eides. „Effective action for alternate electromagnetic field and perturbation theory“. In: *Sov. J. Nucl. Phys* 33 (1981), p. 569.

[MN04] J. V. Moloney and A. C. Newell. *Nonlinear Optics*. Oxford, UK: Westview Press, 2004.

[MNT15] Peter J. Mohr, David B. Newell, and Barry N. Taylor. „CODATA Recommended Values of the Fundamental Physical Constants: 2014“. In: (2015). arXiv: 1507.07956.

[MS06] M. Marklund and P. K. Shukla. „Nonlinear collective effects in photon-photon and photon-plasma interactions“. In: *Rev. Mod. Phys.* 78 (2006), p. 591.

[MSE05] M. Marklund, P. K. Shukla, and B. Eliasson. „The intense radiation gas“. In: *Europhys. Lett.* 70.3 (2005), pp. 327–333.

[Nor+96] P. A. Norreys et al. „Efficient Extreme UV Harmonics Generated from Picosecond Laser Pulse Interactions with Solid Targets“. In: *Phys. Rev. Lett.* 76 (11 1996), pp. 1832–1835. DOI: 10.1103/PhysRevLett.76.1832. URL: http://link.aps.org/doi/10.1103/PhysRevLett.76.1832.

[NR64] A. I. Nikishov and V. I. Ritus. „Quantum processes in the field of a plane electromagnetic wave and in a constant field I“. In: *Sov. Phys. JETP* 19.2 (1964), pp. 529–541.

[Nyq28] H Nyquist. „Certain Topics in Telegraph Transmission Theory“. In: *American Institute of Electrical Engineers, Transactions of the* 47.2 (1928), pp. 617–644.

[Pau+58] Wolfgang Pauli et al. *Die allgemeinen prinzipien der wellenmechanik*. Springer Berlin, 1958.

[Pau33] Wolfgang Pauli. *Die allgemeinen Prinzipien der Wellenmechanik*. Springer, 1933.

[PFT] William H Press, Brian P Flannery, and Saul A Teukolsky. *Numerical recipes*.

[Pik+14] OJ Pike et al. „A photon-photon collider in a vacuum hohlraum“. In: *Nature Photon.* 8.6 (2014), pp. 434–436.

[PR72] V. O. Papanyan and V. I. Ritus. In: *Sov. Phys. JETP* 34.1195 (1972), p. 1195.

[PS95] Michael E. Peskin and Daniel V. Schroeder. *An Introduction to quantum field theory*. 1995. ISBN: 9780201503975, 0201503972. URL: http://www.slac.stanford.edu/spires/find/books/www?cl=QC174.45%3AP4.

[PV] INFN Trieste. *The PVLAS experiment*. http://pvlas.ts.infn.it/index.html.

[Péc12] Hans L Pécseli. *Waves and oscillations in plasmas*. CRC Press, 2012.

[Rad+08] S. Radnor et al. „Carrier-wave steepened pulses and gradient-gated high-order harmonic generation". In: *Phys. Rev. A* 77 (2008), p. 033806. DOI: 10.1103/PhysRevA.77.033806. URL: http://link.aps.org/doi/10.1103/PhysRevA.77.033806.

[Rei62] H. R. Reiss. „Absorption of Light by Light". In: *J. Math. Phys.* 3.1 (1962), pp. 59–67. DOI: http://dx.doi.org/10.1063/1.1703787.

[Rit85] V. I. Ritus. „Quantum effects of the interaction of elementary particles with an intense electromagnetic field". In: *J. Russ. Laser Res.* 6.5 (1985), pp. 497–617.

[Ros07] T. D. Rossing. *Springer Handbook of Acoustics*. Springer, 2007.

[Roz93] N. N. Rozanov. „Four-wave interactions of intense radiation in vacuum". In: *Sov. Phys. JETP* 76 (1993), p. 991.

[Rud95] O. V. Rudenko. „Nonlinear sawtooth-shaped waves". In: *Physics-Uspekhi* 38.9 (1995), pp. 965–989. DOI: 10.1070/PU1995v038n09ABEH000104. URL: http://ufn.ru/en/articles/1995/9/b/.

[Ryd96] L. H. Ryder. *Quantum Field Theory (second edition)*. Cambridge, 1996.

[Sau31] F. Sauter. „Über das Verhalten eines Elektrons im homogenen elektrischen Feld nach der relativistischen Theorie Diracs". In: *Z. Phys.* 69 (1931), pp. 742–764. DOI: 10.1007/BF01339461.

[SBN04] Albert Stolow, Arthur E Bragg, and Daniel M Neumark. „Femtosecond time-resolved photoelectron spectroscopy". In: *Chemical Reviews* 104.4 (2004), pp. 1719–1758.

[Sch13] Matthew D Schwartz. *Quantum field theory and the standard model*. Cambridge University Press, 2013.

[Sch51] J. Schwinger. „On gauge invariance and vacuum polarization". In: *Phys. Rev.* 82 (1951), pp. 664–679.

[Sch91] W. E. Schiesser. *The numerical method of lines integration of partial differential equations*. Vol. 17. Academic Press San Diego, 1991.

[Sei+16] D Seipt et al. „Caustic structures in x-ray Compton scattering off electrons driven by a short intense laser pulse". In: *New Journal of Physics* 18.2 (2016), p. 023044.

[Ser35] Robert Serber. „Linear modifications in the Maxwell field equations". In: *Physical Review* 48.1 (1935), p. 49.

[Sha49] Claude E Shannon. „Communication in the presence of noise". In: *Proceedings of the IRE* 37.1 (1949), pp. 10–21.

[She91] Michael Shearer. *Viscous profiles and numerical methods for shock waves*. Vol. 56. Siam, 1991.

[SN11] Jun John Sakurai and Jim Napolitano. *Modern quantum mechanics*. Addison-Wesley, 2011.

[Sre07] Mark Srednicki. *Quantum field theory*. Cambridge University Press, 2007.

[Str04] John C Strikwerda. *Finite difference schemes and partial differential equations*. SIAM, 2004.

[Sza11] Richard J Szabo. *An introduction to string theory and D-brane dynamics: with problems and solutions*. World Scientific, 2011.

[Tav+13] R. Taverna et al. „Probing magnetars magnetospheres through X-ray polarization mesaurements“. In: (2013). eprint: `arXiv:1311.7500`.

[Tho13] James William Thomas. *Numerical partial differential equations: finite difference methods*. Vol. 22. Springer Science & Business Media, 2013.

[TKN05] JCA Tyrrell*, P Kinsler, and GHC New. „Pseudospectral spatial-domain: a new method for nonlinear pulse propagation in the few-cycle regime with arbitrary dispersion“. In: *Journal of modern optics* 52.7 (2005), pp. 973–986.

[TM10] D. Tommasini and Humberto Michinel. „Light by light diffraction in vacuum“. In: *Phys. Rev. A (R)* 82 (2010), p. 011803.

[Tol52] John Sampson Toll. „The dispersion relation for light and its application to problems involving electron pairs“. PhD thesis. Princeton U., 1952.

[Tor13] Eleuterio F Toro. *Riemann solvers and numerical methods for fluid dynamics: a practical introduction*. Springer Science & Business Media, 2013.

[Trä07] Frank Träger. *Springer handbook of lasers and optics*. Springer Science & Business Media, 2007.

[Ueh35] EA Uehling. „Polarization effects in the positron theory“. In: *Physical Review* 48.1 (1935), p. 55.

[Wat51] G. N. Watson. *Theory of Bessel Functions*. 200 Euston Road, London, NW1: Cambridge, 1951.

[Wei36] V. Weisskopf. „Über die Elektrodynamik des Vakuums auf Grund der Quantentheorie des Elektrons“. In: *Kgl. Danske Videnskab. Selskab, Mat.-fys. Medd.* 14 (1936), p. 6.

[Whi11] Gerald Beresford Whitham. *Linear and nonlinear waves*. Vol. 42. John Wiley & Sons, 2011.

[Won15] Rachel Won. „High-harmonic generation: Vacuum effect“. In: *Nat Photon* 9.11 (2015). Research Highlights, pp. 707–707. ISSN: 1749-4885. URL: `http://dx.doi.org/10.1038/nphoton.2015.219`.

[WR12] Inc. Wolfram Research. *Mathematica*. Version 9.0. Champaign, Illinois: Wolfram Research, Inc., 2012.

[WSG08] Carsten Winterfeldt, Christian Spielmann, and Gustav Gerber. „ ***Colloquium*** : Optimal control of high-harmonic generation“. In: *Rev. Mod. Phys.* 80 (1 2008), pp. 117–140. URL: `http://link.aps.org/doi/10.1103/RevModPhys.80.117`.

[Yan+08] V. Yanovsky et al. „Ultra-high intensity- 300-TW laser at 0.1 Hz repetition rate“. In: *Opt. Express* 16 (2008), pp. 2109–2114.

[Zav+12] G. Zavattini et al. „Measuring the magnetic birefringence of vacuum: The PVLAS experiment“. In: *Int. J. Mod. Phys. A* 27 (2012), p. 1260017.

[ZF82] V. V. Zheleznyakov and A. L. Fabrikant. „Electromagnetic shock waves in a magnetized vacuum“. In: *Sov. Phys. JETP* 55 (1982), p. 794.

[Di +12] A. Di Piazza et al. „Extremely high-intensity laser interactions with fundamental quantum systems“. In: *Rev. Mod. Phys.* 84 (2012), pp. 1177–1228.